TU/e EINDHOVEN UNIVERSITY OF TECHNOLOGY

Atomic layer deposition for 2-D materials beyond graphene

Citation for published version (APA):
Sharma, A. (2018). *Atomic layer deposition for 2-D materials beyond graphene*. [Phd Thesis 1 (Research TU/e / Graduation TU/e), Applied Physics]. Technische Universiteit Eindhoven.

Document status and date:
Published: 12/12/2018

Document Version:
Publisher's PDF, also known as Version of Record (includes final page, issue and volume numbers)

Please check the document version of this publication:

• A submitted manuscript is the version of the article upon submission and before peer-review. There can be important differences between the submitted version and the official published version of record. People interested in the research are advised to contact the author for the final version of the publication, or visit the DOI to the publisher's website.
• The final author version and the galley proof are versions of the publication after peer review.
• The final published version features the final layout of the paper including the volume, issue and page numbers.

Link to publication

General rights
Copyright and moral rights for the publications made accessible in the public portal are retained by the authors and/or other copyright owners and it is a condition of accessing publications that users recognise and abide by the legal requirements associated with these rights.

• Users may download and print one copy of any publication from the public portal for the purpose of private study or research.
• You may not further distribute the material or use it for any profit-making activity or commercial gain
• You may freely distribute the URL identifying the publication in the public portal.

If the publication is distributed under the terms of Article 25fa of the Dutch Copyright Act, indicated by the "Taverne" license above, please follow below link for the End User Agreement:

www.tue.nl/taverne

Take down policy
If you believe that this document breaches copyright please contact us at:

openaccess@tue.nl

providing details and we will investigate your claim.

Download date: 15. Jul. 2022

Atomic Layer Deposition For 2-D Materials Beyond Graphene

PROEFSCHRIFT

ter verkrijging van de graad van doctor aan de Technische Universiteit Eindhoven, op gezag van de rector magnificus prof.dr.ir. F.P.T. Baaijens, voor een commissie aangewezen door het College voor Promoties, in het openbaar te verdedigen op woensdag 12 december 2018 om 11:00 uur

door

Akhil Sharma

geboren te Manoh Sihal, India

Dit proefschrift is goedgekeurd door de promotoren en de samenstelling van de promotiecommissie is als volgt:

voorzitter:	prof.dr.ir. G.J.F. van Heijst
1e promotor:	dr. A.A. Bol
2e promotor:	prof.dr.ir. W.M.M. Kessels
leden:	prof.dr. P.E. de Jongh (Universiteit Groningen)
	dr. A. Delabie (Katholieke Universiteit Leuven)
	prof.dr. J.C.T. Eijkel (Universiteit Twente)
	prof.dr. M.K. Matters-Kammerer
adviseur(s):	dr. R.S. Sundaram (Oxford Instruments Plasma Technology)

Het onderzoek dat in dit proefschrift wordt beschreven is uitgevoerd in overeenstemming met de TU/e Gedragscode Wetenschapsbeoefening.

This research was financially supported by NWO-TTW through the VIDI program on "Novel bottom-up nanofabrication techniques for future carbon-nanoelectronics" (VIDI 12379) and by the European Research Council (Grant Agreement No. 648787-ALDof2DTMDs).



Printed and bound by Ipskamp Printing, Enschede
Cover brief by : Akhil Sharma
Cover design by : Mohsin Raza, Media Outreach Network, New Delhi, India

A catalogue record is available from the Eindhoven University of Technology Library,
ISBN: 978-90-386-4658-9

Table of Contents

Chapter 1	Introduction	7
Chapter 2	ALD of sulphides and characterization of 2-D MoS_2	27
Chapter 3	Low-temperature plasma-enhanced atomic layer deposition of 2-D MoS_2: large area, thickness control and tuneable morphology A. Sharma, M. A. Verheijen, L. Wu, S. Karwal, V. Vandalon, H. C. M. Knoops, R. S. Sundaram, J. P. Hofmann, W. M. M. Kessels, A. A. Bol, *Nanoscale* **2018**, 10, 8615	57
Chapter 4	Tuning the wettability of MoS_2 nanostructures using plasma-enhanced atomic layer deposition In preparation for publication	91
Chapter 5	High performance MoS_x thin films for hydrogen evolution reaction prepared by plasma enhanced atomic layer deposition In preparation for publication	103
Chapter 6	Plasma enhanced atomic layer deposition enabled uniform large area patterned growth of high quality MoS_2 In preparation for publication	121
Chapter 7	Atomic layer deposition of HfO_2 using $HfCp(NMe_2)_3$ and O_2 plasma A. Sharma†, V. Longo†, M. A. Verheijen, A. A. Bol and W. M. M. Kessels, *Journal of Vacuum Science & Technology A*, 2016, **35**, 01B130. † A. Sharma and V. Longo contributed equally	149

Chapter 8 Conclusions and outlook 169

Summary 177

Contributions of the author 181

List of peer-reviewed publications 183

Acknowledgements 185

Curriculum Vitae 189

1

Introduction

"There's plenty of room at the bottom" : this famous lecture by Prof. Richard Feynmann at Caltech on December 29, 1959[1] embarked the idea of nanotechnology. In his lecture, Prof. Feynmann talked about the possibility of manufacturing computers and manipulating matter at the infinitesimal level which laid the foundation for future generation advanced electronics devices. Needless to say, today we are actually relishing the technology once a dream, be it the palm-sized smart phones, advanced personal computers, smart home appliances *etc*. Thanks to the advancement in the field of micro/nano electronics which has brought a digital revolution across the globe and has changed our lives. The electronics evolution has for a large part been driven by the continuous shrinking of the dimensions of field-effect transistors (FETs) – an integral in numerous electronic devices allowing them to achieve energy-efficient high-speed switching. This continuous shrinking or scaling has tracked Moore's law, a trend predicted by Gordon Moore (back in 1965) that the constituent transistors on an integrated circuit will double every 18-24 months.[2] Traditional FETs are, by far, based on bulk or 3D semiconductor channels composed of silicon, germanium and III-V semiconductors.[3] Remarkably, the semiconductor industry has established long-term strategies and research goals by successfully scaling down the dimensions of the conventional materials to the nanoscale, keeping Moore's law afloat for more than 50 years now (Figure 1.1).

However, as the scaling demands are getting more rigorous, the further reduction in dimensionalities of semiconducting materials is about to hit the fundamental limit causing the degradation of carrier transport properties and device to device variations. So, there is a need for substitute channel materials for FETs which can contribute to the miniaturization of electronic systems and facilitate to sustain the further progress labeled as 'More Moore'. In this context, a number of emerging research materials are in contention to drive the development and further scaling of transistors. A few to name are III-V nanowires, carbon nanotubes, graphene and 2-D materials beyond graphene. All of these materials have unique, useful properties and potential to satisfy the number of projected roadmap parameters laid out by the 'International roadmap for devices and systems' (IRDS). In fact, it has been predicted by IRDS that after 2027, there will be no headroom for 2-D geometry scaling anymore and the aforementioned emerging materials will play a key role in devising new strategies based on sequential/stacked integration in 3-D, very large scale integration of circuits and systems.[4] However, a number of challenges need to be addressed to warrant the successful incorporation of

these emerging materials into high volume manufacturing. The most vital and obvious requirement is the synthesis of high-quality materials by a viable, robust method capable of providing the potential solution on a technologically relevant scale for commercial applications. This thesis work focuses on synthesis of one of such emerging 2-D materials beyond graphene namely molybdenum disulphide (MoS_2), which belongs to a class of materials called as transition metal dichalcogenides (TMDs).

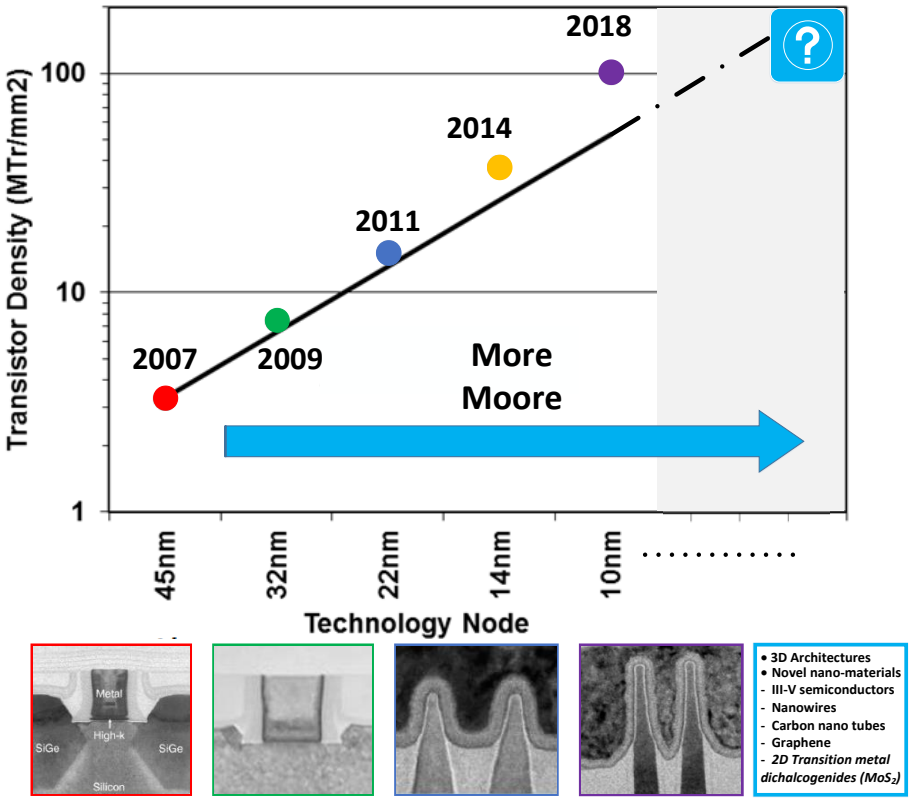


Figure 1.1 The development of the transistor technology in integrated circuits showing that the transistor density has almost doubled with each new generation. (bottom panel) The cross sectional images of transistor devices with innovative strategies (strained Si, High-k metal gate, 3D transistor architectures) adopted by Intel to sustain Moore's law. Image taken from [5].

1.1 2-D transition metal dichalcogenides (TMDs) as future materials

The exploration of other 2-D materials beyond graphene got stimulated after the landmark invention of graphene in 2004 by Geim and Novoselov[6] in a quest of future generation nano-electronics. To qualify for successful integration into monolithic architectures, an ideal FET should possess high *on-off ratio*[a] and steep *subthreshold slope*[b] as key figures of merit. (which are also recognized by IRDS as the crucial parameters).[4, 7] Graphene, despite its extraordinary electrical, optical, mechanical properties lacks a natural bandgap and is semi-metallic in nature.[8] This limits its applicability as a FET channel material because of its small on-off ratio (~30) as compared to the desired much higher order (10^4 - 10^7) for faster device switching. A number of approaches like quantum confinement of charge carriers from 2-D to 1-D in graphene nanoribbons, chemical doping, application of strain *etc*. have been demonstrated to tailor the electronic structure of graphene for opening up the band gap.[9-11] However, most of these methods remain extremely difficult and irreproducible towards commercialization of graphene for device applications. Nonetheless, despite the lack of a bandgap, graphene is still a strong contender for a variety of other applications including but not limited to radiofrequency applications, batteries, energy storage, flexible displays, conductive ink, heat spreader *etc*.[12, 13]

Fortunately, a broader family of materials, namely 2-D TMDs, exists which have comparable properties with graphene and have opened up a vast avenue for both fundamental researchers and future devices applications. The 2-D TMDs are inherently layered materials and contemplated as 'cousins' of graphene, with weak van der Waals interlayer interactions enabling the isolation down to a monolayer of these materials. Furthermore, their pristine surfaces without any dangling bonds and the natural in-plane confinement of charge carriers lead to excellent gate electrostatics resulting in superior device performance.[14] TMDs have a generalized formula MX_2 where M = metal from group IV-VII and X is a chalcogen atom (S, Se, Te). Although a variety of TMDs have been shown to exist, there is only a limited number of materials which are stable under

[a] The on-off ratio is defined as the ratio of the currents in the on- and off-states of a field effect transistor device.

[b] A device characterized by steep subthreshold slope exhibits a faster transition between off (low current) and on (high current) states.

ambient conditions. Most of these materials are easily exfoliated down to a monolayer level owing to the 'van der Waals' interlayer interaction analogous to graphene. The quantum confinement effect results in a new set of properties which in combination with their natural ultra-thin bodies make them interesting candidates for a variety of next-generation nano-electronics applications.

Amongst TMDs, MoS_2 is one of the most studied materials owing to its high abundance in earth, stability in ambient and amenability with other 2-D materials (such as graphene) to form heterostructures. MoS_2 resembles structurally with graphene having individual layers stacked upon each other to form the bulk. Each 2-D crystal layer of MoS_2 is ~ 0.65 nm thick[c] and has a plane of hexagonally arranged molybdenum atoms sandwiched between two planes of hexagonally arranged sulphur atoms.[15]

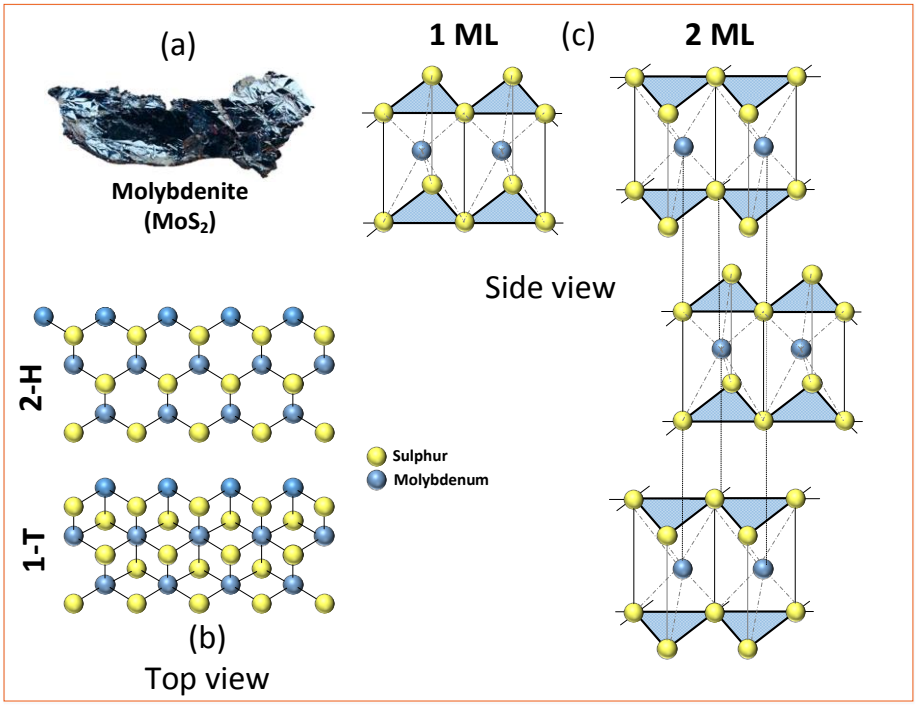


Figure 1.2 (a) An exfoliated flake of MoS_2 from a bulk crystal (b) Schematic top view of two polytypes i.e. 2-H (top) and 1-T (bottom) of MoS_2. A monolayer and trilayer for 2-H polytype are shown in (c) .

[c] The thickness of a monolayer is expressed as the distance between two Mo atomic planes in a bilayer of MoS_2.

The S-Mo-S unit is covalently bonded in a trigonal prismatic arrangement forming a hexagonal crystal structure. The two most commonly found crystal structures for MoS_2 are the hexagonal and octahedral configuration. While the former is specified as 2-H MoS_2 and is semiconducting in nature, the latter is known as 1-T MoS_2 with metallic nature. H and T represent hexagonal and trigonal symmetry of the crystal structure, respectively. In theory, the 2-H structure is more stable than 1-T. The Mo-S bond length is 2.4 Å, the crystal lattice constant is 3.2 Å and the distance between upper and lower sulphur atoms is 3.1 Å.[16]

MoS_2 has been demonstrated to possess a very high mechanical strength with a Young's modulus greater than steel.[17] Furthermore, the crystal layers of MoS_2 can be deformed by up to 11% without fracture and bent to a curvature of the radius of 0.75 mm[18] without losing their electronic properties which renders it highly promising material for flexible electronics applications. Electronically, MoS_2 has a natural band gap of 1.3 eV in the bulk regime and thus has an inherent advantage over graphene for nano-electronics applications (Figure 1.3). Strikingly, there is a transition from indirect band gap in bulk MoS_2 to a direct band gap of 1.8 eV in its mono-to-few layered regime which renders it super exciting for optoelectronics and new physical phenomena at the atomic scale.[19] A detailed explanation of the band gap transition will be discussed in chapter 2. It is therefore no wonder that MoS_2 has emerged as a strong candidate for plethora of applications such as field effect transistors, phototransistors, capacitive memories, humidity and gas sensors, heterostructures based architectures, electrocatalysis *etc.*[15]

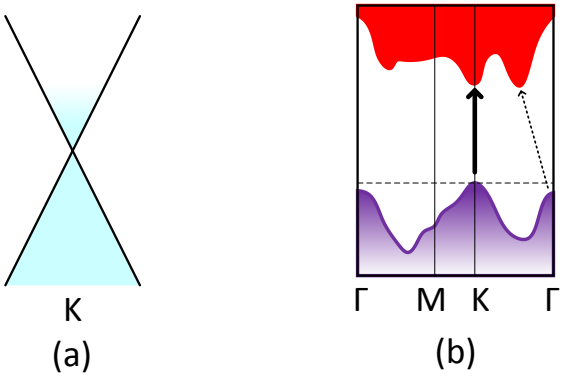


Figure 1.3 Electronic band structure for monolayer of (a) graphene and (b) MoS_2.

One of the outstanding features of MoS_2 is the possible thickness scaling down to a monolayer with unperturbed electronic properties providing a well - controlled electrostatics for ultrashort transistors.[20] For example, it has been demonstrated that the monolayer and few layer MoS_2 (< 5 nm) result in more than two orders of magnitude reduction in leakage current relative to Si as a channel layer in a nanoscale transistor device.[20] These qualities make MoS_2 a very strong candidate for the channel material of future transistor devices at the sub - 5 nm scaling limit.

At the other end of the spectrum, bulk MoS_2 is a conventional lubricant and is a popular dehydrosulphurization agent in the oil industry. In the 1980's, some studies were performed to analyze the effect of morphology of MoS_2 on its lubricating properties.[21, 22] In these studies, it had been shown that the MoS_2 can co-exist in two variant morphologies i.e. in-plane and out-of-plane oriented and it was found that the former morphology results in better lubricating properties.[23] Interestingly, as a matter of fact, after almost two decades it has been found that the latter morphology (i.e. out-of-plane oriented films) is rather also an interesting candidate in the field of electrocatalysis most prominently for hydrogen evolution reaction (HER) during water splitting.[24] This applicability is attributed to the highly energetic edge sites and it enables 2-D materials including MoS_2 to serve as potential alternatives to expensive noble metals in the field of electrocatalysis. In this context, Jaramillo *et al.* demonstrated that the HER activity of MoS_2 nanoparticles scaled up linearly with the increasing number of edge sites.[25] Since then, a plethora of reports have surfaced showing the applicability of 2-D materials for electrocatalysis. This has resulted into the emergence of *morphology engineering* for 2-D materials as an active research field and researchers all across the world are putting a tremendous effort into it. A number of papers including our work (see Chapter 3) have reported on the growth of vertically aligned/ edge oriented/ out-of-plane oriented MoS_2 films and on their further tuning to enhance the number of edge sites and hence the improved eletrocatalytic performance of MoS_2.

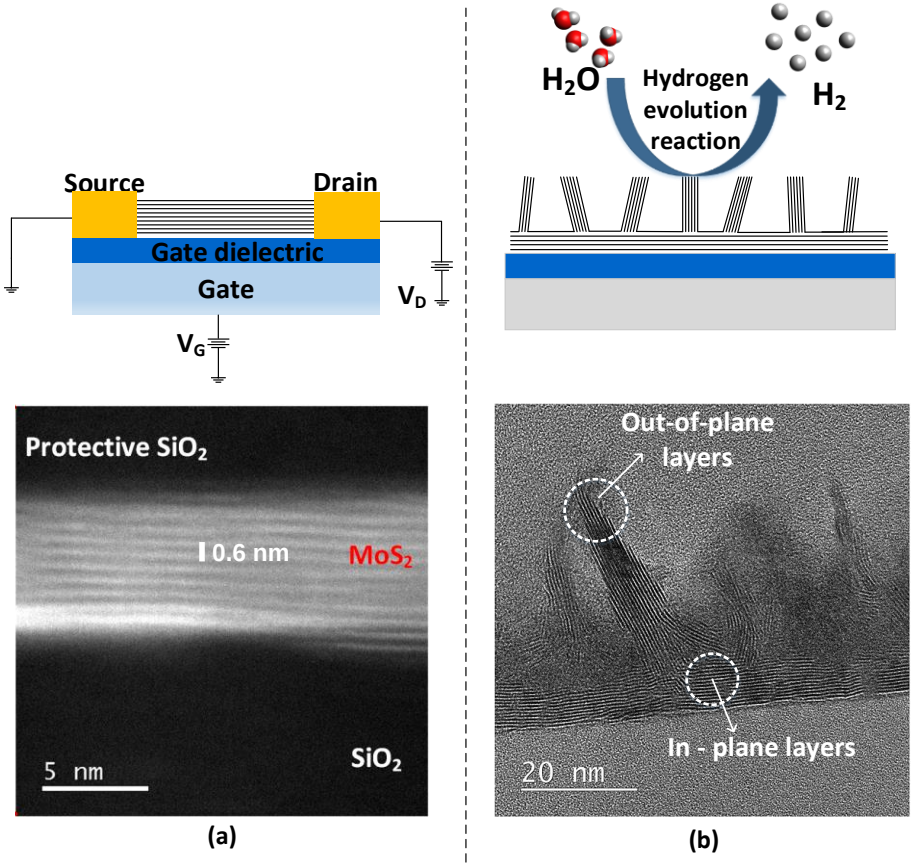


Figure 1.4 The morphology dependent applicability of 2-D MoS_2 thin films: (a) The atomically thin bodies of in-plane layers make them a promising candidate as a channel material for future field effect transistor device replacing silicon (as shown in the sketch on top). The high resolution transmission electron microscope (TEM) image is shown (bottom) for the in-plane layers synthesized by ALD based process in this work. (b) The active edge sites of out-of-plane oriented films render them suitable for electrocatalysis (HER) as shown in sketch (top). Shown at the bottom is a cross-sectional TEM image for film with mixed morphology as synthesized by PEALD process in this work.

1.1.1 Synthesis of MoS_2

One of the vital research fields for future 2-D TMDs based applications is the reliable synthesis of atomically thin 2-D layers of MoS_2 via scalable approaches. Hitherto, the

two major strategies which have been employed to obtain mono to few layered MoS_2 films are *top-down* methods such as mechanical or chemical exfoliation[26-28] and *bottom-up* synthetic methods like chemical vapor deposition[29, 30] *etc*. *'Top-down'* methods like 'scotch tape' exfoliation yield high quality and up to micrometer - sized crystal layers. However, the absence of layer number controllability and low productivity keeps the suitability of mechanical cleavage methods only up to fundamental research and proof-of-concept device fabrication scale. On the other hand, the chemical exfoliation of TMDs relies on the wet chemistry method in which the produced materials might be promising for solution based or printable electronics. However, often some extrinsic defects are introduced during the exfoliation process which requires a post treatment to reconstruct the structure of TMDs and thus makes this method less favorable for industrial applications.

Alternatively, the *bottom-up* methods such as chemical vapor deposition (CVD), sulphurization of metal (metal oxide) thin films provide a pool of parameters aiming at better control of thickness and properties of TMDs. Furthermore naturally, the bottom-up approach is the practical way of scalable production of TMDs and realizing their potential for device applications. Therefore, a lot of effort has been put into the research field of controlled synthesis of 2-D TMDs. In this context, the aforementioned techniques like CVD has been demonstrated as a promising method to yield high quality materials, yet it suffers from issues like reproducibility, non-uniformity of films over large area and most importantly the precise thickness control over number of layers in TMDs which is essential to gain maximum advantage from extraordinary properties of TMDs. Therefore, there is still a need for exploration of additional *bottom-up* methods capable of addressing the above stated issues to make the transition to industrial applications of TMDs. Such a deposition technique which might be able to meet the requirements is atomic layer deposition (ALD).

1.2 Atomic layer deposition (ALD)

ALD is a modified CVD technique designed specifically for the deposition of ultra-thin films at the nanoscale. The unique surface-chemistry driven self-limiting nature of ALD enables precise control of thickness at atomic scale, large-area uniformity and excellent conformality over intricate 3-D structures. In 2007, Intel introduced ALD in the process flow for the fabrication of high-k metal gate stack in transistor devices.[31] A number of

other application areas for ALD include but are not limited to deposition of high-κ oxides and metals for DRAM capacitors, passivation layers in solar cells and spacers for self-aligned multiple patterning (SAP) to increase the feature density during photolithography process for current and next generation nano-architectures.[32]

A schematic of a typical ALD cycle is shown in Figure 1.5. As shown, the surface is exposed to two or more gas/vapor phase reactants in a sequential manner. This sequence of steps generally can be categorized as two "half cycles". In some cases, there can be multiple "sub-cycles" depending on the material to be grown. In the first half-cycle, the substrate is exposed to the gaseous molecules, commonly referred to as 'precursor'. The precursor molecules adsorb on the available surface sites via chemical reactions (Figure 1.5 (a)). The adsorption however is self-limiting and stops once the sites are either depleted or physically unavailable (e.g. due to steric hindrance). After this point, no growth/deposition occurs irrespective of the precursor supply due to absence of favorable chemistry. The unwanted reaction products or excess precursor molecules are flushed away in the intermittent purge step leaving the surface with a sub-monolayer of adsorbed precursor molecule (together with ligands) as shown in Figure 1.5 (b).

In the second half cycle of the ALD process, the co-reactant is introduced in the chamber which apart from incorporating non-metal atoms in the films serves to (a) remove the ligands of the precursor (b) replenish the surface with identical groups at the beginning of ALD cycle (Figure 1.5 (c)). Once the co-reactant finishes the reaction with adsorbed precursor molecules (again in a self-limiting fashion), the subsequent purge step removes any unwanted by-product and the surface becomes ready for the first step of cycle again (Figure 1.5 (d)). The surface reactions are either driven by thermal energy or by providing additional energy to the co-reactant step for example by generating plasma. The former type of ALD is referred to as "Thermal ALD" while for latter the term "Plasma-ALD or "Plasma enhanced ALD (PEALD)" is used. PEALD offers several potential benefits in addition to the typical merits of thermal ALD like wide choices of precursors and materials due to the high reactivity of plasma radicals, improved material properties, deposition at low substrate temperatures, higher growth rates, increased processing versatility *etc*.[33, 34]

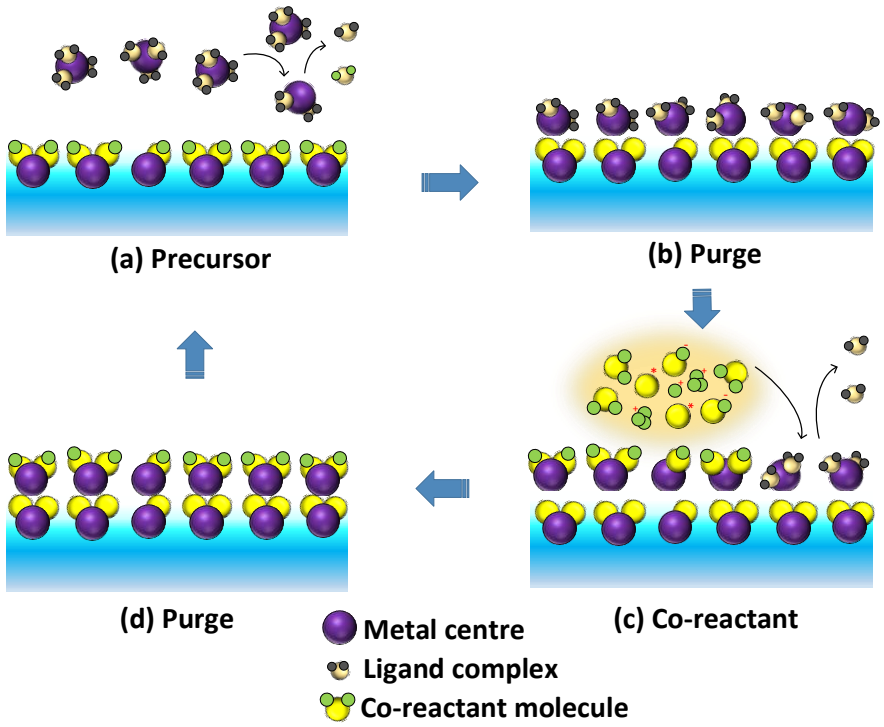


Figure 1.5 A schematic representation of typical steady-state PEALD cycle (a) Precursor step where self-limiting adsorption of precursor molecules on the existing surface groups occur. (b) Purging step in which unwanted reaction byproducts and unreacted precursor molecules are removed. (c) Co-reactant step where removal of ligands from the surface of adsorbed precursor molecules by energetic plasma species occur. In addition, the re-establishment of original surface species is acquired. (d) The final purging step for removing reaction products. This results in a surface similar to the starting surface in (a) covered with a sub-monolayer of the material to be deposited. The cycle can be repeated as many times as desired to reach the targeted thickness.

The highly repeatable and well controlled amount of material deposited by these sequence of steps is referred to as the growth-per-cycle (GPC). The repetitive nature of ALD cycle results in film deposition with sub-nanometer thickness control. The desired film thickness can therefore be reached by simply repeating the cycle as many times as required. Furthermore, the self-limiting nature of the surface reactions leads to growth which is completely independent of the precursor dosage.

That means, once the reactions are saturated (e.g. adequate precursor and co-reactant have been introduced), no further growth occurs irrespective of the additional surface exposure to any of the reactants. This scenario is illustrated in Figure 1.6. The schematic graphs shown in Figure 1.6 are referred to as 'saturation curves' which serve as the basis to design a recipe for a particular ALD process and attain the ultimate control over thickness.

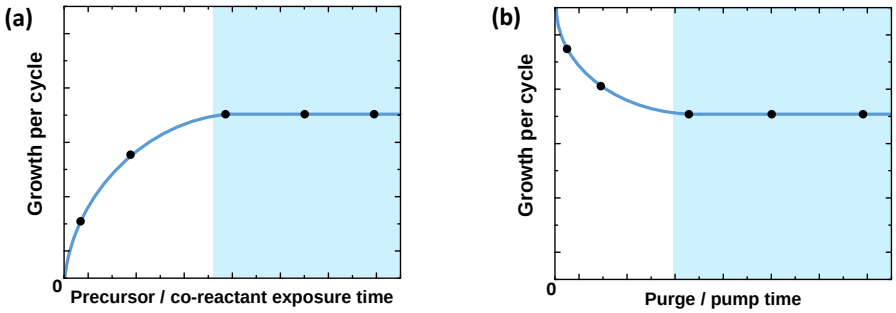


Figure 1.6 The schematic illustration of typical 'saturation curves' of an ALD process. (a) The exemplar plot showing the saturation behavior of the precursor or co-reactant steps. It is evident that the growth per cycle (GPC) of the film increases only until a certain point and then saturates despite the additional dosage of precursor or co-reactant. (b) Saturation of the pump or purge steps. An elevated GPC can be obtained under the insufficient purging/pumping due to undesired reactions in the gaseous phase. The saturated regime is highlighted (blue) in both cases.

Furthermore, a well-designed ALD process also offers many other advantages over conventional deposition techniques. Firstly, the incorporation of impurities can be minimized by the choice of precursor and co-reactant, e.g., the plasma co-reactant generally results in very low impurity concentrations in the resulting film. Furthermore, the self-limiting nature of ALD ensures large-area film uniformity upto the wafer scale. Additionally, ALD provides highly conformal films irrespective of the surface geometry i.e. a good step coverage is possible to obtain even in 3-dimensional structures with a high aspect ratio which is difficult to achieve with conventional techniques like sputtering or evaporation (physical vapor deposition, PVD). The difference between other deposition techniques (as stated above) and ALD is illustrated in Figure 1.7.

As aforementioned, depending on the choice of precursor and co-reactant, ALD is able to deposit a wide spectrum of materials including but not limited to metal-oxides

(e.g. Al_2O_3, Co_3O_4), metals (e.g. Pt, Pd), nitrides (e.g. SiN_x), fluorides (e.g. AlF_3) and sulphides (e.g. MoS_2).[35] Several reviews on different aspects of ALD (surface chemistry, precursor groups, ALD for variety of applications, atomic scale simulation, advanced ALD processes *etc*.), have been published in literature which the readers may find useful.[36-39]

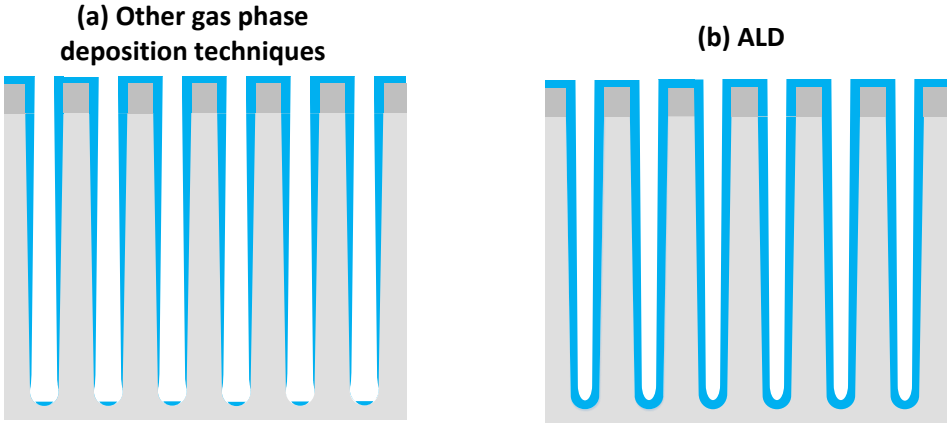


Figure 1.7 Schematic illustrating the difference between film profile (blue) deposited by (a) other gas phase techniques such as physical vapor deposition (PVD) and (b) ALD on high aspect ratio structures. While a conformal film coating is achievable via ALD throughout the trench structures, PVD fails to provide sufficient penetration of film at the bottom of the trenches.

One of the other conceivable implementation of the ALD technique is to combine it with some other processing technique to synthesize a material with the desired properties. Of utmost importance for the synthesis of 2-D materials are the properties like precise thickness control and high quality films over a large area. In our case, this opportunity has been translated to produce high quality, patternable MoS_2 thin films by combining low temperature PEALD process (50°C) with high temperature (900°C) thermal sulphurization process. The ultra-thin films of MoO_x were grown using PEALD which were sulphurized subsequently to obtain MoS_2 films which retain the inherent benefits of ALD process including precise thickness controllability, reproducibility, large area thickness uniformity and high conformality. The exploitation of ALD's features using this indirect approach will be discussed in Chapter 2 and Chapter 6 in detail.

1.3 Goals, context and outline

1.3.1 Goals and objectives

The extraordinary properties of MoS_2 make it a promising nanomaterial for plethora of (opto-) electronic applications. As aforementioned, the synthesis of high quality MoS_2 films with precise thickness and morphology control over a large area at low temperature is still one of the major challenges to realize its true potential. The main goal of this work is to explore the capabilities of ALD to yield MoS_2 films with desired properties. The sub-monolayer thickness control offered by ALD as an inherent attribute makes it a method of choice for synthesis of 2-D materials including MoS_2. Even though some first reports about synthesis of MoS_2 by ALD are available in literature, the structural properties and functional implications of films synthesized by ALD require a broader and comprehensive investigation which serves as the main motivation for this work.

Low temperature PEALD for 2-D MoS_2 with tuneable properties

The application of ALD processes for synthesis of 2-D materials is still in an infancy stage and slowly gaining attention in the scientific community. In this work, several key challenges have been identified amongst which one of the challenges is to obtain crystalline material at the relative low ALD processing temperatures with wafer-scale uniformity. Therefore, the following objectives are addressed in this thesis:

- To evaluate if incorporation of a plasma-enhanced co-reactant step (consisting of a H_2S based gas mixture) in ALD is able to deliver crystalline 2-D MoS_2 films at low processing temperatures.
- To assess if the ALD criterions are met for the as-synthesized MoS_2 films i.e. large area uniformity and precise thickness control.

To exploit ALD to its maximum, it is equally important to explore how ALD can manipulate the properties of 2-D materials at the atomic scale. Therefore, in this thesis the following objectives will be addressed as well:

- To analyze the influence of process parameters (e.g. plasma gas composition, temperature) on film properties mainly wetting, morphology and chemical composition.
- To evaluate the performance of films synthesized using PEALD process for eletrocatalytic applications

Synthesis of patterned MoS_2

The integration of MoS_2 for device applications generally requires *top-down* etching and/or a transfer step using a polymer based approach (further details in Chapter 6) which might induce some defects and result in degraded device performance. It is therefore of high technological relevance to synthesize high quality, patterned MoS_2 on device ready substrates. In order to achieve this, an approach by combining low temperature PEALD and high temperature thermal sulphurization has been explored to address the following objectives:

- To assess the structural properties (crystallinity, morphology, chemical composition *etc.*) of 2-D MoS_2 films synthesized using the combinatorial approach.
- To exploit the compatibility of low temperature PEALD with conventional e-beam lithography process aiming at synthesis of patterned MoS_2 films.
- To assess the electrical properties of films synthesized using combinatorial approach by fabricating a FET device.

1.3.2 Context

The research presented in this thesis has been carried out in the *Plasma and Materials Processing* (PMP) group at the department of Applied Physics of the *Eindhoven University of Technology* (TU/e) in the Netherlands. The PMP group has extensive experience in the development of ALD processes and the related applications. Furthermore, within PMP, extensive work on CVD growth of graphene and device integration using graphene has been performed. Therefore, this work aims at the synthesis of 2-D materials beyond graphene namely TMDs as aforementioned. The foremost work was the establishment of a low temperature PEALD process for synthesis of 2-D MoS_2 and subsequent analysis of its properties. In parallel, the implementation of ALD synthesized films in the area of electrocatalysis was realized in close collaboration with the chemistry department (Dr. J.P. Hofmann) at TU/e.

The experience gained with the CVD growth of graphene in the group was translated to synthesize high quality MoS_2 films by combining a PEALD process (for MoO_x films) with furnace based thermal sulphurization. This approach also enabled the patterned growth of MoS_2 films with precise thickness control and is a major advancement

towards attaining high quality films directly on device ready substrates omitting the need of etching and/or transfer step.

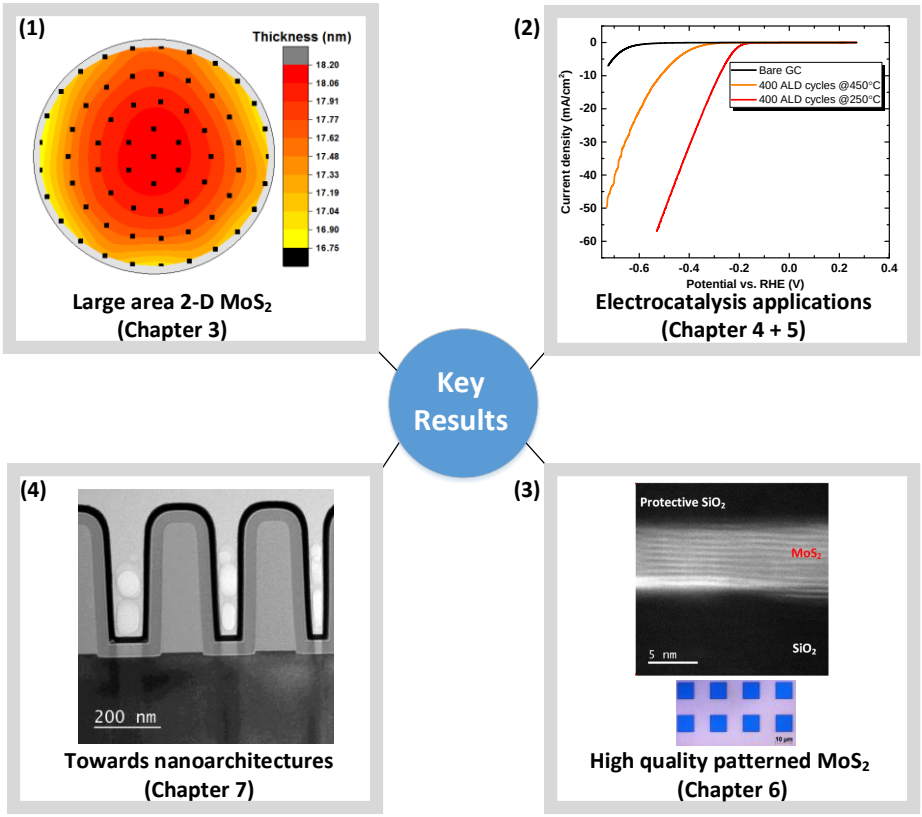


Figure 1.8 An overview of the key results in a nutshell. Starting from top left and proceeding clockwise: (1) A step forward towards large area synthesis of 2-D MoS_2 in combination with precise thickness control has been taken using PEALD process. (2) The functionalities of films deposited by PEALD are demonstrated for electrocatalysis applications (hydrogen evolution reaction (HER)). The films deposited at low temperature (250 °C) are found to be highly active for HER applications. (3) High quality (defect free) and patterned films are synthesized by combining PEALD and thermal sulphurization. (4) A PEALD process has been developed for a high-κ material (HfO_2) with a comprehensive analysis of properties. The integration of both ALD synthesized MoS_2 and HfO_2 will open up a new avenue towards nanoarchitectures for next-generation nanodevices.

The integration of 2-D materials and high-κ materials is shown as promising method for obtaining next generation high performance electronics devices. Keeping that in

perspective, a PEALD process is established to deposit high quality HfO_2 thin films. Subsequently, the comprehensive analysis of properties is carried out thereafter. An overview of the key results obtained in this PhD project is represented in Figure 1.8.

With the establishment of two approaches for synthesis of MoS_2 films for variety of applications, the next step is the further integration of films for next generation device architectures including heterostructures. Within PMP this work is continued through a ERC Consolidator grant which focusses on the synthesis of 2-D TMDs by ALD and fabrication of devices.

1.3.3 Outline of the thesis

The quest to obtain precise thickness control during synthesis of MoS_2 has led to the development of various ALD processes by several groups and are reported in the literature. Chapter 2 starts with an overview of the existing state-of-the art ALD processes (hitherto). The properties and applications of the films obtained by different processes are discussed in brief. Furthermore, since the films synthesized by PEALD in this work have been demonstrated as promising electrocatalysts, a theoretical framework explaining the basic principle and setup for hydrogen evolution reaction is presented. Chapter 3 describes a low-temperature PEALD process to synthesize uniform, mono-to-few layered MoS_2 films over large area where ultimate control over film thickness is attained. Furthermore, it discusses the synthesis of out-of-plane oriented films and their application as electrocatalysts.

Chapter 4 and 5 focus on the tuning of the film properties and applications respectively. Chapter 4 presents the tuneable surface wettability of as-synthesized out-of-plane oriented films attained by modification of plasma parameters during PEALD process. Chapter 5 continues with the exploration of eletrocatalytic performance of amorphous MoS_x films synthesized at low temperature.

Chapter 6 investigates the approach of combining low temperature PEALD with high temperature thermal sulphurization to attain high quality, layered 2-D MoS_2 films. It demonstrates how low temperature during PEALD is leveraged to obtain patterned MoS_2 films on device ready substrates.

The integration of 2-D TMDs with high-κ materials has been shown as an important step towards achieving high performance devices in the literature. Chapter 7 makes the switch to ALD of such a high-κ material i.e. HfO_2. The uniform, highly conformal HfO_2

thin films are prepared using a PEALD process and the film properties are discussed in detail.

Finally, a summary of the main findings with an outlook for further research is given in Chapter 8.

References

1. R. P. Feynman, *Journal of Microelectromechanical Systems*, 1992, **1**, 60-66.
2. G. E. Moore, *IEEE Solid-State Circuits Society Newsletter*, 2006, **11**, 33-35.
3. R. Chau, B. Doyle, S. Datta, J. Kavalieros and K. Zhang, *Nature Materials*, 2007, **6**, 810.
4. International Roadmap for devices and systems (IRDS), *Emerging Research Materials*, 2017.
5. https://newsroom.intel.com/newsroom/wp-content/uploads/sites/11/2017/03/Kaizad-Mistry-2017-Manufacturing.pdf, *Journal*.
6. K. S. Novoselov, A. K. Geim, S. V. Morozov, D. Jiang, Y. Zhang, S. V. Dubonos, I. V. Grigorieva and A. A. Firsov, *Science*, 2004, **306**, 666-669.
7. F. Schwierz, *Nature Nanotechnology*, 2010, **5**, 487.
8. A. K. Geim and K. S. Novoselov, *Nature Materials*, 2007, **6**, 183.
9. M. Y. Han, B. Özyilmaz, Y. Zhang and P. Kim, *Physical Review Letters*, 2007, **98**, 206805.
10. X. Fan, Z. Shen, A. Q. Liu and J.-L. Kuo, *Nanoscale*, 2012, **4**, 2157-2165.
11. G. Gui, J. Li and J. Zhong, *Physical Review B*, 2008, **78**, 075435.
12. E. P. Randviir, D. A. C. Brownson and C. E. Banks, *Materials Today*, 2014, **17**, 426-432.
13. F. Torrisi, T. Hasan, W. Wu, Z. Sun, A. Lombardo, T. S. Kulmala, G.-W. Hsieh, S. Jung, F. Bonaccorso, P. J. Paul, D. Chu and A. C. Ferrari, *ACS Nano*, 2012, **6**, 2992-3006.
14. M. Chhowalla, D. Jena and H. Zhang, *Nature Reviews Materials*, 2016, **1**, 16052.
15. R. Ganatra and Q. Zhang, *ACS Nano*, 2014, **8**, 4074-4099.
16. E. S. Kadantsev and P. Hawrylak, *Solid State Communications*, 2012, **152**, 909-913.
17. A. Castellanos-Gomez, M. Poot, G. A. Steele, H. S. J. van der Zant, N. Agraït and G. Rubio-Bollinger, *Advanced Materials*, 2012, **24**, 772-775.
18. S. Bertolazzi, J. Brivio and A. Kis, *ACS Nano*, 2011, **5**, 9703-9709.
19. K. F. Mak, C. Lee, J. Hone, J. Shan and T. F. Heinz, *Physical Review Letters*, 2010, **105**, 136805.
20. S. B. Desai, S. R. Madhvapathy, A. B. Sachid, J. P. Llinas, Q. Wang, G. H. Ahn, G. Pitner, M. J. Kim, J. Bokor, C. Hu, H.-S. P. Wong and A. Javey, *Science*, 2016, **354**, 99-102.
21. J. Moser and F. Levy, *Journal of Materials Research*, 1993, **8**, 206-213.
22. J. Moser, F. Lévy and F. Bussy, *Journal of Vacuum Science & Technology A*, 1994, **12**, 494-500.
23. P. D. Fleischauer, *A S L E Transactions*, 1984, **27**, 82-88.
24. D. Kong, H. Wang, J. J. Cha, M. Pasta, K. J. Koski, J. Yao and Y. Cui, *Nano Letters*, 2013, **13**, 1341-1347.

25. T. F. Jaramillo, K. P. Jørgensen, J. Bonde, J. H. Nielsen, S. Horch and I. Chorkendorff, *Science*, 2007, **317**, 100.
26. K. S. Novoselov, D. Jiang, F. Schedin, T. J. Booth, V. V. Khotkevich, S. V. Morozov and A. K. Geim, *Proc. Natl. Acad. Sci. U. S. A.*, 2005, **102**, 10451-10453.
27. M. Chhowalla, H. S. Shin, G. Eda, L.-J. Li, K. P. Loh and H. Zhang, *Nat Chem*, 2013, **5**, 263-275.
28. G. Eda, H. Yamaguchi, D. Voiry, T. Fujita, M. Chen and M. Chhowalla, *Nano Letters*, 2011, **11**, 5111-5116.
29. S. Najmaei, Z. Liu, W. Zhou, X. Zou, G. Shi, S. Lei, B. I. Yakobson, J.-C. Idrobo, P. M. Ajayan and J. Lou, *Nat Mater*, 2013, **12**, 754-759.
30. J. Chen, W. Tang, B. Tian, B. Liu, X. Zhao, Y. Liu, T. Ren, W. Liu, D. Geng, H. Y. Jeong, H. S. Shin, W. Zhou and K. P. Loh, *Advanced Science*, 2016, **3**, 1500033-n/a.
31. K. Mistry, C. Allen, C. Auth, B. Beattie, D. Bergstrom, M. Bost, M. Brazier, M. Buehler, A. Cappellani, R. Chau, C. Choi, G. Ding, K. Fischer, T. Ghani, R. Grover, W. Han, D. Hanken, M. Hattendorf, J. He, J. Hicks, R. Huessner, D. Ingerly, P. Jain, R. James, L. Jong, S. Joshi, C. Kenyon, K. Kuhn, K. Lee, H. Liu, J. Maiz, B. McIntyre, P. Moon, J. Neirynck, S. Pae, C. Parker, D. Parsons, C. Prasad, L. Pipes, M. Prince, P. Ranade, T. Reynolds, J. Sandford, L. Shifren, J. Sebastian, J. Seiple, D. Simon, S. Sivakumar, P. Smith, C. Thomas, T. Troeger, P. Vandervoorn, S. Williams and K. Zawadzki, 2007.
32. A. Pakkala and M. Putkonen, in *Handbook of Deposition Technologies for Films and Coatings (Third Edition)*, ed. P. M. Martin, William Andrew Publishing, Boston, 2010, DOI: https://doi.org/10.1016/B978-0-8155-2031-3.00008-9, pp. 364-391.
33. H. B. Profijt, S. E. Potts and M. C. M. de Sanden, *J. Vac. Sci. Technol. A*, 2011, **29**, 050801.
34. W. M. M. Kessels, S. B. S. Heil, E. Langereis, J. L. Van Hemmen, H. C. M. Knoops, W. Keuning and M. C. M. Van De Sanden, 2007.
35. R. W. Johnson, A. Hultqvist and S. F. Bent, *Materials Today*, 2014, **17**, 236-246.
36. R. L. Puurunen, *Journal of Applied Physics*, 2005, **97**, 121301.
37. M. Leskelä and M. Ritala, *Thin Solid Films*, 2002, **409**, 138-146.
38. R. Mikko and L. Markku, *Nanotechnology*, 1999, **10**, 19.
39. S. D. Elliott, *Semiconductor Science and Technology*, 2012, **27**.

2

ALD of sulphides and characterization of 2-D MoS_2

The bottom-up synthesis of 2-D materials including MoS_2 over large area with precise thickness control is of paramount importance. Atomic layer deposition (ALD) is an excellent tool to achieve atomic level control over the film thickness which can be instrumental for the synthesis of 2-D materials. In this chapter, an overview of existing ALD processes for MoS_2 in the literature is given. Next, the two popular characterization techniques for MoS_2 i.e. Raman and photoluminescence spectroscopy are discussed to facilitate the reader for a better understanding of the results in subsequent chapters. Finally, the concept of hydrogen evolution reaction (HER) during water splitting mechanism is introduced. Since MoS_2 films are emerging as potential electrocatalysts for HER, a short description related to HER is given which is also relevant for Chapter 3 and Chapter 4.

2.1 ALD of MoS_2

As mentioned in Chapter 1, the majority of established atomic layer deposition (ALD) processes to date correspond to the metal oxides, nitrides *etc*. However, novel application areas such as energy storage, catalysis and optoelectronics are driving the interest in growing sulphides by ALD. In fact, a lot of progress has been made recently in ALD of sulphides spanning a diverse pool of accessible materials. Interestingly, the history of ALD of sulphides traces back to the earlier stages of ALD in the 1970s.[1] At that time, ALD used to be referred to as atomic layer epitaxy (ALE) and the first demonstrated ALE process was ZnS. The first commercial application of ZnS thin films developed by ALE was exhibited in a electroluminescent display which operated in Helsinki airport from 1983 to 1998.[2] However, the precursor chemistry used in ALD of sulphides typically consisted of toxic H_2S gas which presents several challenges for incorporation in ALD. Meanwhile, the industrial focus was shifted to the development of metal oxides which got a widespread popularity after the stringent requirement of ultra-thin gate oxides in complementary metal oxide semiconductor (CMOS) industry. Nevertheless, with the technological evolution, the designs of ALD reactors are constantly improved for H_2S compatibility. This has led to the development of a number of binary and few multicomponent sulphides by ALD. Some of the examples since early 90s are PbS,[3] In_2S_3,[4] Cu_xS,[5] WS_2,[6] TiS_2,[7] Sb_2S_3,[8] SnS,[9] GaS_x,[10] GeS,[11] MoS_2,[12] Li_2S,[13] $CuInS_2$,[14] MnS,[15] $V_xIn_{(2-x)}S_3$,[16] NiS_x,[17] AlS_x,[18] Bi_2S_3,[19] and $CuSbS_2$.[20]

The focus material of this PhD project, as mentioned in Chapter 1, is MoS_2 and the rest of the discussion in this section thus will be centred around ALD of MoS_2 in particular. In the near past, a considerable number of reports for ALD of MoS_2 have surfaced exhibiting the potential of ALD for the synthesis of 2-D MoS_2. The first reports for ALD of MoS_2 were presented in 2014 by multiple groups and ever since the interest in development of new ALD processes for MoS_2 has raised aiming to precisely control the thickness and subsequently its properties. In Table 2.1, we attempt to recapitulate the work and give an overview of ALD processes for MoS_2 developed by several groups in chronological order. Table 2.1 lists the precursor type, co-reactant, temperature window, growth per cycle (GPC), the phase of film obtained and any applications demonstrated. For the development of ALD process, choosing the precursor(s) is of vital importance as it may influence the final film properties. Typically, for an ALD precursor, the following requirements needs to be fulfilled:

- Volatility: the precursor ideally should have a sufficient vapor pressure under the given conditions to ensure a proper precursor delivery to the reactor at reasonable dosing duration.
- Stability: the precursor needs to be chemically stable at the deposition temperatures used (ideally over a wide temperature range) in order to avoid thermal decomposition which could lead to undesired reactions and CVD-like growth.
- Reactivity: the precursor should be reactive enough towards the surface groups present during the ALD process and also towards the co-reactant used in the second half cycle of ALD process to ensure uninterrupted film growth.
- Availability: the earth abundance of precursor elements (e.g. Mo in our case) is naturally favourable for the mass production of thin films. Furthermore, the chemical synthesis of the precursor should be feasible and well established.

So far, there is a limited choice for precursors for development of ALD processes of MoS_2 thin films. From Table 2.1, it is evident that the majority of ALD reports are thermal in nature and have utilized either carbonyl or halide based precursors as metal source in combination with H_2S or $(CH_3)S_2$ as co-reactant. It is to be noted that the ALD processes based on carbonyl based precursors have a narrow ALD temperature range with a maximum allowable temperature up to 250 °C due to their limited thermal stability. This results mostly in as-deposited amorphous films which, depending on the application, need high temperature post-annealing to improve the structural quality accordingly. The other popular precursor has been $Mo(Cl)_5$, which on the contrary, requires >250 °C for successful incorporation in an ALD process. Many groups have demonstrated the formation of nano-crystalline MoS_2 thin films with the use of $Mo(Cl)_5$ precursor leveraging the upper temperature limit up to ~500 °C. However, there is a possibility of generation of corrosive chlorine containing by-products such as HCl which can be detrimental for both the process and reactor.

We will now discuss few selective reports based on carbonyl and halide based precursors and try to point out the most significant results obtained.

Nandi *et al.* were amongst the first ones to demonstrate a thermal ALD process based on $Mo(Co)_6$ precursor in combination with H_2S gas as co-reactant to yield amorphous

MoS_2 films with a growth-per-cycle (GPC) of 0.25 nm/cycle at 170 °C[21]. These films were shown to exhibit promising performance as efficient electrode (anode) for lithium ion batteries. The self-limiting behaviour of the ALD process was analysed using a quartz crystal microbalance (QCM) and this was verified using spectroscopic ellipsometry (SE). The dissociative chemisorption and removal of metal carbonyl species during ALD cycle was shown using *in-situ* Fourier transform infra-red (FTIR) spectroscopy where the corresponding signature peaks were obtained accordingly. A thorough evaluation of the as-deposited amorphous MoS_2 films as an anode material in a lithium battery configuration was performed.

Following up, Tan *et al.* employed $Mo(Cl)_5$ in combination with H_2S gas as a co-reactant to demonstrate a self-limiting ALD process at 300 °C[12]. The as-deposited film was nano-crystalline in nature and a growth per cycle of ~0.15 nm/cycle was achieved. A precise thickness control of films as a function of number of ALD cycles was demonstrated. In order to improve the crystallinity of the as-deposited film, a high temperature post-anneal was performed at 800 °C under saturated sulphur vapour environment. Figure 2.1 (a) shows the scanning electron microscope (SEM) image of the annealed film deposited on a sapphire substrate by using 10 ALD cycles where triangular MoS_2 flakes are visible. Figure 2 (b) displays atomic force microscope (AFM) image which shows the individual ~2 μm wide triangular flakes with a thickness of ~0.8 nm. It is clearly observable though that the flakes are discontinuous and the film until this stage is thus not closed. A sharp increase in Raman and photoluminescence (PL)[a] signals were also obtained after post-annealing the films. The two characteristic Raman peaks (i.e. E^1_{2g} and A_{1g}) were clearly visible in Raman spectrum. The PL spectrum showed two distinct peaks for a monolayer corresponding to the direct band gap excitonic emission.

[a] Raman and PL techniques for MoS_2 are described later in this chapter

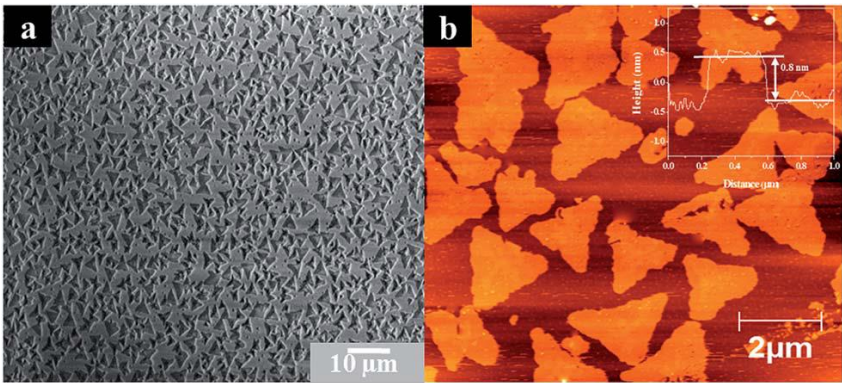


Figure 2.1 (a) SEM and (b) AFM images of a monolayer ALD MoS_2 film obtained after post annealing at 800 °C in sulphur environment. The inset shows the height profile of the triangular flakes. Reproduced from [12] with permission from The Royal Society of Chemistry.

As mentioned in Chapter 1, another variant of ALD is plasma enhanced ALD (PEALD), in which typically a high quality material can be obtained at relatively low temperatures owing to the high reactivity of the energetic species in the plasma enhanced co-reactant step. Such a PEALD process for MoS_2 thin films was reported by Jang *et al.* in 2016,[22] where $Mo(Co)_6$ was employed in combination with H_2S plasma at 175 °C to obtain a GPC of ~0.05 nm/cycle. The as-deposited films were nano-crystalline and stoichiometric in nature with negligible C impurities (~0.1 at.%). The large area wafer scale film uniformity and high conformality on 3-D trench structures were demonstrated as inherent attributes of ALD. However, this report did not discuss any details about the film microstructure and therefore the viability of as-synthesized films for applications is unclear. Furthermore, the low growth per cycle obtained despite plasma enhanced co-reactant step (which typically leads to a high growth rate) indicates towards the low reactivity of $Mo(Co)_6$ with H_2S plasma.

Another approach adopted by Kwon *et al.* was to combine $Mo(Co)_6$ with $(CH_3S)_2$ as a co-reactant to obtain MoS_2 thin films at 100 °C.[23] The focus of this work was to demonstrate the ability of ALD to conformally coat high surface area substrates such as carbon fiber paper with MoS_2 and subsequently implement the MoS_2/CFP samples for the application of hydrogen evolution reaction (HER)[b] during water splitting. In this

[b] The details of HER are given later in this chapter.

way, ALD was exhibited as a powerful tool to design efficient catalysts with excellent performance and stability for HER.

It is until recently that few groups have shown the use of non-carbonyl and non-halide based precursors such as $Mo(NMe_2)_4$ ($(NMe_2)_4$ = tetrakis(dimethyl-amido)) and $Mo(thd)_3$ (thd = 2,2,6,6-tetramethyl-3,5-heptanedione) in combination with H_2S to obtain MoS_2 thin films.[24, 25] Jurca *et al.* have reported the low temperature ALD process by combining $Mo(NMe_2)_4$ and H_2S in the temperature range between 60 -120 °C.[24] The self-limiting behaviour was demonstrated at 60 °C with a GPC of 0.12 nm/cycle. The as-deposited films were amorphous in nature and were annealed under sulphur vapor for 5 h at 1000 °C which resulted in nano-crystalline films.

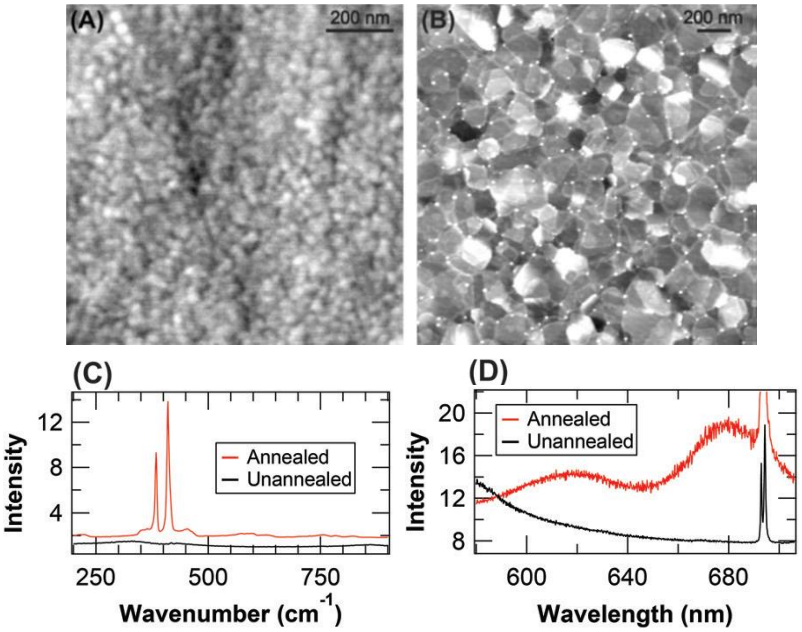


Figure 2.2 AFM topographic images of (A) as-deposited amorphous and (B) annealed nanocrystalline MoS_2 film. (C) Raman spectra showing the emergence of vibrational modes after annealing the MoS_2 film. (D) Photoluminescence spectra showing the excitonic peaks for annealed film. Adapted from [24].

Figure 2.2 (A) and (B) show the AFM images of as-deposited amorphous and annealed crystallized films respectively. The characteristic peaks corresponding to Raman

vibrational modes are also evident for post-annealed film as shown in Figure 2.2 (C). Likewise, a PL signal is visible for post-annealed film (Figure 2.2 (D)) which further corroborates the good quality of the film after annealing. The low temperature processing (60 °C) was leveraged for demonstrating a lithographic lift-off patterning scheme to obtain patterned MoS_2 films over a large area.

Mattinen *et al.* have introduced $Mo(thd)_3$ as a precursor in combination with H_2S gas as a co-reactant.[25] The self-limiting behaviour of the ALD process was analysed at 300 °C and a low GPC of ~0.003 nm/cycle was obtained. The low GPC was ascribed to the possible steric hindrance between the adsorbed precursor molecules due to the bulky metal thd precursor. The as-deposited MoS_2 films were nano-crystalline in nature with a textured morphology as confirmed by AFM and X-ray diffraction (XRD) measurements. Interestingly, substrate dependent growth was observed since a slightly higher growth per cycle was obtained on soda-lime glass, whereas almost no growth occurred on ALD grown Al_2O_3 substrates respectively. The explanation for the former was the likely diffusion of alkali metal into the film which might affect the precursor adsorption and subsequently the growth. For the latter, 'surface poisoning' was mentioned to likely cause the hindered nucleation.

Very recently, Jeon *et al.* have developed an inhibitor-utilizing atomic layer deposition (iALD) as a novel method to achieve high quality 2-D MoS_2 thin films for micro-electronic applications.[26] The self-limiting growth was established at 250 °C and a GPC of 0.065 nm/cycle was observed. In essence, the focus of this work was to modify the surface by the utilization of an inhibitor molecule namely, diethyl sulphide ($CH_3CH_2SCH_2CH_3$), DES) before the chemisorption of primary precursor $Mo(Co)_6$. The steric hindrance provided by DES was found to inhibit the chemisorption of $Mo(Co)_6$ molecules which ultimately resulted in decreased nucleation density of MoS_2 nuclei enabling the formation of highly crystalline and continuous thin film with a grain size up to 75 nm. Figures 2.3 (a) and (b) display the microstructures of MoS_2 thin films deposited without and with inhibitor molecule. The former shows the regions with non-crystalline film indicating the discontinuous nature of crystalline MoS_2 (Figure 2.3 (a)). For film deposited with inhibitor molecule, a continuous layered structure of MoS_2 film is evident as shown in Figure 2.3 (b). The larger grain size in film deposited with inhibitor molecule was reflected in the excellent performance of field effect transistor

(FET) devices which were demonstrated to exhibit an on-off ratio of 10^8 and mobility of 13.9 $cm^2V^{-1}s^{-1}$ as shown in figure 2.3 (c). Despite these excellent results, the thermal stability of the carbonyl precursor used in this work at 250 °C remains questionable as most of the ALD reports indicate about the low thermal stability (<225 °C) of carbonyl precursor. Furthermore, a post anneal at 450 °C is still required to improve the crystallinity of the film. Overall, this work has provided new prospects for achieving 2-D materials with better electrical properties while inheriting the large area uniformity and thickness control from ALD technique.

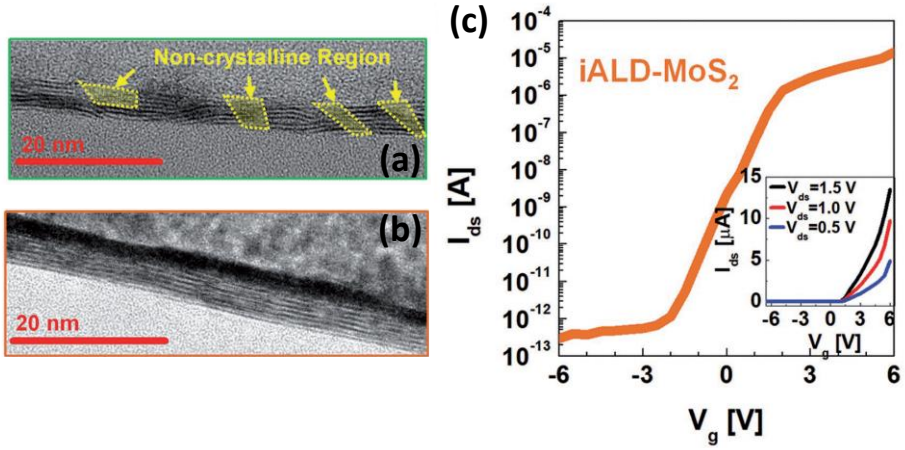


Figure 2.3 Cross sectional TEM images of MoS_2 films deposited (a) without utilizing inhibitor molecule (b) with inhibitor molecule (c) Transfer curve (drain current vs gate voltage) for MoS_2 based FET device at V_{ds} = 1.5 V. The inset shows the V_g - I_{ds} curves as a function of V_{ds}. Adapted from [26].

Based on the above studies, it can be concluded that most of the ALD processes have a limited ALD temperature window accompanied by low growth rates. Furthermore, the structural quality of as-synthesized films is poor and often requiring a high temperature post-annealing to improve the crystallinity and attain the layered 2-D structure. Therefore, a continued advancement in this promising film growth technique for MoS_2 thin films is contingent on the development of new precursor and co-reactant chemistries capable of delivering self-limiting type surface reactions. Most importantly, the ALD synthesis of high quality 2-D MoS_2 films at low temperature is still a challenge. In this research work (Chapter 3), we have explored a low temperature PEALD process based on bis(tert-butylimido)-bis(dimethylamido) molybdenum

([(NtBu)$_2$(NMe$_2$)$_2$Mo]) as metal precursor in combination with H_2S based plasma as the co-reactant. Our PEALD process offers a relatively wide ALD temperature range (Figure 2.4) up to 450 °C which yields as-synthesized high quality, layered 2-D MoS_2 films without any need of post annealing. The current work offers an viable alternative for synthesis of high quality 2-D MoS_2 films at low temperature and contributes towards a major advancement in establishing low temperature PEALD as a scalable route for applications ranging from electronics to catalysis.

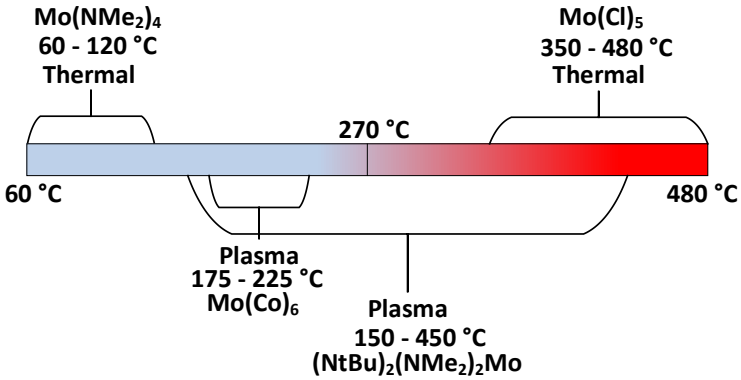


Figure 2.4 The schematic showing the ALD temperature ranges for various precursors employed in literature so far. Our PEALD process using the [(NtBu)$_2$(NMe$_2$)$_2$Mo] precursor clearly spans over a large part of temperature window.

Table 2.1 An overview of the reports on ALD of MoS_2 in the literature. For each paper, the Mo precursor and co-reactant are listed. Also, the other parameters like GPC, deposition temperature, phase of as-deposited films, details of post annealing and corresponding application are given. It should be noted that the as-synthesized films which are reported to exhibit crystalline nature have been classified as nanocrystalline (NC) and polycrystalline (PC) according to the corresponding grain sizes i.e. nano and micron sized grains respectively. (Status: September 2018)

Precursor	Co-reactant	Temp. (°C)	GPC (nm/cyc)	Phase & Post anneal	Appli-cation	Ref.
$Mo(Co)_6$	H_2S	155-170	0.25	Amorphous No	Li ion battery	[21]
$MoCl_5$	H_2S	300	0.15 - 0.2	Amorphous Yes-800°C†	-	[12]
$Mo(Co)_6$	$(CH_3S)_2$	100	0.11	Amorphous Yes-900°C‡	-	[27]
$Mo(Co)_6$	$(CH_3S)_2$	100	0.11	Amorphous No	HER[c]	[28]
$MoCl_5$	H_2S+Ar	390	0.09	NC[a] No	FET[d]	[29]
$Mo(Co)_6$	H_2S plasma	175-225	0.05	NC	-	[22]
$Mo(Co)_6$	H_2S	155-175	0.08	Amorphous Yes-900°C§	-	[30]
$Mo(Co)_6$	$(CH_3S)_2$	100	0.11	Mixed phase No	HER	[23]
$MoCl_5$	H_2S	500-900	-	PC[b]	FET	[31]
$MoCl_5$	H_2S	375-475	0.02	NC Yes-920°C†§	-	[32]
$Mo(Co)_6$	H_2S	200	-	NC No	OER[e]	[33]
$MoCl_5$	H_2S	450	PCM[f]	NC No	-	[34]
$MoCl_5$	H_2S	390-480	0.25	NC No	PE[g]	[35]
$MoCl_5$	H_2S	250-325	-	NC No	HER	[36]
$Mo(NMe)_4$	$HS(CH_2)_2SH$	50	-	Amorphous Yes-800°C‖	-	[37]

$Mo(Co)_6$	H_2S plasma	200	0.05	NC No	SC[h]	38
$Mo(NMe_2)_4$	H_2S	60-120	0.12	Amorphous Yes-1000°C[†]	FET	24
$Mo(thd)_3$	H_2S	300	0.003	NC No	-	25
$Mo(Co)_6$	$(CH_3S)_2$ $(CH_3)_2S$	250	0.065	NC Yes-450°C[₸]	FET	26
MoF_6	H_2S	200	0.04	NC Yes-350°C[‖]	-	39
$Mo(Co)_6$	$((CH_3)_3Si)_2S$	150	0.004	Amorphous Yes-800°C[†]	FET	40
$(NtBu)_2(NMe_2)_2Mo$	H_2S+Ar+H_2 plasma	150-450	0.1	NC No	HER	41 & Chapt. 3

[a] = Nanocrystalline, [b] = Polycrystalline, [c] = Hydrogen evolution reaction, [d] = Field effect transistor, [e] = Oxygen evolution reaction, [f] = Partly continuous monolayer per cycle, [g] = Piezoelectricity, [h] = Superconductor, [†]Sulfur vapor, [₸] Ar atmosphere, [§]H_2S atmosphere, [‖]H_2 atmosphere

2.2 Indirect ALD for MoS_2

An alternative approach under investigation for the synthesis of high quality 2-D MoS_2 centres around the deposition of molybdenum oxide and subsequent high temperature thermal sulphurization. Here, it is important to realize that the uniformity and precise thickness control of the parent molybdenum oxide is imperative to achieve large area, thickness controlled MoS_2 film. In this context, ALD is instrumental to provide extremely uniform and ultra-thin metal oxide films which are subsequently thermally sulphurized to obtain high quality, layer controlled MoS_2 thin films over large area.

Although this approach offers a great way to obtain 2-D MoS_2, only a handful of reports using this indirect methodology are available in literature (Table 2.2). Wang *et al.* have exploited ALD's feature of high conformality on substrates with high surface areas using the indirect approach.[42] To this purpose, CFP substrates were first conformally coated with MoO_3 thin films using an ALD process employing $Mo(Co)_6$ and ozone as a co-reactant at 165 °C. The MoO_3/CFP substrate was then thermally sulphurized in a tube furnace at 600 °C to attain vertically oriented 2-H MoS_2 thin films which were demonstrated to serve as efficient electrocatalysts for HER. The as-

synthesized 2-H semiconducting films were then converted to 1-T metallic films using Li intercalation. This phase conversion of as-synthesized films was leveraged to achieve tuning of their catalytic activities for HER application.

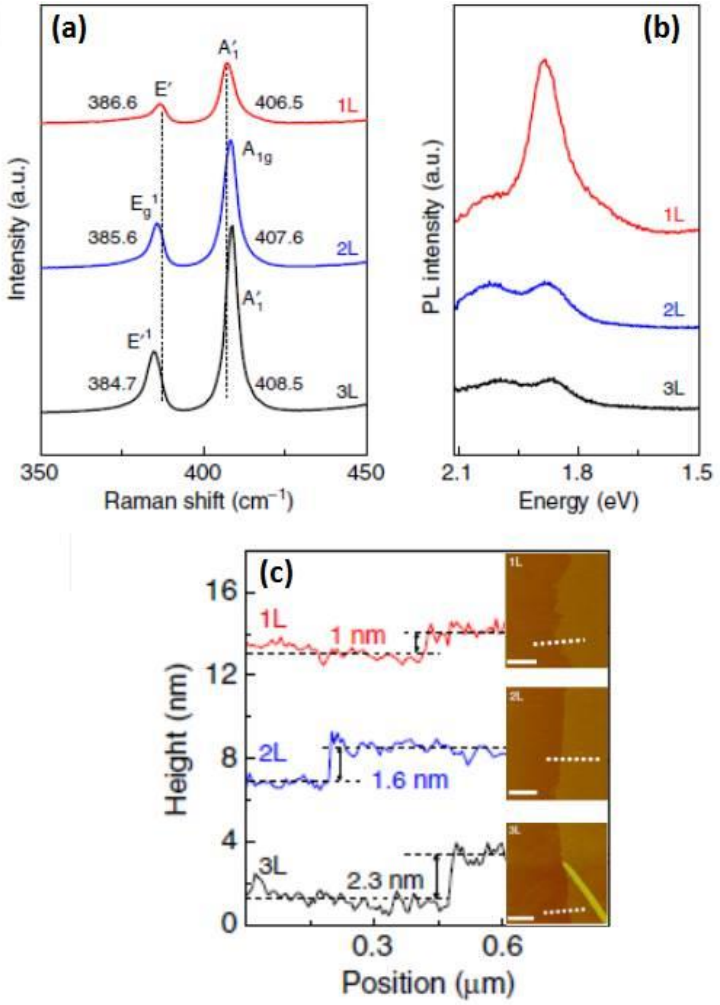


Figure 2.5 (a) Raman spectra and (b) PL spectra for the mono, bi and tri-layered MoS_2 films synthesized by thermal sulphurization of ultra-thin films prepared by 6, 9 and 12 PEALD cycles respectively. (c) The height profiles of transferred MoS_2 on SiO_2 substrates for mono, bi and tri-layered MoS_2 films as measured by AFM. The insets show AFM images accordingly. Reproduced from [43] with permission from Nature Communications.

Song *et al.* reported the high temperature sulphurization (at 1000 °C) of ultra-thin MoO_x films deposited by PEALD using $Mo(Co)_6$ and O_2 plasma at 200 °C.[43] The precise control over thickness of MoS_2 films was demonstrated by tuning the number of PEALD cycles for parent MoO_x films. The Raman spectra for mono-, bi- and tri-layered films are shown in Figure 2.5 (a). The frequency difference between two Raman vibrational modes were found to be 19.9, 22 and 23.8 cm^{-1} for mono, bi and tri layered MoS_2 films respectively. Likewise, the PL spectra (Figure 2.5 (b)) for mono, bi and tri layered shows the strongest peak for the thinnest sample. The intensity of the PL peak decreases with the number of layers due to the band gap transition from direct to indirect. Further, Figure 2.5 (c) shows the AFM images and height profiles of the MoS_2 films which were measured as ~1, 1.6 and 2.3 nm corresponding to 6, 9 and 12 ALD cycles for parent MoO_x films respectively. Overall, these results showed the excellent layer controllability of MoS_2 films using the ALD process.

Table 2.2 An overview of the reports using ALD indirectly for synthesis of MoS_2 as available in the literature. For each paper, the Mo precursor and co-reactant are listed for the parent MoO_x film. Also, the parameters like sulphur source, processing temperature and any demonstrated application are given.

ALD Molybdenum Oxide			**Sulphurization**			
Precursor	**Co-reactant**	**Temp. (°C)**	**Sulphur source**	**Temp. (°C)**	**Application**	**Ref.**
$Mo(Co)_6$	O_3	165	Sulphur powder	600	HER	[42]
$Mo(Co)_6$	O_2 plasma	200	H_2S + Ar	1000	Photodetector	[43]
$Mo(Co)_6$	O_3	160	Sulphur powder	850	-	[44]
$(NtBu)_2(NMe_2)_2Mo$	O_2 plasma & O_3	150 300	Sulphur powder	1000	-	[45]
$(NtBu)_2(NMe_2)_2Mo$	O_2 plasma	50	H_2S + Ar	900	FET	Chapt. 6

The remainder of this chapter will be devoted to explain the two main characterization tools employed for assessing the quality of 2-D materials *i.e.* Raman and Photoluminescence (PL) spectroscopy. These two techniques by far have established

themselves as the main *goto* methods for determining the thickness (number of layers), structural quality and any defects present in the films. Finally, the last section of this chapter is dedicated to explain the working principle, setup and parameters related to hydrogen evolution reaction (HER) which has evolved as one of the main applications of MoS_2 thin films establishing them as efficient electrocatalysts and possible alternative for state-of-the art expensive Pt based electrocatalysts for energy storage.

2.3 Raman spectroscopy of transition metal dichalcogenides

Raman spectroscopy has been widely adopted as a standardized technique for TMDs. The reason is that Raman spectroscopy provides a quick, non-invasive, non-destructive and efficient method for characterizing the 2-D materials. Moreover, the measurements can be performed at room temperature in ambient conditions without any need of sample preparation processes. Raman scattering is based on the inelastic scattering of the incident light (photons) in a material, where the energy (wavelength) of scattered light either decreases by exciting an elementary excitation of the solid material (i.e. a phonon) or increases by absorbing a phonon. A typical Raman spectra gives the intensity of the scattered light as a function of the energy shift from the incident light (Raman shift).

The molecular vibrations for the stabilized crystal symmetry are classified using the character tables for point groups. The character tables originate from the *group theory* treatment of the symmetry operations present in the common molecules and are useful in the study of molecular symmetry. There are 32 common point groups and the character tables for these 32 point groups are available in any standard *group theory* text[46]. For example, for a monolayer of MoS_2, there are a total of nine phonon branches at the Γ point, which according to the corresponding character table are notated as: $\Gamma = 2A_2'' + 2E' + A_1' + E''$[47]. It is to be noted that the modes denoted by "E" are doubly degenerate. Further here, A_2'' and E' are acoustic phonons, the other E' mode is both infra-red (IR) and Raman active. The second A_2'' mode is IR active. The Raman active phonon modes are A_1', E' and E''. All these modes are depicted in Figure 2.6 (a).

For layered TMDs including MoS_2, the crystal symmetry changes as a function of number of layers and structural phase which makes Raman spectroscopy a powerful tool to obtain structural information. For example, 2-H MoS_2, for its bulk phase, has D_{6h} point group symmetry while for few-layered regime it shows a reduction in symmetry.

The odd number of layers possess the D_{3h} point group symmetry and the even number of layers has the D_{3d} point group.[48] Therefore, depending on the point groups, the number of Raman vibrational modes and the symmetry labels can differ, but the vibrations in essence remain the same.

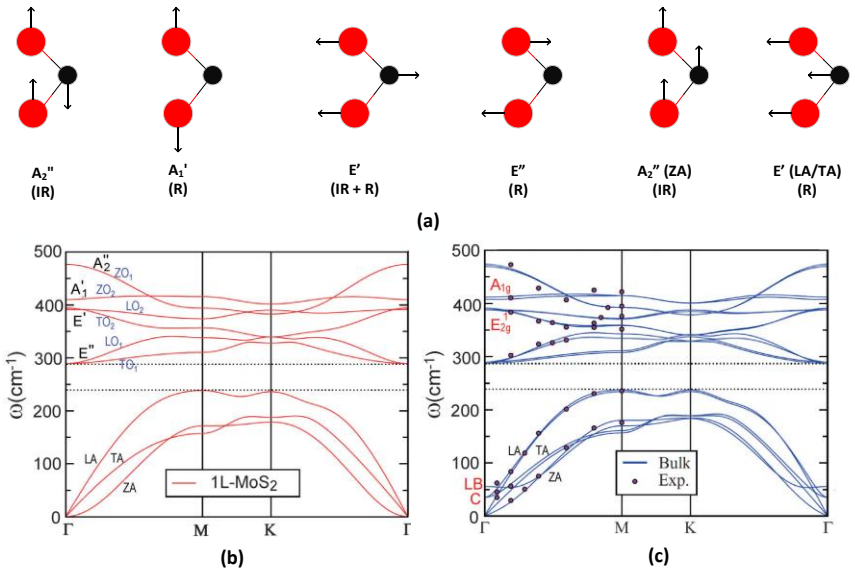


Figure 2.6 (a) The symmetry and normal displacements of each optical vibrational mode for a monolayer of MoS_2. The Raman-active (R) and infra-red active (IR) modes are indicated accordingly. The calculated phonon dispersion curves of (b) monolayer MoS_2 and (c) bulk MoS_2. Reproduced from [48] with permission from The Royal Society of Chemistry.

For bulk MoS_2, each of the nine normal vibrational modes in a monolayer are split into two modes making it a total of 18 normal vibrational modes and expressed as $\Gamma = 2A_{2u} + 2E_{1u} + 2B_{2g} + 2E_{2g} + A_{1g} + E_{1g} + B_{1g} + E_{2u}$ irreducible representations of the point groups[47]. Out of these, A^1_{2u} and E^1_{2u} phonon modes belong to acoustic branches while $2B_{2g}$, B_{1u} and E_{2u} are inactive (or silent) modes. The four Raman active optical phonon modes are A_{1g}, E_{1g} and $2E_{2g}$ which simply correspond to monolayer Raman modes A_1', E' and E" respectively.

Away from the Γ point, the normal vibrational modes for MoS_2 are dispersive in nature with respect to the phonon wave vector q. The phonon dispersion curves for both monolayer and bulk as calculated by density functional theory within the local density

approximation are shown in Figure 2.6 (b) and (c). The phonon dispersion of a monolayer has three acoustic and six optical branches as derived from the Γ point.

The momentum conservation restriction only allows the phonons with wavevector $q \approx 0$ (i.e. Γ point) to contribute to the first-order Raman scattering. The second order Raman process involves two phonons with opposite wavevector q. The second order Raman scattering is generally much weaker than first-order scattering. However, it can be resonantly enhanced by the interband transition due to the presence of defects which causes relaxation in Raman selection rules and hence enables the detection of phonons at the edge of the Brillouin zone (e.g. M and K points).[49] Given this background, in a typical Raman spectrum for bulk MoS_2, the two predominant first order peaks at high frequency ~ 383 cm^{-1} (E^1_{2g}) and ~ 408 cm^{-1} (A_{1g}) are observed.[50] Furthermore, as stated above, the presence of defects in the material can also activate the modes involving phonons at the zone edge of the Brillouin zone. Two of such defect induced peaks in close proximity to the first order peaks appear at ~ 357 cm^{-1} and ~ 411 cm^{-1} which are assigned to the TO and ZO branches at the M point respectively. Another feature at ~ 377 cm^{-1} has been identified as a defect related peak as well and assigned to LO (M) at the edge of Brillouin zone. Finally, the low-frequency region of the Raman spectrum also consists of an peak located at ~ 227 cm^{-1} which is referred to as LA (M) and has been demonstrated as a metric to assess the quality of MoS_2.[49, 51]

One of the other remarkable features of the Raman vibrational spectrum for MoS_2 is its sensitivity to the thickness of material. The evolution of peak parameters for the predominant in-plane and out-of-plane vibrational modes (i.e. E^1_{2g} and A_{1g}) as a function of increasing number of layers has been extensively reported in the literature (Figure 2.7 (a)).[52, 53] It is worth mentioning that the two modes are referred to as E^1_{2g} and A_{1g} despite the number of layers in MoS_2 (as discussed above) which is a common practice in this field and will also be followed in this thesis. Strikingly, it has been demonstrated that the in-plane E^1_{2g} vibration softens (red shifts), while the A_{1g} vibration stiffens (blue shifts) with increasing number of layers of MoS_2. This Raman frequency difference (Δ) between two peaks increases gradually from ~ 19 cm^{-1} to 25.8 cm^{-1} with increasing number of layers in synthetic MoS_2 and therefore serves as an indicator for the film thickness.[50] (See Figure 2.7 (b))

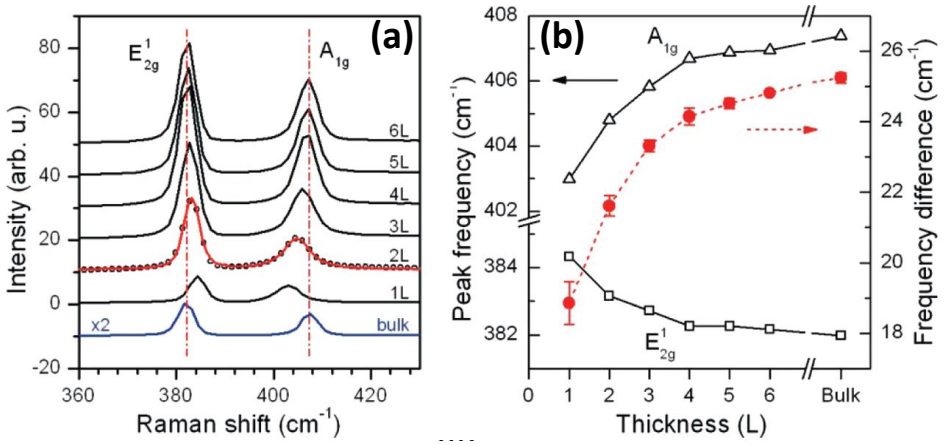


Figure 2.7 (a) Raman spectra of bulk and mono to few-layered MoS_2 films. The two predominant vibrational peaks i.e. in-plane (E^1_{2g}) and out-of-plane (A_{1g}) are highlighted by (red) dotted lines. (b) The plot shows the frequencies of E^1_{2g} and A_{1g} modes (left vertical axis) and the frequency difference between two peaks (right vertical axis) as a function of layer thickness. Reproduced from [50] with permission from American Chemical Society.

Different approaches have been developed to explain this relation between the vibrational modes within thin layers and those of bulk material. From a classical model (for coupled harmonic oscillators) perspective, the E^1_{2g} and A_{1g} modes are expected to stiffen due to increasing restoring forces acting on the atoms as additional layers are added with increasing thickness.[53] However, only out-of-plane vibrational mode (A_{1g}) confers with this prediction and the in-plane mode (E^1_{2g}) shows an anomalous behaviour. This opposite progression for E^1_{2g} mode has been attributed to either stacking-induced structural changes and/or long-range Coulombic interlayer interactions. For the latter, it has been argued that even though the interlayer interactions in MoS_2 are nominally weak, they can affect the intralayer bonding and lattice dynamics which can lead to such anomaly.[50] Alternatively, it has been shown that the long-range Coulomb interaction part of the self-interaction remains negligible for S atoms, whereas for Mo atoms it decreases considerably with the increase in number of layers. Since in E^1_{2g} mode both Mo and S atoms vibrate in-plane, the increased screening and consequent increase in dielectric tensor with the number of layers causes the E^1_{2g} mode to soften.[54]

2.4 Photoluminescence spectroscopy

MoS_2 is an indirect bandgap (~1.3 eV) material in its bulk form. However, in the monolayer regime, the quantum confinement effect in MoS_2 manifests the transition to a direct band gap (~1.8 eV). The origin of this unique PL behavior in the atomically thin regime of MoS_2 has been explained in terms of change in electronic structure when going from bulk to monolayer. Figure 2.8 (a - d) shows the band structures (as calculated by employing density functional theory) of MoS_2 with different thicknesses.[55] It can be observed that the direct excitonic transition energy at the *K* point of the Brillouin zone barely changes with the layer thickness. However, the indirect bandgap at the Γ point increases monotonically with decreasing layer thickness. This electronic structural change further stems from the nature of d-electron orbitals comprising the MoS_2 conduction and valence bands. Literature reports have shown that the highest occupied band at the *K* point is chiefly composed of strongly localized d orbitals pertaining to Mo atom sites, while that at the Γ point is found to emerge from a linear combination of d orbitals corresponding to Mo atoms and p_z orbitals on S atoms. Since Mo atoms are sandwiched between S atoms in a S-Mo-S unit, the direct bandgap state at *K* point has a less dependence than the indirect bandgap on the number of layers (or interlayer coupling). Therefore, as the thickness of MoS_2 decreases, the indirect bandgap increases whereas the direct bandgap does not vary much.[47]

This emergence of luminescence behaviour in atomically thin exfoliated MoS_2 nanosheets was first reported by Splendiani *et al*.[55] They observed that a photoluminescence (PL) spectrum of a monolayer MoS_2 shows two pronounced emission peaks corresponding to direct excitonic transitions. These excitonic peaks were located at ~677 nm (1.8 eV) and ~627 nm (2.0 eV). The energy difference between the two peaks has been attributed to the spin-orbital splitting of the valence band and the two resonant peaks were labelled as the A1 and B1 excitons, respectively. Figure 2.8 (e) displays the photoluminescence spectrum for monolayer, bilayer, hexalayer and bulk MoS_2 as obtained by Splendiani *et al*.[55] Other than the PL peaks, the apparent Raman peaks were also visible in the low-wavelength region. It is evident that the PL signal is strongest for the thinnest sample i.e. monolayer MoS_2, which gradually decreases with increasing thickness and diminishes for bulk owing to the indirect bandgap.

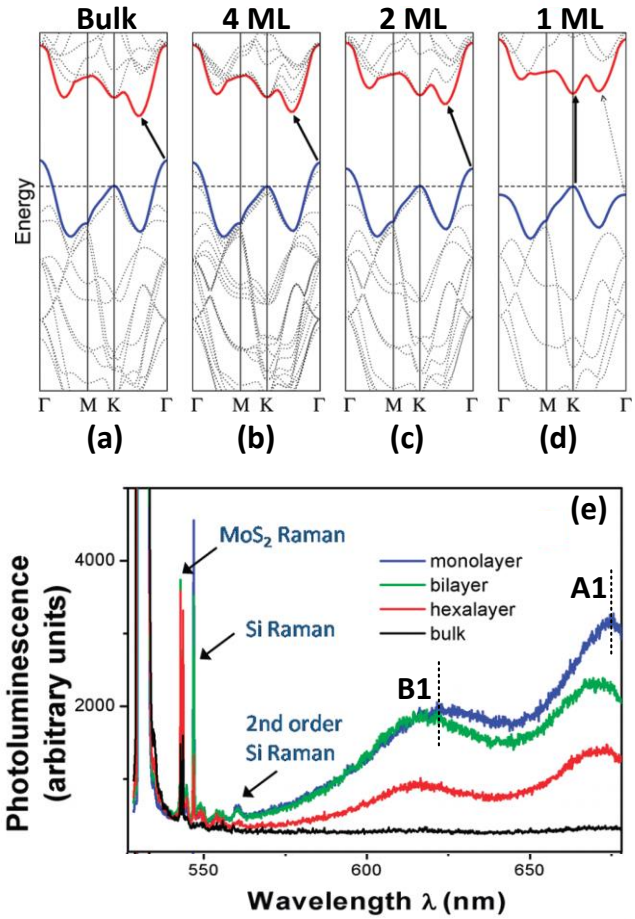


Figure 2.8 The calculated band structures of (a) bulk (b) quadrilayer (c) bilayer and (d) monolayer MoS_2. While the bulk MoS_2 exhibits an indirect bandgap, the monolayer MoS_2 becomes a direct bandgap semiconductor. (e) Photoluminescence spectra of a monolayer, bilayer, hexalayer and bulk MoS_2 films. The two direct band gap excitonic peaks are indicated with dashed lines and labelled as A1 and B1 respectively. Different Raman peaks have been labelled accordingly. Reproduced from [55] with permission from American Chemical Society.

2.5 Hydrogen evolution reaction

The quest to reduce dependence on fossil fuels has led to the development of various alternative strategies for the production of clean, sustainable energy. One of such

strategies is constructing a *hydrogen based* energy infrastructure where hydrogen can be used as a primary host of energy source. However, hydrogen does not exist naturally on earth, and therefore needs to be produced. Currently, approximately 44.5 million tons of hydrogen are produced worldwide annually.[56, 57] There are three main pathways industrially to produce hydrogen, that is, steam methane reforming, coal gasification and water electrolysis (Figure 2.9). Out of these, the first two methods account for more than 95% of the whole hydrogen production.[58] Clearly, the idea of reducing the overdependence on non-renewable sources is violated indirectly. In this context, the third method of water electrolysis provides a sustainable way of hydrogen production and therefore a continuous technological improvement for this method is underway. During water electrolysis, one of the two half reactions is the hydrogen evolution reaction (HER) which requires efficient electrocatalysts to catalyse the conversion of protons and electrons into dihydrogen. The efficacy of hydrogen evolving electrocatalysts is defined by the Gibbs free energy of hydrogen adsorption (ΔG_H). It is known that if ΔG_H is large and positive, the hydrogen atoms adsorb strongly on the electrode surface making the overall hydrogen evolution reaction unfavourable. Simultaneously, if ΔG_H is large and negative, the hydrogen atoms have a weak interaction with the electrode surface which also limits the overall turnover rate of hydrogen evolution. Therefore, an optimal value of ΔG_H (nearly zero) is desirable for efficient HER activity. For instance, for Pt, the value of ΔG_H is approximately zero[59] and correspondingly the best known solid-state hydrogen evolution catalyst. However, Pt is very expensive and non-abundant. Therefore, with the aim of providing cost-competitive hydrogen, there is an ongoing research for potential inexpensive alternative electrocatalysts. MoS_2 is one of such potential alternative electrocatalysts which has been demonstrated to exhibit high HER activity. For MoS_2, the value of ΔG_H has been calculated to be +0.08 eV for 25% of hydrogen coverage on the edge sites.[60] This makes MoS_2 a very competitive electrocatalyst and a tremendous effort is being put to develop numerous strategies in order to maximize the HER activity of this material.

Technology	Governing reaction
Steam methane reforming	$CH_4 + 2H_2O \longrightarrow 4H_2 + CO_2$
Coal gasification	$C + 2H_2O \longrightarrow 2H_2 + CO_2$
Water electrolysis	$2H_2O \longrightarrow 2H_2 + O_2$

Figure 2.9 The three main industrial pathways for hydrogen production

2.5.1 Key figures of merit for catalytic activity

A number of performance parameters are helpful in evaluating an electrocatalyst's efficacy. Although a variety of methods for assessing the activity of HER catalysts have been described in the literature, there are only few strategies which seem to be adopted by the majority of groups in order to compare different catalysts in a consistent manner. We therefore will focus on such key figures of merit which are important and have been used in this thesis work to provide a fair and useful framework to assess the catalytic activity of PEALD synthesized MoS_2 thin films.

The foremost figure of merit is the total electrode activity which is typically the first step in characterizing a HER electrocatalyst. To this purpose, the catalytic current as a function of potential is measured by using a voltammetry technique. The electric signal is recorded using a potentiostat (the specifications are provided in the further chapters). Depending on the experimental purpose, the voltammograms are either recorded in a linear or cyclic manner. The former mode is called linear sweep voltammetry (LSV) while the latter is referred to as cyclic voltammetry (CV). For water splitting reactions, the potential scale is typically calibrated to the reversible hydrogen electrode (RHE). The cathodic current is often normalized to the geometric electrode area.

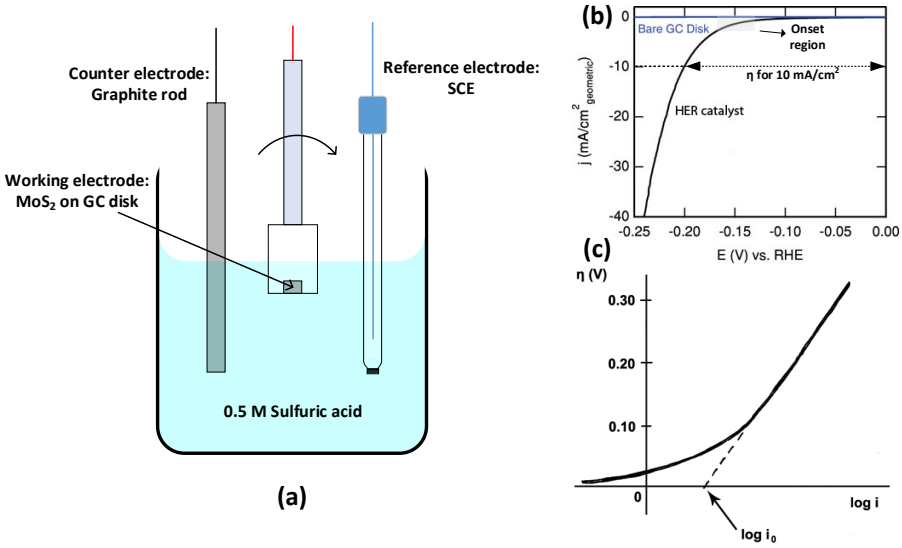


Figure 2.10 (a) The schematic of a typical three electrode setup used for HER electrochemical measurements. The electrodes are connected to a potentiostat (not shown) which measures the I-V response. (b) The cathodic polarization plot as measured by the LSV technique showing the HER activity for a bare GC disk (blue) and a HER catalyst (MoS_2 in this case) (black). The onset region is highlighted and overpotential to reach a current density of 10 mA/cm^2 is shown by a dashed line. (c) Tafel plot for a HER catalyst showing the Tafel slope (slope of the linear region) and the exchange current density (linear extrapolation to $\eta = 0$).

Figure 2.10 (a) shows the typical three electrode setup used for electrochemical testing consisting of a working electrode (MoS_2 in our case), a reference electrode (saturated calomel electrode) and a counter electrode (graphite rod). The electrochemical measurements are typically conducted in a 0.5 M H_2SO_4 as electrolyte. At times, the effused H_2 gas continuously forms bubbles on the surface of working electrode. To remove these bubbles, the working electrode is constantly rotated as indicated in Figure 2.10 (a). The working electrode acts as the cathode, the counter electrode as the anode and the reference electrode measures the *true* electrode potential of the cathode. During electrolysis, at the negatively charged cathode, a reduction reaction takes place with electrons from the cathode being given to hydrogen cations to form hydrogen gas. The half reaction in a typical acidic medium is:

Reduction at cathode: $2H^+(aq) + 2e^- \rightarrow H_2(g)$ (1)

At the negatively charged anode, an oxidation reaction occurs which generates oxygen gas and provides electrons to the anode to complete the circuit:

Oxidation at anode: $2H_2O(l) \rightarrow O_2(g) + 4H^+(aq) + 4e^-$ (2)

Figure 2.10 (b) shows the characteristic cathodic polarization curve as measured by LSV for a bare glassy carbon (GC) disk and a HER catalyst. It is clearly evident that the bare GC disk shows no/very little HER activity, while the HER catalyst yields an increasing current density (y-axis) as a function of potential which indicates a noticeable hydrogen evolution. Furthermore, some additional information can be extracted by using the LSV plot: (a) the onset region (b) Overpotential (η) required to reach a specific current density value. The former indicates the potential at which the catalytic current is first observed. However, the definition of onset potential is ambiguous as different onset potentials can be assigned depending on the observers. One reason is that a large fraction of the total current in the onset region may be a result of non-Faradaic capacitive current which makes it difficult to define strictly a specific value for onset potential. Therefore, a suitable range of current value from 0.05 - 5 mA/cm^2 for the onset is widely considered as a definition for the onset region. The comparison of different catalysts is done based on a more relevant metric which is the overpotential required to reach an operating current density of interest. A widely accepted figure of merit is the overpotential required to reach 10 mA/cm^2 and is used to compare the total electrode activities of the MoS_2 HER catalysts.[61, 62]

The other important HER activity metrics are the *Tafel slope* and exchange current density (i_0). Figure 2.10 (c) displays the Tafel plot for a HER catalyst which is basically a graph between overpotential and natural logarithm of current density. The linear portion of the Tafel plot is fit to the Tafel equation: $\eta = a + b \log i$, where b is the Tafel slope. From the Tafel equation, the aforementioned two important parameters can be derived: Tafel slope (b) and exchange current density (i_0). The *Tafel slope* determines the additional voltage required in order to increase the catalytic current by an order of magnitude. The units of *Tafel slope* are generally specified in mV/decade. The *Tafel slope* is typically related to the catalytic mechanism of the electrode reaction. In the literature, three possible steps have been suggested for which different values of Tafel slopes are calculated.[63] The first step is the primary discharge step and is referred to as the Volmer step:

$$H_3O^+ + e^- \rightarrow H_{ad} + H_2O \quad (3)$$

(subscript $_{ad}$ means adsorbed to the catalyst)

Tafel slope (b) ~ 120 mV/dec

After the Volmer step, the reaction can proceed via either of the two possible steps. The first one is the Heyrovsky reaction:

$$H_{ad} + H_3O^+ + e^- \rightarrow H_2 + H_2O \quad (4)$$

Tafel slope (b) ~ 40 mV/dec

The other is a Tafel reaction:

$$H_{ad} + H_{ad} \rightarrow H_2 \quad (5)$$

Tafel slope (b) ~ 30 mV/dec

The rate determining step for any HER catalyst thus can be estimated by using the value of obtained *Tafel slope* and comparing that with the theoretical numbers for three mechanisms as stated above. However, in most cases, the Tafel slope alone cannot be used to identify the mechanism unambiguously and therefore additional experiments are required generally.[64, 65]

The exchange current density (i_0) describes the intrinsic catalytic activity of the electrode material under equilibrium conditions at $\eta = 0$. It can be obtained by the linear extrapolation using Tafel plot as shown in Figure 2.10 (c). In general, an electrocatalyst having a high i_0 and small Tafel slope (b) is desirable.

One of the other crucial factors for a good electrocatalyst is the structural and catalytic stability in the acidic working environment. The stability of an electrocatalyst can be assessed either by measuring the current variation with time (i.e. the I-t curve) or by conducting the repetitive cycles in a CV measurement. Furthermore, the best way to understand the catalyst's performance is to measure its intrinsic activity. This is achieved by measuring the activity of each catalytic site and relate it to the site's physical and chemical properties. A fundamental understanding of origin of a material's catalytic activity can help designing highly active electrodes. However, different materials might need different methods and the measurements are often complicated due to non-Faradaic current, catalyst instability, and/or transport limitations. A common strategy for determining the intrinsic per-site activity is to first measure the total

electrode activity and then perform a separate measurement to determine the total number of active sites and finally infer the average *turnover frequency*[c].

Measuring the electrochemically active surface area (ECSA) as opposed to the geometrical electrode area is one of the most common approaches for estimating the number of catalytic sites.[66, 67] The number of active sites often scales with the catalyst's surface area which makes this strategy appropriate especially for non-precious materials. Typically, the methods for measuring the active surface area include both gaseous adsorption techniques (like Brunauer - Emmett - Teller theory) and electrochemical measurements. The latter method is preferred because of more accurate estimation of active sites. One of such popular electrochemical techniques is the double layer capacitance measurement which basically measures the non-Faradaic current associated with the electrochemical double layer charging at the catalyst surface.[64, 66-68] The capacitive currents are measured as a function of voltage scan rates which typically results in a linear relationship. The slope of this plot yields the double layer capacitance (C_{dl}) value which is then compared to the material's specific capacitance (determined using a flat reference material) to estimate the catalyst's ECSA accordingly.[61] Other than this, the electrochemical probe molecule adsorption which involves methods like underpotential deposition of lead or copper, is another common technique to determine ECSA.

However, the above mentioned techniques might fail to accurately estimate the ECSA in case of electrocatalysts with structural or chemical heterogeneous sites with different activity. Therefore, for such materials, the supporting techniques that enable a direct determination of number of active sites are also preferred. This is because of the fact that the number of active sites may not scale directly with the overall surface area or ECSA. For instance, MoS_2 HER catalysts comprise of catalytically active edge sites and inert basal plane sites. Some groups have therefore employed scanning tunneling microscopy or transmission electron microscopy to identify the active edge sites.[60, 65] Figure 2.11 illustrates this situation for crystalline 2-H MoS_2. The difference between geometrical surface area and electrochemically active surface area is evident. Furthermore, the basal plane sites and active edge sites are explicitly highlighted. It can

[c] Turnover frequency is defined as the number of reactant that a catalyst can convert to a desired product per catalytic site per unit of time.

be inferred that for MoS_2, a geometry with basal planes oriented perpendicular to the surface would result in a higher catalytic activity due to exposure of more active edge sites. We have leveraged this attribute of MoS_2 and have demonstrated the out-of-plane nanostructures synthesized by PEALD as efficient electrocatalysts for HER in Chapter 3. Furthermore, in order to estimate the ECSA for PEALD synthesized films, the method based on double layer capacitance measurement (as discussed above) has been adopted in this work.

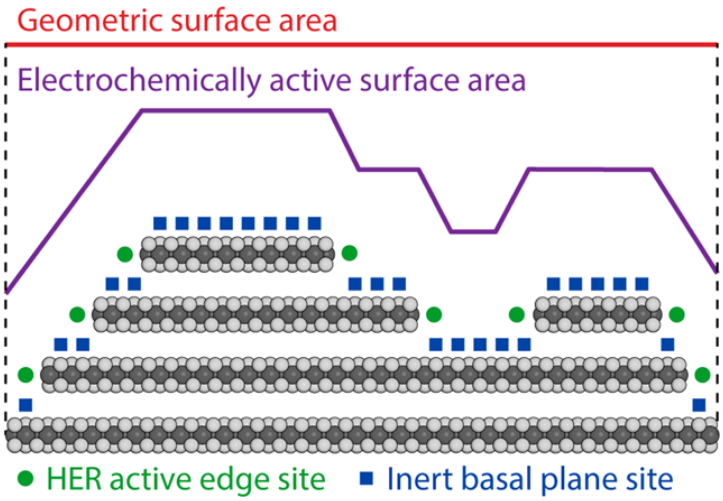


Figure 2.11 The two-dimensional representation of electrochemically active surface area for crystalline 2-H MoS_2. The catalytically active edge sites and inert basal plane sites are indicated by green and blue squares respectively. Reproduced from [64] with permission from American Chemical Society.

References

1. S. M. George, *Chemical Reviews*, 2010, **110**, 111-131.
2. R. L. Puurunen, *Chemical Vapor Deposition*, 2014, **20**, 332-344.
3. M. Leskelä, L. Niinistö, P. Niemela, E. Nykänen, P. Soininen, M. Tiitta and J. Vähäkangas, *Vacuum*, 1990, **41**, 1457-1459.
4. T. Asikainen, M. Ritala and M. Leskelä, *Applied Surface Science*, 1994, **82-83**, 122-125.
5. B. Meester, L. Reijnen, A. Goossens and J. Schoonman, *J. Phys. IV France*, 2001, **11**, Pr3-1147-Pr1143-1152.
6. T. W. Scharf, S. V. Prasad, T. M. Mayer, R. S. Goeke and M. T. Dugger, *Journal of Materials Research*, 2004, **19**, 3443-3446.
7. V. Pore, M. Ritala and M. Leskelä, *Chemical Vapor Deposition*, 2007, **13**, 163-168.
8. R. B. Yang, J. Bachmann, M. Reiche, J. W. Gerlach, U. Gösele and K. Nielsch, *Chemistry of Materials*, 2009, **21**, 2586-2588.
9. J. Y. Kim and S. M. George, *The Journal of Physical Chemistry C*, 2010, **114**, 17597-17603.
10. X. Meng, J. A. Libera, T. T. Fister, H. Zhou, J. K. Hedlund, P. Fenter and J. W. Elam, *Chemistry of Materials*, 2014, **26**, 1029-1039.
11. S. B. Kim, P. Sinsermsuksakul, A. S. Hock, R. D. Pike and R. G. Gordon, *Chemistry of Materials*, 2014, **26**, 3065-3073.
12. L. K. Tan, B. Liu, J. H. Teng, S. Guo, H. Y. Low and K. P. Loh, *Nanoscale*, 2014, **6**, 10584-10588.
13. X. Meng, D. J. Comstock, T. T. Fister and J. W. Elam, *ACS Nano*, 2014, **8**, 10963-10972.
14. N. Schneider, M. Bouttemy, P. Genevée, D. Lincot and F. Donsanti, *Nanotechnology*, 2015, **26**.
15. S. C. Riha, A. A. Koegel, X. Meng, I. S. Kim, Y. Cao, M. J. Pellin, J. W. Elam and A. B. F. Martinson, *ACS Applied Materials and Interfaces*, 2016, **8**, 2774-2780.
16. R. F. McCarthy, M. S. Weimer, R. T. Haasch, R. D. Schaller, A. S. Hock and A. B. F. Martinson, *Chemistry of Materials*, 2016, **28**, 2033-2040.
17. Y. Çimen, A. W. Peters, J. R. Avila, W. L. Hoffeditz, S. Goswami, O. K. Farha and J. T. Hupp, *Langmuir*, 2016, **32**, 12005-12012.
18. X. Meng, Y. Cao, J. A. Libera and J. W. Elam, *Chemistry of Materials*, 2017, **29**, 9043-9052.
19. N. Mahuli, D. Saha and S. K. Sarkar, *Journal of Physical Chemistry C*, 2017, **121**, 8136-8144.
20. S. C. Riha, A. A. Koegel, J. D. Emery, M. J. Pellin and A. B. F. Martinson, *ACS Applied Materials & Interfaces*, 2017, **9**, 4667-4673.
21. D. K. Nandi, U. K. Sen, D. Choudhury, S. Mitra and S. K. Sarkar, *Electrochimica Acta*, 2014, **146**, 706-713.
22. Y. Jang, S. Yeo, H.-B.-R. Lee, H. Kim and S.-H. Kim, *Applied Surface Science*, 2016, **365**, 160-165.
23. D. H. Kwon, Z. Jin, S. Shin, W.-S. Lee and Y.-S. Min, *Nanoscale*, 2016, **8**, 7180-7188.
24. T. Jurca, M. J. Moody, A. Henning, J. D. Emery, B. Wang, J. M. Tan, T. L. Lohr, L. J. Lauhon and T. J. Marks, *Angewandte Chemie International Edition*, 2017, **56**, 4991-4995.

25. M. Mattinen, T. Hatanpää, T. Sarnet, K. Mizohata, K. Meinander, P. J. King, L. Khriachtchev, J. Räisänen, M. Ritala and M. Leskelä, *Advanced Materials Interfaces*, 2017, DOI: 10.1002/admi.201700123, 1700123-n/a.
26. W. Jeon, Y. Cho, S. Jo, J.-H. Ahn and S.-J. Jeong, *Advanced Materials*, 2017, **29**, 1703031.
27. Z. Jin, S. Shin, D. H. Kwon, S.-J. Han and Y.-S. Min, *Nanoscale*, 2014, **6**, 14453-14458.
28. S. Shin, Z. Jin, D. H. Kwon, R. Bose and Y.-S. Min, *Langmuir*, 2015, **31**, 1196-1202.
29. B. Robert, P. Prasanna, S. Raj, J. T. Douglas, S. Paul and E. David, *Materials Research Express*, 2015, **2**, 035006.
30. J. J. Pyeon, S. H. Kim, D. S. Jeong, S.-H. Baek, C.-Y. Kang, J.-S. Kim and S. K. Kim, *Nanoscale*, 2016, **8**, 10792-10798.
31. Y. Kim, J.-G. Song, Y. J. Park, G. H. Ryu, S. J. Lee, J. S. Kim, P. J. Jeon, C. W. Lee, W. J. Woo, T. Choi, H. Jung, H.-B.-R. Lee, J.-M. Myoung, S. Im, Z. Lee, J.-H. Ahn, J. Park and H. Kim, *Scientific Reports*, 2016, **6**, 18754.
32. A. Valdivia, D. J. Tweet and J. F. Conley, Jr., *Journal of Vacuum Science and Technology A: Vacuum, Surfaces and Films*, 2016, **34**.
33. D. Xiong, Q. Zhang, W. Li, J. Li, X. Fu, M. F. Cerqueira, P. Alpuim and L. Liu, *Nanoscale*, 2017, **9**, 2711-2717.
34. L. Liu, Y. Huang, J. Sha and Y. Chen, *Nanotechnology*, 2017, **28**.
35. Y. Huang, L. Liu, J. Sha and Y. Chen, *Applied Physics Letters*, 2017, **111**.
36. T. A. Ho, C. Bae, S. Lee, M. Kim, J. M. Montero-Moreno, J. H. Park and H. Shin, *Chemistry of Materials*, 2017, **29**, 7604-7614.
37. S. Cadot, O. Renault, M. Fregnaux, D. Rouchon, E. Nolot, K. Szeto, C. Thieuleux, L. Veyre, H. Okuno, F. Martin and E. A. Quadrelli, *Nanoscale*, 2017, **9**, 538-546.
38. D. K. Nandi, S. Sahoo, S. Sinha, S. Yeo, H. Kim, R. N. Bulakhe, J. Heo, J. J. Shim and S. H. Kim, *ACS Applied Materials and Interfaces*, 2017, **9**, 40252-40264.
39. A. U. Mane, S. Letourneau, D. J. Mandia, J. Liu, J. A. Libera, Y. Lei, Q. Peng, E. Graugnard and J. W. Elam, *Journal of Vacuum Science & Technology A*, 2017, **36**, 01A125.
40. Z. Tianbao, W. Yang, X. Jing, C. Lin, Z. Hao, S. Qingqing, D. Shijin and Z. David Wei, *2D Materials*, 2018, **5**, 015028.
41. A. Sharma, M. A. Verheijen, L. Wu, S. Karwal, V. Vandalon, H. C. M. Knoops, R. Sundaram, J. P. P. Hofmann, W. Kessels and A. A. Bol, *Nanoscale*, 2018, DOI: 10.1039/C8NR02339E.
42. H. Wang, Z. Lu, S. Xu, D. Kong, J. J. Cha, G. Zheng, P.-C. Hsu, K. Yan, D. Bradshaw, F. B. Prinz and Y. Cui, *Proceedings of the National Academy of Sciences*, 2013, **110**, 19701-19706.
43. J. G. Song, G. H. Ryu, S. J. Lee, S. Sim and C. W. Lee, *Nature Communications*, 2015, DOI: 10.1038/ncomms8817.
44. C. Martella, P. Melloni, E. Cinquanta, E. Cianci, M. Alia, M. Longo, A. Lamperti, S. Vangelista, M. Fanciulli and A. Molle, *Advanced Electronic Materials*, 2016, **2**, 1600330.
45. B. D. Keller, A. Bertuch, J. Provine, G. Sundaram, N. Ferralis and J. C. Grossman, *Chemistry of Materials*, 2017, **29**, 2024-2032.
46. V. Heine, *Physics Today*, 2008, **61**, 57-58.
47. A. Bera and A. K. Sood, in *MoS2: Materials, Physics, and Devices*, ed. Z. M. Wang, Springer International Publishing, Cham, 2014, DOI: 10.1007/978-3-319-02850-7_7, pp. 155-215.

48. X. Zhang, X.-F. Qiao, W. Shi, J.-B. Wu, D.-S. Jiang and P.-H. Tan, *Chemical Society Reviews*, 2015, **44**, 2757-2785.
49. S. Mignuzzi, A. J. Pollard, N. Bonini, B. Brennan, I. S. Gilmore, M. A. Pimenta, D. Richards and D. Roy, *Physical Review B*, 2015, **91**, 195411.
50. C. Lee, H. Yan, L. E. Brus, T. F. Heinz, J. Hone and S. Ryu, *ACS Nano*, 2010, **4**, 2695-2700.
51. M. Elisha, G. Andy, M. Jonathan, C. Mike and S. S. Ravi, *Journal of Physics D: Applied Physics*, 2017, **50**, 184005.
52. K. F. Mak, C. Lee, J. Hone, J. Shan and T. F. Heinz, *Physical Review Letters*, 2010, **105**, 136805.
53. H. Li, Q. Zhang, C. C. R. Yap, B. K. Tay, T. H. T. Edwin, A. Olivier and D. Baillargeat, *Advanced Functional Materials*, 2012, **22**, 1385-1390.
54. A. Molina-Sánchez and L. Wirtz, *Physical Review B*, 2011, **84**, 155413.
55. A. Splendiani, L. Sun, Y. Zhang, T. Li, J. Kim, C.-Y. Chim, G. Galli and F. Wang, *Nano Letters*, 2010, **10**, 1271-1275.
56. M. Balat, *International Journal of Hydrogen Energy*, 2008, **33**, 4013-4029.
57. M. Wang, Z. Wang, X. Gong and Z. Guo, *Renewable and Sustainable Energy Reviews*, 2014, **29**, 573-588.
58. X. Zou and Y. Zhang, *Chemical Society Reviews*, 2015, **44**, 5148-5180.
59. J. K. Nørskov, T. Bligaard, A. Logadottir, J. R. Kitchin, J. G. Chen, S. Pandelov and U. Stimming, *Journal of the Electrochemical Society*, 2005, **152**, J23-J26.
60. T. F. Jaramillo, K. P. Jørgensen, J. Bonde, J. H. Nielsen, S. Horch and I. Chorkendorff, *Science*, 2007, **317**, 100.
61. J. D. Benck, Z. Chen, L. Y. Kuritzky, A. J. Forman and T. F. Jaramillo, *ACS Catalysis*, 2012, **2**, 1916-1923.
62. E. Parzinger, E. Mitterreiter, M. Stelzer, F. Kreupl, J. W. Ager, A. W. Holleitner and U. Wurstbauer, *Applied Materials Today*, 2017, DOI: 10.1016/j.apmt.2017.04.007.
63. D. Y. Chung, S.-K. Park, Y.-H. Chung, S.-H. Yu, D.-H. Lim, N. Jung, H. C. Ham, H.-Y. Park, Y. Piao, S. J. Yoo and Y.-E. Sung, *Nanoscale*, 2014, **6**, 2131-2136.
64. J. D. Benck, T. R. Hellstern, J. Kibsgaard, P. Chakthranont and T. F. Jaramillo, *ACS Catalysis*, 2014, **4**, 3957-3971.
65. Z. Chen, D. Cummins, B. N. Reinecke, E. Clark, M. K. Sunkara and T. F. Jaramillo, *Nano Letters*, 2011, **11**, 4168-4175.
66. J. Kibsgaard, Z. Chen, B. N. Reinecke and T. F. Jaramillo, *Nature Materials*, 2012, **11**, 963.
67. D. Merki and X. Hu, *Energy & Environmental Science*, 2011, **4**, 3878-3888.
68. S. Trasatti and O. A. Petrii, *Journal of Electroanalytical Chemistry*, 1992, **327**, 353-376.

3

Low-temperature plasma-enhanced atomic layer deposition of 2-D MoS_2: large area, thickness control and tuneable morphology*

Low-temperature controllable synthesis of monolayer-to-multilayer thick MoS_2 with tuneable morphology is demonstrated by using plasma enhanced atomic layer deposition (PEALD). The characteristic self-limiting ALD growth with a growth-per-cycle of 0.1 nm/cycle and digital thickness control down to a monolayer are observed with excellent wafer scale uniformity. The as-deposited films are found to be polycrystalline in nature showing the signature Raman and photoluminescence signals for the mono-to-few layered regime. Furthermore, a transformation in film morphology from in-plane to out-of-plane orientation of the 2-dimensional layers as a function of growth temperature is observed. An extensive study based on high-resolution transmission electron microscopy is presented to unravel the nucleation mechanism of MoS_2 on SiO_2/Si substrates at 450 °C. In addition, a model elucidating the film morphology transformation (at 450 °C) is hypothesized. Finally, the out-of-plane oriented films are demonstrated to outperform the in-plane oriented films in the hydrogen evolution reaction for water splitting applications.

*A. Sharma, M. A. Verheijen, L. Wu, S. Karwal, V. Vandalon, H. C. M. Knoops, R. S. Sundaram, J. P. Hofmann, W. M. M. Kessels, A. A. Bol, *Nanoscale* **2018**, 10, 8615.

3.1 Introduction

The discovery of graphene and subsequent efforts to thoroughly understand its remarkable physical properties have stimulated the exploration of other layered two-dimensional (2-D) materials beyond graphene.[1-4] In recent years, transition metal dichalcogenides (TMDs) have been the focal point of this research activity amongst which molybdenum disulphide (MoS_2) is the most studied material.[3, 5-7] MoS_2 is a typical two-dimensional layered material with a honeycomb structure. A weak intra-layer van der Waals interaction enables its exfoliation down to a single stoichiometric unit (S-Mo-S) thick monolayer analogous to graphene.[8, 9] Electronically, MoS_2 possesses an indirect band gap of ~1.3 eV in its bulk form, which transitions to a direct band gap of ~1.8 eV for the monolayer regime due to quantum confinement phenomena.[10, 11] Furthermore, the absence of inversion symmetry in monolayer MoS_2 (as compared to the bulk material) gives rise to interesting applications like valleytronics and spintronics.[12, 13] Thus, the reduction of the dimensions of MoS_2 opens up new avenues for a vast range of (opto-) electronic devices.[14-20] It has also been demonstrated that MoS_2 films in which the 2-D layers have out-of-plane orientations (with exposed edge sites) possess excellent electrocatalytic properties. The presence of dangling bonds and vacancies on the edge sites render these films highly catalytically active for the hydrogen evolution reaction in water splitting.[21-25] Therefore, MoS_2 has emerged as one of the frontrunner materials not only for future electronics,[12, 13, 26, 27] but also as a potential alternative for precious noble metals in the area of electrocatalysis.[28-30] To capitalize on the extraordinary properties of MoS_2 there has been a quest for scalable, facile synthesis methods with ability to control both the thickness as well as the morphology. To date, most of these studies have focused on the synthesis of mono-to-few layers with in-plane orientation of the 2-D layers. A large variety of both top-down and bottom-up synthetic routes are reported in literature aiming at the synthesis of monolayer to few-layered MoS_2 thin films, for example, micro-mechanical and chemical exfoliation,[1, 6, 9, 15, 31-33] hydrothermal[34] and electrochemical methods,[35, 36] physical vapor deposition,[37, 38] chemical vapor deposition (CVD),[25, 39-43] thermal vapor sulphurization of Mo or MoO_3[44-46] *etc.* In contrast, despite the technological significance, there are only a few studies on controlling the film morphology, i.e. selective growth of out-of-plane oriented (OoPO) films. Most of these reports are based on high temperature techniques like CVD and rapid sulphurization of metal/metal oxide. For example, Li *et al.* have reported the synthesis of such OoPO nanostructures

by using gas phase CVD at 750 °C.[23] Likewise, the rapid sulphurization of parent metal films (Mo films) at 550 °C -800 °C is also reported to yield out-of-plane growth of MoS_2 thin films.[22, 47] Most of these techniques, however, provide insufficient control over thickness and tailoring of the morphology is not possible. Additionally, the requirement of a high processing temperature may hamper the development of this material on a technologically relevant scale. This paper discusses the use of atomic layer deposition (ALD) to deposit MoS_2 films with control over both thickness and morphology at a relatively low temperature (450 °C). ALD is a cyclic process based on self-limiting surface reactions which ensures Å-level thickness controllability and uniformity over large areas. The accurate thickness control offered by ALD has established it as a method of choice for high-k oxides in semiconductor industry.[48] Additionally, ALD offers a high conformality on intricate structures which are difficult to coat with any other gas phase technique. The application of ALD for 2-D materials is therefore of high interest and can be instrumental in the synthesis of high quality, large-area MoS_2. In literature, only a handful of reports on the synthesis of MoS_2 by means of ALD are available. Most of these studies have implemented either halide or carbonyl based metal precursors in combination with H_2S or CH_3SSCH_3 as co-reactant.[49-51] Some other groups have implemented $Mo(thd)_3$ and $Mo(NMe_2)_4$ as metal precursors in combination with H_2S.[52, 53] These processes are shown to produce MoS_2 over a large area with a good control over thickness and thus exhibited the potential of ALD in 2-D world. However, most of these processes rely on high temperature post-annealing to improve the structural quality of the as-deposited 2-D films which is undesirable for industrial scalability (as discussed above) and remains an addressable issue.[50, 54] Recently, anisotropic growth of 'edge-on' (OoPO) MoS_2 thin films by ALD using $MoCl_5$ in combination with H_2S has been reported.[55] However, the observed lateral inhomogeneity in growth rate over the wafer hints towards a possible CVD component in this process, which will disrupt the typical self-limiting ALD behavior and result in loss of precise thickness control.

In this work, we demonstrate that plasma enhanced ALD based on $[(NtBu)_2(NMe_2)_2Mo]$ and H_2S at 300 °C - 450 °C is able to deliver archetypical precise thickness control and tuneable texture of the as-deposited MoS_2 films, while preserving the essence of ALD (i.e. self-limiting behaviour). We will first discuss the detailed investigation of the self-limiting behaviour, chemical composition of the as-deposited film and wafer-scale uniformity of the ALD process. Furthermore, the precise control

over thickness from mono-layer to few layered regime is discussed. In the following sub-section, the influence of deposition temperature on the film morphology and crystallinity is presented. Next, the nucleation mechanism of MoS_2 thin films on SiO_2/Si substrates is elucidated and a model explaining the possible mechanism pertaining to the morphology transformation from in-plane to out-of-plane orientation for films deposited at 450 °C is also discussed. Finally, the control over film morphology is showcased by implementing the films with variant morphologies as electrocatalysts for the hydrogen evolution reaction (HER).

3.2 Experimental section

ALD process specifications

The MoS_2 thin films were deposited in an Oxford Instruments FlexALTM ALD reactor[56, 57] on 4" Si wafers with a thermally grown 450 nm thick oxide layer on top. To maintain consistency throughout, all reported temperatures here refer to the set temperature of the substrate table which is called the 'growth temperature'. The Mo precursor employed was $[(NtBu)_2(NMe_2)_2Mo]$, (98%, Strem Chemicals) and was contained in a stainless steel canister which was heated to 50 °C. At this temperature, the vapor pressure of the precursor is reported to be 0.13 Torr.[58] The delivery lines were kept at 90 °C to avoid condensation of the precursor while the reactor walls were heated to 150 °C. For the precursor delivery to the deposition chamber a 100 sccm Ar (>99.999 % purity) bubbling flow was employed. An intermediate Ar purge step with 100 sccm of Ar flow was applied after each precursor and plasma exposure steps. As the co-reactant, a H_2 + H_2S + Ar plasma (8 sccm H_2; 2 sccm H_2S; 40 sccm Ar) plasma gas mixture generated in an inductively coupled plasma (ICP) source was used. The plasma power was 100 W with a reactor pressure of 6.6 mTorr during the plasma step. The ALD recipe was established with the first half cycle consisting of precursor dosing for 6s followed by 6s purge and 4s pump down. The second half cycle used 20 s of plasma exposure with the same scheme for subsequent purge and pump as in the first half cycle. The film thickness evolution during deposition was monitored by *in-situ* spectroscopy ellipsometry (J.A. Woollam M2000F, 1.25 eV - 5 eV). The thickness values were extracted by employing the 'B-spline' model.

Film crystallinity and surface morphology

Grazing incidence X-ray diffraction (GI-XRD) was employed to determine the crystalline phases of the MoS_2 thin films. The XRD analysis was performed on a

Panalytical X'Pert PRO MRD employing Cu Kα (1.54 Å) radiation with an incidence angle of 0.5° with respect to the substrate plane. Furthermore, Raman spectroscopy (RS) and photoluminescence (PL) spectroscopy measurements were performed with a Renishaw Raman microscope equipped with a 514 nm laser, integrated switchable gratings with 600 or 1800 lines/mm, and a CCD detector. For each scan, 5 accumulations with acquisition time of 10 s were taken. The surface morphology was studied by scanning electron microscopy (SEM) using a ZeissSigma Nanolab operating at an acceleration voltage of 2 kV. Additionally, atomic force microscopy (AFM) was also employed to study the surface topology of the as-deposited films. The images were acquired at room temperature on Veeco dimension 3100 operated in tapping mode using Al coated Si tip (PointProbe Plus-NCHR) having a radius < 7 nm. Images were processed in Gwyddion software with OpenGL interface and RMS roughness was obtained statistically from a scan area of 500 x 500 nm^2.

Chemical composition

To determine the elemental composition, X-ray photoelectron spectroscopy (XPS) was performed using a Thermo Scientific K-alpha spectrometer (Thermo Fisher Scientific, Waltham, MA) equipped with a monochromatic Al Kα X-ray radiation source (hν = 1486.6 eV). For the XPS analysis, a 400 µm diameter spot was used and photoelectrons were collected at a take-off angle of 60°. The samples were neutralized during the XPS analysis using an electron flood gun in order to correct for differential or non-uniform charging. All peaks in the XPS survey scans are referenced to the binding energy of the C1s peak of adventitious carbon (284.8 eV) for charge correction and quantification of the survey scans have been performed using Avantage software. Furthermore, Rutherford backscattering spectroscopy (RBS) was employed to determine the absolute chemical composition of the films. RBS was performed using a 1.523 MeV He+ ion beam and a scatter angle of 170°.

Film microstructure

The film microstructure was determined by HRTEM analysis using a JEOL ARM 200F operated at 80 kV. For the top planar view images, MoS_2 films were grown on SiN_x TEM windows, coated with ~5 nm ALD SiO_2. Selected area electron diffraction (SAED) patterns were acquired from a 1.3 µm diameter area on each sample. For the cross-sectional imaging, the MoS_2 film was coated with a SiO_x film stack as a protective layer and subsequently prepared using a standard FIB lift-out TEM sample preparation scheme.

Electrochemical testing

MoS_2 films were deposited on glassy carbon plates polished by 0.3 μm Al_2O_3 slurry for electrochemical tests. The measurements were performed in a three-electrode electrochemical workstation (Type: PGSTAT302N, Metrohm Autolab) with saturated calomel electrode (0.269 V vs. reversible hydrogen electrode (RHE) as a reference electrode, Pt foil (1 x 2 cm^2) as a counter electrode and glassy carbon working electrode. All measurements were performed in 0.5 M H_2SO_4 electrolyte prepared using 18 MΩ·cm deionized Milli-Q water purged with Ar for 20 min. Linear sweep voltammetry (LSV) experiments were conducted with a scan rate of 5 mV/s and AC electrochemical impedance spectroscopy was recorded at open circuit potential (OCP) in the frequency range of 10 kHz to 0.1 Hz. To calculate the Tafel slope, the linear portion at low overpotential region was fit to the Tafel equation using the internal resistance corrected LSV curves. Cyclic voltammetry (CV) stability tests were conducted with a scan rate of 50 mV/s starting at OCP from -0.52 V to 0.62 V.

3.3 Results and Discussions

3.3.1 Characterization of the ALD process

3.3.1.1 Self-limiting growth, thickness control and uniformity

The self-limiting growth characteristics of the ALD process were investigated at a growth temperature of 250 °C. At this temperature, a saturated growth-per-cycle (GPC) of 0.1 nm/cycle is observed at the optimized precursor dose step and plasma exposure time of 6 s and 20 s, respectively. The saturation curves for the precursor dose step and plasma exposure time confirming the typical ALD behaviour are shown and further discussed in the Appendix (Figure A.3.1).

We measured the nominal film thickness as a function of number of cycles by *in-situ* spectroscopic ellipsometry (SE). This was performed for ALD depositions over a large temperature range (150 °C - 450 °C). The plot in Figure 3.1 (a) shows the evolution of film thickness as a function of number of ALD cycles for the entire investigated temperature range. Based on this plot, few observations can be made. Up to 300 °C, a linear relationship between film thickness and number of ALD cycles is observed, signifying the typical ALD behaviour. Above 350 °C, a non-linear increase in thickness is observed after 50 cycles, implying an increase in GPC during growth which is ascribed to a change in morphology by faster growth at the edge sites of MoS_2 as is

discussed below. Also, it is worth mentioning that for all temperatures the film growth shows no nucleation delay during initial cycles, which is a highly valuable attribute for reproducible synthesis of mono-layer to thick MoS_2 films. Both from SE (Figure 3.1 (a)) and Rutherford backscattering spectroscopy (RBS) conducted for bulk regime i.e. film of 300 ALD cycles in each case (Figure 3.1 (b)), it is clear that the GPC increases with increasing temperature. This elevated growth rate at higher growth temperatures is most likely due to enhanced precursor adsorption owing to the formation of high surface area films with out-of-plane oriented (OoPO) morphology at higher growth temperatures. Additionally, it can also be speculated that the enhanced surface diffusion of metal atoms towards chemically more favourable edge sites (as compared to basal planes) of MoS_2 film deposited at higher growth temperature may contribute to the accelerated growth rate. The detailed discussion on the formation of OoPO films is provided later in this paper. To confirm that at 450 °C, the higher GPC is not a result of precursor decomposition in CVD - like reactions, a saturation study for the precursor half cycle was also performed at this temperature. The corresponding plot is shown in Figure A.3.1 (d) (Appendix) which shows a plateau for the GPC with varying precursor dose and therefore ALD is confirmed at 450 °C precluding any role of precursor decomposition. The chemical composition of the as-deposited films was examined by X-ray photoelectron spectroscopy (XPS). The corresponding surface survey scan for the film deposited at 300°C is shown in Figure A.3.2.1 (a) (Appendix). This figure reveals that apart from characteristic Mo and S peaks, a small amount of O and C is also present on the film surface most probably due to atmospheric contamination. A high resolution X-ray photoelectron spectrum for the Mo 3d region (Figure A.3.2.1 (b) in Appendix) shows the doublet for MoS_2 (Mo^{4+}) with the 3d5/2 peak at 228.9 eV and the 3d3/2 peak at 232.1 eV which is in accordance and the 3d3/2 peak at 232.1 eV which is in accordance with the binding energy positions given in the literature.[45,59,60] Furthermore, a small fraction of Mo^{6+} is also detected corresponding to MoO_3 with binding energy position at 233.1 eV in line with the literature. The oxygen and carbon contaminants are only confined to the surface since a mild sputtering with Ar^+ ions results into almost complete removal of the two species with atomic % below the detection limit of XPS (Figure A.3.2.1 (c, d) in Appendix). In addition, it was observed that the film composition is fairly stoichiometric in nature over the whole investigated growth temperature range. Table A.3.1 in the Appendix shows that the composition changes from slightly over-stoichiometric at low temperatures to under-stoichiometric at high temperatures, which has been frequently reported in the literature since the films

produced by bottom-up synthesis methods can either be S-rich or possess S vacancies depending on the process parameters. It is worth mentioning that the growth temperature also influences the structure of material i.e. amorphous and crystalline (See sec. 3.3.2), which is reflected in the film stoichiometry as aforementioned. The amorphous films synthesized at lower temperatures (150 °C - 250 °C) are S rich which is attributed to the presence of additional S_2^{2-} species as will be discussed in Chapter 5 of this thesis. However, despite being structurally different from the polycrystalline MoS_2 films, a self-limiting ALD growth behavior is still obtained for amorphous films which can be inferred from the linear relationship between thickness and number of ALD cycles as mentioned and shown in Figure 3.1 (a). Since the 2-D nanocrystalline MoS_2 is of high interest for various applications, the bulk of the research work presented in this chapter focusses on nanocrystalline films synthesized at 450 °C.

Subsequently, the film uniformity was analysed on a 4" Si wafer as shown in Figure 3.1 (c). Spectroscopic ellipsometry (SE) was employed to measure the film thickness spatially across the wafer for a film deposited with 200 ALD cycles at a growth temperature of 300 °C. A small variation in film thickness is found over the scanned areas on the wafer (non-uniformity (% 1σ ((std. dev.)/(Avg.)) = 2.4) clearly exhibiting a good thickness uniformity. The uniformity of the grown film is a direct result of the typical self-limiting nature of an ALD process. A Raman line scan was also performed on the same 4'' wafer to study the uniformity in crystallinity of the as-deposited film. Figure 3.1 (d) shows the corresponding spectra with the signature vibrational peaks for crystalline MoS_2. The two characteristic Raman modes correspond to the in-plane (E^1_{2g}) and out-of-plane (A_{1g}) vibrational peak frequencies typically appearing at 382 cm^{-1} and 408 cm^{-1}, respectively[61]. In addition, the frequency difference between two modes (Δ) and relative Raman peak intensities as a function of measurement position are plotted as shown in Figure 3.1 (d). Very small variations in Δ: 24.8 - 26 cm^{-1} and in relative Raman peak intensity ($I(E^1_{2g})/I(A_{1g})$): 0.56 - 0.58, are found for the five measurements points, displaying a good uniformity over large area. Therefore, both SE and Raman analyses show that the synthesis of 2-D MoS_2 by our PEALD process is readily scalable.

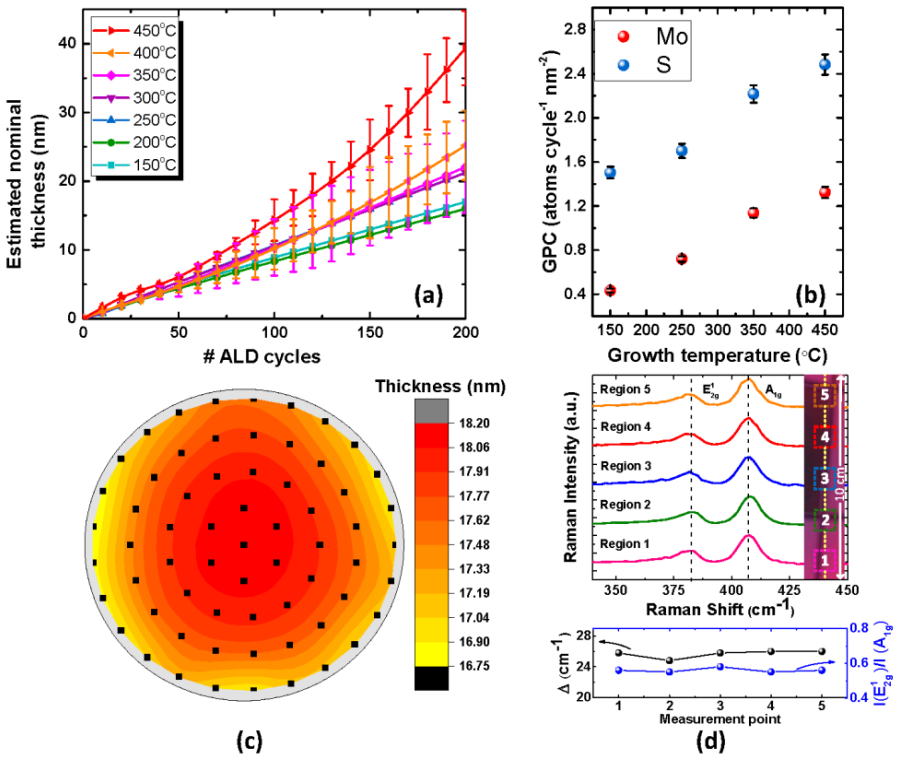


Figure 3.1 (a) Layer thickness evolution as a function of number of ALD cycles over the whole investigated temperature range of 150 °C - 450 °C. At higher growth temperatures, an increase in GPC can be seen. The error bars shown represent the sum of the measurement error, SE model fitting error and film roughness values. (b) RBS analysis showing a linear increase in individual GPC (atoms cycle^{-1} nm^{-2}) for both 'Mo' and 'S' with increasing growth temperatures. (c) Map of the thickness variation for film deposited at 300 °C (200 cycles) over a 4" wafer carried out by *ex-situ* SE showing a small thickness variation with a standard deviation of 0.4%. The black points on the wafer are the actual measurement points with 5 mm edge exclusion. (d) (top) Raman spectroscopy line scan (for the same wafer as in (c)) showing the five selective measurement points (step size ~ 2 cm) having consistent spectral features for a polycrystalline MoS_2 film registering a homogenous film over large area. (bottom) Plot showing the frequency difference (black) and relative Raman intensities (blue) for five measurement points.

3.3.1.2 Thickness control in the mono-to-few layer regime: Raman and PL analysis

Figure 3.2 (a) shows the control over film thickness in the initial phase of growth (first 50 ALD cycles) at 450 °C as measured by *in-situ* SE analysis. However, in the mono layer to few layer regime, it is not easy to extract the exact thickness by SE, because of uncertainty in the optical properties of mono-to-few layer MoS_2.[62] Moreover, the change in surface termination groups (e.g. starting with -OH to possibly -SH) during subsequent ALD cycles might result into inaccurate thickness determination by SE analysis for a sub-nm thick film. This is the reason that despite the formation of a monolayer after 10 cycles (as will be shown below by Raman and PL analyses), the thickness extracted by SE modelling gives a value of ~1.3 nm than the expected ~0.6 nm for a monolayer of MoS_2. Therefore, to validate the systematic control over thickness of ultra-thin MoS_2 films from monolayer to bulk by tuning the number of ALD cycles, the films deposited at 450 °C were also characterized by Raman and photoluminescence (PL) spectroscopy. Raman plots for the samples deposited using 10 - 50 ALD cycles are shown in Figure 3.2 (b). The two characteristic Raman peaks for MoS_2 corresponding to the vibrational modes (E^1_{2g} and A_{1g}) are observed for all the cases confirming continuous coverage with the 2H phase of MoS_2. The intensity and frequency difference between the two modes increases monotonically with the number of cycles as expected,[63] thus reflecting an excellent control over thickness with atomic scale precision. Importantly, the film after 10 cycles yields a frequency difference of ~20.6 cm^{-1} which is typically correlated with a monolayer of MoS_2.[39,64] The photoluminescence (PL) spectra are shown in Figure 3.2 (c). For 10 cycles, a strong peak at ~656 nm and a weak signal at ~612 nm are observed, which corresponds to the A and B excitonic peaks respectively and confirm the direct band gap in monolayer MoS_2.[11] The PL signal intensity is found to decrease as the film thickness increases with number of cycles. For MoS_2, this reduction in PL signal is generally attributed to a change in the electronic structure for thicker films (i.e. transition from direct to indirect band gap) which causes an increase in the intraband relaxation rate from the excitonic states.[11] Thus, the presence of one MoS_2 monolayer after 10 ALD cycles is evidenced by both Raman and PL analyses. This is further corroborated by RBS analysis which shows that approximately ~13.2 Mo atoms/nm^2 are deposited after 10 cycles at 450 °C, which is very close to an ideal MoS_2 monolayer (approx. 11.6 Mo atoms/nm^2) for (001) plane.[65]

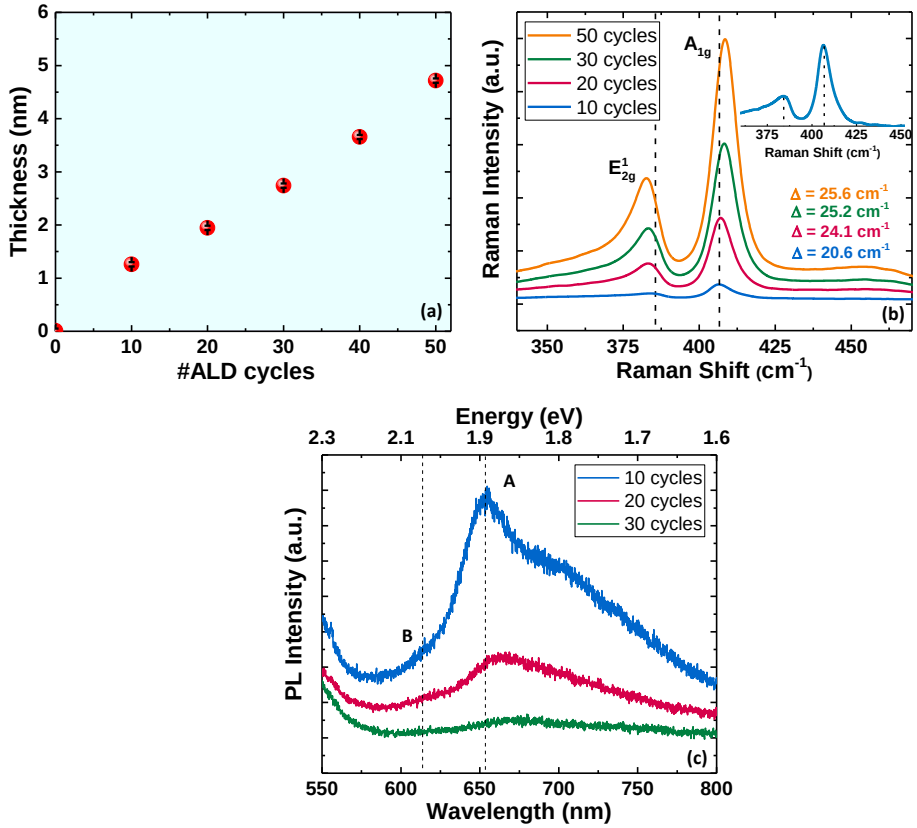


Figure 3.2 (a) Thickness evolution of MoS_2 films in the initial phase of deposition at 450 °C as recorded by *in-situ* SE analysis. (b) Raman evolution as a function of increasing number of cycles (at 450 °C) exhibiting excellent control over film thickness. The increasing frequency difference (Δ) between two vibrational modes with number of ALD cycles is an indicator for thickness increase. For clarity, the inset shows the enlarged Raman plot with two distinctive vibrational modes for a sample with 10 ALD cycles. The two vibrational modes are indicated by dotted lines. Also, the Raman peaks are normalized to the corresponding Si peak in each case. (c) The corresponding PL peak (λ_{ex}= 514 nm) for the thinnest film (10 cycles) is related to the direct band gap excitonic transition (positions for excitons A and B are highlighted with dotted lines) for a monolayer of MoS_2. The peak broadening is a clear indication of possible disorders present in the film.

A close inspection of Raman peaks reveals an asymmetric broadening for both vibrational modes which suggests the presence of structural disorder in the as-deposited

films. This broadening is commonly observed for MoS_2 grown at low temperatures by bottom-up synthesis methods. We have used the Voigt fitting strategy based on the report from Mignuzzi *et al.*[66] to deconvolute the Raman spectrum for the film deposited after 10 cycles at 450 °C, and the corresponding plot is shown in Figure A.3.3 (a) (Appendix). Apart from the two predominant vibrational peaks (i.e. E^1_{2g} and A_{1g}), three additional defect-induced peaks are observed that can be assigned to transverse optical (TO), longitudinal optical (LO) and out-of-plane optical (ZO) branches originating at the M point of the Brillouin zone.[63]

Furthermore, in the low-frequency region of the Raman spectrum, a broad peak located at ~227 cm^{-1} is also observed (Figure A.3.3 (b) in Appendix). This peak is attributed to the disorder induced LA(M) band and has been demonstrated as a metric for quantification of structural defects in MoS_2 by several groups.[43, 63] Overall, the strong E^1_{2g} and A_{1g} modes combined with the low LA(M) peak shows that our process enables the deposition of good quality MoS_2 films at relatively low temperatures.

3.3.2 Control over film morphology

Tuning of the film morphology was achieved by modulating the growth temperature, providing an opportunity to adjust the density of active sites for eletrocatalytic applications. The effect of growth temperature on the morphology and crystallinity of the resulting film was initially examined by scanning electron microscopy (SEM) and Raman spectroscopy analyses, respectively. Top view SEM images and corresponding Raman spectra of films deposited in the temperature range 200 °C - 450 °C (200 cycles each) are shown in Figure 3.3 (a - f). The film grown at 200 °C is found to be predominantly amorphous in nature with no characteristic Raman peaks except for the peak from the Si substrate (520 cm^{-1}). As the growth temperature is increased to 250 °C, a few nano-crystallites are recognizable in SEM. This small crystalline fraction yields very weak Raman signals due to the considerable contribution from the amorphous background.

The characteristic Raman peaks for polycrystalline material become clear and distinct at a growth temperature of 300 °C where the density of crystallites is clearly higher, evidencing the poly-crystalline nature of the film. For growth temperatures from 350 °C to 450 °C, the crystallite size is larger, and the film appears to become highly textured

with out-of-plane orientation (OoPO film). The corresponding Raman signal shows clear, distinctive vibrational peaks confirming the polycrystalline nature of the film. High-angle annular dark-field (HAADF) and high-resolution transmission electron microscopy images of a film grown at 450 °C (200 ALD cycles) are shown in Figure A.3.4 ((a) & (b) in Appendix) where out-of-plane nanostructures uniformly distributed over the substrate are clearly observable. These nanostructures are found to be rough (root mean square roughness : 5.2 nm) in nature as evident in the AFM image (Figure A.3.4 (c) in Appendix).

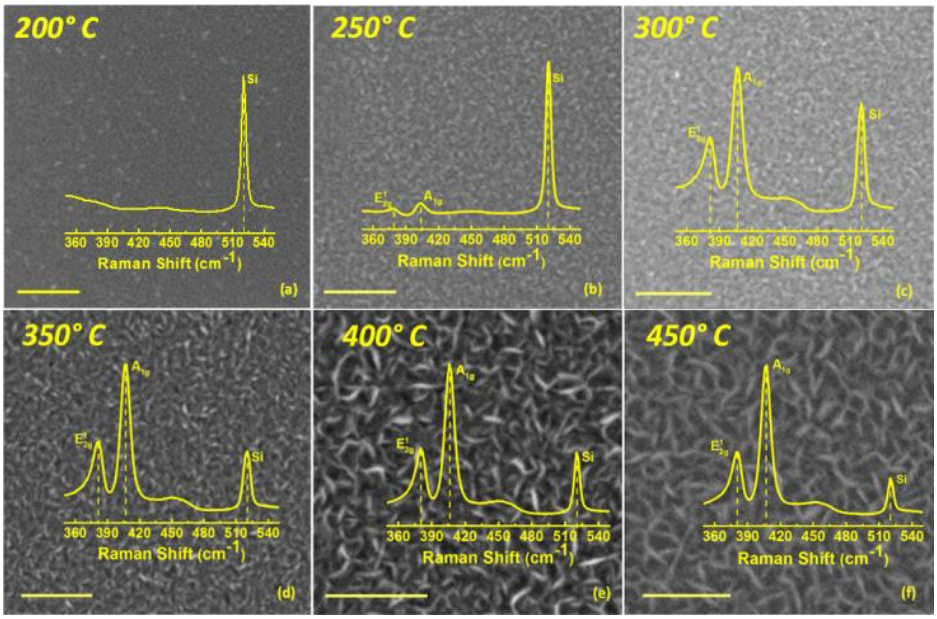


Figure 3.3 (a-f) Top view SEM images (the scale bar in each image is 200 nm) showing the microstructure of the films grown at various growth temperatures for 200 cycles. The film morphology changes from amorphous to polycrystalline as the growth temperature increases from 200 °C to 450 °C. The overlying Raman spectra show the vibrational mode peaks evidencing an increase in the crystalline nature of the film at higher growth temperatures.

To complement SEM and Raman analysis, the influence of temperature on crystallinity and a possible preferred growth orientation of the films was analysed by X-ray diffraction (XRD) using two different detection geometries. First, grazing-incidence XRD (GI-XRD) studies were performed on samples grown for 200 cycles in the entire

temperature range (200 °C - 450 °C). GI-XRD is a technique well suited for analysing thin samples, because of the increased interaction volume as compared to a *gonio* (symmetric θ-2θ) scan. The GI X-ray diffractogram in Figure 3.4 (a) shows broad peaks at ca. 14.3° for growth temperatures of 200 °C and 250 °C. This peak corresponds to the (002) reflection of the semiconducting 2H phase of MoS_2.[67] However, the broad nature of the peaks at 200 °C and 250 °C indicates a predominant amorphous nature of the films at these temperatures as was already revealed by SEM and Raman analyses.

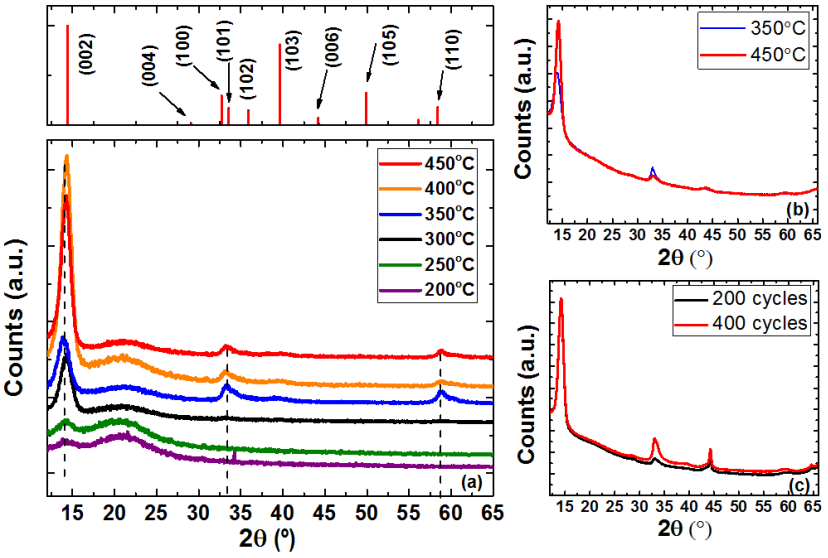


Figure 3.4 (a) Grazing X-ray diffractograms of as-deposited MoS_2 films on SiO_2/Si substrates at various growth temperatures (200 cycles each). The position of peaks corresponding to (002), (100) and (110) is highlighted with dotted lines. The powder diffractogram for 2-H MoS_2 (JCPDF 037-1492) is shown as a reference for the reader (top panel). Gonio scans (symmetric θ - 2θ) for (b) films deposited at 350 °C and 450 °C (200 cycles each) (c) films deposited with varying number of cycles at 450 °C.

At 300 °C, a clear (002) peak is present, which can be correlated to the increased density of nano-crystallites as observed in SEM images. Comparison with the powder diffraction spectrum displayed in Figure 3.4 (a) (top panel) indicates that this film has a clear <002> texture. For growth temperatures ≥ 350 °C, two additional peaks at 33.4° and 58.8° corresponding to the (100) and (110) reflections are detected, implying a change in texture. To investigate this change in more detail, *gonio* scans were performed for a selection of samples. Figure 3.4 (b) shows diffractograms of samples

deposited for 200 cycles at 350 °C and 450 °C. The change in relative peak heights implies an increase in <002> texture at higher temperatures. Note that there is a factor of 2 difference in layer thickness for these samples (see Figure 3.1 (a)). This also needs to be taken into account which is investigated in more detail by comparing the crystallographic orientation of the films deposited with 200 and 400 cycles at 450 °C.

Figure 3.4 (c) demonstrates that the intensity of the (002) peak is identical for both samples, while the (100) and (110) peaks increase for higher number of ALD cycles. Here, it is essential to realize that the (100) and (110) planes are oriented orthogonal to the 2-D planes. This can be explained by a change in growth mode from in-plane growth for the lower part of the layer to out-of-plane growth for the later growth cycles. Comparison of Figures 3.4 (b) and 3.4 (c) indicates that the transformation to OoPO growth occurs at an earlier stage (lower number of cycles) at lower temperatures.

3.3.3 Nucleation mechanism of PEALD of MoS_2 on SiO_2/Si

In order to improve control over the thickness and morphology of the MoS_2 formed by ALD, it is of key importance to understand the nucleation behaviour and appearance of out-of-plane growth mode of the MoS_2 on SiO_2. Generally, the crystal growth of MoS_2 begins with the nucleation of flat, crystal domains with in-plane orientation, as is reported in numerous bottom-up synthesis methods.[39, 68] However, the film morphology transformation from the in-plane to out-of-plane mode is also reported. In literature, the out-of-plane growth of MoS_2 and graphene has been shown by using mainly high temperature CVD or metal/metal oxide sulphurization techniques. Several reasons responsible for such morphology are mentioned. For instance, Li *et al.* have shown that during CVD growth, the compression and extrusion between MoS_2 island layers ultimately leads to structural distortions resulting in out-of-plane standing MoS_2 nanosheets.[23] In another report by Kong *et al.*, it is argued that the rapid sulphurization of Mo films renders the perpendicular orientation to the MoS_2 films.[22] For growth of graphene by electron cyclotron resonance chemical vapor deposition (ECR-CVD),[69] the role of plasma species, causing localized hot spots and chemical potential gradients on the substrate, has been ascribed as one of the factors enhancing out-of-plane growth. Another conceivable factor which cannot be ruled out is stress development in the film, which upon relaxation may distort the basal plane oriented film morphology and promote out-of-plane growth.

In our PEALD process, most of the above-mentioned factors can play a role for the morphology transformation. Therefore, to further elucidate the nucleation mechanism of MoS_2 on SiO_2/Si and gain deeper insight into the observed morphology transformation, HAADF-STEM analysis was performed on films grown at 450 °C at different stages of growth by varying the number of ALD cycles from 5 till 200. The corresponding images are shown in Figure 3.5 (a - f). A clear progression from nucleation of the film to the formation of OoPO films can be observed. A close inspection reveals that the film growth starts with the formation of discrete flat MoS_2 islands which appear as triangular or star shaped domains as highlighted in Figure 3.5 (a). The formation of such flat triangular or star shaped domains with in-plane orientation is typical for synthesis of MoS_2 via bottom up techniques as mentioned earlier.

After 10 ALD cycles, these discrete islands are found to extend in the lateral direction and merge at certain points to form an almost continuous film. Some bi- to few-layer fragments can be observed as well. Thereafter, in case of 20 cycles, the emergence of stripe-like patterns representing nano-scale out-of-plane nanostructures, can be observed which have been highlighted in Figure 3.5 (c). This suggests that the transformation from in-plane to out-of-plane plane growth mode is thickness dependent and takes place after a closed film of horizontally oriented domains is formed. The size and density of these out-of-plane nanostructures is found to increase with increasing number of ALD cycles. At 200 cycles, the out-of-plane growth mode is clearly dominating as shown Figure 3.5 (f). Figure 3.5 (g) shows the corresponding selective area electron diffraction (SAED) patterns for films grown with increasing number of cycles.

It can be observed that the film after 5 cycles has weak, diffuse diffraction rings as can be expected because of the limited size of the islands. In case of 20 cycles, a set of sharp diffraction rings is present, characteristic for a polycrystalline film with small grain sizes. In the present case of SAED under normal incidence of the electron beam on the sample, the vertically oriented crystallographic planes are visualized in the SAED pattern. The absence of (002) and (006) rings and the presence of the closed (100) and (110) rings indicates the presence of a <001> texture within in-plane rotational freedom of the domains. For a higher number of cycles (200 cycles), the intensity of the rings increases as more volume is probed. In addition, (002) and (006) orientations are clearly visible, representing the out-of-plane orientation of the 2-D planes, in agreement with the observation of nanostructures for this sample.

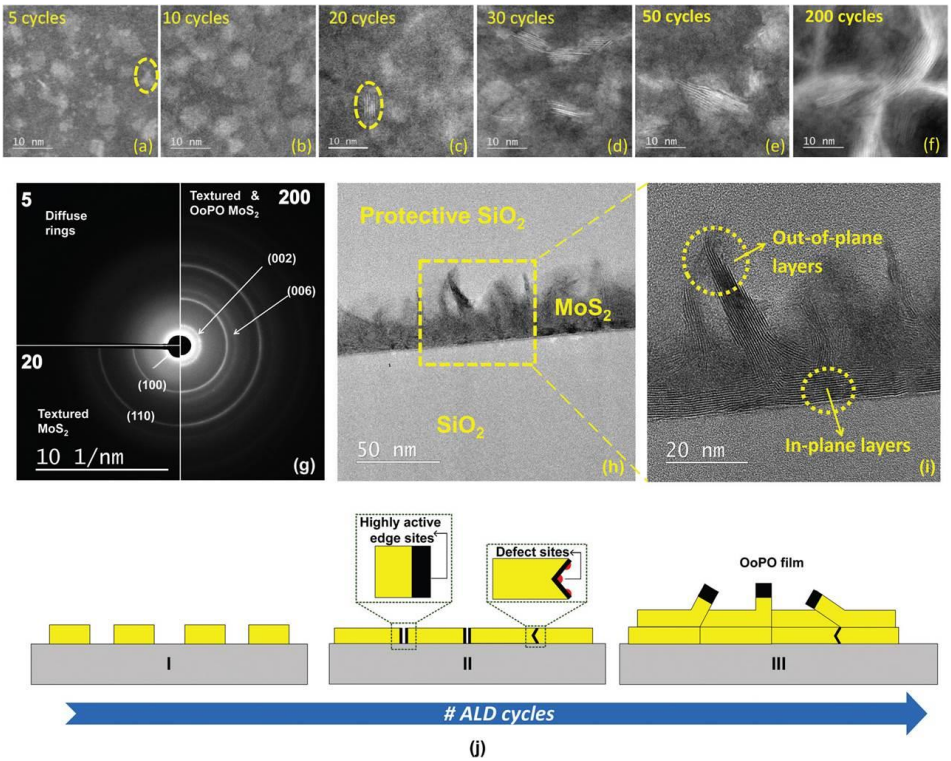


Figure 3.5 (a - f) HAADF-STEM images showing the nucleation of MoS_2 on SiO_2/Si substrates as a function of number of ALD cycles and the variation of morphological structures. The in-plane flat, triangular domain and out-of-plane stripe-like patterns are highlighted by encircling (dashed line) in (a), (c) respectively. (g) The formation of textured and out-of-plane standing MoS_2 nanostructures is supported by the electron diffraction patterns showing bright rings corresponding to (002) and (006) crsytal orientations. The diffraction patterns are labelled with the corresponding number of ALD cycles (5, 20, 200) accordingly. (h) Cross sectional TEM image of a MoS_2 thin film deposited at 450 °C (200 cycles) on SiO_2/Si substrate with a top SiO_2 layer deposited for protection during sample preparation. (i) The magnified view reveals the transformation from in-plane growth to out-of-plane standing structures. (j) Schematic showing the growth model for the development of OoPO nanostructures with random orientations.

To further elucidate the morphology of the OoPO growth mode, cross-sectional TEM analysis was carried out on a thick MoS_2 film as depicted in Figure 3.5 (h). The magnified image in Figure 3.5 (i) clearly shows the two types of morphologies: 2-D layers parallel to the substrate surface close to the interface and emergence of OoPO nanostructures which seem to start out from a large variation in orientations but are

driven out-of-plane due to crowding with increasing film thickness. A close look reveals that the transformation from in-plane to out-of-plane growth mode occurs most likely at the grain boundaries. The final resulting film therefore comprises of a mixed morphology as shown earlier (Figure A.3.4 in Appendix). The in-plane orientation of the first few layers points towards the negligible role of the substrate on the out-of-plane growth mode. To prove this hypothesis, we considered various substrates (ALD grown Al_2O_3, Au coated Si, exfoliated MoS_2 flakes, Glassy carbon) and carried out similar depositions under identical conditions.

The resulting film morphology (i.e. OoPO) was consistent irrespective of the substrate used including the mechanically exfoliated MoS_2 flakes. This indicates that the development of the OoPO growth mode is independent of the substrate used and is rather related to the growth mechanism for this material. The corresponding top view SEM images are shown in Figure A.3.5 (Appendix).

Based on these results, a growth model is postulated and schematically illustrated in Figure 3.5 (j). In this model, it is shown that the film growth starts with the formation of islands with horizontal basal plane orientation on the substrate. The growth at the edges of these islands is faster than growth on top of the basal planes. This can be ascribed to the fact that the edge of a 2-D layer consists of dangling bonds, which act as preferable sites for precursor adsorption, unlike the inert basal planes. Adding a new 2-D layer on top of the basal plane implies nucleation of a new layer, which is energetically less favourable than lateral growth of already existing planes. Next, when the discrete islands coalesce, defect sites at the grain boundaries might occur due to the different in-plane orientations of the individual crystals (as concluded from SAED). These defect sites can act as new active sites for precursor adsorption, from which new MoS_2 crystals form. However, due to crowding effects these new crystals do not necessarily grow in-plane, but have random out-of-plane orientation as observed above.

Overall, the morphology transformation can be a result of a complex interplay of different factors. To sum up, we hypothesize an additional possible governing mechanism i.e. the enhanced adsorption of precursor on the edge and defect sites during ALD growth ultimately giving rise to out-of-plane growth mode.

3.3.4 Hydrogen evolution reaction (HER) performance

Electrolytic water splitting is one of the most efficient and sustainable ways to produce hydrogen from water.[70] Out-of-plane oriented transition metal dichalcogenides (TMDs) thin films with catalytically active edge sites synthesized by various bottom-up methods have emerged as an inexpensive alternative to the precious noble metals (e.g. Pt) for HER.[21,71] ALD provides an excellent opportunity to modulate the thickness and height of the out-of-plane oriented films which can be a great advantage over other bottom-up synthesis techniques. In past, several groups have demonstrated the HER performance of ALD synthesized amorphous and polycrystalline MoS_2 films.[72, 73] However, the poor stability of amorphous films and requirement of post annealing calls for further investigation of ALD synthesized MoS_2 films for HER mechanism. In this work, we therefore focus on assessment of the HER performance of as-deposited polycrystalline films with different morphologies which can be easily modulated by using our PEALD process and might be a valuable asset for electrocatalysis applications.

Glassy carbon (GC) plates were chosen as substrates since they are conductive, chemically stable, electrochemically inert in a large potential window and can be polished to a mirror finish. These substrates were subjected to an increasing number of ALD cycles (10 - 600 cycles) at 450 °C under optimum conditions. While a flat film was obtained after 10 cycles (as shown previously), for 100, 400 and 600 cycles, OoPO films of different thicknesses were obtained. Figure 3.6 (a) shows the cathodic polarization curves for MoS_2 films and a bare GC substrate as reference. It is clearly observed that all MoS_2 coated samples possess a much lower onset overpotential (η) for HER than the bare GC substrate. Notably, the sample with 10 ALD cycles shows a substantial catalytic activity which suggests the presence of active edge sites in the early growth stages of the film. This confirms the TEM observation that for 10 ALD cycles the layer is not completely closed yet and edges of 2-D islands are exposed. The samples possessing OoPO films (100, 400 and 600 cycles) have higher cathodic current densities (at η = 500 mV). This indicates an enhanced HER performance owing to an increased number of active edge sites of the OoPO nanostructures. Table 3.1 summarizes the figures of merit for all investigated samples. Generally, the overpotential required to drive a cathodic current density of 10 mA/cm^2 (η_{10}) is used as a figure of merit for the overall performance of electrocatalysts.[74] It is to be noted that the value of η_{10} reduces with an increase in ALD cycles from 10 to 100 most likely due

to morphology transformation implying an increase in the number of edge sites causing a higher HER performance. However, the further increment in number of ALD cycles (from 100 till 600) does not show a considerable improvement in HER performance which is attributed to the saturation of active surface area as reflected in double layer capacitance measurements shown in Figure A.3.6 (a) (Appendix).

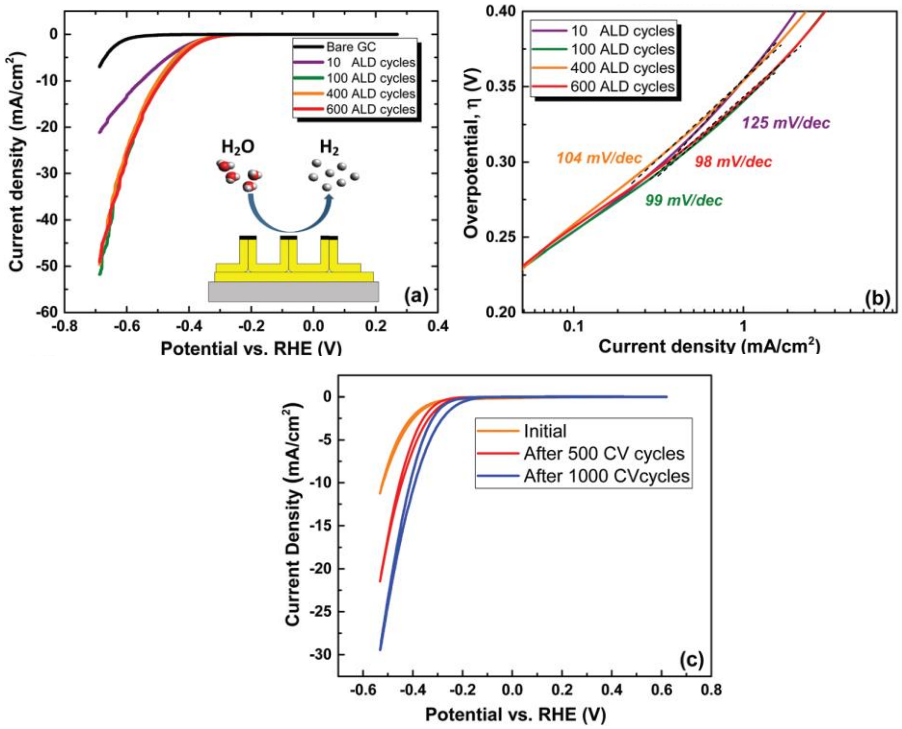


Figure 3.6 (a) HER polarization curve (linear sweep voltammetry) for OoPO MoS_2 films deposited on GC substrate showing an onset overpotential of around −0.26 V. In the inset, a cartoon is shown where the hydrogen evolution by splitting of water molecule assisted by OoPO films is depicted. (b) Tafel plot showing the calculated Tafel slopes for all the investigated samples.(c) Cyclic voltammetry repeated for 1000 cycles showing an improved activity for the as-deposited OoPO MoS_2 film (400 ALD cycles).

It should be noted that the double layer capacitance value for the sample with 10 cycles is overestimated, because of the high surface roughness (RMS 3.6 nm) of the polished GC substrate as shown in the inset of Figure A.3.6 (a). Furthermore, the

corresponding Tafel plots are shown in Figure 3.6 (b) revealing Tafel slopes for the investigated samples in the range of 98 - 125 mV/dec. In literature, the value of Tafel slope for MoS_2 based catalysts has shown a large spread ranging from 40 to 220 mV/dec depending on the material preparation and modification methods.[75]

It is worth mentioning that the HER performance of our OoPO MoS_2 films (Tafel slopes: 98 - 125 mV/decade and exchange current density values: 1.8 - 1.9 $\mu A/cm^2$) is comparable to the films with similar morphology (viz. vertically aligned, edge enriched MoS_2 thin film *etc.*) prepared by other techniques as reported in the literature.[22, 75] The stability of as-deposited OoPO MoS_2 films was assessed by taking continuous cyclic voltammograms (CV). The corresponding CV curves before and after 1000 cycles are shown in Figure 3.6 (c). Interestingly, the performance is improved after 1000 cycles of continuous CV test which can be attributed to the formation of sulphur vacancies during HER. It is well known that the introduction of sulphur vacancies may result in higher reactivity owing to the generation of additional catalytic sites.[76, 77]

It is important to mention that all samples subjected to HER tests have been used as-deposited and therefore further optimization of the overall HER performance should be possible and follow-up work will be done accordingly. Yet, these results confirm the viability of the PEALD process to modulate the film morphology and thickness of out-of-plane nanostructures for efficient utilization in electrocatalysis. The large area growth and low temperature processing possible by PEALD are the other virtues which can be highly advantageous for eletrocatalytic applications.

Table 3.1: Key parameters extracted from the electrochemical characterization of different samples with varying number of PEALD cycles.

Sample	Tafel slope (mV/decade)	η_{10} (mV)
10 cycles	125	−553
100 cycles	99	−487
400 cycles	104	−503
600 cycles	98	−488

3.4 Conclusions

In summary, we report on a large-scale, low temperature PEALD process for synthesizing uniform, high quality 2-D MoS_2 films. Our process shows precise thickness control down to a monolayer and provides possibilities to tune the morphology of the layers by varying the growth temperature from 150 - 450 °C. Extensive film characterization has helped in understanding the influence of growth temperature on film morphology, crystallinity and chemical composition. Moreover, based on the detailed TEM investigation, we have proposed that during ALD growth, the enhanced precursor adsorption on the highly energetic edge sites of MoS_2 may play a role in the transformation to out-of-plane oriented films at 450 °C. Furthermore, the excellent control over morphology is showcased in electrocatalysis using the hydrogen evolution reaction (HER) in which the out-of-plane oriented films outperform flat, in-plane oriented films. These results show that ALD might be instrumental in realizing not only the uniform large area growth of high-quality 2-D materials but can also be applied as a tool to control the morphology of thin films which might result into interesting structures (including heterostructures) for multiple applications.

Acknowledgements

The authors would like to thank J. van Gerwen and C.A.A. van Helvoirt for technical assistance and N.F.W. Thissen for fruitful discussions. A. Omahony from Oxford Instruments is acknowledged for carrying out the thickness uniformity measurements. This work was financially supported by NWO and the Technology Foundation STW through the VIDI program on 'Novel bottom-up nanofabrication techniques for future carbon-nanoelectronics'. Dr. B. Barcones is acknowledged for the FIB preparation of the TEM samples. Solliance and the Dutch province of Noord-Brabant are acknowledged for funding the TEM facility. L.W. and J.P.H. appreciate funding via the program "CO_2-neutral fuels" (project 13-CO26) of the late Foundation for Fundamental Research on Matter (FOM), financially supported by the Netherlands Organization for Scientific Research (NWO) and co-financed by Shell Global Solutions International B.V.

Appendix

A.3.1 ALD saturation curves

The self-limiting growth characteristic for the ALD process was investigated at growth temperature of 250 °C and 450 °C. The plots in Figure A.3.1 (a) & (b) show the self-limiting behaviour of the process (at 250 °C) for both half cycles.

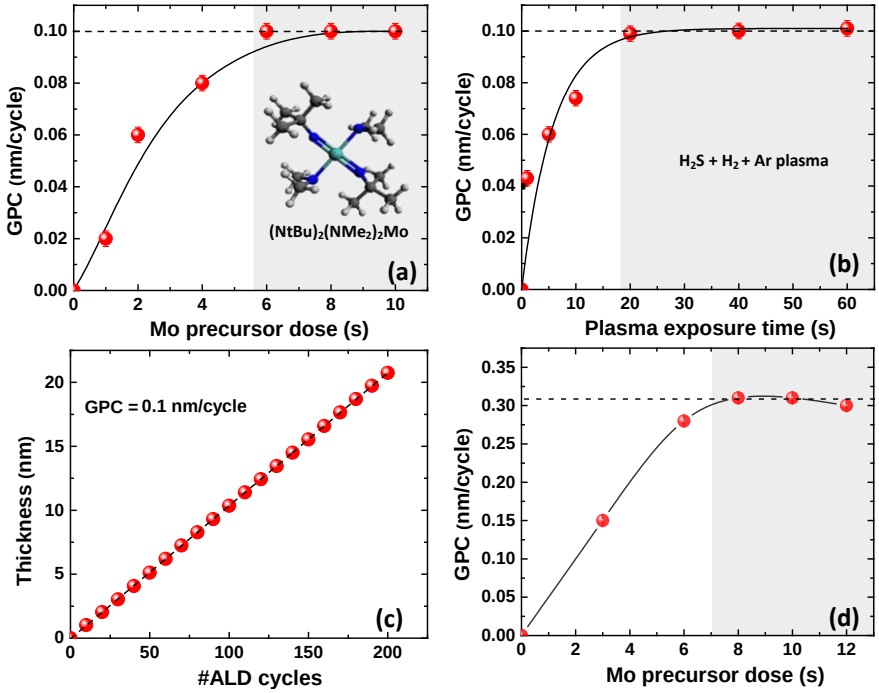


Figure A.3.1 Typical ALD saturation curves (for growth temperature of 250 °C) showing the growth per cycle (GPC) as a function of (a) Mo precursor dose (the precursor molecule is shown in inset) and, (b) H_2S based plasma exposure. The saturated regimes for both half cycles are highlighted in grey, the saturation levels are indicated by horizontal dashed black lines and the solid black lines serve as a guide to the eye in both cases. (c) Linear relation between thickness and number of ALD cycles demonstrating precise control over film thickness (d) Half cycle saturation curve for Mo precursor dosing showing a clear saturated growth-per-cycle after a finite dosing time indicating the typical self-limiting ALD growth mode at a growth temperature of 450 °C. A plasma exposure time of 20 s was used. The same description is valid for grey area, horizontal dashed and solid black lines in this case.

The growth per cycle (GPC) saturates to a value of 0.1 nm/cycle after 6 s of Mo precursor dose while keeping a constant plasma exposure time of 20 s for varying precursor dose (Figure A.3.1 (a)). Likewise, a plasma exposure time of 20 s is required before the GPC saturates (Figure A.3.1 (b)). The Mo precursor dose was fixed at 6s in first half-cycle in the latter case. In addition, no growth was observed when each half ALD cycle was performed in absence of either Mo precursor or H_2S based plasma co-reactant respectively (i.e. Mo precursor dose / H_2S plasma exposure time = 0 s), confirming the exclusion of any possibility of uncontrolled thermal decomposition of either of the reactants. Further, the optimum sequential dosing for each half cycle (Mo dose = 6 s, plasma exposure time = 20 s) yielded a linear relationship between thickness and number of ALD cycles as depicted in Figure A.3.1 (c) which shows an Å level control over film thickness.

Additionally, the film growth shows no nucleation delay during the initial cycles which is a highly valuable attribute for reproducible synthesis of mono-layer to thick MoS_2 films. The 2-D materials including MoS_2 are generally seen as an inert flat land with no out-of-plane dangling bonds and therefore intuitively should be unavailable for any chemisorption reactions necessary for ALD process to proceed. However, surface chemistry studies for general ALD of sulphides have shown that the surface thiols (-SH) mimic the role of surface hydroxyls (-OH) as in oxide ALD and are mainly responsible for driving the ALD process mechanism. In our case, we believe that the plasma chemistry is accountable for inducing the surface thiols which are facilitating the chemisorption of metal precursor in the subsequent steps. The adsorption of precursor species however can be anisotropic on the basal planes or edge planes of the film grown as discussed in the main text.

A.3.2 Chemical composition analysis

A.3.2.1 XPS analysis of MoS_2 films

The X-ray photoelectron spectroscopy (XPS) has been used to determine the chemical composition of the MoS_2 films. Figure A.3.2.1 shows the XPS surface scan and the resolved spectra for Mo3d, O1s and C1s regions respectively. A depth profile was recorded by using energetic Ar+ ion beam (~200 eV) to etch the film and determine the content of contaminants (O, C) within the bulk of the film. It is found that a 50 s etch cycle results in the preferential sputtering of S

from MoS_2 species leading to formation of additional metallic Mo component by ion bombardment as shown in Figure A.3.2.1 (b).

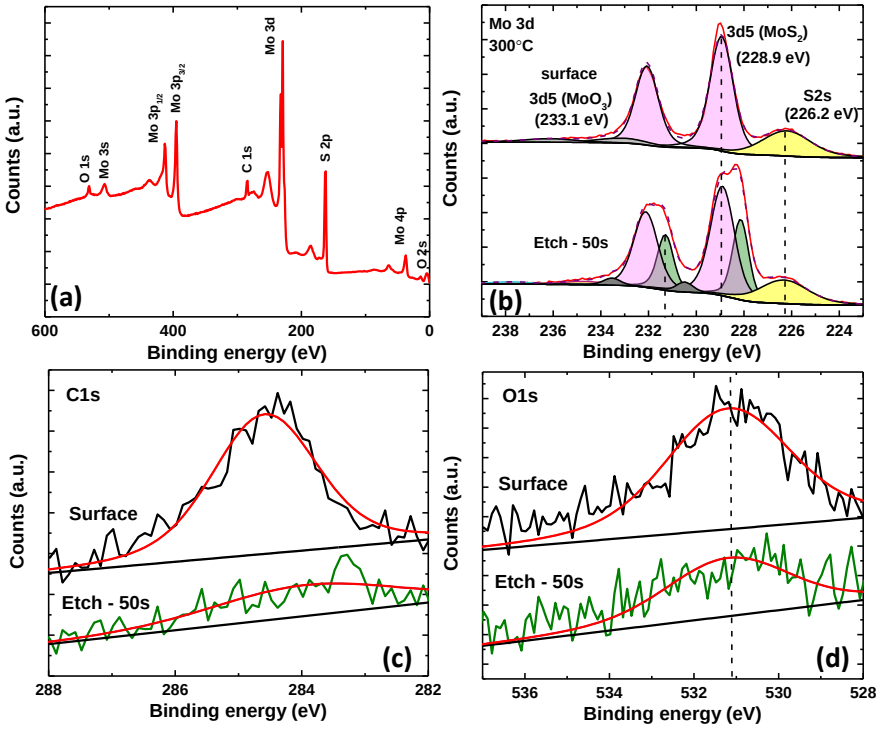


Figure A.3.2.1 (*upper panel*) (a) XPS spectrum scan of ca. 20 nm thick MoS_2 film deposited at 300°C. (b) Resolved spectrum of the Mo3d region showing predominant peaks corresponding to MoS_2 as highlighted. The peak corresponding to S2s is also visible. A small doublet peak corresponding to MoO_3 species is also observed. The red curve is the experimental data while the dashed line represents the fitted data. (*lower panel*) (c, d) Individual scans for C1s and O1s regions; almost complete removal of both species was observed after a 50 s sputter cycle (peak at bottom) confirming the confinement of C and O contaminants to the surface region and with only a trace amount within bulk.

A.3.2.2 RBS analysis of MoS_2 films

The RBS analysis was performed to study the absolute stoichiometry of MoS_2 films grown at different temperatures. Figure A.3.2.2 shows the RBS spectra in which two

peaks are assigned to sulphur and molybdenum respectively. The steep edges represent the Si substrate.

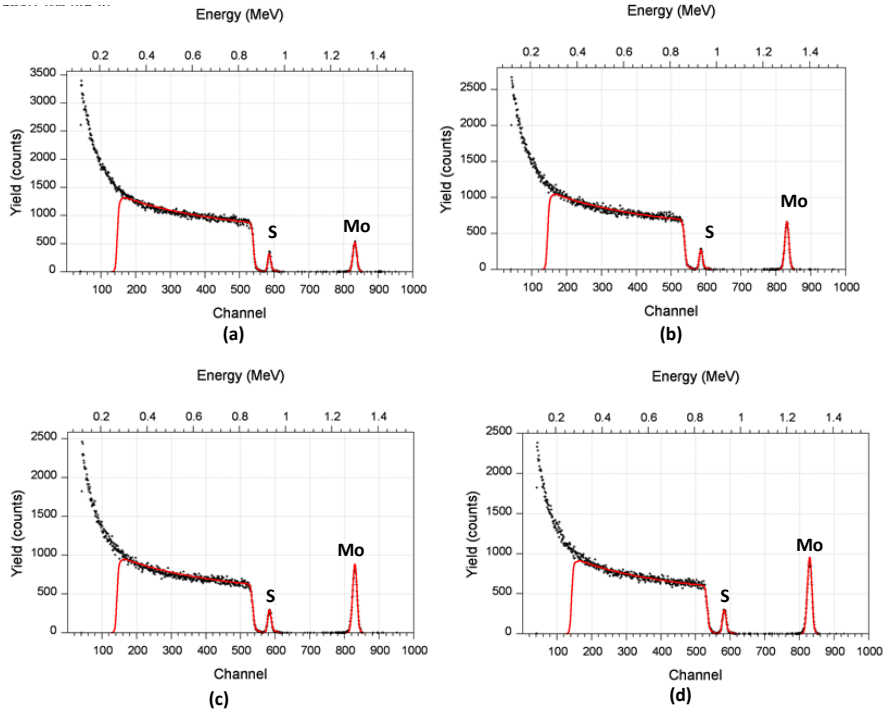


Figure A.3.2.2 RBS spectra for MoS_2 films deposited at the growth temperature of (a) 150 °C (b) 250 °C (c) 350 °C and (d) 450 °C respectively. The black points in each case represent the experimental data while the red curves are the fitted curves. It can be seen that a good agreement is obtained between the experimental and fitted curves.

In Table A.3.1, an estimation of stoichiometry obtained by XPS analysis and an absolute ratio (S/Mo) measured by RBS is given. For XPS, the surface compositions (in atomic%) were obtained by considering the integrated peak areas for Mo3d, S2p regions and the respective sensitivity factors. In case of RBS, the absolute concentrations of both sulfur and molybdenum were extracted by using a model, which were subsequently used to obtain S/Mo ratio. A good agreement between both measurement techniques is obtained showing almost the similar film stoichiometry as a function of growth temperature. At low growth temperatures (150 °C and 250 °C), films are found to be over-stoichiometric which may be attributed to the presence of thiol groups on the film surface. Thus, the stoichiometry obtained at low growth temperatures may be rather

inaccurate in absence of information regarding 'H' content in the films. On the contrary, at high growth temperatures (350 °C and 450 °C), the extracted stoichiometry indicates sulphur vacancies in the film which is expected for a polycrystalline MoS_2 film deposited with a bottom-up synthesis method.

Table A.3.1: The stoichiometry for as-deposited MoS_2 films obtained by XPS and RBS at various growth temperatures. The typical corresponding errors are indicated accordingly.

Growth temperature (°C)	**Stoichiometry (S/Mo)**	
	XPS	**RBS**
150	3.4 ± 0.1	3.47 ± 0.18
250	2.5	2.36 ± 0.12
350	1.8	1.95 ± 0.10
450	1.7	1.88 ± 0.09

A.3.3 Deconvolution of Raman spectra

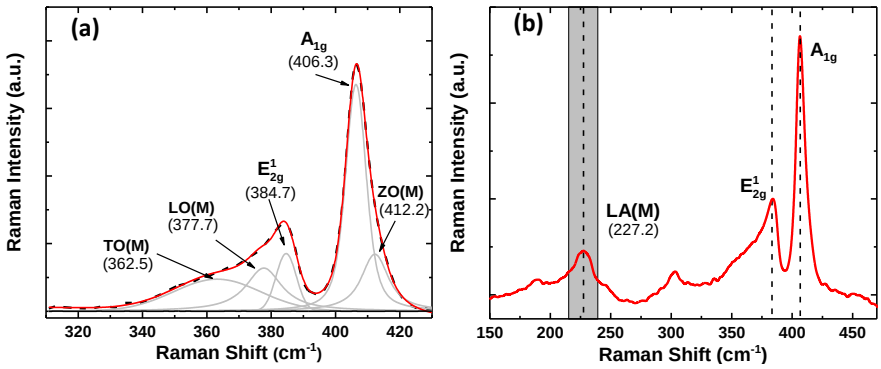


Figure A.3.3 (a) The deconvoluted Raman spectrum for film deposited after 10 cycles at 450 °C. The deconvolution reveals the presence of additional defects induced peaks (TO (M), LO (M), ZO (M)) other than the predominant in-plane and out-of-plane vibrational modes (E^1_{2g} and A_{1g}). The full width at half maximum (FWHM) values of the fitted peaks for the two components (E^1_{2g} and A_{1g}) were found to be 6.9 cm^{-1} and 8.6 cm^{-1} respectively. (b) The spectrum showing the low frequency region where a broad defect induced peak (LA(M)) is clearly visible at ~227 cm^{-1} (highlighted in grey).

A.3.4: High resolution TEM and AFM images of OoPO film

The microstructure of OoPO films formed at 450 °C is analysed by high angle annular dark field (HAADF) and high-resolution transmission electron microscope (HRTEM) imaging. Figure A.3.4 shows the corresponding images revealing the out-of-plane oriented MoS_2 films deposited by PEALD on a SiO_2/Si substrate. Further, AFM analysis depicts the high roughness of the film deposited at growth temperature of 400 °C.

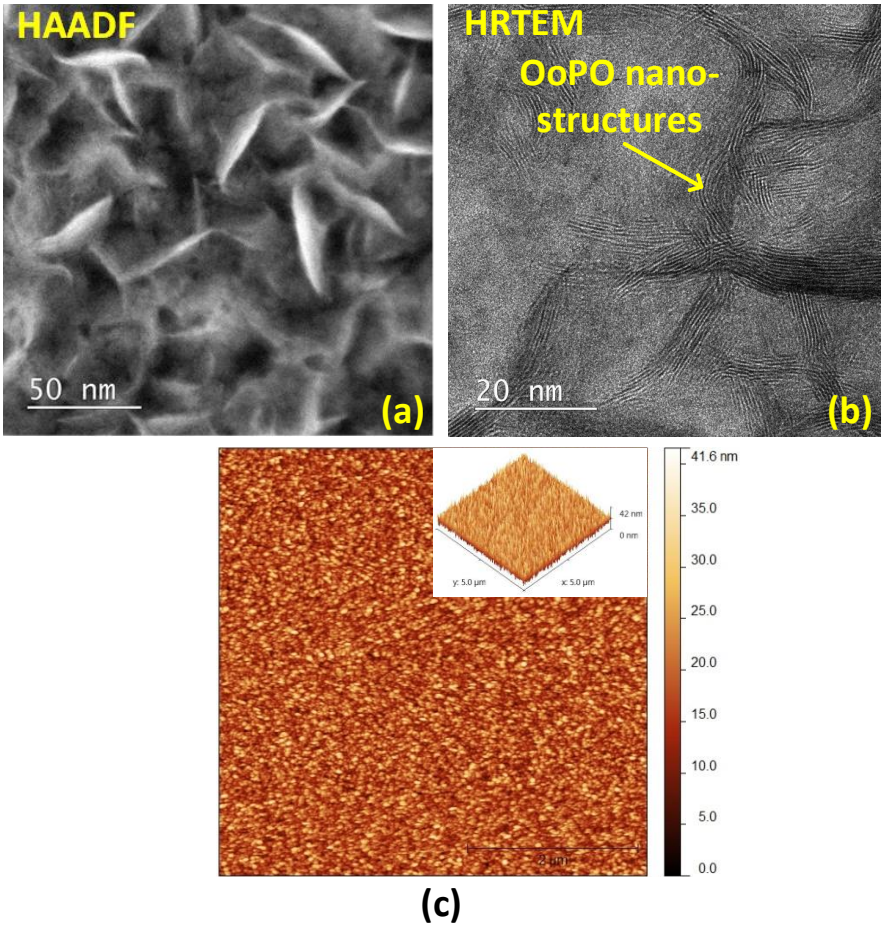


Figure A.3.4 (a) The high angle annular dark field (HAADF) image of MoS_2 film deposited at PEALD growth temperature of 450 °C clearly depicting the out-of-plane nanostructures. (b) High-resolution TEM image showing the mixed morphology of the film in the bulk. The distinctive flat regions correspond to the in-plane oriented film while the stripe-like structures correspond to the out-of-plane oriented MoS_2 film. (c) AFM image depicting the topography of ~25 nm thick film MoS_2 film deposited at 400 °C. A high RMS roughness of 5.2 nm was observed. The 3-D view is also shown in the inset.

A.3.5: Surface morphology of MoS_2 films on various substrates

Figure A.3.5 shows the morphology of MoS_2 film deposited at 450 °C (200 cycles each) on different substrates: Si substrate with 450 nm thermally grown SiO_2, Si substrate with 250 nm Al_2O_3 (deposited by thermal ALD), Si substrate coated with 100 nm Au (e-beam evaporation), SiO_2/Si substrate with mechanically exfoliated MoS_2 flakes from a natural MoS_2 single crystal (bought from Manchester Nanomaterials, UK) and glassy carbon substrate which is used for HER tests.

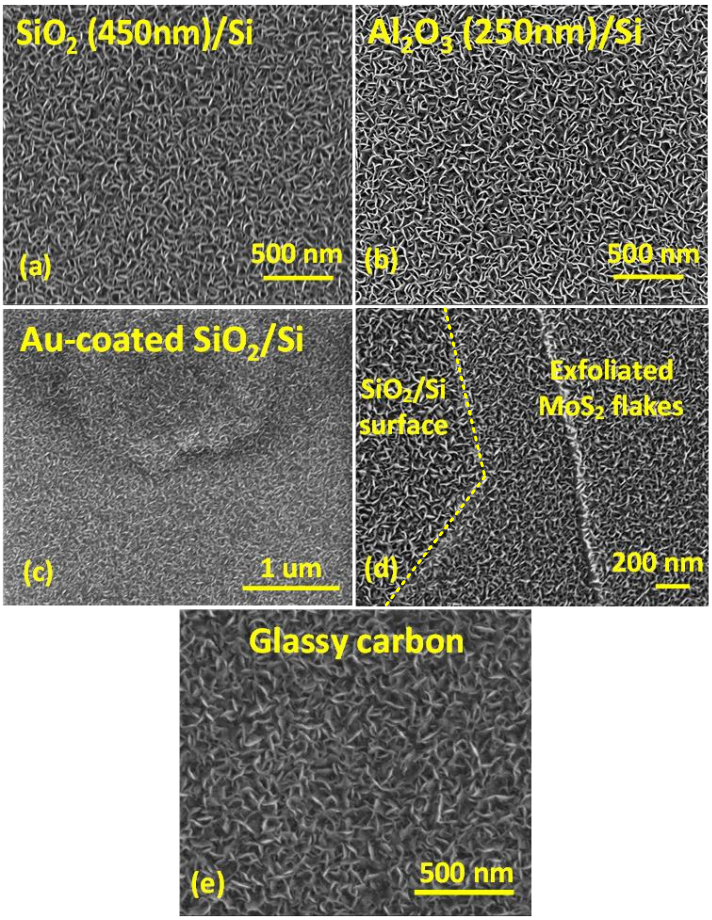


Figure A.3.5 The top-view SEM images of the MoS_2 films grown at 450 °C on different substrates. The development of out-of-plane nanostructures was observed irrespective of the substrate used (a) SiO_2/Si, (b) Al_2O_3, (c) Au-coated SiO_2, (d) Mechanically exfoliated MoS_2 flakes and (e) Glassy carbon.

A.3.6: Electrochemical Impedance Spectroscopy of MoS_2 on glassy carbon

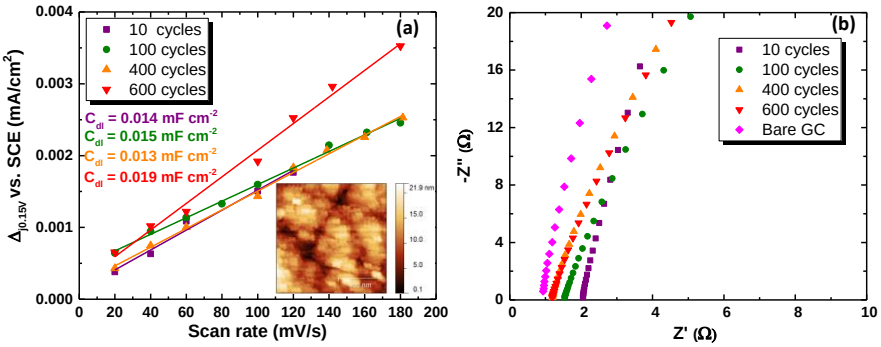


Figure A.3.6 (a) The plot showing estimated double layer capacitance (C_{dl}) for the investigated samples at various scan rates (20 - 180 mVs^{-1}). The inset shows an AFM micrograph of a polished glassy carbon plate using Al_2O_3 polishing slurry (0.3 μm). It is evident that the post-polished surface becomes rough in nature with RMS roughness value of 3.6 nm. (b) Electrochemical impedance spectroscopy (EIS): Nyquist plots of bare glassy carbon substrate and as-deposited MoS_2 films with various ALD cycles collected at open circuit potential in 0.5 M H_2SO_4 electrolyte with an AC amplitude of 10 mV. The charge transfer resistances were evaluated to be 2.3 Ω (Bare GC), 2.1 Ω (10 cycles), 1.5 Ω (100 cycles), 1.2 Ω (400 cycles) and 1.2 Ω (600 cycles), respectively.

References

1. K. S. Novoselov, D. Jiang, F. Schedin, T. J. Booth, V. V. Khotkevich, S. V. Morozov and A. K. Geim, *Proc. Natl. Acad. Sci. U. S. A.*, 2005, **102**, 10451-10453.
2. M. Xu, T. Liang, M. Shi and H. Chen, *Chemical Reviews*, 2013, **113**, 3766-3798.
3. X. Huang, Z. Zeng and H. Zhang, *Chemical Society Reviews*, 2013, **42**, 1934-1946.
4. H. Zhang, *ACS Nano*, 2015, **9**, 9451-9469.
5. K. Kang, S. Xie, L. Huang, Y. Han, P. Y. Huang, K. F. Mak, C.-J. Kim, D. Muller and J. Park, *Nature*, 2015, **520**, 656-660.
6. M. Chhowalla, H. S. Shin, G. Eda, L.-J. Li, K. P. Loh and H. Zhang, *Nat Chem*, 2013, **5**, 263-275.
7. R. Ganatra and Q. Zhang, *ACS Nano*, 2014, **8**, 4074-4099.
8. P. Joensen, R. F. Frindt and S. R. Morrison, *Materials Research Bulletin*, 1986, **21**, 457-461.
9. G. Eda, H. Yamaguchi, D. Voiry, T. Fujita, M. Chen and M. Chhowalla, *Nano Letters*, 2011, **11**, 5111-5116.
10. K. F. Mak, C. Lee, J. Hone, J. Shan and T. F. Heinz, *Physical Review Letters*, 2010, **105**, 136805.
11. A. Splendiani, L. Sun, Y. Zhang, T. Li, J. Kim, C.-Y. Chim, G. Galli and F. Wang, *Nano Letters*, 2010, **10**, 1271-1275.

12. SuzukiR, SakanoM, Y. J. Zhang, AkashiR, MorikawaD, HarasawaA, YajiK, KurodaK, MiyamotoK, OkudaT, IshizakaK, AritaR and IwasaY, *Nat Nano*, 2014, **9**, 611-617.
13. K. F. Mak, K. He, J. Shan and T. F. Heinz, *Nat Nano*, 2012, **7**, 494-498.
14. Q. H. Wang, K. Kalantar-Zadeh, A. Kis, J. N. Coleman and M. S. Strano, *Nat Nano*, 2012, **7**, 699-712.
15. B. Radisavljevic, A. Radenovic and J. Brivio, *Nature Nanotechnology*, 2011, **6**, 147-150.
16. B. Radisavljevic, M. B. Whitwick and A. Kis, *ACS Nano*, 2011, **5**, 9934-9938.
17. Z. Yin, H. Li, H. Li, L. Jiang, Y. Shi, Y. Sun, G. Lu, Q. Zhang, X. Chen and H. Zhang, *ACS Nano*, 2012, **6**, 74-80.
18. O. Lopez-Sanchez, D. Lembke, M. Kayci, A. Radenovic and A. Kis, *Nat Nano*, 2013, **8**, 497-501.
19. K. F. Mak and J. Shan, *Nat Photon*, 2016, **10**, 216-226.
20. R. S. Sundaram, M. Engel, A. Lombardo, R. Krupke, A. C. Ferrari, P. Avouris and M. Steiner, *Nano Letters*, 2013, **13**, 1416-1421.
21. H. Wang, Z. Lu, S. Xu, D. Kong, J. J. Cha, G. Zheng, P.-C. Hsu, K. Yan, D. Bradshaw, F. B. Prinz and Y. Cui, *Proceedings of the National Academy of Sciences*, 2013, **110**, 19701-19706.
22. D. Kong, H. Wang, J. J. Cha, M. Pasta, K. J. Koski, J. Yao and Y. Cui, *Nano Letters*, 2013, **13**, 1341-1347.
23. H. Li, H. Wu, S. Yuan and H. Qian, *Scientific Reports*, 2016, **6**, 21171.
24. F. Lan, Z. Lai, Y. Xu, H. Cheng, Z. Wang, C. Qi, J. Chen and S. Zhang, *Scientific Reports*, 2016, **6**, 31980.
25. A. K. Min, K. K. Seong, H. Jin Kyu, K. Seong Jun, C. Sung-Jin, P. Chong-Yun, M. Sung, S. Wooseok, L. Sun Sook, L. Jongsun and A. Ki-Seok, *2D Materials*, 2017, **4**, 025042.
26. S. B. Desai, S. R. Madhvapathy, A. B. Sachid, J. P. Llinas, Q. Wang, G. H. Ahn, G. Pitner, M. J. Kim, J. Bokor, C. Hu, H.-S. P. Wong and A. Javey, *Science*, 2016, **354**, 99-102.
27. L. Kai-Shin, W. Bo-Wei, L. Lain-Jong, L. Ming-Yang, C. Chia-Chin Kevin, H. Cho-Lun, L. Chang-Hsien, C. Yi-Ju, C. Chun-Chi, W. Chien-Ting, C. Min-Cheng, S. Jia-Min, Y. Wen-Kuan, C. Yu-Lun, Y. Fu-Liang and H. Chenming, 2016.
28. R. R. Chianelli, *Catalysis Reviews*, 1984, **26**, 361-393.
29. D. Merki and X. Hu, *Energy & Environmental Science*, 2011, **4**, 3878-3888.
30. F. Wang, T. A. Shifa, X. Zhan, Y. Huang, K. Liu, Z. Cheng, C. Jiang and J. He, *Nanoscale*, 2015, **7**, 19764-19788.
31. J. N. Coleman, M. Lotya, A. O'Neill, S. D. Bergin, P. J. King, U. Khan, K. Young, A. Gaucher, S. De, R. J. Smith, I. V. Shvets, S. K. Arora, G. Stanton, H.-Y. Kim, K. Lee, G. T. Kim, G. S. Duesberg, T. Hallam, J. J. Boland, J. J. Wang, J. F. Donegan, J. C. Grunlan, G. Moriarty, A. Shmeliov, R. J. Nicholls, J. M. Perkins, E. M. Grieveson, K. Theuwissen, D. W. McComb, P. D. Nellist and V. Nicolosi, *Science*, 2011, **331**, 568-571.
32. A. Y. S. Eng, A. Ambrosi, Z. Sofer, P. Šimek and M. Pumera, *ACS Nano*, 2014, **8**, 12185-12198.
33. Y. Yao, Z. Lin, Z. Li, X. Song, K.-S. Moon and C.-p. Wong, *Journal of Materials Chemistry*, 2012, **22**, 13494-13499.
34. P. Yiya, M. Zhaoyu, Z. Chang, L. Jun, Y. Weichao, J. YunBo and Q. Yitai, *Chemistry Letters*, 2001, **30**, 772-773.
35. T. Stephenson, Z. Li, B. Olsen and D. Mitlin, *Energy & Environmental Science*, 2014, **7**, 209-231.

36. P. K. Kannan, D. J. Late, H. Morgan and C. S. Rout, *Nanoscale*, 2015, **7**, 13293-13312.
37. J. Tao, J. Chai, X. Lu, L. M. Wong, T. I. Wong, J. Pan, Q. Xiong, D. Chi and S. Wang, *Nanoscale*, 2015, **7**, 2497-2503.
38. H. Jyun-Hong, C. Hsing-Hung, L. Pang-Shiuan, L. Li-Syuan, W. Chien-Ting, C. Cheng-Tung, L. Yao-Jen, L. Lain-Jong, C. Wen-Hao and H. Tuo-Hung, *Materials Research Express*, 2016, **3**, 065007.
39. S. Najmaei, Z. Liu, W. Zhou, X. Zou, G. Shi, S. Lei, B. I. Yakobson, J.-C. Idrobo, P. M. Ajayan and J. Lou, *Nat Mater*, 2013, **12**, 754-759.
40. A. M. van der Zande, P. Y. Huang, D. A. Chenet, T. C. Berkelbach, Y. You, G.-H. Lee, T. F. Heinz, D. R. Reichman, D. A. Muller and J. C. Hone, *Nat Mater*, 2013, **12**, 554-561.
41. J. Chen, W. Tang, B. Tian, B. Liu, X. Zhao, Y. Liu, T. Ren, W. Liu, D. Geng, H. Y. Jeong, H. S. Shin, W. Zhou and K. P. Loh, *Advanced Science*, 2016, **3**, 1500033-n/a.
42. X. Ling, Y.-H. Lee, Y. Lin, W. Fang, L. Yu, M. S. Dresselhaus and J. Kong, *Nano Letters*, 2014, **14**, 464-472.
43. M. Elisha, G. Andy, M. Jonathan, C. Mike and S. S. Ravi, *Journal of Physics D: Applied Physics*, 2017, **50**, 184005.
44. Y. C. Lin, W. Zhang, J. K. Huang, K. K. Liu, Y. H. Lee and C. T. Liang, *Nanoscale*, 2012, DOI: 10.1039/C2NR31833D.
45. Y. Zhan, Z. Liu, S. Najmaei, P. M. Ajayan and J. Lou, *Small*, 2012, **8**, 966-971.
46. N. Choudhary, J. Park, J. Y. Hwang and W. Choi, *ACS Applied Materials & Interfaces*, 2014, **6**, 21215-21222.
47. Y. Jung, J. Shen, Y. Liu, J. M. Woods, Y. Sun and J. J. Cha, *Nano Letters*, 2014, **14**, 6842-6849.
48. K. Mistry, C. Allen, C. Auth, B. Beattie, D. Bergstrom, M. Bost, M. Brazier, M. Buehler, A. Cappellani, R. Chau, C. H. Choi, G. Ding, K. Fischer, T. Ghani, R. Grover, W. Han, D. Hanken, M. Hattendorf, J. He, J. Hicks, R. Huessner, D. Ingerly, P. Jain, R. James, L. Jong, S. Joshi, C. Kenyon, K. Kuhn, K. Lee, H. Liu, J. Maiz, B. McIntyre, P. Moon, J. Neirynck, S. Pae, C. Parker, D. Parsons, C. Prasad, L. Pipes, M. Prince, P. Ranade, T. Reynolds, J. Sandford, L. Shifren, J. Sebastian, J. Seiple, D. Simon, S. Sivakumar, P. Smith, C. Thomas, T. Troeger, P. Vandervoorn, S. Williams and K. Zawadzki, 2007.
49. L. K. Tan, B. Liu, J. H. Teng, S. Guo, H. Y. Low and K. P. Loh, *Nanoscale*, 2014, **6**, 10584-10588.
50. Z. Jin, S. Shin, D. H. Kwon, S.-J. Han and Y.-S. Min, *Nanoscale*, 2014, **6**, 14453-14458.
51. A. Valdivia, D. J. Tweet and J. F. Conley, Jr., *Journal of Vacuum Science and Technology A: Vacuum, Surfaces and Films*, 2016, **34**.
52. M. Mattinen, T. Hatanpää, T. Sarnet, K. Mizohata, K. Meinander, P. J. King, L. Khriachtchev, J. Räisänen, M. Ritala and M. Leskelä, *Advanced Materials Interfaces*, 2017, DOI: 10.1002/admi.201700123, 1700123-n/a.
53. T. Jurca, M. J. Moody, A. Henning, J. D. Emery, B. Wang, J. M. Tan, T. L. Lohr, L. J. Lauhon and T. J. Marks, *Angewandte Chemie International Edition*, 2017, **56**, 4991-4995.
54. J. J. Pyeon, S. H. Kim, D. S. Jeong, S.-H. Baek, C.-Y. Kang, J.-S. Kim and S. K. Kim, *Nanoscale*, 2016, **8**, 10792-10798.
55. T. A. Ho, C. Bae, S. Lee, M. Kim, J. M. Montero-Moreno, J. H. Park and H. Shin, *Chemistry of Materials*, 2017, **29**, 7604-7614.

56. S. B. S. Heil, J. L. v. Hemmen, C. J. Hodson, N. Singh, J. H. Klootwijk, F. Roozeboom, M. C. M. v. d. Sanden and W. M. M. Kessels, *Journal of Vacuum Science & Technology A: Vacuum, Surfaces, and Films*, 2007, **25**, 1357-1366.
57. J. L. van Hemmen, S. B. S. Heil, J. H. Klootwijk, F. Roozeboom, C. J. Hodson, M. C. M. van de Sanden and W. M. M. Kessels, *Journal of The Electrochemical Society*, 2007, **154**, G165-G169.
58. M. F. J. Vos, B. Macco, N. F. W. Thissen, A. A. Bol and W. M. M. Kessels, *Journal of Vacuum Science & Technology A*, 2016, **34**, 01A103.
59. N. H. Turner and A. M. Single, *Surface and Interface Analysis*, 1990, **15**, 215-222.
60. I. Alstrup, I. Chorkendorff, R. Candia, B. S. Clausen and H. Topsoe, *Journal of Catalysis*, 1982, **77**, 2, 397-409.
61. H. Li, Q. Zhang, C. C. R. Yap, B. K. Tay, T. H. T. Edwin, A. Olivier and D. Baillargeat, *Advanced Functional Materials*, 2012, **22**, 1385-1390.
62. A. Molina-Sánchez, K. Hummer and L. Wirtz, *Surface Science Reports*, 2015, **70**, 554-586.
63. C. Lee, H. Yan, L. E. Brus, T. F. Heinz, J. Hone and S. Ryu, *ACS Nano*, 2010, **4**, 2695-2700.S. Mignuzzi, A. J. Pollard, N. Bonini, B. Brennan, I. S. Gilmore, M. A. Pimenta, D. Richards and D. Roy, *Physical Review B*, 2015, **91**, 195411.
64. J. Jeon, S. K. Jang, S. M. Jeon, G. Yoo, Y. H. Jang, J. H. Park and S. Lee, *Nanoscale*, 2015, **7**, 1688-1695.
65. F. Dumeignil, D. Wang, E. W. Qian, S. Inoue, A. Muto, T. Kabe and A. Ishihara, *Research on Chemical Intermediates*, 2005, **31**, 819-832.
66. S. Mignuzzi, A. J. Pollard, N. Bonini, B. Brennan, S. I. Gilmore, A. M. Pimenta, D. Richards and D. Roy, *Physical Review B*, 2015, **91**, 19, 195411
67. R. G. Dickinson and L. Pauling, *Journal of the American Chemical Society*, 1923, **45**, 1466-1471.
68. S. Wang, Y. Rong, Y. Fan, M. Pacios, H. Bhaskaran, K. He and J. H. Warner, *Chemistry of Materials*, 2014, **26**, 6371-6379.
69. S. Ghosh, K. Ganesan, S. R. Polaki, T. Mathews, S. Dhara, M. Kamruddin and A. K. Tyagi, *Applied Surface Science*, 2015, **349**, 576-581.
70. X. Zou and Y. Zhang, *Chemical Society Reviews*, 2015, **44**, 5148-5180.
71. Y. Yang, H. Fei, G. Ruan, Y. Li and J. M. Tour, *Advanced Functional Materials*, 2015, **25**, 6199-6204.
72. S. Shin, Z. Jin, D. H. Kwon, R. Bose and Y.-S. Min, *Langmuir*, 2015, **31**, 1196-1202.
73. S. Oh, J. B. Kim, J. T. Song, J. Oh and S.-H. Kim, *Journal of Materials Chemistry A*, 2017, **5**, 3304-3310.
74. E. Parzinger, E. Mitterreiter, M. Stelzer, F. Kreupl, J. W. Ager, A. W. Holleitner and U. Wurstbauer, *Applied Materials Today*, 2017, DOI: 10.1016/j.apmt.2017.04.007.
75. S. Li, S. Wang, M. M. Salamone, A. W. Robertson, S. Nayak, H. Kim, S. C. E. Tsang, M. Pasta and J. H. Warner, *ACS Catalysis*, 2017, **7**, 877-886.
76. C. Tsai, H. Li, S. Park, J. Park, H. S. Han, J. K. Nørskov, X. Zheng and F. Abild-Pedersen, 2017, **8**, 15113.
77. H. Li, C. Tsai, A. L. Koh, L. Cai, A. W. Contryman, A. H. Fragapane, J. Zhao, H. S. Han, H. C. Manoharan, F. Abild-Pedersen, J. K. Norskov and X. Zheng, *Nat Mater*, 2016, **15**, 48-53.

4

Tuning the wettability of MoS_2 nanostructures using plasma-enhanced atomic layer deposition*

The surface wettability of an electrocatalyst can play a crucial role in determining its catalytic properties. Here, we demonstrate that plasma-enhanced atomic layer deposition (PEALD) is a robust, reproducible method to tune the wettability of molybdenum disulphide (MoS_2) edge oriented nanostructures, an emerging electrocatalyst for the hydrogen evolution reaction (HER). This is accomplished by modulating the plasma gas composition and substrate bias (mainly affecting ion energy) during PEALD. The tuneable wettability has been demonstrated on for catalysis relevant carbon fibre paper (CFP) and SiO_2/Si substrates. The water contact angle (WCA) could be varied from ~129° to near superhydrophobic 146° (MoS_2 on CFP) and from ~109° to 133° (MoS_2 coated SiO_2/Si). A comprehensive SEM analysis showed a strong correlation between the morphology of edge oriented nanostructures and the WCA. This study might contribute to future MoS_2 based applications such as efficient water splitting and desalination where tuneable wettability can play a significant role.

* Akhil Sharma, Vincent Vandalon, W. M. M. (Erwin) Kessels and Ageeth A. Bol, *to be submitted*

4.1 Introduction

Recently, molybdenum disulphide (MoS_2), a conventional solid lubricant, has gained widespread attention due to its extraordinary electrical, optical and mechanical properties on the nanoscale.[1-4] Its atomically thin flat body combined with a direct band gap for the monolayer regime renders MoS_2 an exciting nanomaterial for a plethora of future (opto) electronic applications. However, a less explored attribute is the wettability of vertically oriented nanostructures of MoS_2 which have potential as coatings for desalination and electrocatalysts for hydrogen evolution reaction (HER) during water splitting.[5-7] It has been demonstrated that the optimization of surface wettability is of importance for improving the electrocatalytic activity for HER.[6-8] The wettability of a surface is generally determined by the water contact angle (WCA). Surfaces possessing a WCA > 150° are considered superhydrophobic. Superhydrophobic surfaces exhibit a higher efficiency in heat and mass transfer, lead to self-cleaning, provide water proofing etc. and therefore are desirable for a variety of applications.[5] For exfoliated bulk MoS_2, the WCA has been reported as ~90° in ambient, which is attributed to airborne hydrocarbon adsorption.[9] On the contrary, the wettability of vertically oriented 'nano-flower structures' has been shown to be tuneable either by adjusting the process parameters during high temperature techniques like chemical vapor deposition (CVD) and/or by mechanical deformation.[5-7] Although, a WCA up to ~159° has been reported using the above mentioned deposition techniques,[6] the highly desired reproducibility on a technological relevant scale might be difficult to achieve. Moreover, the high processing temperature and poor conformality of CVD makes it further challenging to scale up. Therefore, there is a clear need for an alternative robust, reproducible technique which can overcome the above stated challenges. In our previous publication,[10] we have reported the use of low temperature PEALD to grow out-of-plane oriented, flower-like MoS_2 films (denominated as 'edge oriented nanostructures' here) on a large scale for the hydrogen evolution reaction during water splitting. In this chapter, we demonstrate that by modulating the plasma chemistry during PEALD, we could attain tuneable wetting of MoS_2 edge oriented nanostructures over demanding 3D structures. In particular, we show that by varying plasma gas composition and applying substrate bias during PEALD, the morphology of nanostructures could be altered at nanoscale enabling tuneable WCA.

4.2 Experimental section

The MoS_2 thin films were deposited at 450 °C in an Oxford Instruments FlexAL™ ALD reactor either on 4" SiO_2 (450 nm)/Si wafers or Spectracarb™ 2050A Gas Diffusion Layer sheets (carbon fiber paper). The PEALD process was based on a combination of a metal organic precursor $[(NtBu)_2(NMe_2)_2Mo]$ and H_2S+H_2+Ar plasma as a co-reactant. The flow rate of H_2S and H_2 was fixed at 8 sccm and 2 sccm while the flow rate of Ar was varied ranging from 0 to 200 sccm. The details of the PEALD process can be found in our previous work.[10] The substrate bias was applied during half duty cycle (i.e. last 10 s for 20 s pulse) of the H_2S+H_2+Ar (Ar = 140 sccm) plasma co-reactant step. The number of ALD cycles used for each sample was 400 throughout this work unless stated otherwise. The samples were cooled down in vacuum to 150 °C before transferring them to the load lock chamber and subsequently to ambient to minimize oxidation in air. For MoS_2 characterization, Raman spectroscopy was performed with a Renishaw Raman microscope equipped with a 514 nm laser, integrated switchable gratings with 600 or 1800 lines/mm, and a CCD detector. The surface chemistry was studied by X-ray photoelectron spectroscopy (XPS) using a Thermo Scientific K-alpha spectrometer (Thermo Fisher Scientific, Waltham, MA) equipped with a monochromatic Al Kα X-ray radiation source (hν = 1486.6 eV). The film morphology was analysed by scanning electron microscopy (SEM) using a FEI Helios 650 DualBeam system. Finally, for the measurement of macroscopic WCAs, a CAM200 goniometer (KSV Instruments Ltd., Helsinki, Finland) on a floating table was used. The static WCA measurements were performed by using 4 μl droplets consistently for all experiments. For the advancing and receding WCA measurements, a fixed volume (0.5 μl) of droplets were inflated and deflated respectively, with an automated dispenser until the contact line changes. The WCA was measured using the software 'one attension (Biolin Scientific)' based on the Young-Laplace equation.[11]

4.3 Results and discussions

The wettability of MoS_2 edge-oriented nanostructures synthesized by varying the Ar partial pressure during the PEALD process was investigated on HER relevant CFP as substrates. The bare CFP possess high surface roughness and is porous in nature, giving it a high surface area, which is ideal for catalysis. Moreover, CFP provides strong adhesion to MoS_2 which is important for stable catalytic activity[12] and is therefore chosen as the supporting substrate. The optimized PEALD process (on SiO_2/Si

substrates) as reported earlier,[10] was used on CFP. This resulted in uniform and conformal MoS_2 films. This was against expectations, as nucleation problems were foreseen due to the hydrophobic nature (as measured contact angle ~ 129°±1.8) and the graphitic structure of CFP. The high reactivity of plasma species during the PEALD process probably functionalizes the CFP surface and creates the necessary nucleation sites for the metal precursor to bind, resulting in subsequent film growth. Figure 4.1 (a) displays the top planar SEM image focused on an individual carbon fiber strand with a coating of MoS_2, while Figure 4.1(b) shows the magnified image where the edge-oriented nanostructures are clearly visible. From the SEM images it is evident that we obtained an excellent conformal coating of MoS_2 edge oriented nanostructures around the fibers of the CFP. This showcases ALD's inherent attribute of conformal deposition irrespective of the surface geometry.

Next, the WCA of MoS_2 nanostructures deposited on CFP using different concentrations of Ar in the plasma step of the PEALD process was measured. Figure 4.1 (c) shows the graph of the WCA as a function of the Ar flow (0 - 200 sccm) during the PEALD process. It is evident that the growth of MoS_2 film on CFP results in an increase of the contact angle to ~139° when no Ar is added to the plasma as compared to bare CFP. With increasing Ar flow, the contact angle is nearing superhydrophobicity (contact angle ~ 146°) at an Ar flow of 100 sccm. This degree of tuneable contact angle achieved by varying the Ar partial pressure in the plasma co-reactant step during PEALD process might be valuable for HER application. It has been demonstrated that the surface wettability is related to the adhesion force between a gas bubble produced during HER and the solid catalyst surface. The manipulation of wettability thus can facilitate the desorption of H_2 gas bubble resulting in enhanced catalytic activity.[7]

In order to analyze the film morphology and understand the effect of the Ar concentration on the WCA, a similar series of deposition by varying the Ar flow in the plasma gas composition was performed on planar SiO_2/Si substrates. We first checked whether the WCA behaves similar on SiO_2/Si substrates. The as-measured WCAs as a function of varying Ar partial pressure show a similar trend as CFP (Figure 4.2 (a)). Noticeably, the WCA obtained without Ar in the plasma is relatively lower (~118°) because of the flat surface of SiO_2/Si substrates.

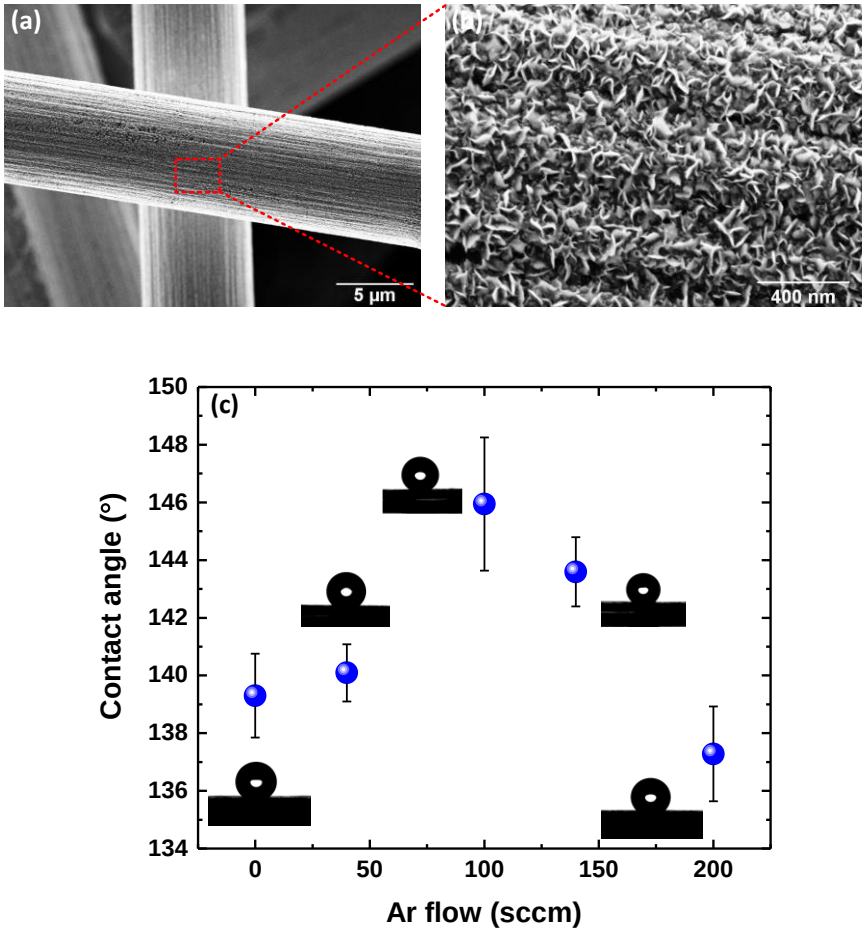


Figure 4.1 Top planar SEM images showing the (a) carbon fiber conformally coated with MoS_2 thin film (b) magnified view elucidating the uniformal presence of edge-oriented nanostructures (c) The plot showing variability in water contact angle as a function of Ar flow during the PEALD process on CFP substrates. The droplet images acquired by goniometer are displayed along with each data point.

Furthermore, the highest WCA is obtained for the sample processed with Ar -100 sccm, as for the CFP. One of the other important measures of surface wettability is contact angle hysteresis (CAH) which is a measure of the adhesion between water and a surface.[4] The CAH is calculated from the difference between the advancing and receding WCAs by using the dynamic sessile drop method. It is considered that large CAH values for rough surfaces lead to a stronger adhesion of water to the surface which

causes the pinning of a water droplet.[13] We note that all the samples with edge oriented nano-structures exhibit droplet pinning (inset of Figure 4.2 (b)) due to the petal effect in the Cassie impregnation wetting regime as described in the literature.[14]

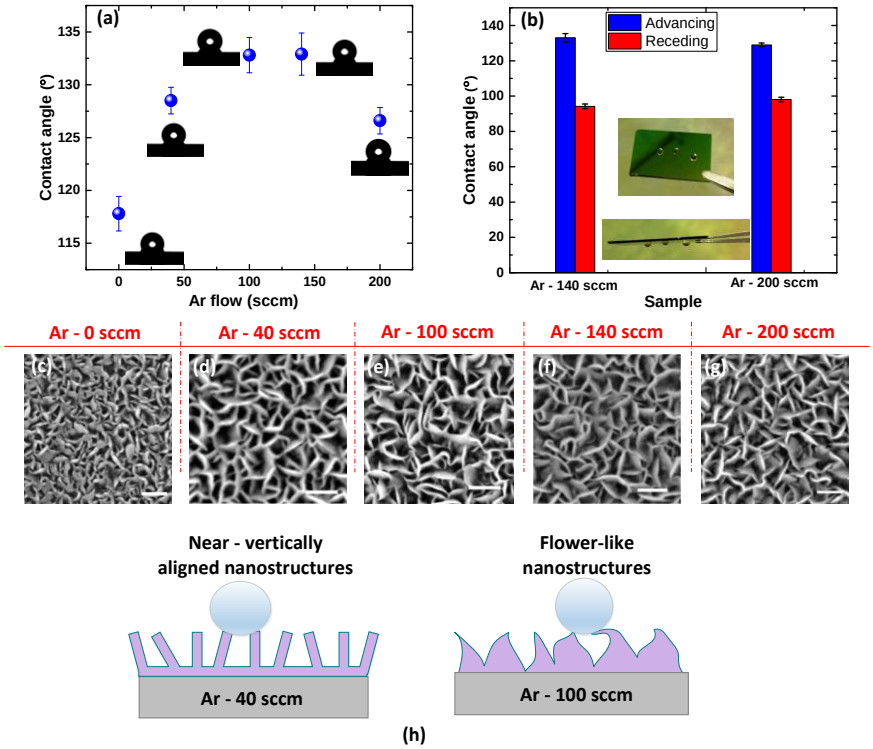


Figure 4.2 (a) The plot showing variability in water contact angle as a function of Ar flow during PEALD process for SiO_2/Si substrates. (inset) The corresponding water droplet images acquired by goniometer are shown next to each data point (b) The bar plots for selective samples displaying a large hysteresis for advancing and receding measurements. (inset) The photographs showing the 'pinning' of the droplets on the edge oriented nanostructures. (c - g) The top planar SEM images show the morphology of as-deposited edge-oriented MoS_2 nanostructures with varying Ar flow in the plasma gas composition during PEALD process (scale bar - 100 nm). (h) The schematic illustrating the change in morphology of nanostructures by varying the Ar concentration (from 40 sccm to 100 sccm).

For our samples, we calculated the CAH by using the above mentioned dynamic sessile drop method. Figure 4.2 (b) compares the advancing and receding WCAs for two selected samples (Ar - 140 sccm and Ar - 200 sccm) which gave a high value of CAH (~30° - 40°) and explains the observed droplet pinning as aforementioned. SEM images

were taken to study the film morphology in detail. It was observed that the complete series resulted in uniform edge oriented nanostructures on the substrates as depicted in Figure 4.2 (c - g). A close inspection of the SEM images reveals that (a) the edge lengths of nanostructures increase as the Ar is introduced in plasma (i.e. Ar - 0 sccm to Ar - 40 sccm). (b) The morphology of nanostructures transforms from near-vertical (for Ar - 40 sccm) to more flower-like (Ar - 100 & 140 sccm) as schematically illustrated in Figure 4.2 (h). This is most likely due to a slight difference in tilt angle of edges causing an apparent increase in void fraction for higher Ar concentration. Furthermore, it is evident that this flower-like morphology with slightly tilted edges yields the highest contact angle (~133°). Therefore, it is clear that these type of hierarchical nanostructures are most favorable for surface to attain the Cassie-Baxter state thus resulting in hydrophobicity.

At this point, it is important to investigate the chemical properties of the film to analyze any film compositional effect on WCA with varying Ar concentration. To this purpose, X-ray photoelectron spectroscopy (XPS) characterization was performed and the corresponding peaks for all samples are shown in Appendix (Figure A.4.1 (a) & (b)). The plots for the Mo3d and S2p regions show virtually identical characteristics irrespective of the Ar concentration condition. In addition, we also performed Raman spectroscopy characterization, which show the typical vibrational modes for MoS_2[15] for all samples indicating the presence of uniform crystalline material, as shown in Figure A.4.1 (c) (in Appendix). Based on these results, we could preclude any role of the chemical composition of the films on the tuneability of the WCA and reinstate that it is a purely morphological effect induced by the modulation of the plasma gas composition during the PEALD process.

From the above results, it is clear that the introduction of heavy Ar species in the plasma gas composition shows a prominent effect on the nano-scale morphology. The admixing of Ar in the plasma gas mixture affects a number of parameters including but not limited to ion energy, ion flux, radical density and plasma pressure. Next, we analysed the effect of substrate biasing during PEALD on the morphology and WCA of MoS_2 films. The application of substrate biasing enables the control over the ion energy during the plasma co-reactant step of a PEALD process which can have a significant effect on the material properties.[16] The detailed know-how of applying substrate biasing during PEALD can be found elsewhere.[17-18] Hereby, we performed an experiment to

apply the substrate bias during plasma co-reactant step (which most likely resulted in increased ion energy) and study the influence on the morphology and contact angle of resulting MoS_2 film. Interestingly, a major effect on the morphology of resulting MoS_2 films is observed as a function of increasing bias voltage. Figures 4.3 (a) & (b) show the top view SEM images for films deposited on SiO_2/Si with bias voltages of -89 V and -142 V respectively. A closer look at the film deposited with bias voltage of -89 V reveals that the density of edge oriented nanostructures is less as compared to the sample processed without any substrate bias (Figure 4.2 (d)). On the contrary, for the film deposited with higher bias voltage (-142 V), the morphology appears altogether different with the presence of protruding lumps of MoS_2. We can speculate that the observable change in morphology is most likely due to stronger impingement of heavy Ar ions during film formation which governs the morphology development of the resulting film.

As a consequence, the WCA followed the change in morphology and varied from 132.9° ± 2 (for film deposited without bias) to 115.5° ± 0.22 and 109.5° ± 0.41 for films deposited with bias voltages of -89V and -142V respectively. Therefore, an additional knob in the form of ion energy enables the tuneability of morphology further and consequently also the WCA. Importantly, the XPS analysis of films deposited with substrate biasing revealed no change in chemical compositions with identical peaks for Mo3d and S2p energy range as in the case without bias application (Figure A.4.2 in Appendix). This again indicates that the WCA is purely altered by changes in film morphology. Furthermore, it is worth mentioning that the application of substrate biasing has also been shown to induce the formation of point defects leading to stress evolution in thin films.[16] We have used Raman spectroscopy to analyse the lattice strain effects in the MoS_2 films deposited with substrate biasing which has been shown as an effective tool for this purpose.[17] Figure 4.3 (c) shows the Raman spectra for films deposited with and without application of substrate bias. As the substrate bias is applied, red shifts in the position of both E^1_{2g} and A_{2g} peaks are observed (380.1 cm^{-1} and 404.2 cm^{-1}), which indicates the development of lattice strain in the film and therefore confirms the argument as stated above. In literature, it has been shown that for some materials, the lattice strain can play a critical role in determining their electrocatlytic properties.[19] Thus, we propose that the application of substrate biasing during PEALD might enable improved performance of MoS_2 films for HER application and prove as an interesting topic for further investigation.

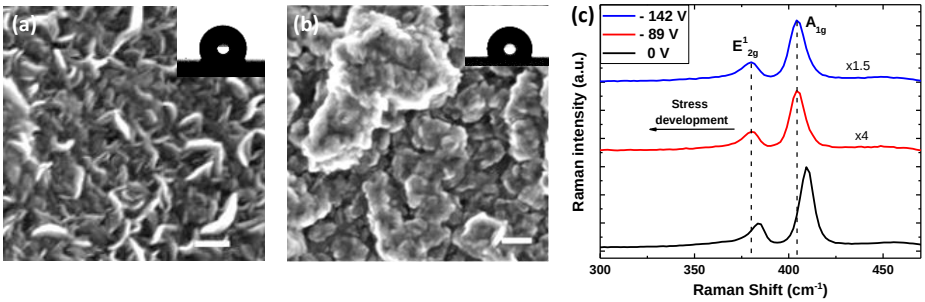


Figure 4.3 The top planar SEM images displaying the variation of film morphology after application of bias voltage of (a) -89 V (b) -142 V respectively (scale bar - 100 nm). The water droplet images are shown in inset. (c) Raman spectra shows the red shift of predominant vibrational modes (indicated by arrow) after substrate biasing as compared to the peaks at ~ 383.5 cm^{-1} and 407.6 cm^{-1} for film deposited without application of substrate bias.

4.4 Conclusions

In conclusion, we have demonstrated that the morphology and wettability of MoS_2 nanostructures can be tuned by varying the plasma parameters during PEALD. The comprehensive SEM analysis of the nanoscale morphology has revealed that the tilt angle of the edges of MoS_2 nanostructures can be varied by changing the plasma parameters, which has a profound effect on the resulting WCA. Furthermore, changing the plasma parameters did not have an effect on the chemical composition of the MoS_2, and therefore the resulting morphology plays a deterministic role in controlling the WCA of edge oriented MoS_2 films synthesized by PEALD. This study will provide a new avenue for designing rough surfaces with controllable wettability and hence contribute towards advancement of future applications utilizing MoS_2 based nano-structured surfaces.

Acknowledgements

The authors would like to thank Jeroen van Gerwen and Cristian van Helvoirt for their technical assistance. Morteza Aghaee is acknowledged for his assistance with contact angle measurements. This work has been financially supported by the European Research Council (Grant Agreement No. 648787- ALDof2DTMDs). Further, the work has also been supported by NWO and Technology Foundation STW through the VIDI program on 'Novel bottom-up nanofabrication techniques for future carbon-nanoelectronics'.

Appendix

A.4.1 Raman and XPS spectra for MoS_2 films

For all samples, the binding energy peak positions corresponding to Mo^{4+} and S^{2-} species were indistinguishable, demonstrating the presence of chemically pure MoS_2 edge oriented structures.

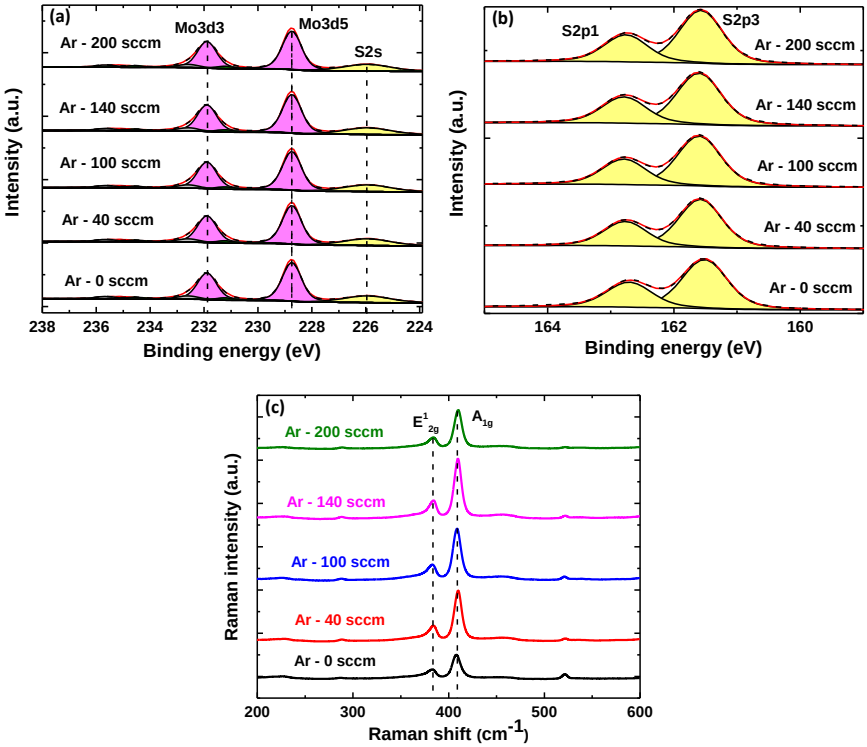


Figure A.4.1 XPS spectra corresponding to varying Ar concentration in plasma gas composition for (a) Mo3d region depicting the peaks corresponding to Mo (IV) and S2s regions. The doublet peak for Mo (IV) and single peak for S2s regions are highlighted with dashed lines respectively. (b) S2p region with a doublet peak corresponding to S2p3 and S2p1 respectively. (c) Raman spectra for samples with varying Ar concentration. The predominant vibrational peaks (i.e. E^1_{2g} and A_{1g}) are positioned at 383.5 cm^{-1} and 407.6 cm^{-1} for each case and highlighted with dashed lines.

A.4.2 XPS spectra for MoS_2 films deposited with substrate biasing

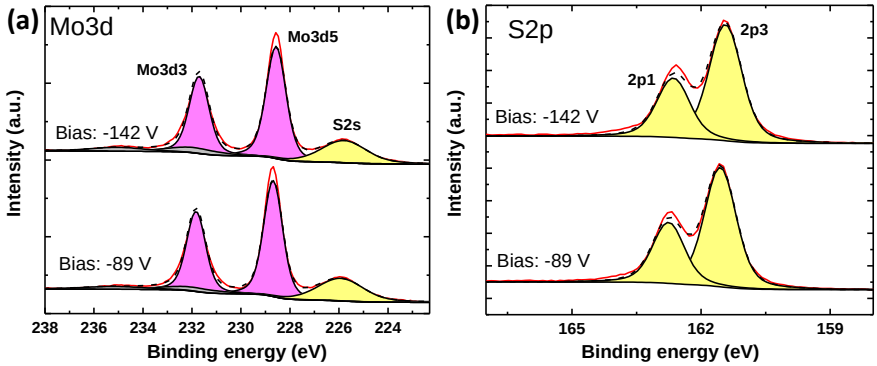


Figure A.4.2 The details of XPS spectra showing the spectral regions for (a) Mo3d and (b) S2p corresponding to the different bias conditions. There are no observable changes in chemical composition of the films deposited with application of varying substrate bias voltages.

References

1. R. Ganatra and Q. Zhang, *ACS Nano*, 2014, **8**, 4074-4099.
2. Q. H. Wang, K. Kalantar-Zadeh, A. Kis, J. N. Coleman and M. S. Strano, *Nat Nano*, 2012, **7**, 699-712.
3. B. Radisavljevic, M. B. Whitwick and A. Kis, *ACS Nano*, 2011, **5**, 9934-9938.
4. K. Kang, S. Xie, L. Huang, Y. Han, P. Y. Huang, K. F. Mak, C.-J. Kim, D. Muller and J. Park, *Nature*, 2015, **520**, 656-660.
5. J. Choi, J. Mun, M. C. Wang, A. Ashraf, S.-W. Kang and S. Nam, *Nano Letters*, 2017, **17**, 1756-1761.
6. G. R. Bhimanapati, T. Hankins, Y. Lei, R. A. Vilá, I. Fuller, M. Terrones and J. A. Robinson, *ACS Applied Materials & Interfaces*, 2016, **8**, 22190-22195.
7. K. Hernandez Ruiz, J. Liu, R. Tu, M. Li, S. Zhang, J. R. Vargas Garcia, S. Mu, H. Li, T. Goto and L. Zhang, *Journal of Alloys and Compounds*, 2018, **747**, 100-108.
8. C. Meng, B. Wang, Z. Gao, Z. Liu, Q. Zhang and J. Zhai, *Scientific Reports*, 2017, **7**, 41825.
9. A. Kozbial, X. Gong, H. Liu and L. Li, *Langmuir*, 2015, **31**, 8429-8435.
10. A. Sharma, M. A. Verheijen, L. Wu, S. Karwal, V. Vandalon, H. C. M. Knoops, R. Sundaram, J. P. P. Hofmann, W. Kessels and A. A. Bol, *Nanoscale*, 2018, DOI: 10.1039/C8NR02339E.
11. W. Sun, Z. Wang, W. Q. Zaman, Z. Zhou, L. Cao, X.-Q. Gong and J. Yang, *Chemical Communications*, 2018, **54**, 996-999.
12. A. F. Stalder, T. Melchior, M. Müller, D. Sage, T. Blu and M. Unser, *Colloids and Surfaces A: Physicochemical and Engineering Aspects*, 2010, **364**, 72-81.
13. D. H. Kwon, Z. Jin, S. Shin, W.-S. Lee and Y.-S. Min, *Nanoscale*, 2016, **8**, 7180-7188.
14. R. H. Dettre and R. E. Johnson, in *Contact Angle, Wettability, and Adhesion*, AMERICAN CHEMICAL SOCIETY, 1964, vol. 43, ch. 8, pp. 136-144.
15. L. Feng, Y. Zhang, J. Xi, Y. Zhu, N. Wang, F. Xia and L. Jiang, *Langmuir*, 2008, **24**, 4114-4119.

16. H. Li, Q. Zhang, C. C. R. Yap, B. K. Tay, T. H. T. Edwin, A. Olivier and D. Baillargeat, *Advanced Functional Materials*, 2012, **22**, 1385-1390.
17. H. B. Profijt, M. C. M. Van De Sanden and W. M. M. Kessels, *Journal of Vacuum Science and Technology A: Vacuum, Surfaces and Films*, 2013, **31**.
18. T. Faraz, H. C. M. Knoops, M. A. Verheijen, C. A. A. van Helvoirt, S. Karwal, A. Sharma, V. Beladiya, A. Szeghalmi, D. M. Hausmann, J. Henri, M. Creatore and W. M. M. Kessels, *ACS Applied Materials & Interfaces*, 2018, DOI: 10.1021/acsami.8b00183.
19. L. Yang, X. Cui, J. Zhang, K. Wang, M. Shen, S. Zeng, S. A. Dayeh, L. Feng and B. Xiang, *Scientific Reports*, 2014, **4**, 5649.

5

High performance MoS_x thin films for hydrogen evolution reaction prepared by plasma enhanced atomic layer deposition*

The hydrogen evolution reaction (HER) performance of an electrocatalyst can be greatly influenced by its structural properties. Here, we present a scalable, facile method to tune the structural properties of molybdenum sulphide (MoS_x) films to attain highly HER active films by adjusting the temperature during plasma enhanced atomic layer deposition (PEALD) process. The PEALD synthesized films at 250 °C and 450 °C are predominantly amorphous and nano-crystalline in nature respectively. A systematic comparison between electrocatalytic performance of these two types of films shows that the predominantly amorphous films perform much better in HER. A high current density at low overpotential (10 mA/cm^2 at $\eta \sim$ 235 mV) with a Tafel slope as low as 47 mV/dec has been achieved. A comprehensive analysis based on X-ray photoelectron spectroscopy and extended X-ray fine absorption spectroscopy has revealed the structural differences between films synthesized at 250 °C and 450 °C which might be the reason for their different HER activities.

*Akhil Sharma, Longfei Wu, Marcel A. Verheijen, Jan P. Hofmann, Wilhelmus M. M. (Erwin) Kessels and Ageeth A. Bol, *to be submitted*

5.1 Introduction

Molybdenum disulphide (MoS_2), a transition metal dichalcogenide, has been identified as an inexpensive catalyst for hydrogen evolution reaction (HER). The low Gibbs free energy of hydrogen adsorption (ΔG_{H*}) for edge sites of MoS_2 makes it an attractive candidate as an alternative to the expensive, non-abundant noble metals like Pt.[1] Bulk MoS_2, however, exhibits a poor HER activity due to predominantly exposed basal planes instead of edge sites, which are catalytically inert as well as the large internal resistance in the bulk semiconductor.[2] Therefore, tremendous efforts have been put into structural engineering of MoS_2 to maximise the exposure of active edge sites. Some of the approaches are based on the synthesis of nanoparticles, mesoporous double-gyroid structures, or vertically aligned films.[3] Interestingly, the amorphous phase of molybdenum sulphide (MoS_x) has also been reported to exhibit high HER activity owing to the abundant active sites on the surface.[4, 5] Several groups have synthesized amorphous MoS_x using methods such as electrochemical deposition, wet chemical synthesis, hydrothermal growth, or atomic layer deposition (ALD).[4, 6-9]

ALD is an excellent method to prepare electrocatalysts owing to its inherent thickness control with atomic scale precision. The amount (loading) of catalysts can be controlled in a facile way by tuning the number of ALD cycles which is a large advantage over other synthesis techniques. Furthermore, the self-limiting nature of ALD also enables uniform and conformal film coatings on high surface area substrates such as carbon fibre paper (CFP) which is an excellent way to increase the electrochemical surface active surface area, i.e. the number of active sites.

In our recent publication,[10] we have reported the synthesis of nanocrystalline, vertically aligned MoS_2 films over large area by using plasma enhanced atomic layer deposition (PEALD) at 450 °C. We have demonstrated that these vertically aligned films are efficient electrocatalysts for HER. Concomitantly, in literature, ALD MoS_x films with a mixed amorphous/nanocrystalline phase have also been shown to exhibit a high HER performance.[9] In the work of Kwon *et al.*[9], CFP was chosen as the supporting substrate because of its large specific surface area and enhanced adhesion of MoS_x. A particle-like growth behaviour was observed which was attributed to the low density of adsorption sites on CFP substrate. Nevertheless, a high cathodic current density at low

overpotential in combination with a low Tafel slope were achieved which demonstrated the potential of ALD to design and prepare electrocatalysts for HER.

Currently, there is no clear understanding of what the success factors for MoS_2 deposited by ALD in HER are, as both amorphous material and nanocrystalline, vertically aligned structures are very active in HER. In this paper, we synthesize both amorphous and nanocrystalline films using our morphology tuneable PEALD process, simply by tuning the process temperature. The films synthesized at 250 °C are predominantly amorphous, whereas the films at 450 °C are nanocrystalline in nature as aforementioned and will be referred to as MoS_x and MoS_2 films respectively, throughout this chapter. We have chosen two HER relevant supporting substrates, glassy carbon (GC) and CFP, to assess HER performance of both types of films synthesized by PEALD. To elucidate the reasons responsible for the improved HER performance for both type of PEALD synthesized films, a systematic comparison has been performed to correlate the observed difference in their electrocatalytic activities with the corresponding structural and chemical properties. In particular, we have employed X-ray photoelectron spectroscopy (XPS), extended X-ray absorption fine spectroscopy (EXAFS), Raman microscopy, and transmission electron microscopy (TEM) to study the influence of electronic and crystallographic structure on HER performance of the films.

5.2 Experimental section

ALD process specifications

MoS_2 thin films were deposited at 250 °C and 450 °C in an Oxford Instruments FlexAL™ ALD reactor on SiO_2 (450 nm)/Si coupons, Glassy carbon substrates (Carbon-Vitreous-3000C-Foil-VC000550, Goodfellow Cambridge Ltd. UK) and Spectracarb™ 2050A Gas Diffusion Layer sheets (carbon fibre paper). The PEALD process was based on a combination of the metal organic precursor $[(NtBu)_2(NMe_2)_2Mo]$ and H_2S+H_2+Ar plasma as a co-reactant. The flow rates of H_2S, H_2 and Ar were fixed at 8 sccm, 2 sccm and 40 sccm respectively. The details of the PEALD process can be found in our previous work.[10]

Film crystallinity and surface morphology

Raman spectroscopy measurements were performed with a Renishaw Raman microscope equipped with a 514 nm laser, integrated switchable gratings with 600 or

1800 lines/mm, and a CCD detector. For each scan, 5 accumulations with acquisition time of 10 s were taken. The surface morphology was studied by scanning electron microscopy (SEM) using a ZeissSigma Nanolab operating at an acceleration voltage of 2 kV.

Chemical composition

To determine the elemental composition, X-ray photoelectron spectroscopy (XPS) was performed using a Thermo Scientific K-alpha spectrometer (Thermo Fisher Scientific, Waltham, MA) equipped with a monochromatic Al Kα X-ray radiation source (hν = 1486.6 eV). For the XPS analysis, a 400 µm diameter spot was used and photoelectrons were collected at a take-off angle of 60°. The samples were charge neutralized during the XPS analysis using an electron flood gun in order to correct for differential or non-uniform charging. All peaks in the XPS survey scans are referenced to the binding energy of the C1s peak of adventitious carbon (284.8 eV) for charge correction and quantification of the survey scans have been performed using Avantage software.

Film microstructure

The film microstructure was determined by HRTEM analysis using a JEOL ARM 200F operated at 80 kV. For the top planar view images, MoS_2 films were grown on SiN_x TEM windows, coated with ~5 nm ALD SiO_2. Selected area electron diffraction (SAED) patterns were acquired from a 1.3 µm diameter area on each sample.

Electrochemical testing

MoS_2 films were deposited on glassy carbon plates polished by 0.3 µm Al_2O_3 slurry and later on cleaned with ethanol and Milli-Q H_2O for electrochemical tests. The measurements were performed in a three-electrode electrochemical workstation (Type: PGSTAT302N, Metrohm Autolab) with saturated calomel electrode (0.269 V vs. reversible hydrogen electrode (RHE) as a reference electrode, Pt foil (1 x 2 cm^2) as a counter electrode and glassy carbon working electrode. All measurements were performed in 0.5 M H_2SO_4 electrolyte prepared using 18 MΩ·cm deionized Milli-Q water purged with Ar for 20 min. Linear sweep voltammetry (LSV) experiments were conducted with a scan rate of 5 mV/s and AC electrochemical impedance spectroscopy was recorded at open circuit potential (OCP) in the frequency range of 10 kHz to 0.1 Hz. To calculate the Tafel slope, the linear portion at low overpotential region was fit to the Tafel equation using the internal resistance corrected LSV curves. Cyclic voltammetry (CV) stability tests for extracting double layer capacitance values were conducted with varying scan rates from 20 - 120 mV/s starting at OCP from -0.52 V to 0.62 V.

EXAFS measurements

EXAFS were recorded at BM26A (DUBBLE beamline) of ESRF, operating at 6 GeV with a beam current of 200 mA. Mo foil was used as a reference for energy calibration, all spectra were collected in fluorescence mode at Mo K-edge (20 keV). EXAFS spectra were background subtracted and fitted with Viper. Scattering paths were calculated by FEFF6 from molybdenite (MoS_2) crystal structure from American Mineralogist Crystal Structure Database. The fitting range of Mo K-edge was Δk = 2-11.06 $Å^{-1}$ and ΔR = 1.06-2.43 Å. Plotted spectra were not phase-corrected and has a k-weight of 2.

5.3 Results and discussion

In our previous study,[10] we observed a clear difference in morphology of the films deposited at 250 °C and 450 °C, respectively. The SEM and Raman analyses showed that while the film at 250 °C was predominantly amorphous in nature, the film at 450 °C was highly textured, possessing out-of-plane orientation. In the current work, we started by assessing the electrochemical activities of PEALD synthesized films at 250 °C and 450 °C, on glassy carbon (GC) substrates. To this purpose, both samples (400 ALD cycles each) were used as working electrode for hydrogen evolution in 0.5 M H_2SO_4 solution. Figure 5.1 (a) shows the polarization curves for films synthesized at 250 °C and 450 °C, respectively. A higher HER activity is obtained for both molybdenum sulphide coated GC substrates as compared to the bare GC substrate. Furthermore, amongst the two samples, a considerable improvement of the HER activity for film synthesized at 250 °C (MoS_x) is visible. The overpotentials required to reach a current density of 10 mA/cm^2 are -281 mV and -503 mV for films synthesized at 250 °C and 450 °C, respectively. The large current density obtained at lower overpotential for the amorphous sample indicates a probable higher number of active sites for HER as is discussed later.

Figure 5.1 (b) displays the Tafel plots for films synthesized at 250 °C and 450 °C, respectively. The Tafel slope is a figure of merit for electrocatalytic activity which is extracted by fitting the Tafel equation to the linear portion of the Tafel plot. Tafel slopes of 54 mV/dec and 94 mV/dec for films synthesized at 250 °C and 450 °C, respectively, indicate two different types of HER mechanisms for the two types of films. There are

three principal steps for converting H^+ to H_2 in acidic medium.[11, 12] The first is a primary discharge step (i.e. Volmer reaction):

$$H_3O^+ + e^- \rightarrow H_{ad} + H_2O$$

which is either followed by the electrochemical desorption step (i.e. Heyrovsky reaction):

$$H_{ad} + H_3O^+ + e^- \rightarrow H_2 + H_2O$$

or a recombination step (i.e. Tafel reaction):

$$H_{ad} + H_{ad} \rightarrow H_2$$

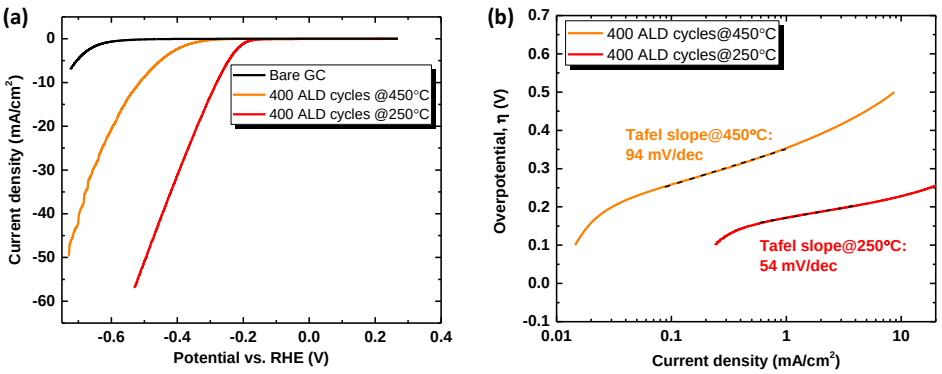


Figure 5.1 (a) Cathodic polarization curves as measured by linear sweep voltammetry (LSV) for MoS_x coated GC substrates. LSV curves were recorded in 0.5 M H_2SO_4 at a scan rate of 5 mV/s and with rotating speed of 800 rpm. (b) Tafel plots derived from LSV curves in (a). The values of Tafel slopes for films synthesized at 250 °C and 450 °C are evaluated to be 54 mV/dec and 94 mV/dec, respectively.

Under a set of specific conditions, considering that the Volmer reaction is the rate-limiting step of HER, the value of Tafel slope should lie around 120 mV/dec, whereas if Heyvrosky or Tafel reactions act as rate-limiting steps, Tafel slopes of 30 and 40 mV/dec can be observed. Therefore, based on the values of Tafel slopes for our PEALD synthesized films at 250 °C and 450 °C, it can be inferred that while for films synthesized at 250 °C, the Volmer-Heyrovsky mechanism may dominate while the major pathway for films synthesized at 450 °C can be the Volmer-Tafel.

Raman spectroscopy was employed to verify the crystallinity of the molybdenum sulphide films. Figure 5.2 (a) displays the Raman spectra for both types of films

showing clear differences. The two characteristic in-plane (E^1_{2g}) and out-of-plane (A_{1g}) vibrational modes are clearly present for the film synthesized at 450 °C showing its crystalline nature. However, the Raman characteristic peaks are weak and broad for the film synthesized at 250 °C. Furthermore, the peaks show a red shift which might be due to the absence/little of long range spatial order in the atomic lattice as reported in the literature.[13, 14] This signifies the predominant amorphous nature for films synthesized at 250 °C. These results are in line with the TEM studies which were performed to elucidate the microstructural differences between two types of films. From TEM images (Figure 5.3 (b) & (c)), it appears that the film synthesized at 450 °C has a significant amount of stacked structures suggesting a stronger degree of crystallinity as compared to film synthesized at 250 °C. This is corroborated by the selective area electron diffraction (SAED) patterns (shown in insets of Figure 5.3 (b) & (c)) showing a diffuse ring and a set of sharp diffraction rings for films synthesized at 250 °C and 450 °C, respectively. This confirms the predominant amorphous and crystalline nature for the two types of films as stated earlier.

The chemical composition and electronic structure of the films were analyzed by using X ray photoelectron spectroscopy (XPS). Shown in Figure 5.2 (b) are the detailed XPS spectra of the S2p region. The S2p region for films synthesized at 450 °C shows the doublets of S^{2-} $2p_{1/2}$ and $2p_{3/2}$ peaks with binding energy positions at 163.5 eV and 162.3 eV, respectively which is in accordance with the literature for MoS_2. However, interestingly, in the case of the film synthesized at 250 °C, there exist two doublets which indicates that the S atoms near the surface exist in multiple oxidation states in the form of S^{2-} and S_2^{2-} species. The binding energies of the $2p_{1/2}$ and $2p_{3/2}$ peaks which appear at 164.6 eV and 163.4 eV, respectively represent the S_2^{2-} species. The presence of S_2^{2-} species in amorphous MoS_x films has been reported by several groups and it can either have a terminal or bridging structure with the formulation $Mo^{IV}(S^{2-})$ (S_2^{2-}).[15, 16] The ratio between S^{2-} and S_2^{2-} species is evaluated to be ~1.3 which is comparable with the literature.[6, 9] Note that the presence of S_2^{2-} species in amorphous MoS_x has been demonstrated to play a major role in enhanced HER performance which in some reports is believed to serve as active sites for hydrogen evolution.[6, 9, 17]

For the Mo3d region, we did not find any apparent difference between films synthesized at 250 °C and 450 °C except a slight shift in binding energies of Mo^{4+} $3d_{5/2}$ core electrons for the latter case (228.8 eV vs 229.1 eV). The detailed spectra of the Mo3d region for films synthesized at 250 °C and 450 °C are given in Figure A.5.1 (a) (Appendix) which shows the doublet corresponding to MoS_2 (Mo^{4+}) in combination with a small fraction of Mo^{5+} and Mo^{6+} indicating the surface oxidation of the sample, most likely due to the exposure to ambient air. The oxygen content remains below 2% which demonstrates the chemically pure nature of the molybdenum sulphide films.

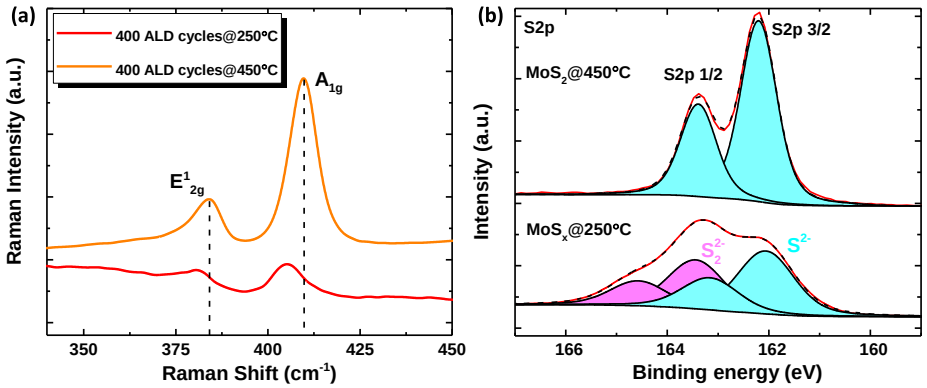


Figure 5.2 (a) Raman spectra showing the characteristic Raman vibration peaks (i.e. E^1_{2g} and A_{1g}) for the films synthesized at 250 °C and 450 °C, respectively. The weak and broad peaks for the sample prepared at 250 °C indicate towards the predominant amorphous nature of films. (b) XPS spectra of the S2p region for films synthesized at (bottom) 250 °C and (top) 450 °C. For the film synthesized at 250 °C, two doublet peaks corresponding to S_2^- and S_2^{2-} species appear.

Noticeably, we evaluated the S/Mo ratios of 2.26 and 1.70 for the films synthesized at 250 °C and 450 °C respectively, which clearly shows the possibility to tune the stoichiometry of MoS_x films by PEALD in a facile way. Furthermore, the valence band spectra for two films (shown in Figure A.5.1 (b) of Appendix) clearly differs indicating towards the differences in their electronic structure which might also play a role in HER performance. This tuning of chemical and electronic structure of MoS_x films thus imparts a favourable chemistry for improved HER performance for films synthesized at 250 °C and establishes our PEALD process as an efficient tool to prepare electrocatalysts with high HER performance.

Although XPS is a very informative technique, it only probes the very first nanometers of a surface. Therefore, in order to gain further insight into the bulk structure of PEALD synthesized films, we used extended X-ray absorption fine structure spectroscopy (EXAFS). This technique provides information about the local bonding environment and can determine short-range (local) order parameters such as interatomic distances in either crystalline or amorphous materials. To understand the difference between the bulk structure of the films synthesized at 250 °C and 450 °C, we probed the GC samples coated with both types of films (400 ALD cycles each).

Figure 5.3 (a) shows the Fourier transform magnitude (FTM) of EXAFS data for both cases. It is worth mentioning that for MoS_2 synthesized at 450 °C, two main peaks (seen at ~1.98 and 2.74 Å) represent the Mo-S and Mo-Mo nearest neighbours corresponding to actual distances of 2.4 Å and 3.1 Å respectively, which is in accordance with the published reports.[18] However, in case of MoS_x synthesized at 250 °C, an additional shoulder (~1.27 Å) is observed adjacent to the main Mo-S peak, which might be attributed to a distorted Mo-S bond with interatomic distance of 1.7 Å . In literature, this additional peak has also been observed for amorphous MoS_x films containing considerable oxygen content.[18] In our case, however, the XPS surface scan shows very low oxygen content in MoS_x films (< 2%) which implies that the bulk should have even lower oxygen content. And since EXAFS reflects the bulk information, it can therefore be argued that the additional peak in the FTM plot may correspond to Mo-S rather than Mo-O bond. The k^2 weighted average plot and the extracted parameters (interatomic distances, coordination numbers *etc.*) from EXAFS data are given in Figure A.5.2 and Table A.5.1 respectively. Overall, we believe that the presence of the distorted Mo-S bond in MoS_x films might also have a role in their higher HER performance, however, a detailed investigation is required in this direction to gain further insight which is beyond the scope of the present work.

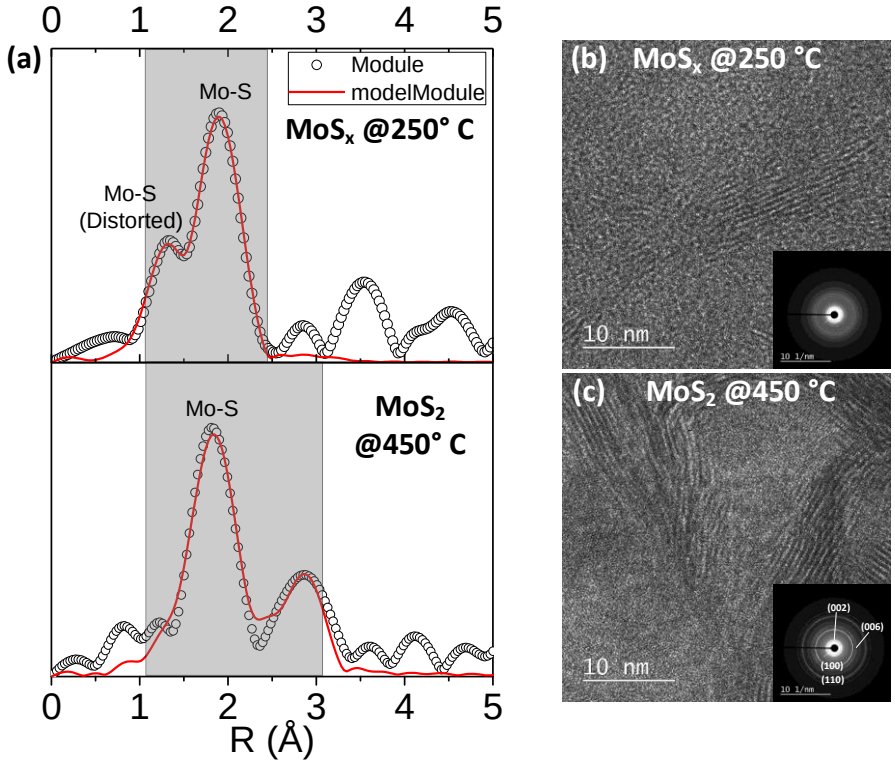


Figure 5.3 (a) Magnitude of the Fourier transform of the EXAFS on GC substrates for (top) PEALD synthesized MoS_x film at 250 °C and (bottom) PEALD synthesized MoS_x films at 450 °C. These plots essentially represent the radial distribution functions around the Mo atoms in the films. The extra shoulder observed in the former case is ascribed to the existence of distorted Mo-S bond in the predominantly amorphous MoS_x films. (b) and (c) Top planar TEM images for films synthesized at 250 °C and 450 °C. The insets show the corresponding SAED patterns.

Next, CFP was used as a supporting substrate for the amorphous MoS_x films, as the HER performance can be further improved due to the porous nature of CFP leading to a large electrochemically active surface area.[19] We performed a series of depositions at 250 °C by varying the number of ALD cycles on CFP substrates. Figure 5.4 (a - e) displays the top planar SEM images of CFP substrates coated with MoS_x prepared by varying number of ALD cycles (100 - 800). From Figure 5.4 (a), it can be observed that very few features are present on the 100 cycles substrate which might be attributed to poor nucleation of MoS_x film on CFP due to its hydrophobic (graphitic like) structure.

As the number of ALD cycles are increased to 200, the density of the granular features also increases (Figure 5.4 (b)). From this point onwards, with increasing number of ALD cycles (400 - 800), while the density and size of features increase, the film morphology eventually appears flake-like (Figure 5.4 (c - e)).

The HER activity of CFP substrates coated with MoS_x prepared by varying the number of ALD cycles and hence different MoS_x loading was assessed. Figure 5.4 (f) shows the polarization curves for MoS_x coated CFP substrates. The overall current density in case of CFP is higher than of GC (for 400 cycles: 38.8 mA/cm^2 vs 13.1 mA/cm^2 @300mV) probably due to its larger catalytically active surface area. The sample with the lowest number of cycles (100) exhibits low current density which might be related to the poor nucleation of MoS_x film as discussed above. The other samples exhibited a high current density at low overpotential. Table 6.1 shows the overpotentials required to reach a current density of 10 mA/cm^2 which are comparable to the previous reports for efficient amorphous MoS_x as electrocatalyst.[4, 6, 8, 9] Furthermore, Figure 5.4 (g) shows the Tafel plots presenting the Tafel slopes for CFP substrates coated with MoS_x prepared by varying ALD cycles. The value of Tafel slopes lie in the range 40 - 48 mV/dec which suggests a Volmer - Tafel type of mechanism.

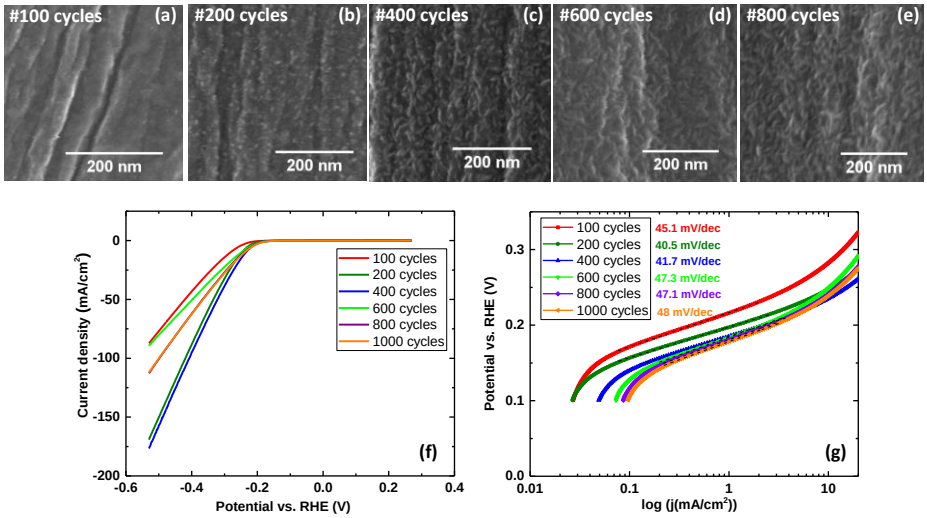


Figure 5.4 (a - e) SEM top planar view images of MoS_x films with varying number of ALD cycles on CFP substrates. (f) Cathodic polarization curves as measured by LSV for MoS_x coated CFP substrates. (g) Tafel plots showing Tafel slopes in the range of 40 - 48 mV/dec.

Another widely used metric to measure the electrochemical reaction at equilibrium (η = 0) is the exchange current density (j_0). The value of j_0 is useful to evaluate the HER activity and generally depends on the Gibbs free energy of the hydrogen adsorption for a HER catalyst. Table 5.1 displays the values of j_0 for MoS_x coated CFP. It is observable that the values of j_0 steadily increase (1 - 1.6 μA/cm^2) with high number of ALD cycles most likely due to increase in electrochemically active surface area (A_e). So, in order to estimate the values of A_e, we determined the double-layer capacitance (C_{dl}) by using cyclic voltammetry (Figure A.5.3 (a) in Appendix). The extracted values of C_{dl} are also shown in Table 5.1. Several groups report the C_{dl} of MoS_2 in the form of a flat thin film to be ~60 μF/cm^2.[4, 20] This implies that up to 200 ALD cycles, the film coverage most likely remains partial due to the poor nucleation as described earlier. Furthermore, the A_e values for the MoS_x coated CFP reaches as high as ~ 3.5 times (for 1000 ALD cycles) as compared to the geometrical area which explains its higher electrochemical activity as compared to GC substrates. It is to be noted that the CFP sample with 1000 ALD cycles exhibits the highest j_0 and C_{dl} values which can be ascribed to a low value of charge transfer resistance as measured by electrochemical impedance spectroscopy (EIS). Figure A.5.3 (b) (in Appendix) shows the Nyquist plots as measured by EIS for MoS_x coated CFP substrates. From this plot, the lowest charge transfer resistance value of 0.76 Ω was evaluated for the CFP sample with ALD 1000 cycles as compared to samples with 600 (1.77 Ω) and 800 ALD cycles (1.46 Ω) respectively.

Table 5.1 The key figures of merit for MoS_x coated CFP substrates.

ALD cycles	Overpotential (η) @ 10 mA/cm^2 (mV)	Exchange current density (j_0) (μA/cm^2)	Double layer capacitance (C_{dl}) (μF/cm^2)
100	283.2	1.03	12.4
200	247.9	1.04	30.4
400	235.1	1.08	86
600	249.0	1.38	99
800	241.6	1.45	159.5
1000	239.4	1.57	215

5.4 Conclusion

In conclusion, we have demonstrated that PEALD is an efficient method to tune the structural properties of molybdenum sulphide films which subsequently results in high HER performance. We have performed a comprehensive comparison between the

electrocatalytic activities of the predominantly amorphous and nanocrystalline molybdenum sulphide films synthesized by PEALD at 250 °C and 450 °C, respectively. The predominantly amorphous films exhibit a higher HER performance which most likely stems from their different structural and chemical properties as compared to the nanocrystalline films. The structural difference between two types of films is highlighted by XPS and EXAFS techniques. The XPS studies show the presence of S_2^{2-} species whereas the EXAFS analysis reveals a distinct peak probably corresponding to a distorted Mo-S bond in the films synthesized at 250 °C. These structural differences might have a profound effect on HER performance of predominantly amorphous MoS_x films and render them better electrocatalysts than nanocrystalline films. Altogether, our work confirms other studies and ascertains ALD, owing to its precise thickness control and ability to yield highly conformal films on high surface area substrates, as a well suited tool to synthesize emerging transition metal dichalcogenides based electrocatalysts.

Acknowledgements

This work is part of the program "CO_2-neutral fuels" (project 13-CO26) of the late Foundation for Fundamental Research on Matter (FOM, now NWO-I), which was financially supported by the Netherlands Organization for Scientific Research (NWO). This research program was co-financed by Shell Global Solutions International B.V. Miao Yue and Marco Etzi Coller Pascuzzi (Eindhoven University of Technology, TU/e) and ESRF beamline BM26A (DUBBLE) staff are acknowledged for the support during EXAFS measurements.

Appendix

A.5.1 XPS analysis

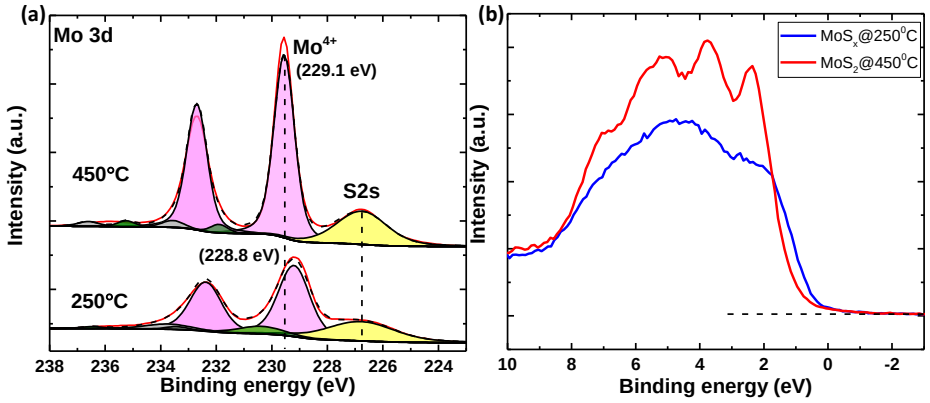


Figure A.5.1 (a) Detailed XPS spectra for Mo 3d region for film synthesized at 250 °C and 450 °C respectively. (b) Valence band spectra for films synthesized at 250 °C and 450 °C, respectively. An apparent difference between two films is visible.

A.5.2 EXAFS analysis

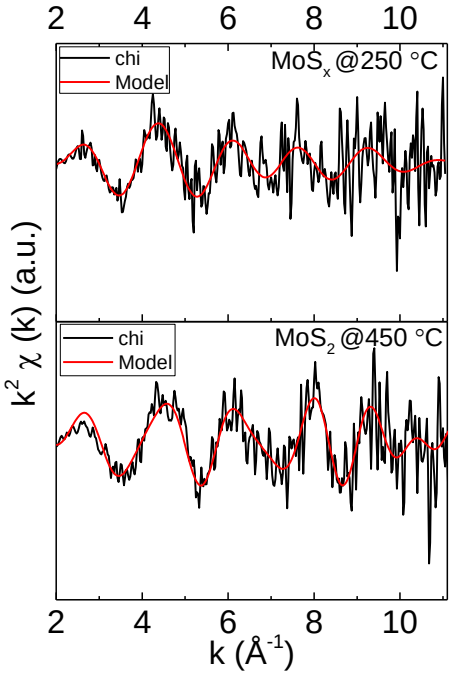


Figure A.5.2 Mo K EXAFS ($k^2.\chi(k)$) for PEALD synthesized (top) MoS_x film at 250 °C (bottom) MoS_2 film at 450 °C, respectively.

Table A.5.1 Key parameters used for fitting the EXAFS data and the extracted values of various parameters like local bonding environment for Mo and coordination number (CN).

Sample	R factor (%)	N_{idp} & k-range fit	N_{var} & R-range fit	Path	CN	R (Å)	σ^2 ($Å^2$)	ΔE (eV)	±CN	±R (Å)	$\pm\sigma^2$($Å^2$) $x10^{-3}$	±ΔE (eV)
2H MoS2 @ 450°C	13.5	13.98 2 – 11.18	7 1.08 – 3.08	Mo - S	4.28	2.385	0.003	-3.20	0.09	0.003	0.093	0.17
	13.5	13.98 2 – 11.18	7 1.08 – 3.08	Mo - Mo	3.06	3.154	0.003	-3.20	0.05	0.015	0.0958	0.17
MoS_x @250°C	3.64	9.92 2 - 11.06	7 1.06 – 2.43	Mo - S	4.60	2.443	0.008	1.69	0.02	0.002 0.03	0.196	0.08
	3.64	9.92 2 - 11.06	7 1.06 – 2.43	Mo – S (distorted)	0.36	1.775	0.001	-1.69	0.03	0.003	0.000	0.08

A.5.3 CV and EIS measurements

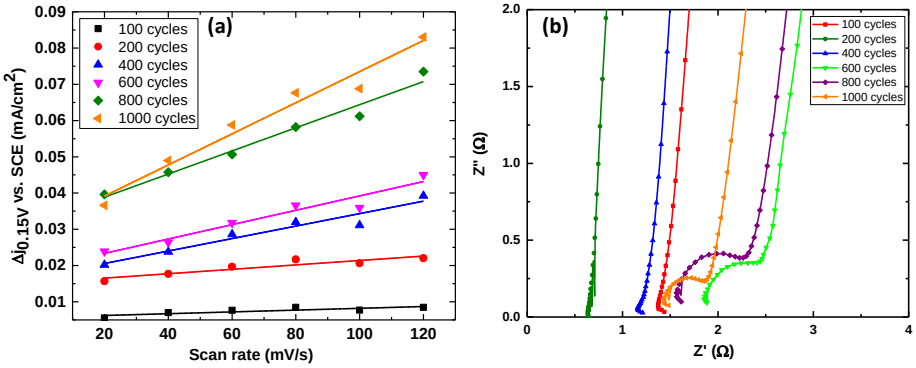


Figure A.5.3 (a) Plots for current density as a function of potential scan rates for MoS_x coated (left) CFP substrates from cyclic voltammetry. The data points for each number of cycles are fitted to a linear curve. The slopes of linear curve correspond to $2*C_{dl}$ values. (b) Nyquist plots for current density as a function of potential scan rates for MoS_x coated CFP substrates as measured by EIS technique.

References

1. T. F. Jaramillo, K. P. Jørgensen, J. Bonde, J. H. Nielsen, S. Horch and I. Chorkendorff, *Science*, 2007, **317**, 100.
2. S. M. Tan, A. Ambrosi, Z. Sofer, Š. Huber, D. Sedmidubský and M. Pumera, *Chemistry – A European Journal*, 2015, **21**, 7170-7178.
3. J. D. Benck, T. R. Hellstern, J. Kibsgaard, P. Chakthranont and T. F. Jaramillo, *ACS Catalysis*, 2014, **4**, 3957-3971.
4. J. D. Benck, Z. Chen, L. Y. Kuritzky, A. J. Forman and T. F. Jaramillo, *ACS Catalysis*, 2012, **2**, 1916-1923.
5. D. Merki, S. Fierro, H. Vrubel and X. Hu, *Chemical Science*, 2011, **2**, 1262-1267.
6. R. Bose, S. K. Balasingam, S. Shin, Z. Jin, D. H. Kwon, Y. Jun and Y.-S. Min, *Langmuir*, 2015, **31**, 5220-5227.
7. H. Vrubel and X. Hu, *ACS Catalysis*, 2013, **3**, 2002-2011.
8. S. Shin, Z. Jin, D. H. Kwon, R. Bose and Y.-S. Min, *Langmuir*, 2015, **31**, 1196-1202.
9. D. H. Kwon, Z. Jin, S. Shin, W.-S. Lee and Y.-S. Min, *Nanoscale*, 2016, **8**, 7180-7188.
10. A. Sharma, M. A. Verheijen, L. Wu, S. Karwal, V. Vandalon, H. C. M. Knoops, R. Sundaram, J. P. P. Hofmann, W. Kessels and A. A. Bol, *Nanoscale*, 2018, DOI: 10.1039/C8NR02339E.
11. R. Ding, Y. Liu, M. Wang, L. Qin, X. Cui, C. Wang, L. Wang and B. Lv, *Electrochimica Acta*, 2017, **248**, 20-28.
12. D. Y. Chung, S.-K. Park, Y.-H. Chung, S.-H. Yu, D.-H. Lim, N. Jung, H. C. Ham, H.-Y. Park, Y. Piao, S. J. Yoo and Y.-E. Sung, *Nanoscale*, 2014, **6**, 2131-2136.

13. Z. Jin, S. Shin, D. H. Kwon, S.-J. Han and Y.-S. Min, *Nanoscale*, 2014, **6**, 14453-14458.
14. G. L. Frey, R. Tenne, M. J. Matthews, M. S. Dresselhaus and G. Dresselhaus, *Physical Review B*, 1999, **60**, 2883-2892.
15. T. Weber, J. C. Muijsers and J. W. Niemantsverdriet, *The Journal of Physical Chemistry*, 1995, **99**, 9194-9200.
16. S. J. Hibble and G. B. Wood, *Journal of the American Chemical Society*, 2004, **126**, 959-965.
17. C.-L. Hsu, Y.-H. Chang, T.-Y. Chen, C.-C. Tseng, K.-H. Wei and L.-J. Li, *International Journal of Hydrogen Energy*, 2014, **39**, 4788-4793.
18. B. Lassalle-Kaiser, D. Merki, H. Vrubel, S. Gul, V. K. Yachandra, X. Hu and J. Yano, *Journal of the American Chemical Society*, 2015, **137**, 314-321.
19. A. B. Laursen, P. C. K. Vesborg and I. Chorkendorff, *Chemical Communications*, 2013, **49**, 4965-4967.
20. J. Kibsgaard, Z. Chen, B. N. Reinecke and T. F. Jaramillo, *Nature Materials*, 2012, **11**, 963.

6

Plasma enhanced atomic layer deposition enabled uniform large area patterned growth of high quality MoS_2*

The large scale production of transition metal dichalcogenides including MoS_2 is an active area of research. Primarily, the precise thickness control and high quality over large area are crucial aspects for realization of TMDs based device applications. Here, we demonstrate the synthesis of high quality MoS_2 thin films over large area using the combination of low temperature plasma enhanced atomic layer deposition (PEALD) and high temperature thermal sulphurization. As an inherent advantage of ALD, we have achieved precise thickness control ranging between a monolayer to few-layered MoS_2 in combination with an excellent quality as demonstrated by transmission electron microscopy analysis. Furthermore, a uniform film and exceptional conformality over 3-D structures are also exhibited. Additionally, the low temperature PEALD process has been exploited to obtain patterned growth of MoS_2 on device ready SiO_2/Si substrates eliminating any etching and transfer step. Finally, a prototypical field effect transistor device based on MoS_2 channel layer has been demonstrated. Overall, this method presents a supplementary path to the range of approaches adopted in literature for obtaining patterned growth of MoS_2 targeting towards future generation devices and integrated circuits.

*A. Sharma, R. Mahlouji, L. Wu, M. A. Verheijen, V. Vandalon, S.H.G. Bloebaum, J. P. Hofmann, W. M. M. (Erwin) Kessels and A. A. Bol, *to be submitted*

6.1 Introduction

The layered two-dimensional (2-D) transition metal dichalcogenides (TMDs) offer an exciting platform for myriad optoelectronic applications owing to their ultra-thin bodies and extraordinary broad spectrum of electrical, mechanical, and optical properties.[1-3] The integration of atomically thin TMDs also gives rise to extremely interesting new physical phenomena, such as interband tunneling, optospintronics *etc.*[4, 5] Amongst the family of TMDs, MoS_2 is one of the most studied materials due to its high earth abundance, stability in ambient and amenability to get aligned in heterostructure based architectures.[6] A massive effort has been put into studying various properties of exfoliated MoS_2 on the lab scale,[7-11] however, the lack of homogeneous spatial distribution and low yield hinders the scalable production of 2-D layers with the exfoliation method. Therefore, there is still a quest for developing scalable growth techniques capable of producing high quality films with precise thickness control over large areas. To address this, bottom-up synthetic methods have been employed to produce 2-D TMDs over large areas. Amongst these methods, chemical vapor deposition (CVD) is the most widely accepted technique,[12-15] and is capable of producing high quality material with large grain size, yet it fails to offer an accurate control over thickness and uniformity. Moreover, the direct large area production of high quality TMDs on device-ready substrates with CVD still remains a challenge, which is one of the foremost prerequisites for realizing high performance electronic devices. Generally, the CVD grown TMDs are transferred to a relevant substrate using a polymer-based transfer technique which often results in polymer contamination causing interface degradation. Subsequently, the device fabrication proceeds with post patterning of transferred material involving usage of a masking layer (usually photo/electron beam resists), followed by an etching step which might further exacerbate the magnitude of degradation. One of the possible solutions to evade this issue is the patterned growth of TMDs directly on device-ready substrates which will not only reduce the device fabrication steps (i.e. typical reactive ion etching of TMDs), but also minimize the degree of possible polymer contamination inferred by the transfer process.

In this work, we demonstrate an approach to achieve transfer-free patterned growth of 2-D MoS_2 directly on technologically relevant SiO_2/Si substrates. Our approach uses a combination of top-down nanoscale patterning with a bottom-up chemical method. The methodology combines a low temperature plasma-enhanced atomic layer deposition

(PEALD) and subsequent thermal sulphurization which eliminates the need of film transfer and any reactive ion etching step to achieve patterned growth of high quality 2-D MoS_2. The patterned growth of TMDs is an important aspect for realizing advanced electronic device architectures as manifested by recent widespread attention in the literature. The majority of work available in the literature is based on either surface functionalization or use of pre-patterned seeded areas. The first methodology relies often on the selective blocking of TMD growth by using pristine graphene or hydrophobic polymers.[16-18] For example, Ling *et al.* have demonstrated that during CVD , pristine graphene effectively blocks the growth of MoS_2 owing to the lack of surface dangling bonds. Conversely, a hydrophilic aromatic molecular seed i.e. perylene-3,4,9,10-tetracarboxylic acid tetrapotassium salt (PTAS) promotes the growth of MoS_2. In this way, the seamless stitching of graphene and MoS_2 has been achieved to realize lateral heterostructures.[16] In a similar approach, the surface modification by using a hydrophobic polymer functional layer (PFL) has been demonstrated as a method to preclude TMD nucleation and growth.[18] The other approach to achieve patterned growth of MoS_2 is the pre-patterning of parent material and subsequent sulphurization which can produce contamination free, high quality MoS_2 films with pristine surfaces. For instance, Han *et al.* have demonstrated the synthesis of MoS_2 monolayer islands at pre-defined locations by sulphurization of lithographically patterned bead shaped MoO_3 *seeds* prepared by physical vapor deposition.[19] This approach has been referred to as *seeded growth* of MoS_2 monolayers. However, small regions of multilayer material and poor pattern fidelity (irregularity in shape of flakes) were observed using this approach which is an undesirable attribute for practical applications. Young *et al.* have used SiN stencils to produce resist free, templated Mo films which are subsequently sulphurized to yield a MoS_2 monolayer on controlled locations with sub-micron feature sizes on sapphire substrates.[20] Although, high quality and layer controlled MoS_2 films are produced by this technique, the preparatory need of the focused ion beam to pattern SiN membranes increases the overall complexity of the process. Additionally, the pattern scaling remains limited due to the lateral dimensions of the SiN membrane. An interesting approach by Song *et al.* based on pre-patterning of an Au-Mo alloy as parent material and subsequent thermal sulphurization enabled the easy transfer of patterned few-layered MoS_2 to arbitrary substrates.[21] However, clustering of metal source and co-existence of unreacted Au-Mo alloy after sulphurization might deteriorate the opto-electronic properties. Overall, there still exists a need for a facile synthesis method to produce patterned MoS_2 with precise thickness control on a wafer scale in combination

with high pattern fidelity. Herein, we attempt to fill this gap and demonstrate the scalable and patternable synthesis of MoS_2 by adopting a combination of a top-down nanoscale patterning technique with a bottom-up chemical method. We employ electron beam lithography (EBL) to prepare islands of MoO_x (deposited by PEALD) which serve as parent material for the controlled growth of mono- to- few layered polycrystalline MoS_2 at predefined locations on SiO_2/Si substrates. The use of PEALD offers several advantages over other bottom-up synthesis techniques such as wafer-scale uniformity, precise film thickness control, high conformality and low temperature processing. In this work, we have exploited the low temperature processing (50°C) to obtain direct patterning of the parent material (MoO_x). Notably, we show that our low temperature PEALD process is compatible with the conventional e-beam resist lift-off technique enabling high pattern fidelity and eliminating the need of any etching step. The patterned MoO_x islands are then subjected to thermal sulphurization at 900°C using H_2S + Ar gas to yield high quality, large area MoS_2 films directly on device-ready substrate with omission of transfer process.

In this chapter, we first demonstrate the excellent control over MoS_2 thickness which is attained in a facile way just by tuning the number of ALD cycles for the parent material. This control is clearly reflected in the Raman and PL spectra of the resulting films. Next, the large area uniformity upto wafer scale and high conformality on 3-D high aspect ratio (HAR) nanostructures enabled by PEALD are displayed. Further, the process flow for achieving patterned growth of MoS_2 and the related results are discussed. Finally, a field-effect transistor (FET) device based on the patterned MoS_2 as channel layer is exhibited.

6.2 Experimental section

ALD specifications

The MoO_x thin films were deposited at 50°C in an Oxford Instruments FlexAL™ ALD reactor on 4" Si wafers with a thermally grown 90 nm or 450 nm thick oxide layer on top. The Mo precursor employed was $[(NtBu)_2(NMe_2)_2Mo]$, (98%, Strem Chemicals) and was contained in a stainless-steel canister which was heated to 50°C. At this temperature, the vapor pressure of the precursor is reported to be 0.13 Torr.[22] The delivery lines were kept at 90°C to avoid condensation of the precursor while the reactor walls were heated to 50°C. For the precursor delivery to the deposition chamber,

a 100 sccm Ar (>99.999% purity) bubbling flow was employed. An intermediate Ar purge step with 100 sccm of Ar flow was applied after each precursor and plasma exposure steps. As the co-reactant, an O_2 plasma (50 sccm) gas generated in an inductively coupled plasma (ICP) source was used. The plasma power was 100 W with a reactor pressure of 6.6 mTorr during the plasma step. The ALD recipe was established with the first half cycle consisting of precursor dosing for 6 s followed by 6 s purge. The second half cycle used 8 s of plasma exposure with the same scheme for subsequent purge and pump as in the first half cycle. The film thickness evolution during deposition was monitored by *in-situ* spectroscopy ellipsometry (J.A. Woollam M2000F, 1.25 eV - 5 eV). The detailed characterization of the PEALD process at 50°C for MoO_x can be found in the previous work from our group.[23] For MoO_x films, a general oscillator model was used to analyze the thickness evolution during PEALD process. A combination of Tauc-Lorentz and Gaussian oscillators were used to account for the interband absorption and absorption inside the band gap at low photon energy (~1eV) respectively. The HfO_2 film as capping layer was deposited at 100 °C by a PEALD process using a combination of $HfCp(NMe_2)_3$, HyALD™ and O_2 plasma as the co-reactant. The detailed description of the process is given elsewhere.[24]

Thermal sulphurization

MoO_x thin films were sulphurized in a tube furnace at 900°C under atmospheric pressure. A combination of H_2S + Ar gas (10% H_2S) was used as sulphurization gas. The recipe for thermal sulphurization is shown in Figure A.6.1 (Appendix).

Patterning and device fabrication

The patterned MoS_2 films were obtained by using conventional EBL. Poly (methyl methacrylate) (PMMA) type A4 was used as e-beam resist. For PMMA layer, a Cauchy dispersion model for *in-situ* spectroscopic ellipsometry was used to extract the thickness values. Furthermore, for device fabrication, the patterned MoS_2 film (7-8 layers) was synthesized on 300 nm thick SiO_2/Si substrate using the process flow as described in the main text. The metal electrodes (10/100 nm Ti/Au) were fabricated by using e-beam evaporation. Electrical characterization was performed using a semiconductor probe station (Keithley 4200 SCS) under ambient conditions.

Characterization

Raman spectroscopy (RS) and photoluminescence (PL) spectroscopy measurements were performed with a Renishaw Raman microscope equipped with a 514 nm laser, integrated switchable gratings with 600 or 1800 lines/mm, and a CCD detector. For

each scan, 5 accumulations with acquisition time of 10 s were taken. Additionally, atomic force microscopy (AFM) was also employed to study the surface topology of the as-deposited films. The images were acquired at room temperature on Veeco dimension 3100 operated in tapping mode using Al coated Si tip (PointProbe Plus-NCHR) having a radius < 7 nm. Images were processed in Gwyddion software with OpenGL interface and RMS roughness was obtained statistically from a scan area of 500 x 500 nm^2. The patterned square islands before and after sulphurization process were characterized with a Zeiss Axio Imager 2 Optical microscope. To determine the elemental composition, X-ray photoelectron spectroscopy (XPS) was performed using a Thermo Scientific K-alpha spectrometer (Thermo Fisher Scientific, Waltham, MA) equipped with a monochromatic Al Kα X-ray radiation source (hν = 1486.6 eV). For the XPS analysis, a 400 µm diameter spot was used and photoelectrons were collected at a take-off angle of 60°. The samples were neutralized during the XPS analysis using an electron flood gun in order to correct for differential or non-uniform charging. All peaks in the XPS survey scans are referenced to the binding energy of the C1s peak of adventitious carbon (284.8 eV) for charge correction and quantification of the survey scans have been performed using Avantage software. The selectivity of MoS_2 line bars was determined by energy dispersive X-ray spectroscopy (EDX) with an EDAX UMSII EDX spectrometer integrated in a scanning electron microscope (FEI Nova 600i DualBeam system). The film microstructure was determined by HRTEM analysis using a probe corrected JEOL ARM 200F operated at 80 kV, using both the bright field TEM mode and the high angle annular dark field (HAADF) scanning TEM mode. Atomic resolution imaging of the poly-crystalline MoS_2 film was performed in HAADF-STEM mode using a camera length of 20 cm; at this camera length, some diffraction contrast is present, enhancing the visibility of the crystal dimensions. For the top planar view images, MoO_x films were grown on SiN_x TEM windows, coated with ~5 nm ALD SiO_2, which were subsequently thermally sulphurized at 900°C. Selected area electron diffraction (SAED) patterns were acquired from a 1.3 µm diameter area on each sample. The conformality of MoS_2 ALD process was determined on substrate coupons with high aspect ratio (HAR) nanostructures. These HAR nanostructures were created by etching PECVD grown SiO_2 on a Si wafer. The SiO_2 nanostructures were then coated with a SiN_x layer deposited by high-temperature CVD, onto which an SiO_2 thin film was deposited using ALD. Prior to focused ion beam (FIB) sample preparation, the MoS_2 sample was coated with a layer of spin-on epoxy to fill the remaining gaps in the trenches and to protect the film from curtaining damage during the subsequent lift-out FIB sample preparation.

6.3 Results and Discussion

6.3.1 High quality, layer controlled 2-D MoS_2 films

The MoO_x films with different thicknesses were obtained by varying number of ALD cycles (10 - 60) during PEALD process. These films were then thermally sulphurized to attain final MoS_2 films. The thicknesses of initial MoO_x (before sulphurization) films as assessed by *in-situ* spectroscopic ellipsometry during PEALD process are given in the Appendix (Table A.6.1). The thickness and crystallinity of post sulphurized MoS_2 films were characterized by Raman spectroscopy. Figure 6.1 (a) shows the progression of Raman vibrational modes with increasing thickness of the MoS_2 film on SiO_2/Si substrates. The two characteristic vibrational modes (i.e. A_{1g} and E^1_{2g}) are clearly visible for all the samples investigated. The frequency difference (Δ) between two vibrational modes generally increases with increasing number of layers present in the MoS_2 film and thus is used as an indicator to determine the number of layers.[25] In our case, 'Δ' increases monotonically (20.6 cm^{-1} - 26.2 cm^{-1}) with increasing number of MoO_x ALD cycles (from 10-60 cycles) which indicates the formation of monolayer to thick film (~ 7-8 layers). By controlling the number of MoO_x ALD cycles, a systematic control over the thickness of the final MoS_2 films is attained. It is noteworthy that the value of 'Δ' increases in a continuous manner with increasing number of ALD cycles, i.e. a value of 21.1 cm^{-1} is obtained (for 12 cycles) between formation of a monolayer (20.6 cm^{-1}) to bilayer (22.3 cm^{-1}). This is a consequence of the typical sub-monolayer film growth per ALD cycle. This is unlike any other deposition technique such as CVD where such intermediate stage between a monolayer and bilayer is not observable. Furthermore, it has been reported that the structural defects in the MoS_2 film can be quantified by assessing a low frequency peak at ~227 cm^{-1} in the Raman spectrum. This peak is assigned to the longitudinal acoustic phonons at the M point of the Brillouin zone and denoted as LA(M)).[26, 27] The Raman spectra in Figure 6.1 (a) show the absence of the LA(M) mode in all the samples investigated, pointing towards the high quality of the films obtained after thermal sulphurization. Moreover, the full width half maximum (FWHM) values of the in-plane vibrational peak (E^1_{2g}) for all samples remain in the range of 4.6 cm^{-1} - 5.0 cm^{-1}, which is comparable with typical CVD grown material,[28, 29] reaffirming the high quality of our samples. The photoluminescence (PL) results are in line with the Raman analysis and the corresponding spectra are shown in Figure 6.1 (b). A strong signal at ~ 674 nm and a weak shoulder at ~ 623 nm are observed for a monolayer (10 ALD cycles) which corresponds to the A and B excitonic peaks

associated with the direct band gap transitions.[30] The PL intensity subsequently becomes weaker with increasing number of layers in the MoS_2 films owing to the transition to the indirect band gap in thick MoS_2.[9]

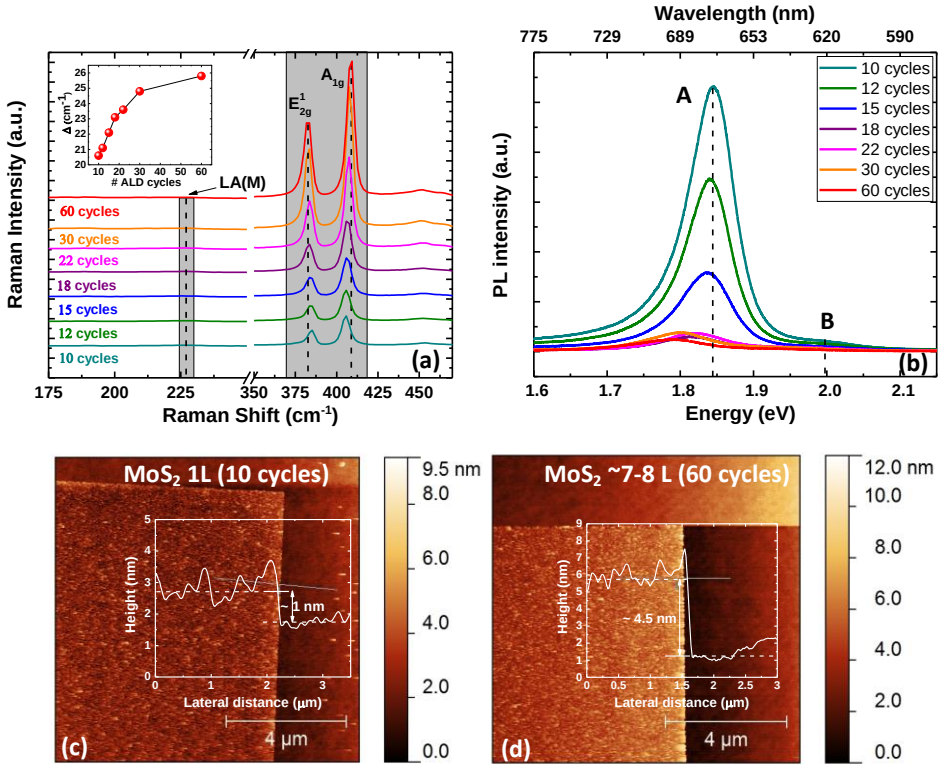


Figure 6.1 (a) Raman spectrum shows the progression of two vibrational modes with increasing thickness of MoS_2 film. The regions with two predominant vibrational modes and LA (M) mode at low Raman frequency region (~227 cm^{-1}) are highlighted in grey. The inset shows the increasing frequency difference (Δ) as a function of increasing film thickness (increasing number of ALD cycles for parent MoO_x film). (b) Photoluminescence (PL) spectrum shows strong emission for a monolayer (10 cycles) associated with the A and B exciton at 1.85 eV and 2.0 eV, respectively. The intensity thereafter reduces as the thickness of MoS_2 film increases with the increasing number of ALD cycles for parent MoO_x films. (c, d) AFM images of the polycrystalline mono and few-layered MoS2 films are presented. The insets in both images show the measured height of 1 nm and 4.5 nm for the mono and few-layered films respectively.

In order to further confirm the precise thickness controllability, atomic force microscopy (AFM) was used to measure the height of selective MoS_2 films. Figure 6.1 (c, d) shows the AFM images for the monolayer (10 ALD cycles) and few layered (60

cycles) samples respectively. The measured heights were ~ 1 nm and 4.5 nm respectively. The larger measured height of a monolayer (1 nm) than expected (0.65 nm) might be attributed to the effect of distinct tip-sample and tip-substrate interactions as reported in the literature.[31] Concurrently, the 4.5 nm (60 cycles) thick sample indicates 7-8 layers, which is in accordance with the Raman analysis (Δ = 25.8 cm^{-1}) and therefore confirms the precise thickness control achievable with ALD. The topography of the films was also studied using AFM. The corresponding images are shown in Figure A.6.2 (in Appendix) which reveals smooth polycrystalline films with roughness in the range between 0.2 - 0.3 nm which is comparable with the roughness of the underlying Si substrate.

The film crystallinity and microstructure were characterized by high resolution transmission electron microscopy (HRTEM) analysis. The cross-sectional HAADF-STEM image for few-layered (~8-9 layers) MoS_2 film (70 cycles) shown in Figure 6.2 (a) reveals the ordered in-plane oriented layers grown on SiO_2/Si substrate corroborating the high quality of the MoS_2 film. The STEM image shown in Figure 6.2 (c) allows to gain additional microstructural insights. The uniform surface coverage of polycrystalline MoS_2 film with grain size in the few to 50 nm range is clearly displayed. The polycrystalline nature of MoS_2 film is further confirmed by SAED (Figure 6.2 (c)) which shows the closed rings corresponding to randomly oriented nanodomains. The presence of the 110 and 010 rings and the absence of a 002 ring reflects the <002> texture of the film. Further, the HAADF-STEM image in Figure 6.2 (d) reveals the hexagonal arrangement of atoms, again displaying the in-plane orientation of the MoS_2 layers of the 2-H phase. An additional analysis of this image is presented in the Appendix (Figure A.6.3). The chemical composition of the films before and after sulphurization was examined by X-ray photoelectron spectroscopy (XPS). It is noteworthy to mention that the MoO_x films deposited at 50°C before sulphurization are sub-stoichiometric in nature. This is evident from a clearly observable shoulder on the Mo3d peak corresponding to oxygen vacancies in agreement with earlier reports.[32] After sulphurization, the oxidation state of the Mo in MoS_2 films was found to be predominantly Mo^{4+} based on the binding energy position for Mo3d peaks. The stoichiometry of the MoS_2 after sulphurization ranged between 2.0 - 2.2 for all samples which confirms the good quality of the films. A more comprehensive discussion of the XPS results, high-resolution spectra of Mo3d, S2p, O1s peaks with detailed peak assignments can be found in the Appendix (Figure A.6.4).

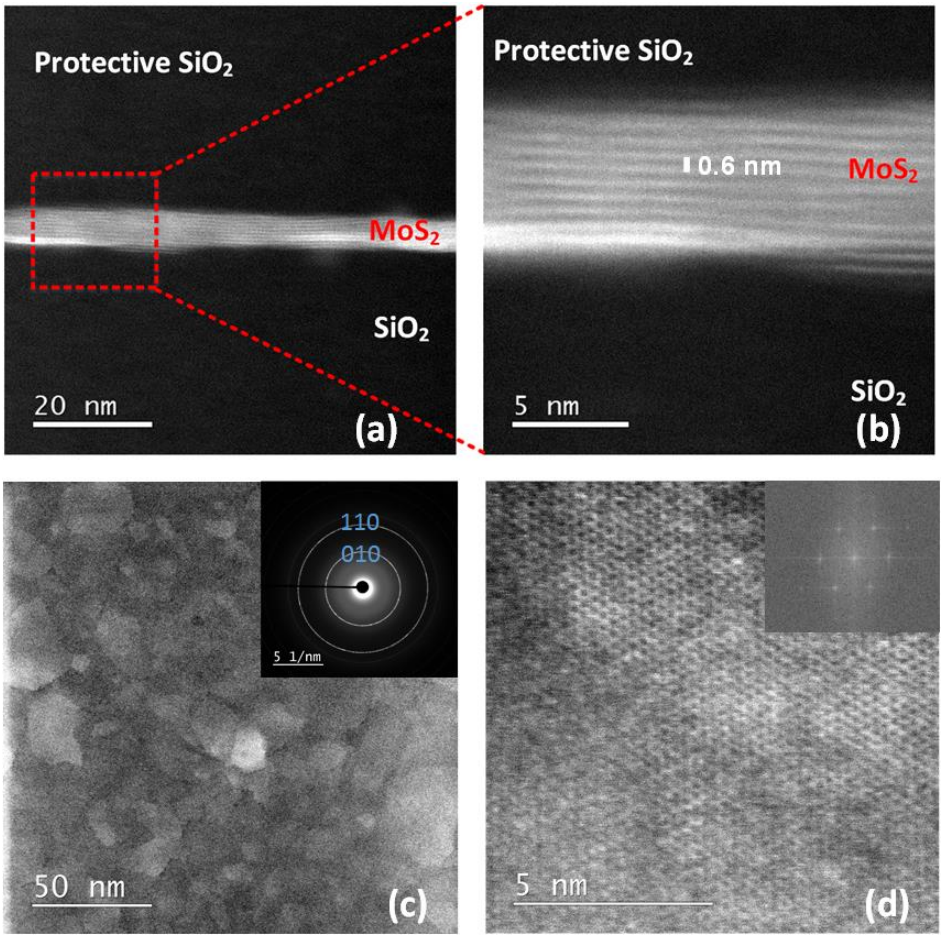


Figure 6.2 (a) Cross-sectional HAADF-STEM image showing a few layered (7-8 layered) MoS_2 film on SiO_2/Si substrate. (b) The magnified image clearly reveals the individual layers stacked on each other with interlayer distance of ~0.6 nm (as highlighted). (c) STEM image showing the uniform coverage of the polycrystalline MoS_2 film. The inset shows a selective area electron diffraction pattern from the same sample which confirms the polycrystalline nature of the film. (d) High resolution STEM image showing the hexagonal atomic arrangement and the corresponding FFT pattern (inset) clearly displaying the sixfold symmetry.

As mentioned earlier, ALD owing to its self-limiting nature is capable of producing films with wafer scale uniformity and high conformality on intricate structures. We therefore assessed both these attributes for our resultant MoS_2 films. In order to confirm the wafer scale uniformity of our process, a Raman line scan was performed over 9

points (1 cm apart) on a 10 cm wafer strip. Figure 6.3 (a) shows the Raman vibrational modes corresponding to measured points for a sample with 7-8 layers (60 ALD cycles). The consistent Raman peaks along the scanned region reveal the homogenous crystalline nature of the MoS_2 film. Furthermore, since the interference enhancement phenomenon affects both vibrational modes equally, we have plotted the integrated intensity ratio between two peaks ($I(E^1_{2g})/I(A_{1g})$) for samples with varying MoS_2 thickness over the 9 measured points (Figure 6.3 (b)).

The consistent intensity ratio over the measured points for the investigated samples with different thicknesses (i.e. 10 cycles, 30 cycles, 60 cycles) demonstrates both the high quality and large area uniformity of MoS_2 films.

The conformality of the films was investigated using high-aspect ratio (HAR) nano-sized trench structures with varying aspect ratios (depth = 394 nm and width = 44 - 650 nm) as shown in Figure 6.3 (c). It is evident that the 7-8 layered thick MoS_2 uniformly coats the trench structures. A magnified image of a trench structure (Figure 6.3 (d)) shows an excellent conformality on both the side walls and planar areas of the HAR structure. A markedly high conformality of 88% (planar area with respect to side walls) was evaluated for a trench structure with a final aspect ratio (AR) of 12 (AR = depth/width). For some next generation 3-D applications based on 2-D materials, this aspect might prove particularly valuable.[33] Based on the above results, it can be concluded that ALD enables a facile way of synthesizing high quality, layer controlled MoS_2 films in combination with high uniformity and excellent conformality over 3-D structures.

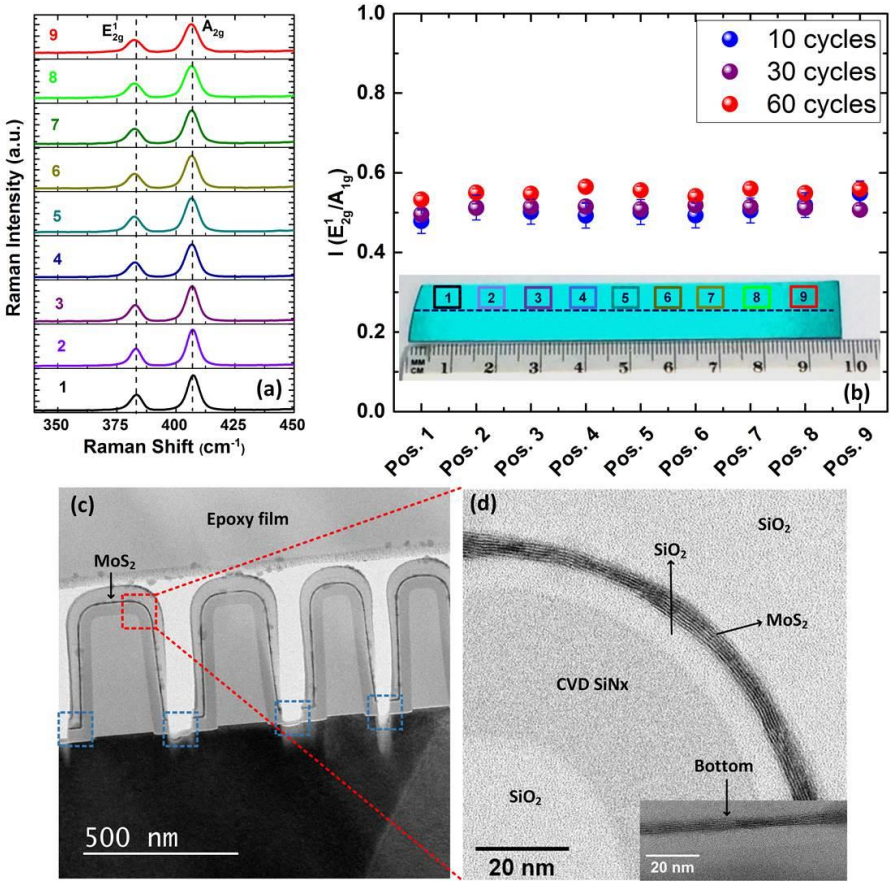


Figure 6.3 (a) The plot shows the homogenous Raman spectral features throughout the 9 different scanned areas on the wafer strip (~10 cm) which is shown as inset of (b). The resultant MoS_2 film is 7-8 layers in this case with 60 cycles of ALD processed for the parent MoO_x film. (b) A consistent intensity ratio between two Raman vibrational modes across the measured points for samples with varying number of ALD cycles confirms the uniform high quality film over large area. The wafer strip (~ 10 cm) with different measurement points is shown in the inset. (c) The cross-sectional TEM image shows the conformal MoS_2 coating on high-aspect ratio nanostructures. Note: The highlighted areas (----) were damaged during FIB preparation of the sample due to insufficient filling of voids by the protective epoxy film as shown. (d) The magnified image of a curved section from one of the trench structures clearly reveals the conformal coverage of layered MoS_2 on the planar surface and side wall and thus registering the conformal nature of our PEALD based approach. The inset shows the bottom planar part of the same trench structure where the similar conformal coverage of MoS_2 is obtained.

6.3.2 ALD enabled patterned growth of MoS_2 and device fabrication

As aforementioned, the MoO_x parent films were grown at low temperature, i.e. 50°C, by PEALD. The use of low temperature processing (in the first part of the process) in combination with the high temperature thermal sulphurization (second part) has ultimately led to the formation of high fidelity patterned MoS_2 films. A simplified scheme of the process flow which we used to obtain the patterned MoS_2 films is given in Figure 6.4 (a - f). As shown, firstly, the SiO_2/Si substrates are spin-coated with Poly (methyl methacrylate) (PMMA) and subsequently patterned using e-beam lithography (Figure 6.4 (a-b)). Thereafter, the MoO_x is deposited using low temperature PEALD which conformally covers the patterned regions and the surrounding PMMA as depicted in Figure 6.4 (c). Next, the resist and unwanted MoO_x are removed using the standard lift-off technique resulting in isolated MoO_x islands (Figure 6.4 (d)). These MoO_x islands are thermally sulphurized at 900°C (Figure 6.4 (e)) finally resulting in patterned MoS_2 squares (Figure 6.4 (f)).

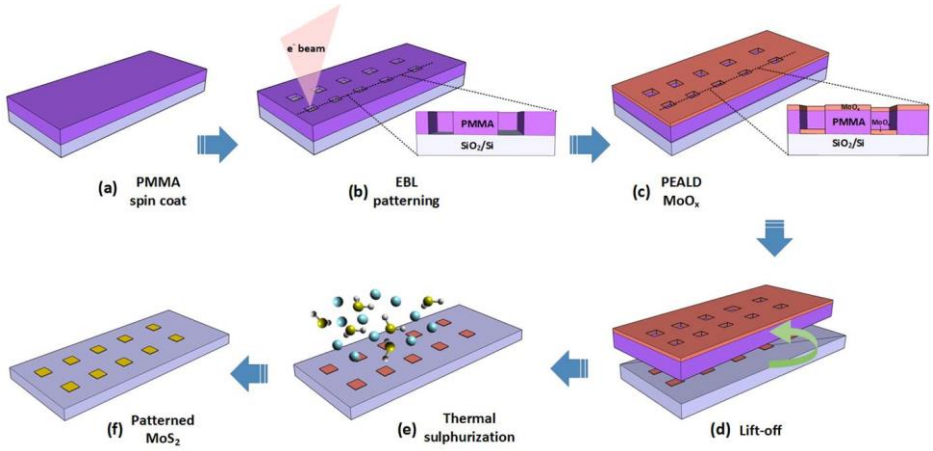


Figure 6.4 (a-f) The scheme shows the process flow for the ALD enabled patterned growth of large area MoS_2. The cross-sections shown in (b), (c) as insets illustrate the film profiles after EBL patterning and PEALD process respectively.

It is to be noted that any residual PMMA remaining after the lift-off process is removed in the subsequent high temperature thermal sulphurization process which ensures pristine MoS_2 films. It is of utmost importance to realize here that the conventional polymers (such as PMMA) used for the lithography process have a low glass transition

temperature, low plasma etch resistance and therefore might suffer from reflowing issues and plasma damage during a ALD process. However, it has been demonstrated that the use of low temperature during PEALD makes it possible to deposit metal oxides on polymer substrates including PMMA without any reflowing issues. In order to investigate this for our case, we monitored the change in thickness of PMMA during MoO_x deposition using *in-situ* spectroscopic ellipsometry (Figure 6.5).

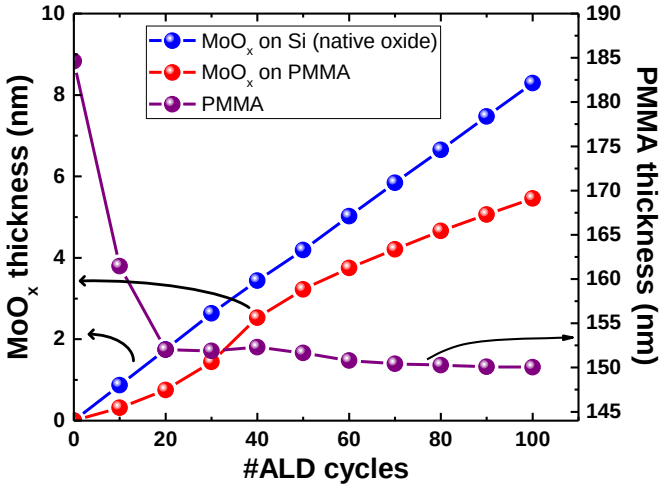


Figure 6.5 The plot shows the thickness evolution of PMMA (purple) and MoO_x on Si (blue) and PMMA coated Si substrate (red) respectively as a function of increasing number of PEALD cycles.

Figure 6.5 shows the MoO_x film thickness evolution plotted as a function of number of ALD cycles on a bare Si substrate and a PMMA coated substrate. The thicknesses of the MoO_x and PMMA layers were extracted using SE modelling. (The details of the models used are mentioned in the experimental section). Notably, the thickness of PMMA shows a rapid reduction during initial ALD cycles (up to ~20 cycles) and thereafter eventually saturates to a steady value with increasing number of ALD cycles. On the other hand, a linear growth behaviour for MoO_x film is obtained on Si substrate. In parallel, the MoO_x film starts to grow on PMMA immediately without any nucleation delay and it can be speculated that at a certain thickness the MoO_x film starts acting as a protection layer preventing any further damage to the underlying PMMA layer. This ensures the preservation of the PMMA layer and facilitates the subsequent lift-off process without any hindrance. In order to reaffirm, the thickness of PMMA before and

after MoO_x deposition was measured by using contact profilometry (Figure A.6.5 in Appendix). The thicknesses measured were ~ 175 nm and ~ 142 nm before and after MoO_x deposition which is in agreement with the SE results and therefore strengthens our hypothesis. To summarize, the use of low temperature (50°C) during PEALD results in (i) MoO_x deposition on PMMA and (ii) insignificant damage/reflowing of PMMA.

Figure 6.6 (a) shows the Raman spectra for the patterned region with and without MoS_2. It is clearly evident that the characteristic Raman signal is visible only for regions with MoS_2 which confirms the patternability achieved using the process flow as described above. Furthermore, notably the MoS_2 squares retain the pre-defined geometry and therefore yield high fidelity of the targeted patterns which is difficult to achieve with some methods based on the 'seeded growth' as described previously.[19] (see Figure A.6.6 in Appendix). In order to assess the homogeneity of the film on the patterned areas, we performed a mapping of the spatial distribution of the out-of-plane Raman vibrational mode using a diffraction-limited beam spot and a step size of ~200 nm. Figure 6.6 (b) shows the area map for fitted peak intensity of the A_{1g} vibrational mode across the area shown in the optical micrograph (inset of Figure 6.6(a)). A homogeneous Raman signal is obtained over the entirety of the patterned area displaying an excellent selectivity of the MoS_2 films while retaining the pre-defined geometry. Further, in order to demonstrate the versatility of our process, we developed a pattern containing the acronym of our research group 'PMP' surrounded by a monolayer MoS_2. The corresponding PL map is shown in inset of Figure 6.6 (b). The Raman frequency difference (Δ) of 20.6 cm^{-1} (not shown) registers the presence of uniform monolayer on the patterned area.

Additionally, an EDX line scan was performed on sub-μm features containing a MoS_2 film (Figure 6.6 (c)), which clearly shows the presence of Mo species in the patterned areas and confirms the nano-scale patternability of our process. These results demonstrate the viability of our ALD based process as a facile route to achieve patterned large area synthesis of mono-to-few layered 2-D MoS_2 thin films.

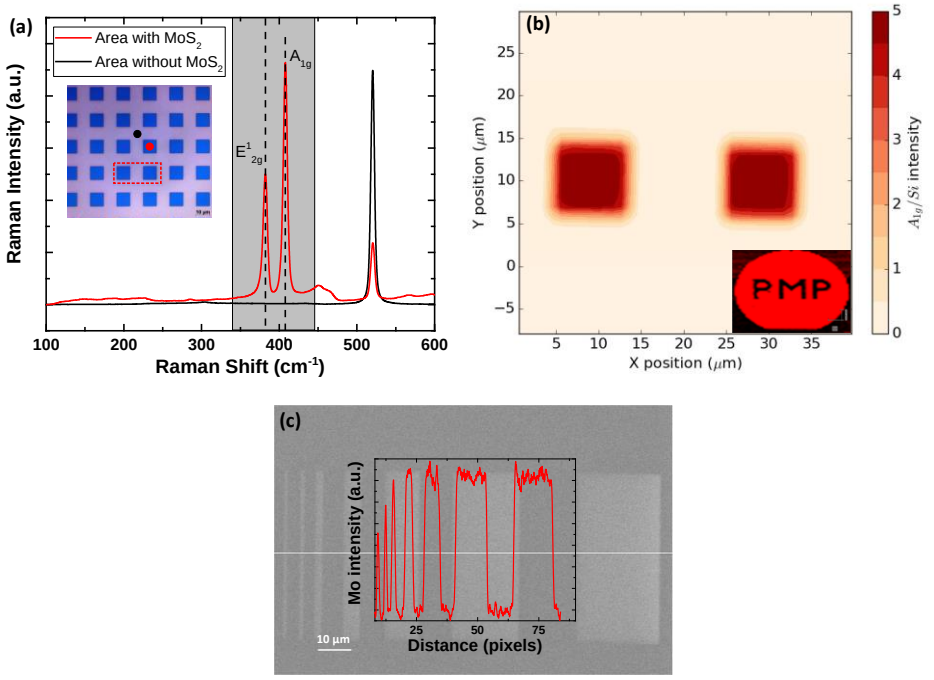


Figure 6.6 (a) Raman spectra of regions with and without patterned MoS_2. These regions are indicated by the red and blue dots on the optical microscopy image of patterned MoS_2 respectively, as shown in the inset. The region with characteristic vibrational Raman modes is highlighted by the grey band. (b) Raman mapping image of the region consisting of two patterned MoS_2 squares highlighted in dashed square in the inset of (a). Note that the intensity drop off observable at the edge regions can be attributed to the large spot size (~ 1 μm) of the laser beam. The inset shows the PL mapping image for a pattern containing the acronym of our group (PMP). The region with letters (black) represents the SiO_2 substrate while the red color corresponds to the MoS_2 monolayer. (c) SEM image showing the patterned MoS_2 line bars with width ranging from 0.8 μm - 25 μm. The EDX line profile (overlaid) clearly displays the Mo signal appearing from the patterned regions.

As aforementioned, the patterned MoS_2 films with desired thickness can be readily achieved on device ready substrates omitting the need of any etch/transfer step for subsequent device fabrication. This provides an opportunity for fabrication of devices directly on SiO_2/Si substrates. To this purpose, bottom gate transistors were prepared by synthesizing the patterned MoS_2 films (7-8 layers thick) on a heavily doped p-type Si wafer with a 300 nm thick SiO_2 layer on top. Figure 6.7 (a) displays the transfer curve for such a FET device with gating voltage ranging from -100 to 100 V at an interval of

10 V. Interestingly, the FET device demonstrates a p-type behavior which probably originates from doping resulting from the fabrication process and/or air-borne contaminants. Furthermore, although the device shows switching, a poor I_{on}/I_{off} is obtained which indicates towards the resistive nature of the film. Furthermore, there can be several other factors which might be responsible for the poor performance of the devices. One of the reasons can be the small grain size of the prepared film. TEM shows a grain size of 20 - 50 nm and therefore a high number of grain boundaries exist in the channel. It is known that grain boundary scattering is one of the governing factors for transport behavior of charge carriers in a semiconducting device and thus a high density of grain boundaries can have a high impact on the device performance. Therefore, it can be argued that in order to improve the device performance the grain size needs to be increased in future work.

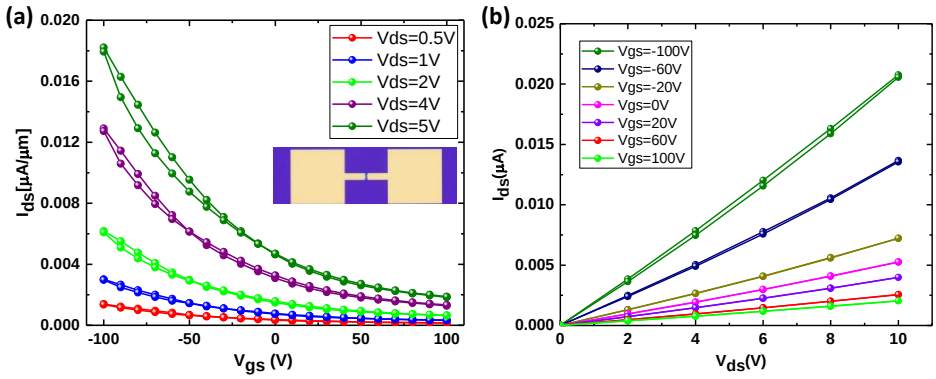


Figure 6.7 Electrical properties of the patterned 7-8 layered thick MoS_2 film (a) Transfer characteristic of FET device with gating voltages (Vgs) ranging from -100 to 100 V. The inset shows the optical microscope image of a fabricated FET device. (b) Output characteristic of the FET device at different Vgs values.

Furthermore, it is worth mentioning that a ~ 30 nm HfO_2 film using a PEALD process was deposited on the MoS_2 channel in anticipation to prevent the oxidation and suppress the Coulombic charge scattering during carrier transport.[34] However, based on the poor device performance, it can be further speculated that the plasma process used for the HfO_2 deposition might have a negative impact on the electrical quality of the films. Hence, it is worth investigating the use of thermal ALD processes for depositing HfO_2 and/or Al_2O_3 films to cap the MoS_2 channel and evade the possible plasma damage. Overall, these results serve as the proof-of-principle for the possible application of

patterned MoS_2 films as channel in FET devices and creates exciting future research areas.

6.4 Conclusion

In conclusion, a low temperature (50°C) PEALD process has been combined with high temperature thermal sulphurization (900°C) to synthesize relatively high quality, large area MoS_2 films. A precise control over thickness ranging from a monolayer to few layers of MoS_2 film could be attained by tuning the number of ALD cycles for the parent MoO_x films. The in-plane oriented layers over large area and polycrystalline nature of the MoS_2 film have been shown using HRTEM analysis. The large area uniformity and a high conformality of layered MoS_2 over intricate 3-D structures have been demonstrated as an inherent advantage of our ALD process. Furthermore, our combinatorial methodology has allowed to achieve patterned MoS_2 thin films over device ready substrates without any need of etching and/or transfer step. As a result, a variety of arbitrary shaped patterns with high fidelity have been demonstrated. Finally, the electrical properties of the patterned MoS_2 thin film have been studied by fabricating a FET device. Our work opens up a new avenue for a variety of future electronic, optoelectronic applications and is potentially extendible to assemble both vertical and lateral heterostructures based on other 2-D materials on a large scale.

Acknowledgements

The authors gratefully acknowledge J. van Gerwen, C.A.A. van Helvoirt, J.J.L.M. Meulendijks, C.O. van Bommel and J.J.A. Zeebregts for their technical assistance. Dr. Beatriz Barcones is acknowledged for carrying out the FIB sample preparation for TEM analysis. Solliance and the Dutch province of Noord Brabant are acknowledged for funding the TEM facility. The authors are also thankful to LAM Research for providing substrates with HAR trench nanostructures. This work has been financially supported by the European Research Council (Grant Agreement No. 648787- ALDof2DTMDs). Further, the work has also been supported by NWO and Technology Foundation STW through the VIDI program on ‘Novel bottom-up nanofabrication techniques for future carbon-nanoelectronics’.

Appendix

A.6.1: Schematics of furnace and thermal sulphurization recipe

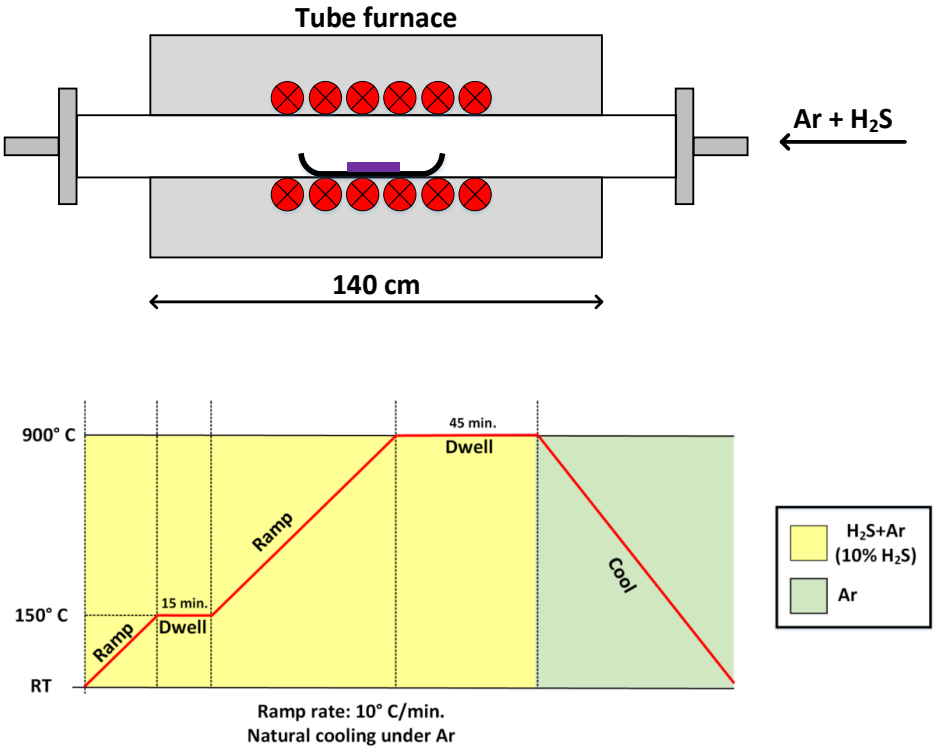


Figure A.6.1 *(top)* The schematic of tube furnace used for sulphurization of MoO_x samples *(bottom)* The thermal recipe used for sulphurization. The sulphurization process was carried out at a maximum temperature of 900°C under atmospheric pressure.

Table A.6.1 The table showing the as-measured nominal thickness of MoO_x films using *in-situ* spectroscopic ellipsometry during PEALD process. The error margins are indicated accordingly.

#ALD cycles	Nominal thickness (nm)
10	0.60±0.06
12	0.73±0.05
15	0.93±0.05
18	1.13±0.05
22	1.40±0.05
30	1.98±0.05
60	4.06±0.07
80	6.23±0.1

A.6.2: AFM images of polycrystalline MoS_2

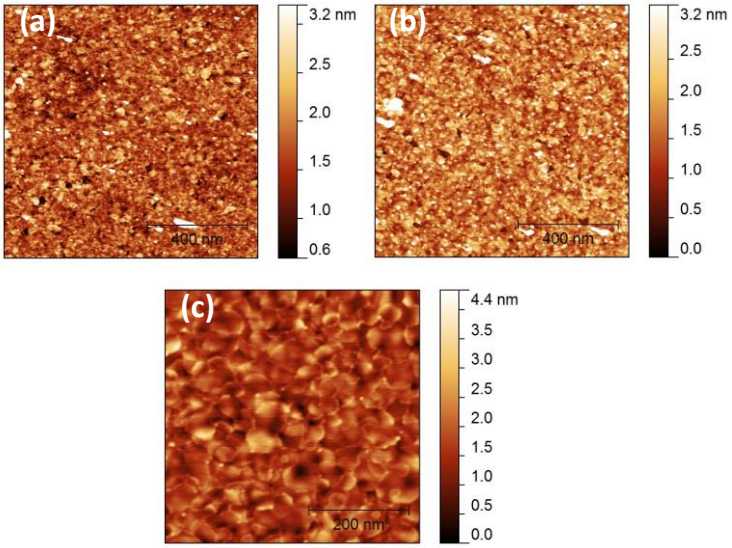


Figure A.6.2 The AFM images showing the topographies for (a) monolayer (10 cycles) (b) bilayer (18 cycles) (c) ~7-8 layers (60 cycles) of MoS_2 films synthesized by PEALD of MoO_x followed by thermal sulphurization. The root mean square roughness of the films are in the range between 0.2 - 0.4 nm.

A.6.3: Additional TEM analysis

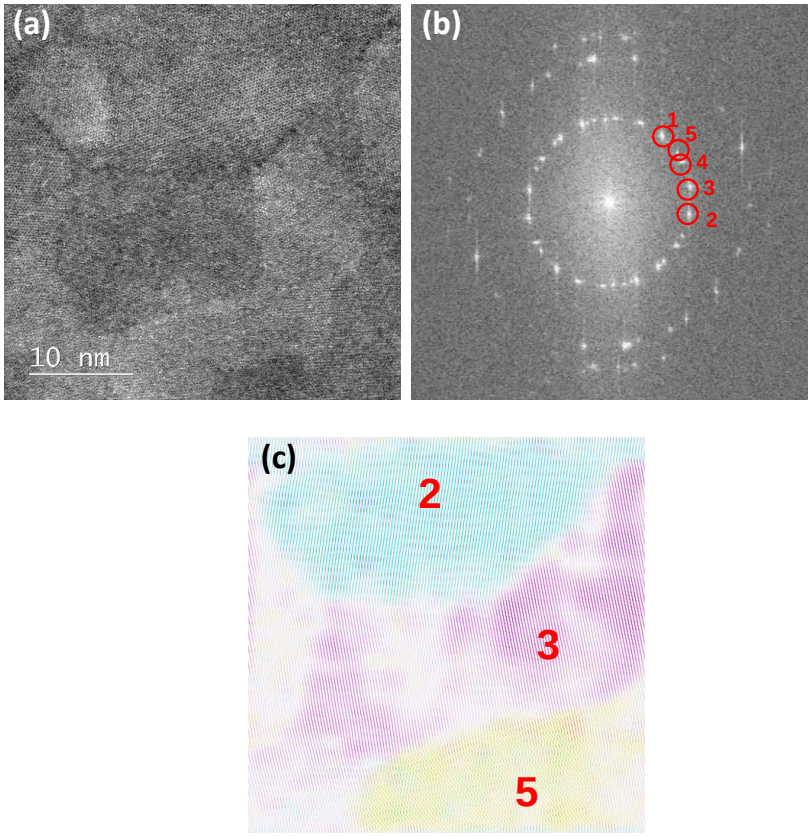


Figure A.6.3 (a) The atomic resolution STEM image displays a poly-crystalline MoS_2 film (b) The corresponding FFT pattern reveals a superposition of the sixfold symmetry patterns of the individual crystals. Individual spots in the FFT pattern corresponding to different crystals are numbered. (c) A RGB color image created by taking an inverse FFT of three spots as labelled also in (b).

A.6.4: XPS analysis

Figure A.6.4 shows the XPS analysis of MoO_x and MoS_2 films before and after sulphurization respectively. The MoO_x film was prepared using 10 ALD cycles (~0.60 nm) which yielded a monoloayer of MoS_2 post sulphurization. The left panel displays the detailed spectra for Mo3d, O1s and S2p in Figure A.6.4 (a), (b) & (c). Likewise, after sulphurization, for a MoS_2 monolayer, the corresponding XPS spectrum is shown in right panel of Figure A.6.4. A high resolution X-ray photoelectron spectrum for the Mo 3d region (Figure A.6.4 (d)) shows the doublet for MoS_2 (Mo^{4+}) with the 3d5/2 peak at 229.1 eV and the 3d3/2 peak at 232.3 eV which is in accordance with the binding energy positions given in the literature.[35-37] A very small fraction of Mo^{5+} and Mo^{6+} is also detected which corresponds to oxide species on the surface due to exposure of sample to ambient. The O1s peak as shown in Figure A.6.4 (e) corresponds to Si-O bond and indicates the complete sulphurization of MoO_x film. Furthermore, the spectrum showing a doublet for S2p is also displayed in Figure A.6.4 (f) with binding energy positions at 161.9 eV and 163.2 eV.

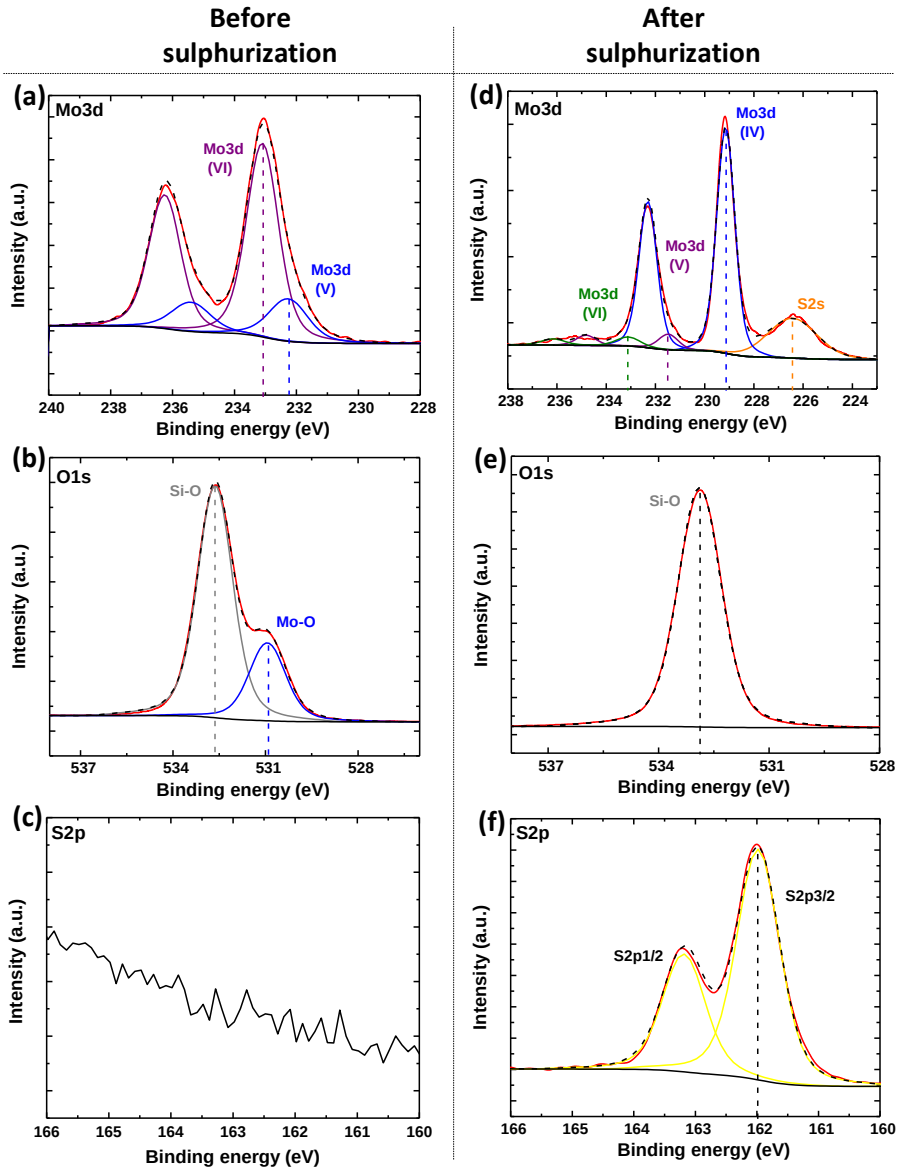


Fig. A.6.4 Details of XPS spectra showing the spectral regions for (left) Mo3d and O1s corresponding to a MoO_x film (10 cycles) before sulphurization (right) Mo3d, O1s and S2p corresponding to a monolayer of MoS_2 obtained after sulphurization. A clear shift in binding energy for Mo3d can be seen upon sulphurization indicating the different oxidation states. Additionally, for the spectral region of O1s the shoulder which corresponds to the metal-oxygen bond (Mo-O) disappears after sulphurization clearly showing the conversion of MoO_x to MoS_2.

A.6.5: Contact profilometry measurement

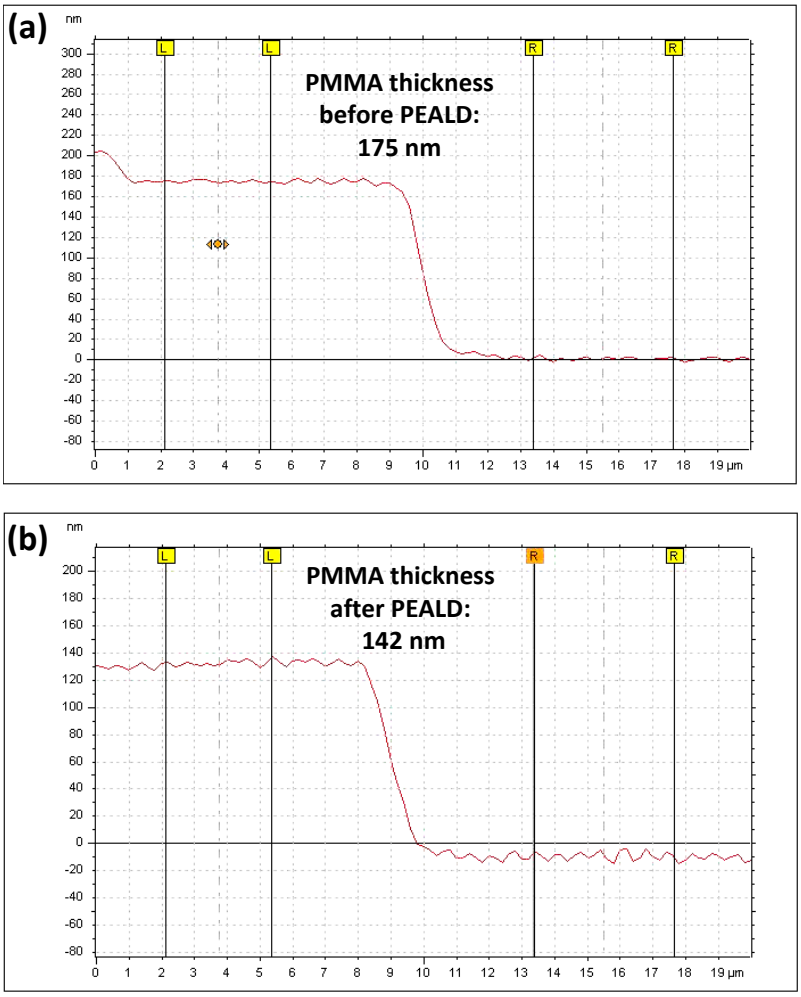
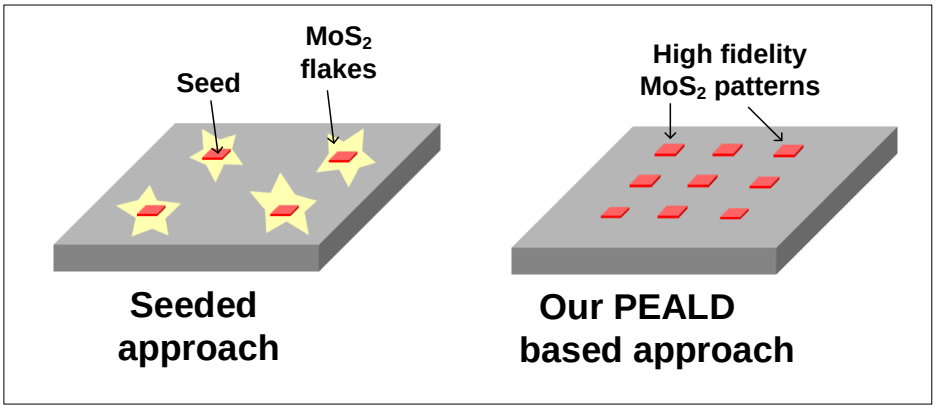


Figure A.6.5 The contact profilometry measurements showing the PMMA thickness (a) before PEALD and (b) after 100 cycles of MoO_x PEALD.

A.6.5: Optical microscopy images: High fidelity patterns



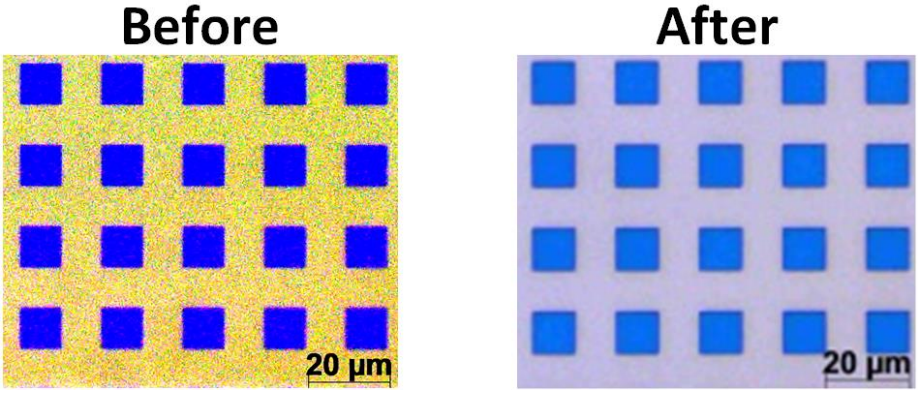


Figure A.6.5 (*top panel*) The schematic showing the difference between a seeded approach and our PEALD based approach. The former approach has been demonstrated to yield uncontrolled fractal crystalline flakes as depicted which might be undesirable for certain device applications while high fidelity patterns are attainable using our approach. (*bottom panel*) Optical microscopy images showing the MoO_x (60 ALD cycles) patterns (*left*) before sulphurization and (*right*) after sulphurization. The preservation of the dimension and the geometry of the patterns upon sulphurization is clearly evidenced.

References

1. X. Huang, Z. Zeng and H. Zhang, *Chemical Society Reviews*, 2013, **42**, 1934-1946.
2. H. Zhang, *ACS Nano*, 2015, **9**, 9451-9469.
3. K. Kang, S. Xie, L. Huang, Y. Han, P. Y. Huang, K. F. Mak, C.-J. Kim, D. Muller and J. Park, *Nature*, 2015, **520**, 656-660.
4. A. Nourbakhsh, A. Zubair, M. S. Dresselhaus and T. Palacios, *Nano Letters*, 2016, **16**, 1359-1366.
5. M. Gmitra and J. Fabian, *Physical Review B - Condensed Matter and Materials Physics*, 2015, **92**.
6. R. Ganatra and Q. Zhang, *ACS Nano*, 2014, **8**, 4074-4099.
7. K. S. Novoselov, D. Jiang, F. Schedin, T. J. Booth, V. V. Khotkevich, S. V. Morozov and A. K. Geim, *Proc. Natl. Acad. Sci. U. S. A.*, 2005, **102**, 10451-10453.
8. M. Chhowalla, H. S. Shin, G. Eda, L.-J. Li, K. P. Loh and H. Zhang, *Nat Chem*, 2013, **5**, 263-275.
9. G. Eda, H. Yamaguchi, D. Voiry, T. Fujita, M. Chen and M. Chhowalla, *Nano Letters*, 2011, **11**, 5111-5116.
10. J. N. Coleman, M. Lotya, A. O'Neill, S. D. Bergin, P. J. King, U. Khan, K. Young, A. Gaucher, S. De, R. J. Smith, I. V. Shvets, S. K. Arora, G. Stanton, H.-Y. Kim, K. Lee, G. T. Kim, G. S. Duesberg, T. Hallam, J. J. Boland, J. J. Wang, J. F. Donegan, J. C. Grunlan, G. Moriarty, A. Shmeliov, R. J. Nicholls, J. M. Perkins, E. M. Grieveson, K. Theuwissen, D. W. McComb, P. D. Nellist and V. Nicolosi, *Science*, 2011, **331**, 568-571.
11. Y. Yao, Z. Lin, Z. Li, X. Song, K.-S. Moon and C.-p. Wong, *Journal of Materials Chemistry*, 2012, **22**, 13494-13499.
12. S. Najmaei, Z. Liu, W. Zhou, X. Zou, G. Shi, S. Lei, B. I. Yakobson, J.-C. Idrobo, P. M. Ajayan and J. Lou, *Nat Mater*, 2013, **12**, 754-759.
13. A. M. van der Zande, P. Y. Huang, D. A. Chenet, T. C. Berkelbach, Y. You, G.-H. Lee, T. F. Heinz, D. R. Reichman, D. A. Muller and J. C. Hone, *Nat Mater*, 2013, **12**, 554-561.
14. J. Chen, W. Tang, B. Tian, B. Liu, X. Zhao, Y. Liu, T. Ren, W. Liu, D. Geng, H. Y. Jeong, H. S. Shin, W. Zhou and K. P. Loh, *Advanced Science*, 2016, **3**, 1500033-n/a.
15. X. Ling, Y.-H. Lee, Y. Lin, W. Fang, L. Yu, M. S. Dresselhaus and J. Kong, *Nano Letters*, 2014, **14**, 464-472.
16. L. Xi, L. Yuxuan, M. Qiong, W. Ziqiang, S. Yi, Y. Lili, H. Shengxi, F. Wenjing, Z. Xu, H. A. L., B. Yaqing, L. Yi-Hsien, Z. Yimei, W. Lijun, L. Ju, J. H. Pablo, D. Mildred, P. Tomás and K. Jing, *Advanced Materials*, 2016, **28**, 2322-2329.
17. X. Chen, Y. J. Park, T. Das, H. Jang, J.-B. Lee and J.-H. Ahn, *Nanoscale*, 2016, **8**, 15181-15188.
18. M. B. Brian, M. E. Sarah, L. Yu-Chuan, Z. Kehao, R. B. Ganesh, F. P. Aleksander, L. Michael, III and A. R. Joshua, *2D Materials*, 2017, **4**, 025083.
19. G. H. Han, N. J. Kybert, C. H. Naylor, B. S. Lee, J. Ping, J. H. Park, J. Kang, S. Y. Lee, Y. H. Lee, R. Agarwal and A. T. C. Johnson, 2015, **6**, 6128.
20. J. R. Young, M. Chilcote, M. Barone, J. Xu, J. Katoch, Y. K. Luo, S. Mueller, T. J. Asel, S. K. Fullerton-Shirey, R. Kawakami, J. A. Gupta, L. J. Brillson and E. Johnston-Halperin, *Applied Physics Letters*, 2017, **110**, 263103.
21. I. Song, C. Park, M. Hong, J. Baik, H.-J. Shin and H. C. Choi, *Angewandte Chemie International Edition*, 2014, **53**, 1266-1269.

22. M. F. J. Vos, B. Macco, N. F. W. Thissen, A. A. Bol and W. M. M. Kessels, *Journal of Vacuum Science & Technology A*, 2016, **34**, 01A103.
23. B. Macco, M. F. J. Vos, N. F. W. Thissen, A. A. Bol and W. M. M. Kessels, *physica status solidi (RRL) – Rapid Research Letters*, 2015, **9**, 393-396.
24. A. Sharma, V. Longo, M. A. Verheijen, A. A. Bol and W. M. M. Kessels, *Journal of Vacuum Science & Technology A*, 2016, **35**, 01B130.
25. C. Lee, H. Yan, L. E. Brus, T. F. Heinz, J. Hone and S. Ryu, *ACS Nano*, 2010, **4**, 2695-2700.
26. S. Mignuzzi, A. J. Pollard, N. Bonini, B. Brennan, I. S. Gilmore, M. A. Pimenta, D. Richards and D. Roy, *Physical Review B*, 2015, **91**, 195411.
27. M. Elisha, G. Andy, M. Jonathan, C. Mike and S. S. Ravi, *Journal of Physics D: Applied Physics*, 2017, **50**, 184005.
28. L. Yi-Hsien, Z. Xin-Quan, Z. Wenjing, C. Mu-Tung, L. Cheng-Te, C. Kai-Di, Y. Ya-Chu, W. J. Tse-Wei, C. Chia-Seng, L. Lain-Jong and L. Tsung-Wu, *Advanced Materials*, 2012, **24**, 2320-2325.
29. Y. Yu, C. Li, Y. Liu, L. Su, Y. Zhang and L. Cao, *Scientific Reports*, 2013, **3**, 1866.
30. A. Splendiani, L. Sun, Y. Zhang, T. Li, J. Kim, C.-Y. Chim, G. Galli and F. Wang, *Nano Letters*, 2010, **10**, 1271-1275.
31. J.-G. Song, J. Park, W. Lee, T. Choi, H. Jung, C. W. Lee, S.-H. Hwang, J. M. Myoung, J.-H. Jung, S.-H. Kim, C. Lansalot-Matras and H. Kim, *ACS Nano*, 2013, **7**, 11333-11340.
32. J. Sungwoo, K. S. Joon, K. Hyeong-Jun, J. D. Hyung, C. Soo-Yeon and J. Hee-Tae, *Advanced Functional Materials*, 2017, **27**, 1703842.
33. T. O. Kääriäinen, S. Lehti, M. L. Kääriäinen and D. C. Cameron, *Surface and Coatings Technology*, 2011, **205**, S475-S479.
34. S.-L. Li, K. Tsukagoshi, E. Orgiu and P. Samorì, *Chemical Society Reviews*, 2016, **45**, 118-151.
35. Y. Zhan, Z. Liu, S. Najmaei, P. M. Ajayan and J. Lou, *Small*, 2012, **8**, 966-971.
36. N. H. Turner and A. M. Single, *Surface and Interface Analysis*, 1990, **15**, 215-222.
37. I. Alstrup, I. Chorkendorff, R. Candia, B. S. Clausen and H. Topsøe, *Journal of Catalysis*, 1982, **77**, 397-409.

7

Atomic layer deposition of HfO_2 using $HfCp(NMe_2)_3$ and O_2 plasma*

HfO_2 thin films are prepared by plasma - enhanced atomic layer deposition (PEALD) using a cyclopentadienyl - alkylamido precursor ($(HfCp(NMe_2)_3$, HyALD™)) and an O_2 plasma over a temperature range of 150 °C - 400 °C at a growth per cycle (GPC) around 1.1 Å/cycle. The high purity of the films has been demonstrated by X-ray photoelectron spectroscopy (XPS) and elastic recoil detection (ERD) analyses which has revealed that by increasing the deposition temperature from 200 °C to 400 °C, the atomic concentrations of residual carbon and hydrogen reduced from 1.0 at% to < 0.5 at% and 3.4 at% to 0.8 at%, respectively. Moreover, Rutherford backscattering spectroscopy **(**RBS) studies has shown an improvement in stoichiometry of HfO_2 thin films with increase in deposition temperature, resulting in Hf/O ratio close to ~0.5 at 400 °C. Furthermore, grazing incidence X-ray diffraction **(**GI-XRD) measurements have detected a transition from amorphous at the deposition temperature of 300 °C to fully polycrystalline films at 400 °C, consisting of a mixture of monoclinic, tetragonal and cubic phases. Finally, the surface morphology and conformality of HfO_2 thin films studied by atomic force microscopy (AFM) and transmission electron microscopy (TEM) are also reported.

*A. Sharma[†], V. Longo[†], M. A. Verheijen, A. A. Bol and W. M. M. Kessels, *Journal of Vacuum Science & Technology A*, 2016, **35**, 01B130.

[†] A. Sharma and V. Longo contributed equally

7.1 Introduction

Atomic layer deposition (ALD) of high-k dielectric materials has been a subject of intensive research over the past many years. Amongst such high-k oxides, hafnium oxide (HfO_2) has been endorsed largely for the application of high-k gate oxide in complementary metal oxide semiconductor devices owing to its high permittivity, fairly large band gap and ability to form a thermodynamically stable interface with Si. [1-5] The application of HfO_2 as a gate oxide material is not only limited to conventional Si based devices but also extending its horizons in novel nanomaterials based devices. For instance, Radisavljevic *et al.* have recently shown that by implementing HfO_2 as gate oxide for a field effect transistor (FET) device based on an emerging 2-D nanomaterial, molybdenum disulphide (MoS_2), the mobility could be drastically boosted owing to the suppression of coulombic scattering via dielectric screening.[6] Furthermore, most recently, the application of a gate stack based on HfO_2/Al_2O_3/III-V($In_{0.53}Ga_{0.47}As$) for metal-oxide-semiconductor capacitor devices has been demonstrated by Djara *et al.*[7] These devices have a HfO_2/Al_2O_3 stack as gate oxide deposited by plasma enhanced ALD (PEALD) and show a low interface trap density *(D_{it})*. Additionally, HfO_2 also finds applications as a protective coating for microelectromechanical systems (MEMS) and as insulator for organic devices such as OLED and OFETs.[8-10]

ALD has been the method of choice for depositing thin films of HfO_2. The self-saturating nature of the ALD process enables atomic level control over thickness and uniformity and this makes ALD ideal for preparing ultra-thin HfO_2 thin films. In particular, the much needed conformality over high aspect ratio structures in combination with the excellent uniformity over large surface areas and the pin-hole free nature of the ALD produced thin films makes ALD a befitting deposition process.[4, 11]

In ALD, the choice of precursor has a large effect on the quality and properties of the deposited thin films. This leads to a continuous effort in precursor synthesis aiming at improving temperature stability and/or reducing impurity concentrations in the resulting film depending on the final application. In literature, a number of Hf precursors have been implemented for HfO_2 ALD processes. The established ALD processes leave a room of improvement in terms of extension of operating conditions. In this contribution, we have investigated a novel precursor, $HfCp(NMe_2)_3$ in combination with O_2 plasma which has yielded into a viable HfO_2 ALD process with a constant growth rate over the widest possible range of operating conditions such that it is suited for a multitude of

applications. The details of the process investigated will be discussed in this paper. However, it is useful to systematically look at established ALD processes as listed in Table 7.1, where a brief overview of efforts reported in literature focusing on detailed investigation of the ALD processes by using four different precursor groups for HfO_2 thin films is given. The most frequently used precursor for HfO_2 ALD is $HfCl_4$ which is combined with H_2O or O_3 as oxygen source.[2, 12-15] However, the limitations associated with this precursor, such as corrosive by-products and poor nucleation on H-terminated Si at high temperatures (≥ 300 °C), make this precursor unfavorable for some specific applications like dynamic random-access memories (DRAM) and therefore have led for a search for alternative precursor chemistries.[2, 15, 16]

Table 7.1 An overview of selected ALD processes reported in the literature for HfO_2 thin film with various Hf precursors

Precursor group	Hafnium precursor/ oxygen source	Growth temperature range (°C)	Substrate(s) used	Growth per cycle (Å)	Ref.
Halides	$HfCl_4/H_2O$	500	Glass	0.5	[12]
	$HfI_4/HfCl_4/H_2O$	300	Si[a]	0.47 - 0.62	[13]
Alkylamides	$Hf[NMeEt]_4/H_2O$	150 - 325	Glass, SiO_2/Si	0.9-1.5	[17]
	$Hf(NEt_2)_4/H_2O$	50 - 500	Si[a]	0.9	[18]
	$Hf[NMeEt]_4/O_3$	120 - 300	SiO_2/Si	0.8 - 1.1	[19]
	$Hf[NMe_2]_4/H_2O$	300	Si[a]	0.78	[3]
	$Hf[NMeEt]_4$/ O_2 plasma	230 - 350	Si[a]	1.0	[20]
Cyclo-pentadienyls	Cp_2HfMe_2/H_2O	300 - 500	SiO_2/Si	0.42	[21]
	$(CpMe)_2Hf(OMe)Me/O_3$	350 - 500	Si[a], SiO_2/Si	0.5	[22]
Alkylamides + ***Cyclo-pentadienyls***	$CpHf(NMe_2)_3/H_2O$	305 - 410	SiO_2/Si	0.23 - 0.36	[23]
	$CpHf(NMe_2)_3/O_3$	250 - 400	SiO_2/Si	0.7 - 0.8	[24]
	$CpHf(NMe_2)_3/O_2$ plasma	150 - 400	Si[a], SiO_2/Si	1.1	This Study

Me = CH_3, Et = C_2H_5, , Cp = C_5H_5, [a] = Hf last treated

One of such a widely applied alternative precursor group for HfO_2 ALD is alkylamide comprising metal-nitrogen bonds, namely $Hf(NEtMe)_4$, $Hf(NEt_2)_4$ and $Hf(NMe_2)_4$ (Et = C_2H_5, Me = CH_3). [3, 17-20] These alkylamide type precursors possess a high volatility and reactivity and yield a high growth per cycle (GPC) in combination with H_2O or O_3 as co-reactants. [17] However, they suffer from a limited thermal stability which can lead to a

parasitic CVD component and might result into high impurity concentrations and poor film uniformity.[25] In addition, Kukli *et al.* have demonstrated that the HfO_2 ALD process using $Hf(NEtMe)_4$ (TEMAH) in combination with H_2O as oxygen source leads to an increment in GPC from 0.9 Å/cycle at 250 °C to 1.5 Å/cycle at 325 °C indicating the decomposition of the precursor at temperatures ≥ 300 °C.[17]

To overcome this, an ALD process using the cyclopentadienyl ($Cp = C_5H_5$) precursor type was investigated. A higher thermal stability was achieved and ALD saturation was realized at a relative high substrate temperature of 400 °C.[22] However, a lower GPC of ~0.5 Å/cycle was obtained when using Cp-precursors like $(CpMe)_2HfMe_2$ and $(CpMe)_2Hf(OMe)Me$ as compared to the alkylamides (~0.9 Å/cycle).[19]

With the aim of combining the benefits of both precursor types, precursors comprising both cyclopentadienyl and alkylamide type ligands have been investigated.[23, 24] A high thermal stability and high GPC attributed to cyclopentadienyl ligands and alkylamide ligands respectively have been demonstrated for both Hf and Zr based ALD processes.[23, 24, 26] For ZrO_2, this combined merit of high thermal stability and high growth per cycle has been manifested by using a chemically analogous precursor i.e. $CpZr(NMe_2)_3$ in combination with H_2O, where a growth per cycle of 0.8 - 1 Å/cycle in the temperature range of 120 °C - 350 °C was obtained.[26] However, a similar Hf precursor containing mixed cyclopentadienyl and alkylamide ligands, i.e. $HfCp(NMe_2)_3$ when applied in combination with H_2O yielded a growth per cycle of only 0.23 - 0.36 Å/cycle in the temperature range of 305 °C - 375 °C.[23] Furthermore, Niinistö *et al*. have shown that the use of a stronger oxidant like O_3 in combination with $HfCp(NMe_2)_3$ yields a higher growth per cycle (0.75 Å/cycle) in the temperature range of 250 °C – 350 °C.[24] The higher growth in the latter case might be attributed to the high reactivity of O_3 at relatively low temperature resulting in efficient removal of the bulky Cp ligands.[24] However, both with H_2O or O_3 as oxidizing agents, depositions have not been reported below 250 °C, which might be necessary for HfO_2 film deposition on temperature-sensitive substrates, in particular for organic device applications and flexible electronics based on novel nano-materials.[10, 27] In this context, another alternative is to employ a plasma enhanced ALD process (i.e. O_2 plasma as oxygen source) in combination with the same Hf precursor [$HfCp(NMe_2)_3$] for growth of HfO_2 thin films. It is well known that the use of plasma chemistry offers potential advantages

like improved material properties, feasibility of lower deposition temperatures and increased flexibility in process conditions.[28]

In the present study, we report the $HfCp(NMe_2)_3$ in combination with an O_2 plasma process which yields a fairly high growth per cycle over a wide ALD temperature window (150 °C - 400 °C) while retaining the high material properties. A detailed characterization of the HfO_2 PEALD process has been carried out. The dependence of film growth rate on various parameters like growth temperature and duration of dose during the plasma enhanced ALD process has been studied. Furthermore, an elaborated material characterization elucidating the film structure and composition depending on growth temperature has been performed. Finally, in order to assert the potential of ALD to deposit conformally on 3-D structures, the film conformality over high aspect ratio structures has also been demonstrated.

7.2 Experimental section

Film deposition

The HfO_2 thin films were deposited in an Oxford Instruments FlexAL™ ALD reactor on 100 - 200 mm Si wafers either with a native oxide layer or H-terminated as created by a HF-last process (1% HF). The Hf precursor employed was $HfCp(NMe_2)_3$, HyALD™, obtained from AirLiquide. The precursor was stored in a stainless-steel canister and heated to 60 °C. At this temperature the vapor pressure of the HyALD precursor is approximately 100 mTorr.[29] For the precursor delivery to the deposition chamber a 100 sccm Ar (>99.999 % purity) bubbling flow was employed. An Ar purge step with 100 sccm of Ar flow was applied after the precursor and plasma exposure steps. To avoid condensation of the precursor the delivery lines were kept at 90 °C while the reactor walls were heated to 120 °C. As the oxidizing agent an O_2 (>99.999 % purity) plasma generated in an inductively coupled plasma (ICP) source was used. The reactor pressure during the plasma step was 15 mTorr. The plasma power used was 400 W. The substrate stage was heated to temperatures in the range of 150 °C - 400 °C during the deposition processes. It is worth mentioning that there was a ~ 20-25% difference between the set temperature value and the actual substrate temperature for the reactor employed in this work.

Film analysis

The thickness and the optical properties of the HfO_2 thin films were measured by spectroscopic ellipsometry (SE). *Ex-situ* measurements (J.A. Woollam M2000D) were

performed to determine the final thickness and the dielectric function in the 1.25 - 6.5 eV spectral range. The film thickness evolution during deposition was monitored by *in-situ* measurements (J.A. Woollam M2000F, 1.25 - 5 eV).

To determine the elemental composition and the density of the films Rutherford backscattering spectroscopy (RBS) was used. Furthermore, elastic recoil detection (ERD) was employed to determine the hydrogen content in the films. Both RBS and ERD were performed using a 2 MeV $^{4}He^{+}$ ion flux (Acctec BV, The Netherlands). X-ray photoelectron spectroscopy (XPS) was also performed using a Thermo Scientific K-alpha spectrometer using monochromatic Al Kα X-ray radiation (hν = 1486.6 eV). XPS was used to quantify C and N contaminations in the films due to the higher sensitivity of XPS compared to RBS for these elements. For the XPS analysis a 400 µm diameter spot was used and photoelectrons were collected at a take-off angle of 60°. The samples were neutralized during the XPS analysis using an electron flood gun in order to correct for differential or non-uniform charging.

Grazing incidence X-ray diffraction (GI-XRD) was employed to determine the crystalline phases of the HfO_2 thin films. The XRD analysis was performed on a Panalytical X'Pert PRO MRD employing Cu Kα (1.54 Å) radiation with an incidence angle of 0.5° with respect to the substrate plane. Atomic force microscopy (AFM) was used to investigate the surface morphology of the films. The AFM scans were performed in tapping mode with a NT-MDT Solver P47 microscope using a TiN coated Si tip (NSG10/TiN, NT-MDT). Cross-sectional TEM analysis was performed using a JEOL ARM 200 operated at 200 kV. For this, the HfO_2 film was coated with a SiO_x/Pt film stack as a protective layer and subsequently prepared using a standard FIB lift-out TEM sample preparation scheme.

The conformality of HfO_2 ALD process was determined on substrate coupons with high-aspect-ratio (HAR) nanostructures. These HAR nanostructures were created by etching SiO_2 grown by PECVD into the Si wafer. The SiO_2 nanostructures were then coated with a SiNx layer deposited by high-temperature CVD, onto which an SiO_2 thin film was deposited using ALD. The HfO_2 sample was coated with a layer of spin-on epoxy to fill the remaining gaps in the trenches in order to protect the film from curtaining damage during the subsequent lift-out FIB sample preparation.

7.3 Results and discussion

7.3.1 ALD growth

The ALD process was characterized by monitoring the growth-per-cycle (GPC) by *in-situ* SE analysis. The influence of dose steps was investigated by varying the duration of the precursor step, the O_2 plasma step and the purge steps between each half cycle. Figure 7.1 (a) - (d) shows the growth-per-cycle (GPC) values obtained at a substrate temperature of 250 °C when varying the HyALD and O_2 plasma exposure steps (Figures 7.1 (a) and (c) respectively), and purge times after the precursor dose and the plasma exposure step (Figures 7.1 (b) and (d), respectively).

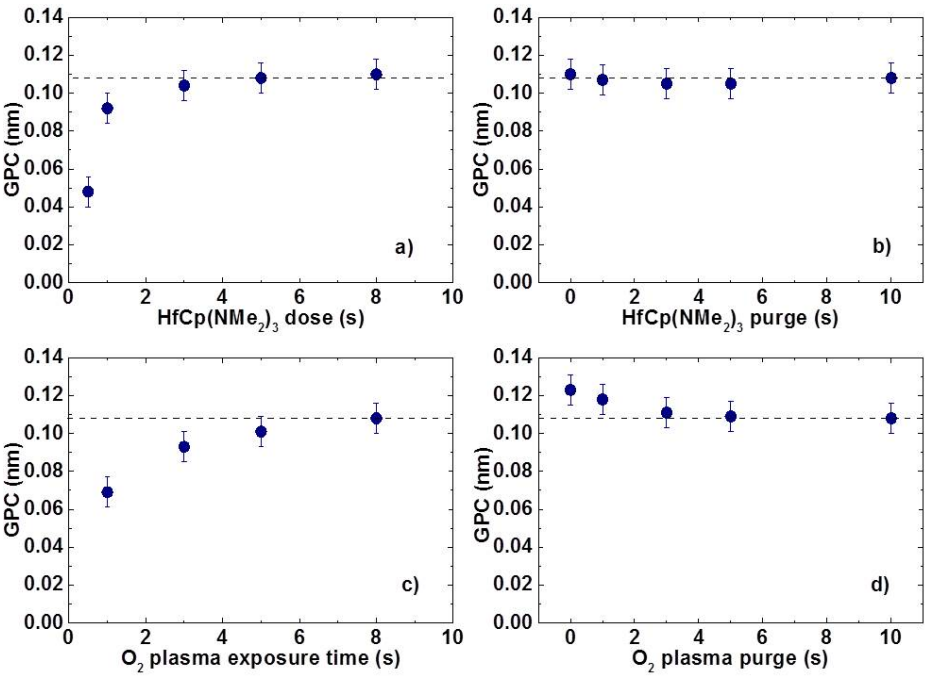


Figure 7.1 Growth-per-cycle (GPC) values as a function of (a) HyALD dose; (b) Ar purge time after precursor dose; (c) O_2 plasma exposure; and (d) purge time after the plasma step. The substrate temperature during the process was 250 °C. The dashed lines serve as a guide to the eyes.

The GPC showed a clear saturation behavior for both the precursor and the plasma half cycles resulting in a GPC value of ~ 1.1 Å /cycle. The Ar purge after the HyALD dose showed a negligible influence on the GPC (Figure 7.1 (b)). Also, when no purge step

was applied after the precursor dose step, the GPC value did not show a remarkable change. By supplying O_2 during all ALD steps, including the precursor dose, it was verified that the HyALD precursor does not react with the molecular oxygen in the process space investigated, thus excluding the presence of a parasitic CVD component. The duration of the purge step applied after the plasma step showed however an influence on the growth, in particular a higher GPC was recorded with a decreasing purge time. This is likely caused due to a parasitic CVD growth component due to chemical reactions between the by-products after the plasma step (i.e. H_2O) and the HyALD precursor when low purge times are employed. On the basis of the results in Figure 7.1, to guarantee a genuine saturation behavior of precursor and purge steps, a precursor/purge/plasma/purge sequence of 5s/2s/8s/5s was chosen in this work.

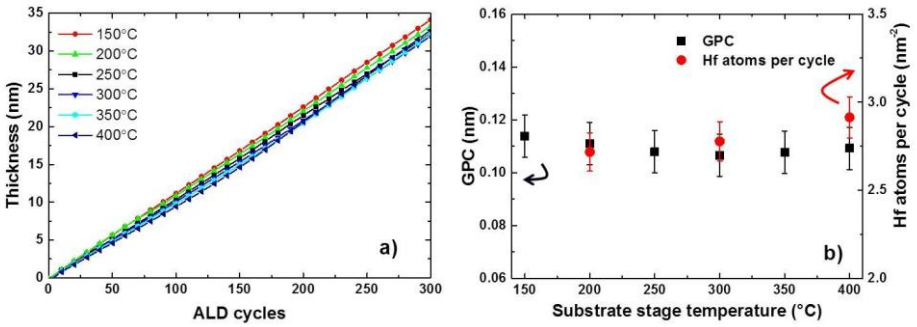


Figure 7.2 (a) Film thickness as a function of number of ALD cycles with temperature ranging between 150 °C and 400 °C. The thickness values have been obtained from *in-situ* SE. (b) GPC values corresponding to the studied substrate stage temperatures and the average number of Hf atoms deposited per ALD cycle as determined from RBS measurements.

The influence of the substrate temperature on the GPC was also determined. Figure 7.2 (a) shows the thickness evolution of HfO_2 films deposited at substrate stage temperatures ranging between 150 °C and 400 °C as obtained from *in-situ* SE. For all temperatures studied, the films showed a linear growth trend without growth delay as expected for a typical O_2 plasma ALD process. Figure 7.2 (b) shows the GPC values as calculated from Figure 7.2 (a), corresponding to the studied substrate stage temperatures and the average number of Hf atoms deposited per ALD cycle as determined from RBS measurements. As mentioned above, the high thermal stability of $HfCp(NMe_2)_3$ allows to explore a larger temperature window.[29] The GPC value remains constant at around

1.1 Å /cycle for the whole range of substrate stage temperatures from 150 °C - 400 °C signifying the decomposition-free deposition.

The relatively higher GPC value at low temperatures (150 °C - 200 °C) can be attributed to a higher incorporation of impurities combined with a lower density of the films for lower deposition temperatures. This hypothesis was confirmed by the elemental composition analysis carried out by XPS and RBS as reported in Table II. The film densities were obtained through the combined RBS and SE analysis and the stoichiometric ratios for Hf/O were determined from the RBS areal density values for Hf and O, respectively. As reported in Table 7.2, the Hf/O ratio increased with increasing deposition temperature and an excellent stoichiometric value close to ~0.5 was achieved at 400 °C.

Table 7.2 The elemental composition of HfO_2 films as determined by Rutherford backscattering (RBS), Elastic recoil detection (ERD) and X-ray photoelectron spectroscopy (XPS). The typical corresponding errors for Hf/O ratio, density values and H content are mentioned. The Tauc band gap values (E_g) are obtained from SE measurements; a dash (-) means not measured.

Substrate stage temperature (°C)	**Hf/O content from RBS**	**Density from RBS (g/cm^3)**	**H content from ERD (at%)**	**E_g (eV)**
150	-	-	-	5.5
200	0.46 ± 0.03	8.7 ± 0.1	3.4 ± 0.2	5.5
250	-	-	-	5.5
300	0.48± 0.03	9.0± 0.1	1.4 ± 0.1	5.4
350	-	-	-	5.3
400	0.49± 0.03	9.3± 0.1	0.8 ± 0.1	5.5

The over-stoichiometric films (i.e. oxygen rich) obtained at lower deposition temperatures might be attributed to the formation of hydroxyl impurities. The hydroxyl impurities are directly related to the H content which decreased with the increasing deposition temperature. Furthermore, the N and C levels were below 1 at% and 2 at% irrespective of the deposition temperature. The corresponding XPS depth profile spectra for the films deposited at the substrate stage temperature of 400 °C is shown in Figure A.7.1 (in Appendix). The low N and C levels obtained are a clear merit as in earlier work the performance of devices with HfO_2 has clearly shown to degrade with

increasing impurity levels.[30, 31] Moreover, as will be shown in the next section, the degree of crystallinity increases for higher deposition temperatures.

As mentioned above, the GPC obtained in this work (1.1 Å/cycle) is considerably higher than the previously reported values in the literature when using $HfCp(NMe_2)_3$ in combination with H_2O (0.23 - 0.36 Å/cycle) or O_3 (0.75 Å/cycle) as oxidizing agents. This can likely be attributed to the creation of a higher density of reactive surface sites for precursor adsorption owing to the higher reactivity of plasma species.[28] It is also worth mentioning that the usage of plasma species leads to reduction in purge time resulting in shorter cycle times which impacts the overall ALD process throughput.[28] This is corroborated by the fact that $HfCp(NMe_2)_3$ in combination with H_2O requires a long post H_2O purge time (30s) [23] as compared to post O_2 plasma purge time (5s) in this work which therefore increases the net ALD throughput.

7.3.2 Optoelectronic properties and crystallinity

The optical properties of HfO_2 films have been analyzed by *ex-situ* spectroscopic ellipsometry (SE). Cauchy and B-spline models were used for obtaining the dielectric functions in the fully transparent and absorbing regions, respectively. Figure 7.3 shows the dielectric function, i.e. the real (ε_1) and imaginary part (ε_2), of ~ 32 nm HfO_2 films deposited in the temperature range studied.

The imaginary part of dielectric function was used to determine the Tauc band gap by plotting $(\varepsilon_2 E^2)^{1/2}$ as a function of photon energy and extrapolating the linear part to zero absorption. The resulting band gap values obtained by this procedure is listed in Table A.7.1 and a Tauc plot corresponding to the film deposited at substrate stage temperature of 400 °C is shown in Figure A.7.2 (in Appendix). As evident in Figure 7.3, the films deposited at higher temperatures have the higher values of ε_1 in the regions with $\varepsilon_2 = 0$. The higher value of ε_1 corresponds to a higher refractive index and is consistent with the elemental analysis: less impurities and a higher density for thin films deposited at high temperatures. Furthermore, the dielectric function of the film deposited at 400 °C shows distinctive sharp features, both in ε_1 and ε_2, compared to the other films. These features can be imputed to a polycrystalline nature of the film leading to sharper electronic transitions. An onset from a smooth dielectric function (< 300 °C) to one with sharper features (400 °C) for the film deposited at 350 °C is visible in the inset of Figure 7.3.

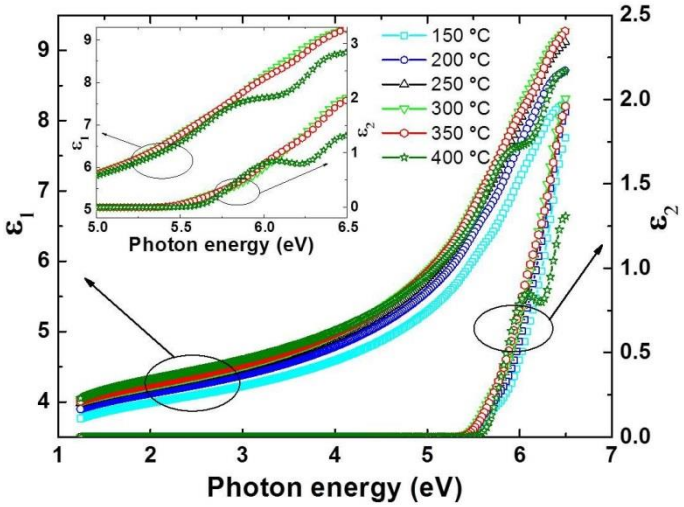


Figure 7.3 The real (ε_1) and imaginary (ε_2) part of the dielectric function as a function of photon energy measured by *ex-situ* SE. The sharp features at a growth temperature of 400 °C indicates the polycrystalline structure of the film. The transition from smooth to sharp dielectric function for films grown at 400 °C can be observed in the inset.

These findings were corroborated by GI-XRD analysis of the same films as shown in Figure 7.4. The GI-XRD spectra of the film deposited at 200 °C showed no distinctive diffraction peaks, and only a broad peak at $2\Theta \sim 32°$ was detected corresponding to amorphous HfO_2. The film deposited at 300 °C also showed a broad peak at $2\Theta \sim 32°$ while a broad diffraction peak with weak intensity, corresponding to the (111) peak of the monoclinic phase, could be detected. This indicates that the HfO_2 thin films studied were mostly amorphous for deposition temperatures up to 300 °C. When increasing the deposition temperature to 350 °C a clear transition in the GI-XRD spectra could be seen. Diffraction peaks corresponding to the monoclinic, tetragonal and cubic HfO_2 phases were detected indicating a higher degree of crystallinity as compared to lower deposition temperatures of 200 °C and 300 °C. By further increasing the substrate stage temperature to 400 °C, peaks having higher intensity were measured indicating a higher degree of crystallinity. The monoclinic phase appeared to be dominant at this deposition temperature.

The GI-XRD patterns obtained in this work are remarkably similar to the ones reported by Niinistö *et al.*,[24] for the HfO_2 ALD process employing the same precursor,

$HfCp(NMe_2)_3$, and O_3 as the oxidizing agent. In their work, Niinistö *et al.* showed a similar temperature dependence of the HfO_2 film crystallinity with a clear transition from amorphous to crystalline films at a deposition temperature of 300 °C. The difference in temperature between this work and the one reported by Niinistö *et al.* at which this transition could be observed is imputed to a ~ 20-25% difference between the set stage temperature value and the actual substrate temperature for the reactor employed in this work.[32] It can be concluded that the crystallization temperature of HfO_2 films is rather independent of the oxygen source used in combination with $HfCp(NMe_2)_3$ during the ALD process. However, the usage of a plasma-assisted ALD process may open the possibility for tuning of the crystalline phase by ion bombardment by employing substrate biasing during processing[33] which is the subject of further investigation.

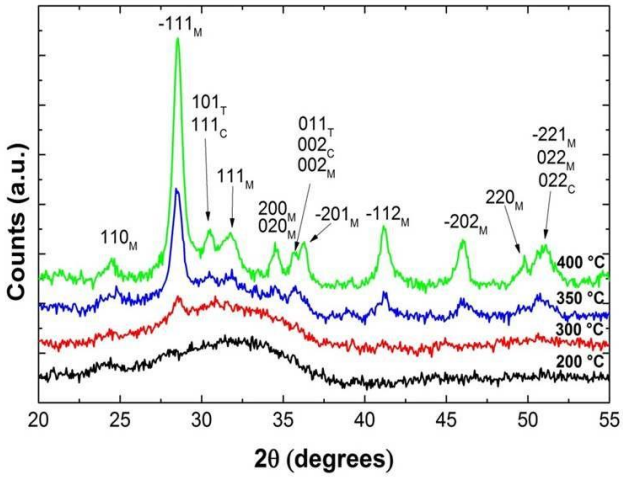


Figure 7.4 The GI-XRD diffractogram for 32 nm thick HfO_2 films prepared by ALD. The substrate stage temperatures during deposition are indicated by the labels. The subscripts M, T, C at indices denote monoclinic, tetragonal and cubic phases, respectively. The spectra show a clear temperature dependence of the HfO_2 film crystallinity with a transition from amorphous to polycrystalline films embarking at a temperature of 300 °C.

Figure 7.5 shows a cross-sectional TEM image of a ~32 nm HfO_2 film deposited at 400 °C on H-terminated Si substrate. The full Si / HfO_2 (32 nm) / SiO_x (~100 nm) / Pt stack is shown in Figure 7.5 (a). The HfO_2 film shows a sharp interface with the underlying Si substrate, while an interface with higher roughness was formed with the overlying protective SiO_x layer due to the crystalline HfO_2 grains. A close inspection of

Figure 7.5 (b) reveals the presence of an amorphous SiO_2 layer at the Si/HfO_2 interface. The amorphous nature of the Si substrate is imputed to damage caused by the focused ion beam used during sample preparation. The TEM image shows that the HfO_2 film is fully crystalline which is in line with the GI-XRD analysis. Furthermore, individual HfO_2 grains can be identified (Figure 7.5 (b)) with an average lateral grain size of ~ 20 - 30 nm.

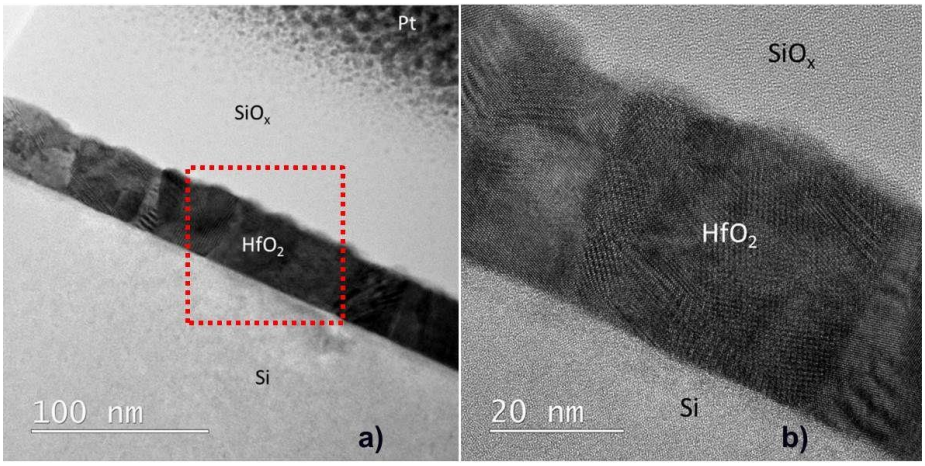


Figure 7.5 (a) Cross-sectional TEM image of a ~32 nm HfO_2 film deposited at 400 °C on a H-terminated Si substrate. The Si/HfO_2 (32 nm)/SiOx (~100 nm) stack demonstrating a sharp interface between HfO_2 and underlying Si has been highlighted within a square. (b) A close up of the cross-sectional TEM image clearly showing the individual crystalline grains of HfO_2 and an amorphous SiO_2 layer at the $Si\text{-}HfO_2$ interface.

7.3.1 Surface morphology

The AFM scans over an area of 500 x 500 nm^2 for the ~32 nm thick HfO_2 films (300 ALD cycles) deposited at 200 °C, 300 °C, 350 °C and 400 °C are depicted in Figure 7.6 (a), (b), (c) and (d), respectively. The root-mean-square (RMS) roughness values obtained from 2 x 2 μm^2 AFM scans of the same samples are indicated in Figure 7.6 (a-d). For the film deposited at 200°C, a very smooth surface (RMS = 1.29 nm) with very few randomly distributed singular features were obtained (See Figure 7.6 (a)). The higher substrate stage temperature of 300 °C and 350 °C yielded an increase in density and size of these singular features as depicted in Figure 7.6 (b) and (c). The RMS roughness values also showed an increment with increasing deposition temperature from 200 °C to 350 °C. AFM scans of the HfO_2 sample deposited at 400 °C revealed a

slightly different film morphology with a decreased RMS roughness value compared to the film deposited at 350 °C (Figure 7.6 (d)).

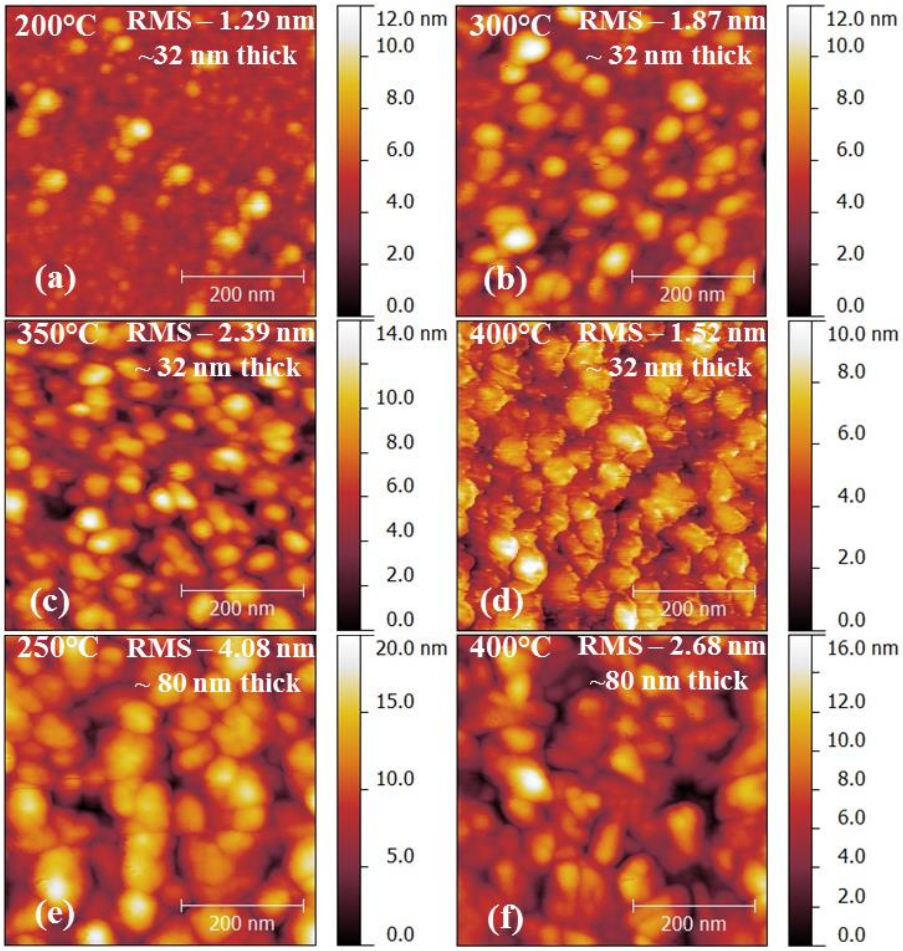


Figure 7.6 (Color online) AFM scans with a scan area of 500 nm x 500 nm of the ~ 32 nm HfO_2 films (300 ALD cycles) deposited at (a) 200 °C (b) 300 °C (c) 350 °C and (d) 400 °C. An increase in amount of the crystallites can be detected from 200 °C to 400 °C indicating enhanced crystallinity with increase in substrate stage temperature. Similar AFM scans of thicker ~80 nm HfO_2 (750 ALD cycles) films deposited at (e) 250 °C and (f) 400 °C show higher roughness.

On the basis of the obtained morphology, it can be argued that the singular features observed might be associated to the increasing degree of crystallinity with the increase in deposition temperature from 200 °C to 350 °C resulting in a transition from

amorphous to polycrystalline films as shown before in Figure 7.3 and Figure 7.4 corresponding to the SE and GI-XRD analyses. Furthermore, the lower RMS roughness value obtained at 400 °C might be attributed to the full crystallization obtained already during the deposition process leading to a laterally homogeneous and smooth HfO_2 thin film, which is also supported by TEM image (Figure 7.5).

This effect was also confirmed for thicker films as depicted in Figure 7.6 (e) and (f) with 500 x 500 nm^2 AFM scans of ~80 nm HfO_2 films deposited at 250 °C and 400 °C, respectively. The RMS roughness values of these two films are also indicated in Figure 7.6 (e, f). The increase in RMS as a function of layer thickness of the samples grown at 400°C can be explained by grain coarsening, i.e. increase in (lateral) grain size as a function of film height. The film deposited at 250 °C shows higher surface roughness compared to the one deposited at 400 °C, most likely because of coalescence of individual crystalline grains at 400 °C in the top part of the layer.

7.3.4 Conformality

The conformality of the above HfO_2 ALD process was determined by depositing a ~20 nm thick HfO_2 film over high-aspect-ratio (HAR) nanostructures with varying aspect ratio (0.6 - 9) at a deposition temperature of 250 °C. Figure 7.7 shows a cross-sectional TEM image of the HAR trench structures conformally covered with the HfO_2 film. It should be noted that the deposition conditions for this purpose were kept the same as implemented for the planar Si substrates.

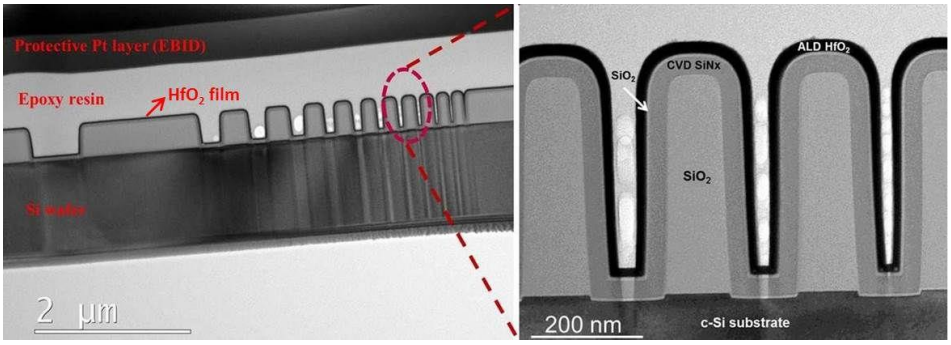


Figure 7.7 (left) Cross-sectional transmission electron microscopy image of a conformal HfO_2 layer deposited on high aspect ratio nanostructures by ALD at 250 °C using $HfCp(NMe_2)_3$ and O_2 plasma. (right) A close up of trench structures with varying aspect ratios shows the conformal HfO_2 thin film.

A comparison of the HfO_2 film thickness on the side walls and planar areas of the nanostructures shows that the HfO_2 films had a conformality of 79% and 72.2% for aspect ratios of 3 and 7.3, respectively. A further optimization of the precursor dose and plasma conditions is required to exclude the recombination-limited or diffusion-limited regimes being the limiting factors for the step coverage.[34]

7.4 Conclusions

In this study, a plasma enhanced atomic layer deposition process for the deposition of HfO_2 thin films using a hafnium precursor [$HfCp(NMe_2)_3$] comprising cyclopentadienyl-alkylamido ligands in combination with O_2 plasma has been evaluated. The growth characteristics clearly show the high thermal stability and high growth rate of the used precursor combined with O_2 plasma yielding a high GPC value of ~1.1 Å/cycle over a wide ALD temperature range of 150 °C - 400 °C. High purity HfO_2 thin films were obtained even at fairly low deposition temperatures with carbon and hydrogen residual impurity contents below 2 at% and 3.5 at% respectively for the whole range of substrate stage temperature investigated. A high substrate stage temperature of 400 °C resulted in fully crystalline, predominantly monoclinic as-deposited HfO_2 thin films with a high refractive index and a smooth surface. It was also found that the $HfCp(NMe_2)_3$ in combination with O_2 plasma requires shorter ALD cycle time relatively as compared to the ALD process using H_2O as oxidizing agent and therefore the plasma - enhanced ALD process offers a promising and viable method complementary to the thermal ALD process for producing high quality HfO_2 thin films.

Acknowledgements

The authors gratefully acknowledge Cristian van Helvoirt for technical assistance, Dr. Harm Knoops, Vincent Vandalon for fruitful discussion and Lam Research for providing substrates with HAR trench structures. We would also like to acknowledge AirLiquide for providing the Hf precursor. Additionally, we would like to acknowledge W. Keuning and Dr. B. Barcones for the FIB sample preparation and Solliance Solar Research for funding the TEM facility. One of the authors (W.M.M. Kessels) would like to acknowledge ‘Gravitation project’ for making this research work possible. This work is part of the Research Centre for Integrated Nanophotonics (NWO-578467 024.002.033), which is partly financed by the Netherlands Organization for Scientific Research (NWO).

Appendix

Table A.7.1 The atomic concentration of C and N contents with increasing substrate stage temperatures; d.l. stands for 'detection limit'

Substrate stage temp. (°C)	N content from XPS (at%)	C content from XPS (at%)
150	0.8 ± 0.1	1.7 ± 0.1
200	0.7	1.0
250	0.6	0.7
300	0.6	0.6
350	0.5	below d.l.
400	0.5	below d.l.

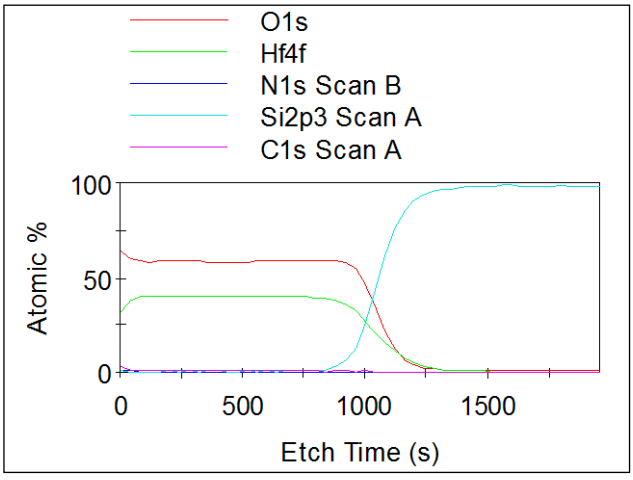


Figure A.7.1 The atomic concentration of ALD grown HfO_2 film at deposition temperature of 400 °C obtained after XPS depth profiling. A very low atomic concentration of N (< 1 at%) and C (< 2 at%) was obtained for the whole deposition temperature range (150 °C - 400 °C) as shown in Table 7.1 (in the main text).

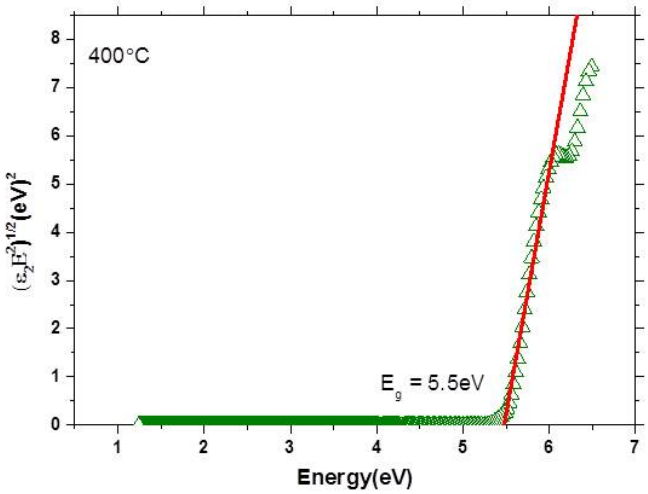


Figure A.7.2 A Tauc plot of $(\varepsilon_2E^2)^{1/2}$ vs photon energy for a HfO_2 thin film deposited at substrate temperature of 400 °C. An indirect optical band gap value (E_g) of ~ 5.5eV was extracted by extrapolating the linear part to zero absorption (HfO_2 was considered as an indirect band gap material).

References

1. M. Houssa, L. Pantisano, L. Å. Ragnarsson, R. Degraeve, T. Schram, G. Pourtois, S. De Gendt, G. Groeseneken and M. M. Heyns, *Materials Science and Engineering: R: Reports*, 2006, **51**, 37-85.
2. E. P. Gusev, C. Cabral Jr, M. Copel, C. D'Emic and M. Gribelyuk, *Microelectronic Engineering*, 2003, **69**, 145-151.
3. M. Cho, H. B. Park, J. Park, S. W. Lee, C. S. Hwang, G. H. Jang and J. Jeong, *Applied Physics Letters*, 2003, **83**, 5503-5505.
4. G. D. Wilk, R. M. Wallace and J. M. Anthony, *Journal of Applied Physics*, 2001, **89**, 5243-5275.
5. M. Gutowski, J. E. Jaffe, C.-L. Liu, M. Stoker, R. I. Hegde, R. S. Rai and P. J. Tobin, *Applied Physics Letters*, 2002, **80**, 1897-1899.
6. B. Radisavljevic, A. Radenovic and J. Brivio, *Nature Nanotechnology*, 2011, **6**, 147-150.
7. V. Djara, M. Sousa, N. Dordevic, L. Czornomaz, V. Deshpande, C. Marchiori, E. Uccelli, D. Caimi, C. Rossel and J. Fompeyrine, *Microelectronic Engineering*, 2015, **147**, 231-234.
8. M. Berdova, C. Wiemer, A. Lamperti, G. Tallarida, E. Cianci, L. Lamagna, S. Losa, S. Rossini, R. Somaschini, S. Gioveni, M. Fanciulli and S. Franssila, *Applied Surface Science*, 2016, **368**, 470-476.
9. L. Zhang, H. Nakanotani, K. Yoshida and C. Adachi, *Organic Electronics*, 2014, **15**, 1815-1821.

10. W.-J. Yoon and P. R. Berger, *Organic Electronics*, 2010, **11**, 1719-1722.
11. S. M. George, *Chemical Reviews*, 2010, **110**, 111-131.
12. M. Ritala, M. Leskelä, L. Niinistö, T. Prohaska, G. Friedbacher and M. Grasserbauer, *Thin Solid Films*, 1994, **250**, 72-80.
13. K. Kukli, M. Ritala, T. Sajavaara, J. Keinonen and M. Leskelä, *Thin Solid Films*, 2002, **416**, 72-79.
14. H. B. Park, M. Cho, J. Park, S. W. Lee, C. S. Hwang, J.-P. Kim, J.-H. Lee, N.-I. Lee, H.-K. Kang, J.-C. Lee and S.-J. Oh, *Journal of Applied Physics*, 2003, **94**, 3641-3647.
15. J. J. Ganem, I. Trimaille, I. C. Vickridge, D. Blin and F. Martin, *Nuclear Instruments and Methods in Physics Research Section B: Beam Interactions with Materials and Atoms*, 2004, **219–220**, 856-861.
16. J. Niinistö, K. Kukli, M. Heikkilä, M. Ritala and M. Leskelä, *Advanced Engineering Materials*, 2009, **11**, 223-234.
17. K. Kukli, M. Ritala, T. Sajavaara, J. Keinonen and M. Leskelä, *Chemical Vapor Deposition*, 2002, **8**, 199-204.
18. D. M. Hausmann, E. Kim, J. Becker and R. G. Gordon, *Chemistry of Materials*, 2002, **14**, 4350-4358.
19. Y. Senzaki, S. Park and H. Chatham, *J. Vac. Sci. Technol. A*, 2004, **22**, 1175-1181.
20. S. B. S. Heil, V. J. L. Hemmen and C. J. Hodson, *Journal of Vacuum Science & Technology A*, 2007, **25**, 1357-1366.
21. J. Niinistö, M. Putkonen, L. Niinistö, S. L. Stoll, K. Kukli, T. Sajavaara, M. Ritala and M. Leskelä, *Journal of Materials Chemistry*, 2005, **15**, 2271-2275.
22. J. Niinistö, M. Putkonen, L. Niinistö and F. Song, *Chem. Mater.*, 2007, **19**, 3319-3324.
23. S. Consiglio, R. D. Clark and G. Nakamura, *J. Vac. Sci. Technol. A*, 2012, **30**, 01A119.
24. J. Niinistö, M. Mäntymäki, K. Kukli, L. Costelle, E. Puukilainen, M. Ritala and M. Leskelä, *Journal of Crystal Growth*, 2010, **312**, 245-249.
25. E. Granneman, P. Fischer, D. Pierreux, H. Terhorst and P. Zagwijn, *Surface and Coatings Technology*, 2007, **201**, 8899-8907.
26. L. Aarik, H. Alles, A. Aidla, T. Kahro, K. Kukli and J. Niinistö, *Thin Solid Films*, 2014, **565**, 37-44.
27. A. Matin, A. B. Robert, M. P. Robert and D. Madan, *Nanotechnology*, 2015, **26**, 115202.
28. H. B. Profijt, S. E. Potts and M. C. M. de Sanden, *J. Vac. Sci. Technol. A*, 2011, **29**, 050801.
29. N. Blasco, personal communication.
30. M. Choi, J. L. Lyons, A. Janotti and C. G. Van de Walle, *Applied Physics Letters*, 2013, **102**, 142902.
31. G. Niu, H.-D. Kim, R. Roelofs, E. Perez, M. A. Schubert, P. Zaumseil, I. Costina and C. Wenger, *Scientific Reports*, 2016, **6**, 28155.
32. V. Longo, N. Leick, F. Roozeboom and W. M. M. Kessels, *ECS Journal of Solid State Science and Technology*, 2012, **2**, N15-N22.
33. H. B. Profijt, M. C. M. van de Sanden and W. M. M. Kessels, *Electrochemical and Solid-State Letters*, 2011, **15**, G1-G3.
34. L. E. Knoops H. C. M., van de Sanden M. C. M., Kessels W. M. M., *J. Electrochem. Soc.* , 2010, **157**, G241-G249.

8

Conclusions and Outlook

Atomic layer deposition (ALD) is an emerging technique for the synthesis of 2-D materials beyond graphene. In this dissertation, different aspects of ALD process development for a 2-D material, i.e. MoS_2, have been studied. Furthermore, the ALD synthesized MoS_2 films have been implemented as electrocatalysts for hydrogen evolution reaction during water splitting and as the channel in a proof-of-principle transistor device. From this work, the following general conclusions can be drawn:

- Wafer scale, highly uniform 2-D MoS_2 films can be synthesized with a precise thickness control ranging from a monolayer to bulk using plasma-enhanced ALD (PEALD). Plasma-enhancement in the co-reactant step (i.e. H_2S based plasma) enables the yield of as-synthesized crystalline 2-D MoS_2 film at relatively low temperature (300 - 450 °C) which otherwise, is only possible at high temperature (> 600 °C) when using techniques like chemical vapor deposition. Furthermore, besides enabling ultimate control over thickness, this work shows that PEALD allows to tune the film morphology, wetting and chemical composition by tuning the process parameters. This tuning of properties has been leveraged to demonstrate successful applications of PEALD synthesized MoS_2 films for electrocatalysis.

- ALD can be combined with a high temperature thermal sulphurization process to yield the high quality, basal plane oriented films. The number of MoS_2 layers could be precisely controlled by tuning the number of ALD cycles for the parent MoO_x films. The use of low temperature during the PEALD process makes it compatible with the conventional e-beam lithography resist. The integrative approach of combining PEALD and

thermal sulphurization thus makes it possible to obtain patterned MoS_2 films on device ready substrates eliminating the need of any transfer/etch step which generally act as a source of contamination and thus resulting in the degradation of film properties.

One of the biggest advantages of using ALD for the synthesis of 2-D materials is its ability to offer atomic level thickness control on a wafer scale. Furthermore, the film properties can be controlled in a facile way by modification of the process parameters. Based on the work presented in this thesis, a brief summary of each chapter is given as follows:

- In **Chapter 3**, a low temperature PEALD process for synthesizing uniform, high quality 2-D MoS_2 films over large area has been introduced. The precise thickness control down to a monolayer and the tuneability of morphology of the 2-D layers by varying the growth temperature from 150 – 450 °C have been achieved. The morphology transformation from in-plane to out-of-plane oriented films has been observed at 450 °C. Based on the transmission electron microscopy (TEM) analysis, it can be concluded that the enhanced precursor adsorption on the highly energetic edge sites as compared to basal planes of MoS_2 can play a major role in the transformation to out-of-plane oriented films. The excellent control over morphology attained by PEALD is leveraged in electrocatalysis using the hydrogen evolution reaction (HER) where the out-of-plane oriented films outperform flat, in-plane oriented films. These results offer the opportunity of using PEALD to not only realize the uniform, large area growth of 2-D materials but also to control the film morphology for multiple applications.

- The use of a plasma co-reactant during the second half cycle of ALD process provides a wide parameter space for material processing. The plasma parameters thus can have a number of effects on film properties like density, composition *etc.*[1] In **Chapter 4**, it has been demonstrated that the morphology and wettability of out-of-plane MoS_2 nanostructures can be tuned by varying the plasma parameters during PEALD. The modulation of plasma gas composition and substrate bias during PEALD can be used to alter the film morphology in a controlled way at the nanoscale with chemical

properties intact. This alteration of morphology can be leveraged to tune the water contact angle ranging from 109° to near superhydrophobic 146° which offers to contribute towards advancement of future applications utilizing MoS_2 based nano-structured surfaces.

- Apart from the out-of-plane oriented films, amorphous molybdenum sulphide (MoS_x) films synthesized by PEALD also deliver excellent HER performance, as is discussed in **Chapter 5.** The change in structural properties of predominantly amorphous MoS_x synthesized at 250 °C compared to nano-crystalline material (synthesized at 450 °C) results in better HER performance. The use of PEALD allows to conformally coat the HER relevant high surface area substrates like carbon fiber paper. A high current density (10 mA/cm^2) at low overpotential (~ 235 mV) has been achieved. The X-ray photo electron spectroscopy analysis has shown the presence of S_2^{2-} species (sulphur dimers) in MoS_x synthesized at 250 °C. Furthermore, the extended X-ray absorption fine spectroscopy (EXAFS) analysis has revealed a peak which most likely corresponds to the presence of distorted Mo - S bond in MoS_x films. Based on these results, it has been concluded that the structural differences collectively might render the predominantly amorphous MoS_x films a higher HER activity. In a nutshell, PEALD has been demonstrated as a well suited tool to synthesize 2-D materials based high performance electrocatalysts for HER applications.

One of the other approaches to synthesize high quality 2-D MoS_2 films is to combine atomic layer deposition with thermal sulphurization. This allows to precisely control the number of layers in MoS_2 films while achieving high quality crystalline films with excellent properties.

- To enable the large area and patternable synthesis of MoS_2, a method combining low temperature (50°C) PEALD process to first deposit ultra-thin MoO_x films and a subsequent high temperature (900°C) thermal sulphurization is introduced in **Chapter 6**. The horizontal basal plane oriented crystalline 2-D layers with a grain size up to ~ 50 nm have been attained. Importantly, the number of layers in MoS_2 could be precisely controlled by tuning the number

of ALD cycles for the parent MoO_x films in a facile way. Using the combined approach, it is possible to conformally coat 2-D MoS_2 layers on high aspect ratio trench structures. The usage of low temperature during PEALD allows for an e-beam lithography compatible process to obtain patterned MoS_2 films with high fidelity. The patterned MoS_2 films have been directly acquired on device ready substrates omitting the need for any etching and transfer step which keeps the film surface pristine and less prone to contamination. This approach might offer opportunities for device applications and to assemble 2-D heterostructures.

- In 2-D materials, the charge carriers are within a confined space and the Coulomb/charged impurities are randomly distributed at the channel/dielectric interface. The charge carriers thus get scattered via the long-range Coulomb interaction with the charged impurities. In literature, it has been demonstrated that the capping of MoS_2 with ALD deposited HfO_2 suppresses the Coulomb scattering resulting in superior device performance.[2] Keeping this in perspective, in **Chapter 7**, a plasma enhanced atomic layer deposition process is introduced for the deposition of HfO_2 thin films using a metal precursor comprising cyclopentadienyl-alkylamido ligands [$HfCp(NMe_2)_3$] in combination with O_2 plasma. The high stability of the used metal precursor allows for a wide processing temperature range (100 - 400 °C) resulting in both amorphous and polycrystalline HfO_2 thin films. The high quality nature of the as-deposited films offers opportunity for their integration with 2-D MoS_2 films and advance towards device applications.

Outlook

The results obtained in this thesis work illustrate that PEALD, both direct and combined with thermal sulphurization, is a promising method for the synthesis of high quality MoS_2 over large area and offer opportunities for myriad device applications. This work can lead to exciting future research areas to be explored. The following examples are only a few of the numerous possible directions which can be investigated for continued research on the topic of atomic layer deposition of 2-D materials:

From Direct ALD perspective

- ALD, besides offering excellent thickness control and highly conformal films is an excellent method for doping the films by introducing an additional dose of the desired dopant during ALD cycle. For MoS_2 films, it has been shown in literature that the doping with some metals like Nb or Mn results in the improvement of electrical properties.[3, 4] Similar kind of doping approach can be adopted during PEALD process to investigate the effect of dopants on the electrical properties of the as synthesized MoS_2 films. Furthermore, the post processing of as-synthesized MoS_2 films is also an area of great interest. For example, the electrocatalytic properties of the out-of-plane oriented MoS_2 films (Chapter 3) can be tailored by decorating them with nanoparticles of Pt and Co using ALD processes. Pt is one of the best known electrocatalysts and therefore a high HER performance can be expected from such Pt/MoS_2 composites. Likewise, it was demonstrated that the ALD coating of TiO_2 on the basal planes of MoS_2 had a positive impact on their HER performance.[5] It can thus be speculated that the ALD coating of TiO_2 might enhance the HER performance of out-of-plane oriented MoS_2 films synthesized in this thesis work and therefore this is worth investigating.

From Indirect ALD and device fabrication perspective

- The 2-D MoS_2 film synthesized using PEALD and thermal sulphurization is polycrystalline in nature with a grain size up to 50 nm. To further improve the FET device performance, different approaches for enhancement of grain size are worth investigating. One method could be to reduce the nucleation density of MoO_x species on SiO_2/Si substrates during ALD process by implementing inhibitor molecules to reduce the density of available surface sites for Mo precursor. This could enhance grain boundary mobility in the lateral direction ultimately resulting in larger grain sizes. Furthermore, single-crystal sapphire and GaN can be investigated as substrates for the synthesis of MoS_2 films. These substrates have a low lattice mismatch and high commensurability with MoS_2 which can suppress the random crystallite orientation resulting in well-defined grain boundaries. For these substrates, it is possible to devise top-gate configuration for fabricating FET devices.

- From a device point of view, the exploration of different dielectric environments either as top gate oxide or capping layer (to suppress the coulombic charge scattering for possible increase in mobility) is also of interest. To this purpose, thermal ALD grown Al_2O_3, HfO_2 or polymers can be investigated. For example, it has been shown that for $MoSe_2$ based FET devices, the use of polymer parylene as a dielectric resulted in 2-3 fold enhancement in mobility.[6] Furthermore, a number of metal contacts to MoS_2 can be explored aiming at reduced contact resistance. In this context, the graphene/metal composite and Mo as metal contacts to MoS_2 are most attractive candidates for investigation as they have been shown to result in low contact resistances and high device performance.[7, 8]

From materials development perspective

- The method devised for patterned synthesis of MoS_2 can be extended to assemble 2-D heterostructures on a large scale. The fabrication of both vertical and lateral heterostructures is possible using the schematic shown in Figure 8.1. In this schematic, the steps I - IV remain essentially the same as described in Chapter 6 where the patterned islands of MoO_x are obtained. The e-beam lithography patterning step needs to be repeated then to attain the patterned PMMA according to the desired profile i.e. for vertical or lateral heterostructure (step V - VI). From this point onwards, the low temperature PEALD for WO_x can be leveraged to deposit WO_x film uniformly without damaging PMMA (step VII). It is to be noted that a low temperature PEALD process for WO_x has already been developed in our group[9] which can be readily incorporated in the proposed process flow. The standard lift-off technique would result in patterned lateral or vertical heterostructures of MoO_x/WO_x which can be subjected to high temperature thermal sulphurization to acquire final 2-D MoS_2/WS_2 van der Waals heterostructures. The heterostructures have been shown for exciting future applications like interband tunneling, optospintronics *etc.*[10, 11] and therefore the fabrication of such heterostructures with controlled thickness might be an valuable attribute. Our approach can potentially be expanded for assembly of other 2-D materials based heterostructures.

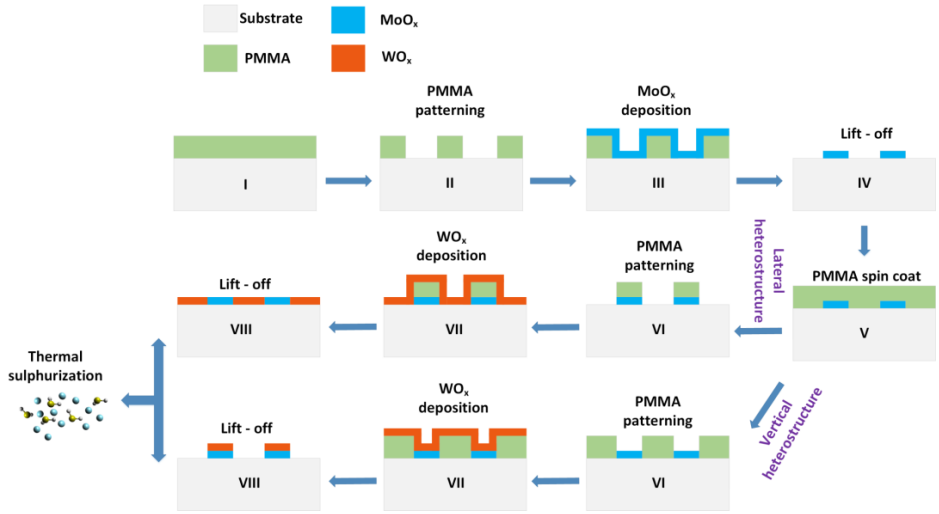


Figure 8.1 The schematic process flow for fabrication of lateral and vertical 2-D van der Waals heterostructures.

References

1. H. B. Profijt, S. E. Potts and M. C. M. de Sanden, *J. Vac. Sci. Technol. A*, 2011, **29**, 050801.
2. B. Radisavljevic, A. Radenovic and J. Brivio, *Nature Nanotechnology*, 2011, **6**, 147-150.
3. M. R. Laskar, D. N. Nath, L. Ma, E. W. Lee, C. H. Lee, T. Kent, Z. Yang, R. Mishra, M. A. Roldan, J.-C. Idrobo, S. T. Pantelides, S. J. Pennycook, R. C. Myers, Y. Wu and S. Rajan, *Applied Physics Letters*, 2014, **104**, 092104.
4. H. Ce, J. Yibo, W. Weiyi, T. Lei, S. Chaoyu and X. Faxian, *Journal of Semiconductors*, 2017, **38**, 033004.
5. Y. Kim, D. H. K. Jackson, D. Lee, M. Choi, T.-W. Kim, S.-Y. Jeong, H.-J. Chae, H. W. Kim, N. Park, H. Chang, T. F. Kuech and H. J. Kim, *Advanced Functional Materials*, 2017, **27**, 1701825-n/a.
6. S.-L. Li, K. Tsukagoshi, E. Orgiu and P. Samorì, *Chemical Society Reviews*, 2016, **45**, 118-151.
7. W. S. Leong, X. Luo, Y. Li, K. H. Khoo, S. Y. Quek and J. T. L. Thong, *ACS Nano*, 2015, **9**, 869-877.
8. J. Kang, W. Liu and K. Banerjee, *Applied Physics Letters*, 2014, **104**, 093106.
9. S. Balasubramanyam, A. Sharma, V. Vandalon, H. C. M. Knoops, W. M. M. Kessels and A. A. Bol, *Journal of Vacuum Science & Technology A*, 2017, **36**, 01B103.
10. A. Nourbakhsh, A. Zubair, M. S. Dresselhaus and T. Palacios, *Nano Letters*, 2016, **16**, 1359-1366.
11. M. Gmitra and J. Fabian, *Physical Review B - Condensed Matter and Materials Physics*, 2015, **92**.

Summary

The landmark invention of graphene in 2009 by Geim and Novoselov has stimulated the exploration of other 2-D materials beyond graphene in a quest for future generation nano-electronics. Besides graphene, molybdenum disulphide (MoS_2), a natural semiconductor, is one of the most studied layered nanomaterials because of its earth abundance, stability in ambient and direct band gap in the monolayer regime. This makes MoS_2 an interesting candidate for future (opto-)electronics applications. Additionally, when the MoS_2 basal planes are oriented out-of-plane, the active edge sites of the basal planes provide a unique opportunity for electrocatalytic applications. However, the synthesis and precise control over the thickness and morphology of these layers at the nano-scale over large areas is still a major challenge. Atomic layer deposition (ALD) is a preparation method for thin films which offers a precise thickness control down to a sub-monolayer and is instrumental for synthesis of 2-D materials. Therefore, the focus of this thesis is to explore the potential of plasma-enhanced ALD (PEALD) process, both in direct and indirect way, for synthesis of 2-D MoS_2 over large area with precise thickness control.

In Chapter 3, a low-temperature plasma-enhanced ALD (PEALD) process was presented to synthesize large area, uniform mono-to-few layered MoS_2 films. The characteristic self-limiting ALD growth with a growth-per-cycle of 0.1 nm/cycle and precise thickness control down to a monolayer combined with excellent wafer scale uniformity was demonstrated. The transformation in film morphology from in-plane 2-D to out-of-plane oriented 3-D layers as a function of growth temperature was observed. A model based on high-resolution transmission electron microscopy analysis was hypothesized to elucidate the film morphology transformation at 450 °C. Therefore, an excellent control not only over thickness but also over morphology could be attained, which was showcased in electrocatalysis where out-of-plane oriented films outperformed in-plane oriented films.

The surface wettability of out-of-plane oriented films can play a crucial role in determining its electrocatalytic properties e.g. hydrogen evolution reaction (HER). It was demonstrated in Chapter 4 that the tuneable wettability of MoS_2 nanostructures

could be attained in a facile way by modulating the plasma gas composition and application of substrate bias (mainly affecting ion energy) during the PEALD process. While a wide range (109° - 133°) of tuneable water contact angles (WCA) was obtained on SiO_2/Si substrates, a close to superhydrophobic (~146°) WCA was achievable on HER relevant carbon fibre paper substrates.

Apart from the out-of-plane oriented films, amorphous molybdenum sulphide (MoS_x) films synthesized by PEALD also deliver excellent HER performance, shown in Chapter 5. A high current density (10 mA/cm^2) at low overpotential (~ 235 mV) for predominantly amorphous MoS_x films was achieved. A detailed analysis using X-ray photoelectron spectroscopy and extended X-ray absorption fine spectroscopy (EXAFS) allowed to conclude that the change in structural properties of MoS_x film synthesized at 250°C compared to nano-crystalline material synthesized at higher temperature results in better HER performance.

Another approach to synthesize high quality, patternable MoS_2 ultra-thin films by combining PEALD and thermal sulphurization was also explored in chapter 6. In this case, low temperature PEALD (50°C) was first used to deposit MoO_x ultra-thin films. Subsequently, a high temperature (900°C) sulphurization process using a H_2S+Ar gas mixture was used to sulphurize MoO_x films. The in-plane, layered morphology variant of MoS_2 with strong photoluminescence signal from a monolayer was obtained. Large area uniformity and excellent conformality over high aspect ratio trench structures were displayed. The low temperature processing during the first step allowed the use of electron beam lithography to pattern MoO_x islands with high fidelity. These MoO_x islands were sulphurized to yield patterned MoS_2 on device ready SiO_2/Si substrates and thus eliminating any need for etching and/or transfer. The thickness of the final MoS_2 patterns could systematically be controlled just by tuning the number of ALD cycles for the parent MoO_x films.

For device integration, the deposition of high-κ dielectrics on MoS_2 has been demonstrated as a crucial step. A PEALD process using a combination of a heteroleptic precursor and O_2 plasma for depositing HfO_2 thin films was investigated in chapter 7. An extensive film characterization was carried out which revealed that both amorphous and polycrystalline HfO_2 films could be deposited depending on the deposition temperature. The film conformality was also assessed on 3-D high aspect ratio nanostructures.

In conclusion, it has been demonstrated that ALD is a viable technique to deposit high quality, large area MoS_2 with an excellent control over both thickness and morphology and therefore this technique is potentially extendable to other 2-D materials. Most of this thesis work has been or will be published in peer-review scientific journals, and provides opportunities for future integration of MoS_2 in devices for a broad range of applications.

Contributions of the author

The work presented in this thesis is the original work of the author (A. Sharma), with the following exceptions:

- TEM images in Chapter 3, 5, 6 and 7 were obtained by Dr. M.A. Verheijen.
- The electrocatalytic (HER) measurements presented in Chapter 3 and 5 were performed in the Chemistry department at TU/e with assistance from L. Wu under supervision of Dr. J.P. Hofmann.
- The fabrication of FET device given in Chapter 6 was performed by R. Mahlouji
- V. Longo and the author (A. Sharma) have contributed equally for the PEALD process of HfO_2 as described in Chapter 7.

List of publications

Low-temperature plasma-enhanced atomic layer deposition of 2-D MoS_2: large area, thickness control and tuneable morphology
Akhil Sharma, Marcel A. Verheijen, Longfei Wu, Saurabh Karwal, Vincent Vandalon, Harm C. M. Knoops, Ravi S. Sundaram, Jan P. Hofmann, W. M. M. (Erwin) Kessels, and Ageeth A. Bol, *Nanoscale* 2018, 10, 8615, DOI: 10.1039/c8nr02339e

Tuning the wettability of MoS_2 nanostructures using plasma enhanced atomic layer deposition
Akhil Sharma, Vincent Vandalon, Ageeth A. Bol, W.M.M. Kessels, *to be submitted*

High performance MoS_x thin films for hydrogen evolution reaction prepared by plasma enhanced atomic layer deposition
Akhil Sharma, Longfei Wu, Marcel A. Verheijen, Jan P. Hofmann, Wilhelmus M. M. (Erwin) Kessels and Ageeth A. Bol, *to be submitted*

PEALD enabled uniform large-area patternable growth of high quality MoS_2
A. Sharma, R. Mahlouji, L. Wu, V. Vandalon, M.A. Verheijen, S.H.G. Bloebaum, J.P. Hofmann, W. M. M. Kessels, and A.A. Bol, *to be submitted*

Atomic layer deposition of HfO_2 using $HfCp(NMe_2)_3$ and O_2 plasma
Akhil Sharma, Valentino Longo, Marcel A. Verheijen, Ageeth A. Bol, W.M.M. Kessels, *Journal of Vacuum Science & Technology A*, 2017, 35, 01B130, DOI: 10.1116/1.4972210

Other work

Tuning Material Properties of Oxides and Nitrides by Substrate Biasing during Plasma-Enhanced Atomic Layer Deposition on Planar and 3D Substrate Topographies
Tahsin Faraz, Harm C. M. Knoops, Marcel A. Verheijen, Cristian A. A. van Helvoirt, Saurabh Karwal, Akhil Sharma, Vivek Beladiya, Adriana Szeghalmi, Dennis M.

Hausmann, Jon Henri, Mariadriana Creatore, and Wilhelmus M. M. Kessels, *ACS Applied Materials & Interfaces* 2018**,** 10(15), 13158-13180, DOI: 10.1021/acsami.8b00183

Plasma-enhanced atomic layer deposition of tungsten oxide thin films using $(^tBuN)_2(Me_2N)_2W$ and O_2 plasma

Shashank Balasubramanyam, Akhil Sharma, Vincent Vandalon, Harm C. M. Knoops, Wilhelmus M. M. (Erwin) Kessels, and Ageeth A. Bol, Journal of Vacuum Science & Technology A 2018, 36, 01B103, DOI: 10.1116/1.4986202

Area-selective atomic layer deposition of platinum using photosensitive polyimide

Rene H.J. Vervuurt, Akhil Sharma, Yuqing Jiao, Wilhelmus (Erwin) M. M. Kessels, Ageeth A. Bol, Nanotechnology, 2016, 27, 405302, DOI: 10.1088/0957-4484/27/40/405302

Acknowledgements

I will remain highly thankful to all those who have helped me throughout the long journey of completion of my PhD thesis. Without their support, it would have been merely a far dream to do all the experimental work, analysis and writing for this thesis. I gratefully acknowledge everyone in the PMP group who has contributed for the excellently productive, congenial time that I spent in PMP.

My foremost gratitude goes to my promotor **Ageeth** who gave me the opportunity to work on a competitive project on 2-D materials. **Ageeth**, you have been an outstanding mentor, motivator throughout my journey at PMP which helped me to keep going without losing inspiration and complete my PhD dissertation. Your strict preference for 'quality' over 'quantity' taught me to do focused research. I highly appreciate the time invested by you in helping me to improve my writing skills and encourage to avoid difficult 'Archaic words'!! Next, I would like to express my sincere thanks to my 2nd promotor **Erwin** who always instilled an inspirational spirit in me. Your matchless dedication and an exemplary eye for detail makes PMP a great group. I appreciate the effort you have put into reviewing my work and help to improve and also to provide me the opportunity to complete this thesis. Next in this list, I am very much obliged to **Marcel** who has provided with the insightful TEM images and for fruitful discussions that led to the development of most of chapters in this dissertation. Thanks a lot for helping me to understand the results better and carrying a lot of TEM work for me (being in TEM business now, I understand much better the magnitude of workload to image and analyse the samples!!).

I would like to express my gratitude to **Fred** whom I met during my Master thesis project at Holst Centre and who actually guided me to become a part of PMP. Thanks for your motivation and inspiring me at the beginning of my PhD. I thank **Adriana** for our brief but insightful discussions about science, meditation and for motivating me to further sharpen my presentation skills.

I am highly thankful to my project collaborators **Longfei** and **Jan Philipp** from Chemistry department for being extremely co-operative, friendly and introducing me to the world of electrocatalysis. **Longfei**, besides all the work you have carried out for me,

it was personally a pleasure to work with you (including the visit to beam line at Saskatoon!). Your dedication for research and hard-working attitude is commendable and exemplary. Thank you and I wish you best of luck for your own thesis.

Going back in time, I would Iike to thank my PMP colleagues who helped me to orient well at the beginning of my PhD when we were located in *TNO* building. **Kashish** for helping me to understand the work culture**, Jan-Willem** for teaching me Raman, ellipsometry tools and for friendly company**, 'The Harm'** for his constant guidance throughout my PhD and fruitful discussions**, Srinath** for useful tips and sharing light moments**, Adrie** for supervising me at the very beginning for CNTs work. I would also like to thank the Italian crew: **Alberto, Ben, Valerio, Valentino** for all the fun time together both at work and outside work including our badminton games in the sports centre.

Now coming to *Flux* era**,** I would first like to thank our whole 2-D group: **Nick** and **René** for their knowledge sharing, fruitful discussions and involving me in their own projects. **Nick**, thanks for including me in your CNT work and for helping me with various work related issues throughout my PhD. Thanks to **René**, with whom I enjoyed working on a project together and who helped me setting up the initial experiments with the sulphur furnace in labtuin. Although not in 2-D team, I would like to thank **Martijn** for sharing his knowledge of the MoO_3 ALD process which served as an integral part of my 'indirect ALD' project. Also, thank you for always being friendly, nice and chatty!

Next, I would like to thank my colleagues who were directly involved in my PhD project. **Vincent**, words are not enough to thank you for being a very good friend, mentor, motivator. It doesn't matter whatever I required: explanation of physics, real (non-google) translation of my mails/letters from Dutch to English, squash partner, general integration and understanding of Dutch culture, long chats about food, culture, travel, life and countless things, you never disappointed me! Apart from an in-depth researcher, your diverse knowledge in Physics, computers, coding, technology, guns, cars, beers….is truly awe-inspiring. I am highly indebted to you for your immense help in shaping my PhD and your selfless effort to help me improve the writing part. I thoroughly enjoy our friendship on and off campus, thank you! My next acknowledgment is addressed to very friendly **Reyhaneh**, who has been an excellent colleague to work with. Thanks a lot for your constant support during my project and I highly appreciate your consistent efforts in the lab to get things done despite numerous hiccups! I also wish to thank you for being friendly and cheerful in the good times, caring and supportive in the bad times and for introducing me to the Persian culture,

language and history. Further, I have really enjoyed working together with other 2-D team members: **Shashank, Saravana, Eldad, Mahdi**. Our 'MoMo after MoMo' has always been very productive and I have learnt a lot from all you guys. Thanks a lot for your cooperation and knowledge sharing and best of luck to all of you for your own PhDs and future jobs.

It's time to acknowledge my office mates who have helped to keep the work spirit high and provided a great atmosphere. **Saurabh**, thank you for being a very good friend, an inexhaustible source of wisdom and for sharing the light moments in our native language which always helped to rejuvenate. I highly appreciate your help and contribution to my 'direct ALD' project, insightful discussions and I would like to wish you best of luck for your own PhD and job. As another native language speaker, I would like to thank **Dibya** for her nice and friendly company at times at coffee corner. I wish to thank **Alfredo** and **Tahsin** for being sources of inspiration, good examples of in-depth researchers and for some fruitful work related discussions. **Morteza**, thanks a lot for your help with contact angle measurements and for friendly discussions especially in the last phase of PhD which helped to keep the morale high. I wish you good luck for your own PhD and future job. I would like to thank all of you roomies (including **Claire, Bart K.**) for sharing jokes, laughs and maintaining a healthy environment.

I am very much obliged to our PMP technicians - **Janneke, Cristian, Jeroen, Caspar and Joris** for their constant technical support in the lab/clean room. **Cristian**, thank you for always being kind, nice and cheerful. Your technical expertise and great help with SE, XPS, XRD was often required and has been immensely useful for me throughout PhD. Thanks for your great sense of humour and I always enjoyed talking to you about variety of things. **Jeroen**, your high priority support for our beloved Flexal-2D is highly appreciated. Also, thanks a lot for friendly interactions inside cleanroom that kept my work spirit high. I would like to thank **Janneke** for always being supportive and helpful in the lab. I would also like to acknowledge the technical skills of **Caspar** and **Joris** in supporting me for setting up of sulphur furnace in the lab tuin and providing the technical support whenever needed. I gratefully acknowledge PMP group secretaries, **Lianne** and **Jeanne,** for all the administrative help during my PhD time and for always being extremely friendly, welcoming and caring.

I thank my bachelor students: **Nina** and **Stijn** for the good time together and to bring out my supervisor skills. Although their work with sulphur furnace in the labtuin could

did not result in a chapter of this thesis, it served as a good basis for learning and eventually for the ‘indirect ALD’ project.

In the end, I would like to thank my friends and family who have constantly supported me to fulfil my ambition. **Gagandeep, Pradeep, Jaspreet** and other close friends, thank you for inspiring me to take on this journey and keeping my spirit high. Mom, dad and my younger brother **Akash** have been inspirational sources of energy to keep me strive for fulfilling my ambition. Thanks for your everlasting support, love and belief in me that brought me to completion of this thesis. Finally, this thesis could not be completed without absolutely invaluable contribution of my wife **Sarita,** who was always there through my thick and thin and supporting to the very end to see me make it happen.

Curriculum Vitae

November 16, 1987	Born in Manoh Sihal, India
2005 - 2009	Bachelor of Technology Electronics and Communication Engineering Punjab Technical University, India
2010 - 2013	Master of Science Micro and Nano Systems Chemnitz University of Technology, Germany Master thesis project at Holst Centre/TNO Eindhoven, The Netherlands
2014 - 2018	PhD Applied Physics Plasma & Materials Processing group, Eindhoven University of Technology, The Netherlands
2018 - Present	Operations Engineer TEM Thermo Fisher Scientific Eindhoven, The Netherlands